Beam Dynamics in Spreaders for Future X-ray Free Electron Laser Facilities

Thesis submitted in accordance with the requirements of

the University of Liverpool for the degree of Doctor in Philosophy
by
Deepa Angal-Kalinin

March 2017

Abstract

Beam Dynamics in Spreaders for Future X-ray Free Electron Laser Facilities

Deepa Angal-Kalinin

This thesis describes various design options for beam spreaders to allow the inclusion of multiple beam lines as an integral part of X-ray Free Electron Laser (FEL) facilities. The accelerator configuration driving an X-ray FEL follows a linear geometry so as to maintain the ultra-bright properties of the electron beam generated at the injector. Bending the beam is typically restricted only to the bunch compressor chicane in order to avoid an increase in transverse emittance due to the emission of coherent synchrotron radiation. Unlike storage ring based light sources, X-ray FELs serve either one experiment at a time or a number of experiments (quasi-simultaneously) by splitting the radiation from a single FEL line; the radiation pulse repetition rate is set by the injector and the technology used for acceleration. Multiple beam lines provide flexibility in experiments and provide access for a greater number of users. However, in providing multiple beam lines, bending the electron beam is unavoidable and its high quality (i.e. low emittance, low energy spread and high peak current) must be ensured by very careful design of the beam spreader. Two main aspects of the beam spreader design (namely, the options for switching and the lattice design) have been studied and are presented here in detail. Two lattice design concepts, one based on a Triple Bend Achromat magnetic lattice and the other based on a Double Bend Achromat magnetic lattice, are discussed. The relative merits, advantages and disadvantages of these design options are detailed, including mitigation of the effects from coherent synchrotron radiation which include increases in both the beam emittance and energy spread. Experimental studies related to the Triple Bend Achromat arc on the ALICE facility are used to recommend beam diagnostics and instrumentation in different spreader design concepts. The results presented in this thesis will be central to the design of an optimised beam spreader for any future UK X-FEL facility.

Contents

Abstract **i**

Contents **vi**

List of Figures **xi**

List of Tables **xiii**

Acknowledgements **xv**

1 Accelerators as Photon Sources **1**

- 1.1 Historical Background to Synchrotron Light Sources 1
- 1.2 Undulators and Undulator Radiation 5
  - 1.2.1 Magnetic Field in an Undulator 5
  - 1.2.2 Electron Trajectory in an Undulator 7
  - 1.2.3 Characteristics of Spontaneous Undulator Radiation 8
- 1.3 Free Electron Lasers 11
  - 1.3.1 Types of FELs 11
  - 1.3.2 Low Gain FELs 13
  - 1.3.3 High Gain FELs 19
  - 1.3.4 Requirements of Electron Beams for FELs 21
- 1.4 Summary 24
- 1.5 Motivation 24
- 1.6 Thesis Outline and Author's Contributions 25

2 Beam Optics and Beam Parameter Definitions **27**

- 2.1 Beam Optics 27
  - 2.1.1 The Co-ordinate System in a Beam Line 27
  - 2.1.2 Beam Rigidity and Expansion of Magnetic Field Seen by the Beam 29
- 2.2 Equation of Motion of an Electron in an Accelerator 31
  - 2.2.1 Matrix Formalism 32
  - 2.2.2 Amplitude and Phase Formalism 39

2.2.3 Transformation of Courant-Snyder Parameters 39
2.2.4 Lattice Design Cells 40
2.3 Electron Beam Distribution 44
2.4 Errors on Magnetic Elements 45
2.5 Initial Beam Parameters for Beam Line Design 46
2.6 Definition of Beam Time Structure 47
2.7 Summary 48

3 FEL Configurations and Beam Dynamics Challenges 49
3.1 Potentially Limiting Beam Dynamics Effects 49
3.1.1 Space Charge 50
3.1.2 Wake Fields 51
3.1.3 Coherent Synchrotron Radiation 51
3.1.4 Incoherent Synchrotron Radiation 53
3.2 Facility Configuration Options 53
3.2.1 Single Pass Linac 54
3.2.2 Re-circulating Linac 55
3.2.3 Energy Recovery Linacs 56
3.2.4 Comparison of Issues in Different Configurations 58
3.3 Subsystems of Single Pass Linac 59
3.3.1 Injector 59
3.3.2 Bunch Compressor 63
3.3.3 Lineariser 65
3.3.4 Example of Bunch Compression, Linearisation, CSR and Wakefields 67
3.3.5 Laser Heater 68
3.3.6 Linac 71
3.3.7 Collimation 72
3.3.8 Beam Spreader/Switchyard 73
3.3.9 FELs 74
3.3.10 Diagnostics 75
3.3.11 Beam Dump 75
3.4 Summary 76

4 Coherent Synchrotron Radiation 77
4.1 Introduction 77
4.2 Shielding due to the Vacuum Chamber 81
4.3 Tracking Including CSR 82
4.3.1 Implementation of 1-D CSR model in *elegant* 83
4.3.2 Convergence Tests for CSR in *elegant* 84
4.3.3 Example of Simulation of Coherent Synchrotron Radiation 87

4.4 Coherent Synchrotron Radiation Mitigation Techniques 91
    4.4.1 Introduction 91
    4.4.2 Optics Balance 92
    4.4.3 Example of Optics Balance 94
    4.4.4 Matrix Approach 95
4.5 Summary 97

5 Beam Spreader Designs **99**
5.1 Introduction 99
5.2 Survey of Beam Spreader Designs 100
    5.2.1 Linac Coherent Light Source - LCLS-I and LCLS-II 101
    5.2.2 FERMI at Elettra 103
    5.2.3 FLASH Facility at DESY 106
    5.2.4 European X-FEL 107
    5.2.5 SwissFEL at PSI 108
    5.2.6 SPring-8 Angstrom Compact free electron LAser (SACLA) . . . 109
    5.2.7 Shanghai X-FEL 110
    5.2.8 PAL X-FEL 111
    5.2.9 New Light Source (NLS) Project in the UK 111
5.3 Beam Spreader Design Considerations 113
    5.3.1 Options for Beam Switching 114
    5.3.2 Lattice Design Options 117
5.4 Beam Spreader Design Based on Triple Bend Achromat 118
    5.4.1 Beam Spreader at 2.2 GeV 118
    5.4.2 CSR Matrix Compensation Method 125
    5.4.3 Beam Tracking With Different Initial Beam Parameters 126
    5.4.4 Beam Spreader Design at 6.6 GeV 131
5.5 Beam Spreader Design Based on Double Bend Achromat 135
    5.5.1 Beam Spreader design at 2.2 GeV 135
    5.5.2 Beam Tracking With Different Initial Beam Parameters 143
    5.5.3 Beam Spreader Design at 6.6 GeV 145
5.6 Lattice Tolerances 148
    5.6.1 Tolerances for 2.2 GeV TBA lattice 148
    5.6.2 Tolerances for 2.2 GeV DBA Lattice 148
    5.6.3 Comparison of Tolerances 149
5.7 Requirements and Importance of Diagnostics and Instrumentation in Beam Spreader 153
5.8 Summary 157

6 Beam Dynamics Studies of ALICE 159

6.1 Background and Context 159

6.2 Overview of ALICE 159

6.3 Longitudinal Beam Transport 163

6.4 Experimental Studies 169

6.4.1 Time of Arrival Measurements 170

6.4.2 Dispersion Measurements 179

6.5 Performance Limitations and Diagnostics 181

6.6 Implications for Beam Spreader Designs 182

6.7 Summary 183

7 Summary, Conclusions and Future Work 185

7.1 Summary 185

7.2 Conclusions 186

7.3 Future Work 188

A Abbreviations and Acronyms 189

B RF Frequencies 191

Bibliography 204

List of Figures

1.1 Peak spectral brightness 4
1.2 Magnetic field of an undulator 6
1.3 Synchrotron radiation spectrum 8
1.4 Condition for constructive interference in an undulator 9
1.5 Phase space trajectory of an electron in low gain FEL 16
1.6 The lineshape curve of undulator radiation and the gain curve in low gain regime 19
1.7 FEL radiation power along the undulator 21

2.1 Co-ordinate system in beam transport line 28
2.2 Cross-section of dipole, quadrupole and sextupole magnets 30
2.3 Photograph of dipole, quadrupole and sextupole magnets 31
2.4 Sector and rectangular dipole magnet 35
2.5 Example of electron trajectory through a FODO beam line 37
2.6 The trace space ellipse of electron motion in a beam line. 37
2.7 Schematic of FODO cell. 41
2.8 Beam optics in FODO cell 41
2.9 Schematic of achromat with one quadrupole 42
2.10 Beam optics in achromat with one quadrupole 42
2.11 Schematic of achromat with quadrupole triplet 43
2.12 Beam optics in achromat with quadrupole triplet 43
2.13 Example of triple bend achromat 44
2.14 Beam optics in triple bend achromat 44
2.15 Beam time structure definitions 48

3.1 Radiation affecting the bunch in a dipole 52
3.2 Accelerator configurations for FEL facility 55
3.3 Generic schematic of FEL facility 61
3.4 Schematic of RF Photoinjector 62
3.5 Principle of bunch compression 63
3.6 Effect of RF curvature 66
3.7 Higher harmonic correction 67

3.8 Schematic of beam line for bunch compression 68
3.9 Bunch properties after bunch compression 68
3.10 Bunch properties after lineariser and wakefields without CSR 69
3.11 Bunch properties including lineariser and wakefields with CSR 70
3.12 Schematic of laser heater 71
3.13 Schematic of NLS spreader 74

4.1 Regimes of synchrotron radiation 79
4.2 Suppression of CSR by vacuum chamber shielding 82
4.3 Convergence tests for CSR induced emittance growth for 3° dipole . . . 85
4.4 Convergence tests for CSR induced emittance growth for 3° dipole . . . 86
4.5 Convergence tests for CSR induced emittance growth for 11.5° dipole . . 86
4.6 Convergence tests for CSR induced emittance growth for 6° dipole . . . 87
4.7 Beam optics in the beam line used for CSR tracking 87
4.8 Change in energy due to steady state CSR 88
4.9 Chage in energy due to steady state and transient CSR 89
4.10 Change in momentum offset and emittance due to CSR 90
4.11 Possible spreader design options 93
4.12 Beam optics in a beam spreader with parallel separation 95
4.13 Cancellation of CSR kicks using matrix formalism 96

5.1 Schematic of LCLS-I facility 104
5.2 Schematic of LCLS-II facility 104
5.3 Schematic of LCLS-I and LCLS-II 104
5.4 Schematic of proposed three way spreader for LCLS-II 105
5.5 Schematic of FERMI at Elettra 105
5.6 Schematic of the beam spreader at FERMI at ELETTRA 105
5.7 Schematic of FLASH facility at DESY 106
5.8 Schematic of European X-FEL at DESY 107
5.9 Schematic of European X-FEL spreader 107
5.10 Schematic of SwissFEL at PSI 108
5.11 Schematic layout of SwissFEL Athos Switchyard 109
5.12 Schematic of SACLA 110
5.13 Schematic of SINAP SXFEL at Shanghai 110
5.14 Schematic of PAL X-FEL in Korea 111
5.15 Schematic of NLS 112
5.16 Beam distribution based on resonant kicker at half of RF frequency . . . 115
5.17 Beam distribution based on high-Q RF deflector and optical delay at gun 116
5.18 Beam distribution based on high repetition rate kicker 116
5.19 Longitudinal phase space at the entry of NLS spreader 119

5.20 Schematic of NLS beam spreader 119
5.21 Schematic of multiple FEL beam lines using the TBA spreader design . . 120
5.22 Optics and tracking through NLS CDR beam spreader with CSR off and ISR on 121
5.23 Optics and tracking through NLS CDR beam spreader with CSR and ISR on 122
5.24 Second order terms in NLS spreader 123
5.25 Schematic of modified design of NLS spreader 123
5.26 Optics and tracking through modified NLS beam spreader with CSR and ISR on 124
5.27 Projected horizontal emittance for different bending angles in arc2 at 2.2 GeV 125
5.28 CSR compensation in arc2 using R-matrix method 126
5.29 Projected emittance in arc2 using R-matrix method 126
5.30 Tracked bunch for beam parameters optimised using R-matrix method . . 127
5.31 Tracking results with Gaussian bunch with different initial beam parameters 128
5.32 Tracking results with flat-top bunch for modified NLS spreader 129
5.33 Tracking results with flat-top bunch with different initial beam parameters 130
5.34 Schematic of TBA spreader at 6.6 GeV 131
5.35 Tracking results with CSR and ISR for TBA spreader at 6.6 GeV 132
5.36 Tracking results with only CSR for TBA spreader at 6.6 GeV 133
5.37 Tracking results with only ISR for TBA spreader at 6.6 GeV 133
5.38 Projected horizontal emittance for different bending angles in arc2 at 6.6 GeV 134
5.39 Schematic of single cell of FODO lattice. 135
5.40 Optics parameters of FODO cell 136
5.41 Phase advance and dispersion in FODO cell with dipoles 136
5.42 Schematic of a beam spreader using 3° dipoles 137
5.43 Tracking results for a beam spreader using 3° dipoles 138
5.44 Schematic of a beam spreader using 3° dipoles not maintaining correct phase advance 138
5.45 Tracking results for a beam spreader using 3° dipoles not maintaining correct phase advance 139
5.46 Schematic of multiple FEL beam lines using FODO based DBA design . . 141
5.47 Tracking results through DBA with 15° short dipoles 142
5.48 Tracking results through DBA with 15° long dipoles 142
5.49 Results of Gaussian bunch tracking with different initial beam parameters 144
5.50 Results of flat-top bunch tracking with different initial beam parameters . 144
5.51 Tracking results with ISR on and CSR off for DBA spreader based on 6° dipoles at 6.6 GeV 146

5.52 Tracking results with ISR off and CSR on for DBA spreader based on 6° dipoles at 6.6 GeV 146
5.53 Tracking results with both ISR and CSR on for DBA spreader based on 6° dipoles at 6.6ĠeV 146
5.54 Tracking results with ISR on and CSR off for DBA spreader based on 12° dipoles at 6.6 GeV. 147
5.55 Tracking results with ISR off and CSR on for DBA spreader based on 12° dipoles at 6.6 GeV. 147
5.56 Tracking results with both ISR and CSR on for DBA spreader based on 12° dipoles at 6.6 GeV. 147
5.57 DBA lattices used for comparison of tolerances 150
5.58 Optics for DBA lattices used for comparison of tolerances 150

6.1 Layout of ALICE 160
6.2 Optics parameters in ALICE 162
6.3 Beam energy and bunch length in ALICE starting from booster exit to beam dump. 162
6.4 ALICE lattice used for beam tracking 163
6.5 Details of ALICE ARC1 164
6.6 ALICE arc quadrupole dependence on R_{56} 165
6.7 Tunability of R_{56} in ALICE arc 166
6.8 Effect of sextupole offset in ALICE arc 167
6.9 Tracking of Gaussian bunch without ARC1 sextupoles 168
6.10 Tracking of Gaussian bunch with ARC1 sextupoles 169
6.11 Tracking with experimental injector settings without ARC1 sextupoles . . 170
6.12 Tracking with experimental injector settings with ARC1 sextupoles 171
6.13 Simulated transverse beam shape with and without ARC1 sextupoles . . 172
6.14 Screen images for ARC1 sextupole settings 172
6.15 Oscilloscope traces to measure time of arrival 173
6.16 Simulated and measured path length without powering sextupoles 173
6.17 Estimated values of R_{56} without sextupoles from path length 174
6.18 Estimated values of T_{566} without sextupoles from path length 174
6.19 Path length for different sextupole settings in ARC1 175
6.20 Simulated path length as a function of energy deviation for SEXT-01 on axis and horizontally offset by +5 mm. 175
6.21 Simulated path length as a function of energy for SEXT-01 on axis and horizontally offset by -5 mm. 176
6.22 Simulated R_{56} for SEXT-01 on axis, and for SEXT-01 offset horizontally by ±5 mm. 176

6.23 Simulated T_{566} for SEXT-01 on axis, and for SEXT-01 offset horizontally by ±5 mm. 177
6.24 Simulated and experimentally measured path length for different sextupole settings 177
6.25 Simulated and measured R_{56} for on and off-axis sextupole 178
6.26 Simulated T_{566} with SEXT-01 on axis and horizontally offset by +2.5 mm compared with the measured T_{566} at the exit of ARC1. 178
6.27 Measured beam positions in ARC1 without sextupole 179
6.28 Measured beam positions in ARC1 with sextupoles 179
6.29 Measured dispersion at BPM-06 as QUAD-01(04) strengths are varied. . 180
6.30 Oscilloscope traces of bunch charge and PI laser power 181
6.31 BPM signal showing variation along the bunch train 182

List of Tables

3.1 Design issues to consider in single pass and re-circulation/energy recovery linacs. 60

3.2 Measured properties of electron bunches and the associated diagnostics devices. 76

5.1 Operational and under construction X-ray FEL facilities 102

5.2 Beam spreader details of X-ray FEL facilities 103

5.3 Possible options for beam switching 114

5.4 Bunch Parameters at undulators at some X-ray FEL facilities 118

5.5 Comparison of DBA spreader lattices based on FODO. 140

5.6 Effect of errors on 2.2 GeV beam spreader based on TBA lattice. 149

5.7 Effect of errors on 2.2 GeV beam spreader based on 6° DBA lattice. . . . 151

5.8 Effect of errors on 2.2 GeV beam spreader based on 3° double DBA lattice. 152

5.9 Possible diagnostics and instrumentation and their locations in TBA and DBA (based on FODO) beam spreaders. 156

6.1 Main ALICE machine and beam parameters 162

6.2 Simulated and measured linear dispersion in ARC1 181

Acknowledgements

My first and foremost thanks go to my supervisor Andy Wolski. Without his patience, encouragement and guidance I wouldn't have been able to complete this thesis.

I am grateful to Swapan Chattopadhyay for pursuing me to register for a PhD (even though this only actually happened 25 years after it was first discussed - it would have been so much simpler to do it then for a number of reasons). My sincere thanks go to John Dainton for his optimism and inspiration which allowed me to keep my head above water during the times when I feared drowning. My genuine thanks go to Susan Smith and Elaine Seddon who gave me strength through their wisdom and steadfast support.

Special thanks go to Peter Williams for his help with the *elegant* code and numerous discussions about CSR, to James Jones for his help with Mathematica, to Frank Jackson for leading the longitudinal dynamics experiments on ALICE, to Bruno Muratori for many conversations related to beam spreader designs and to Neil Thompson for clarifying some FEL fundamentals. My appreciation also goes to ASTeC/STFC for funding my studies, to colleagues in ASTeC/Daresbury Laboratory/Cockcroft Institute for supporting me in many ways and to the ALICE, NLS and VELA/CLARA teams, for educating me on the challenges related to fourth generation light sources.

Underpinning all the above, my heartfelt thanks go to my daughter Darya and my family who supported me through trying times and often tolerated my irrational behaviour. Finally, my eternal gratitude goes to both my husband Alexander Kalinin, without whom I would not have ventured on this journey - I wouldn't be here and who I am today without him, and to my mother who instilled in me the importance of strong willpower and believed in me enormously. I feel sorry that neither could be here to see this thesis completed.

Chapter 1

Accelerators as Photon Sources

Over the past half century, tremendous progress has been made in the quality of radiation beams produced by particle accelerators, and synchrotron radiation sources have become a fundamental tool for research in several scientific disciplines. This chapter gives a brief account of the development of particle accelerators as photon sources, describes the basic principles of the latest accelerator based photon sources and summarises the requirements on accelerators to drive these radiation sources. Based on this background, the motivation for the work presented in this thesis is given in Section 1.5.

1.1 Historical Background to Synchrotron Light Sources

Even though accelerator based photon sources have been an indispensable tool for research for several decades, the foundations of the theory of synchrotron radiation were first developed by Liénard in 1898, more than a century ago. In his historic paper [1] he worked out the basic theory of synchrotron radiation and the formula for the rate of energy loss by an electron travelling in a circular path. This work was later extended by Wiechert in 1900 [2], resulting in the so-called “Liénard-Wiechert" potentials that are used to describe the time-varying electromagnetic fields emitted by a point-charge in arbitrary motion. The theory of synchrotron radiation was later expanded by Schott in his essay on Electromagnetic Radiation in 1912 [3], in which many properties of synchrotron radiation were derived, such as the frequency and angular distribution and polarisation state. The next important step in the history of radiation sources was made after more than three decades. In 1944, Iwanenko and Pomeranchuk published an article [4], in which they pointed out that electron accelerators are limited by radiation losses. In 1946, Blewett suggested a search for the radiation losses at the 100 MeV General Electric Betatron, but only indirect evidence was found in the observation of the shrinking orbit when the electrons approached energy of around 90 MeV [5]. A direct observation was not possible due to the opaque doughnut-shaped beam tube. In 1947, Pollock and his group completed a 70 MeV synchrotron at the same laboratory, where a 100 MeV betatron was built. This new machine was not entirely covered by an opaque shielding, so that there was the possibility to detect the radiation directly. As a result, Pollock and his group observed the radiation visually in the same year [6, 7]. The theoretical foundations developed and presented by Schwinger in his paper in 1949 [8] still provide a comprehensive reference on the properties of synchrotron radiation. A paper written by Blewett in 1998 on the 50^{th} anniversary of the first visual observation of synchrotron radiation summarises the scientific history of synchrotron radiation [9].

Originally, synchrotrons were used exclusively in high-energy physics or nuclear physics. However, synchrotron radiation is emitted whenever high-energy electrons are forced to travel in a circular orbit. This radiation which was originally seen as nuisance as it limited the maximum energy reach, was found to possess unique properties such as: a broad spectrum from microwaves to hard X-rays, high intensity, well-defined angular distribution, polarisation, pulsed time structure and high stability. These properties opened up the use of synchrotron radiation in a wide range of non-destructive, high-resolution, rapid, in-situ, real-time imaging and analysis techniques.

For users of synchrotron radiation, the important quantity is brightness of photons (also called brilliance). The spectral brightness describes the intensity of a radiation source taking into account its spectral purity and is given by:

$$B = \frac{\Phi}{4\pi^2 \Sigma_x \Sigma_{\theta x} \Sigma_y \Sigma_{\theta y}}, \tag{1.1}$$

where Φ is the spectral photon flux defined as the number of photons per second and within a specified spectral bandwidth, and $\Sigma_x, \Sigma_{\theta x}, \Sigma_y$ and $\Sigma_{\theta y}$ are measures of the transverse (x horizontal and y vertical) beam sizes and angular divergences of the electron and the photon beam. These are expressed as $\Sigma_x = \sqrt{\sigma^2_{x,photon} + \sigma^2_{x,electron}}$ and $\Sigma_{\theta x} = \sqrt{\sigma^2_{\theta x,photon} + \sigma^2_{\theta x,electron}}$, where σ_x and $\sigma_{\theta x}$ are the transverse rms sizes and divergences of the photon and electron beams in the horizontal plane x. Similar expressions can be written in the vertical plane y.

Synchrotron radiation sources have evolved through four generations since their first use. A comprehensive list of storage ring based light sources is given in [10]. Each generation has exceeded the performance of previous sources by an order of magnitude or more in an important parameter such as brightness, coherence (a fixed phase relationship between the electric field values at different locations or at different times), or pulse duration.

First-generation synchrotron light sources were basically beam lines built onto existing synchrotrons designed for particle physics experiments (electron-positron colliders) e.g. a 5 GeV synchrotron NINA at Daresbury Laboratory [11], the 6 GeV synchrotron at DESY, Hamburg [12], VEPP-3 in Novosibirsk [13], CESR at Cornell [14] as well as machines like Tantalus [15], which was designed as a test machine for advanced particle accelerator concepts and was operated as a synchrotron radiation user facility. The high energy electron-positron colliding-beam accelerators were operated to provide the highest possible collision rates while maintaining good beam quality, a condition that generally meant low beam currents. These facilities date from the early 1970s and at first there were just a few scientists using the radiation. Later on most high energy electron-positron colliders either included the synchrotron radiation facilities from the design stage or added them after beginning operation. Radiation from the bending (dipole) magnets of first generation rings provided about 10^5 times more tunable, continuum radiation than conventional sources, including rotating-anode X-ray tubes.

The brightness determines how much monochromatic radiation power can be focussed onto a target. Focusing the beam to a smaller size necessarily increases the beam divergence, and vice-versa; apertures can help reduce beam size and divergence but only at the expense of reduced flux. The best way to achieve high brightness therefore is by proper design of the source, i.e. the electron beam in the storage ring. The size and divergence of the electron beam are determined by the storage ring design. It was soon realized that optimized designs of rings could produce radiation with many special and desirable properties. This led to the development of the second generation of synchrotron light sources based on storage rings dedicated to synchrotron radiation applications, with the radiation mainly produced from bending magnets. Synchrotron Radiation Source (SRS) at Daresbury Laboratory [16] was widely recognised as the first of the second generation synchrotron light sources. It was followed by a few more e.g. NSLS, ALADDIN, CAMD in U.S.A., Photon Factory and UVSOR in Japan, BESSY-I, MAX-I in Europe. These rings were also the test bed for new technologies for light sources, such as insertion devices (additional magnetic elements other than bending magnets) known as wigglers and undulators. These devices have a periodic magnetic structure designed to take maximum advantage of the intrinsic brightness that could be provided by a storage ring. Both undulators and wigglers have been retrofitted into older storage rings, and in some cases, second generation rings were designed with the possibility of incorporating insertion devices.

The third generation of sources followed the tremendous progress made in the development of insertion devices since the 1980s [17]. These sources were designed specifically to achieve very high brightness, with the emphasis on research with insertion devices, so the lattices (arrangement of magnets in a storage ring) were optimized to incorporate several long insertion devices and to achieve low emittance. The low energy rings (<2 GeV) e.g. ALS, ELETTRA, MAX-II, BESSY-II generated vacuum ultra-violet and soft X-ray radiation whereas high energy rings (6-8 GeV) such as ESRF, APS, SPring-8, PETRA-III generated hard X-rays. The intermediate energy (2.5 -3.5 GeV) storage rings such as SLS, DIAMOND, SOLEIL, ANKA provided cost effective facilities generating photon beams in the hard X-ray region. The enormous spectral coverage and high brightness of these third generation sources has allowed them to be the dominant tool for crystallography, X-ray spectroscopy and many other areas of X-ray science for the last several decades. Third

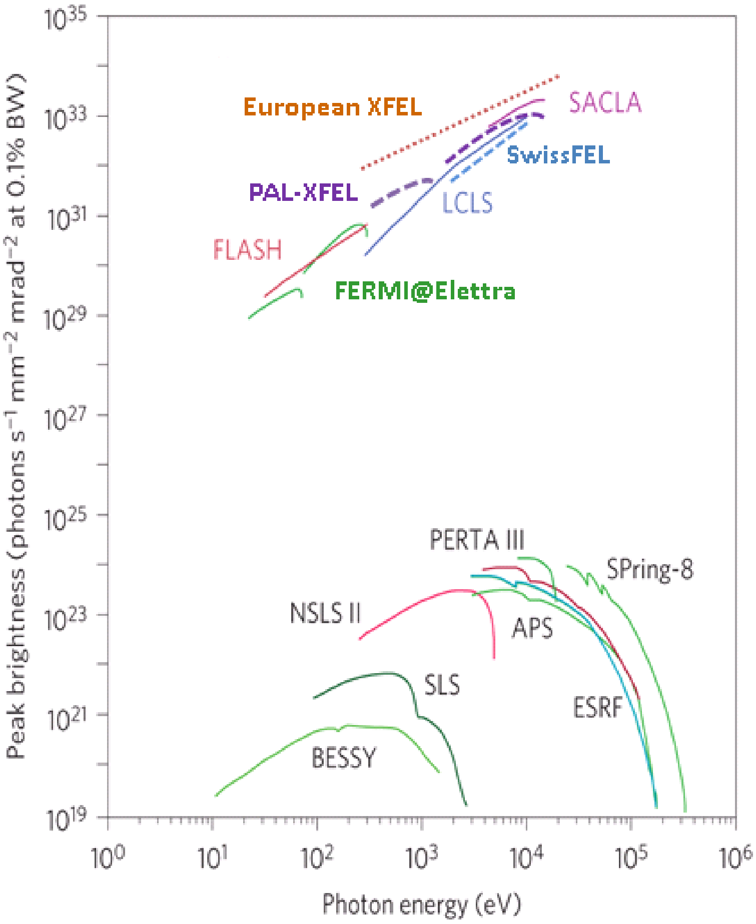

Figure 1.1: Peak spectral brightness (brilliance) of third and fourth generation accelerator-based light sources at 0.1% band width (BW). (Figure adapted from [19, 20]).

generation light sources provide typically a few tens of beam lines on a single synchrotron storage ring for the use of synchrotron radiation in research in a number of scientific disciplines. There are more than 20 third generation light sources in operation worldwide in addition to a few new ones under construction and proposed.

Nevertheless, the brightness of third generation sources does have limits, especially if a narrow spectral bandwidth or a short pulse is selected. With advanced pulse slicing techniques, these sources can provide sub-picosecond temporal resolution but only with a tiny photon flux which severely limits their utility for investigating systems in which rapid changes are taking place. On the other hand, conventional lasers can produce extremely short pulses (<5 fs) at very high brightness [18]; but these capabilities are limited to a restricted spectral range (0.5-5 eV). A breakthrough to a new area in photon science has been accomplished by accelerator-driven Free Electron Lasers (FELs), so-called fourth generation light sources. FELs are radiation sources based on the coherent emission of synchrotron radiation from relativistic electrons within an undulator. The wavelength of the radiation depends on the electron beam energy and the undulator properties, and can be tuned over the entire spectrum from microwave to X-ray. FELs operate in pulsed mode and therefore one has to distinguish between peak brightness, the brightness during the short duration of the photon pulse, and average brightness. For many scientific experiments, peak brightness is the figure of merit. Figure 1.1 shows the significant increase in the peak spectral brightness (brilliance) of photons from fourth generation compared to third generation light sources. The spectral range is much larger than that covered by conventional lasers and the pulses are typically a thousand times shorter and millions of times brighter than can be provided by a storage ring based light source. Compared to storage ring based third generation light sources which provide synchrotron radiation in pulses between 10-50 psec duration, the fourth generation light sources based on FELs provide extremely intense photon pulses with duration ranging from femtoseconds to 100's of attoseconds; this is the time scale at which bond-breaking and bond-formation happen within molecules at which primary electronic processes take place within atoms. FELs thus allow for the first time detailed studies of matter in extreme and in non-equilibrium states. The difference with respect to storage ring light sources is their ability to take movies instead of pictures. The science coming out from the few operational fourth generation sources in last few years [21, 22, 23], confirms that these FELs are likely to have a revolutionary impact on the science done using light. The rest of this chapter describes how an FEL works and what demands it places on the electron beam as a driver for FELs.

1.2 Undulators and Undulator Radiation

The main components of an FEL are an accelerator providing a bunched relativistic electron beam and an undulator magnet. The spontaneous radiation from an undulator described in this section is fundamental to the operation of an FEL.

1.2.1 Magnetic Field in an Undulator

An undulator is a periodic arrangement of short bending (dipole) magnets with alternating polarity. There are two main types of undulators: planar and helical (or elliptical). In a planar undulator, the magnetic field vector is everywhere parallel to a fixed direction and its amplitude oscillates along the axis, the radiation produced is linearly polarised. In a helical undulator, the magnetic field vector rotates around the axis of the undulator as a function of axial distance. By changing the relative positions of the magnetic poles, it is possible to control the rotation of the field, allowing the undulator to provide variable polarisation. The magnetic fields in undulators can be generated using a wide range of technologies: pulsed or DC electromagnets, permanent magnets (as shown in Fig. 1.2) and superconducting magnets. The field amplitude can vary from a fraction of Tesla to over 1 T, and the period from around 1 cm to many centimetres.

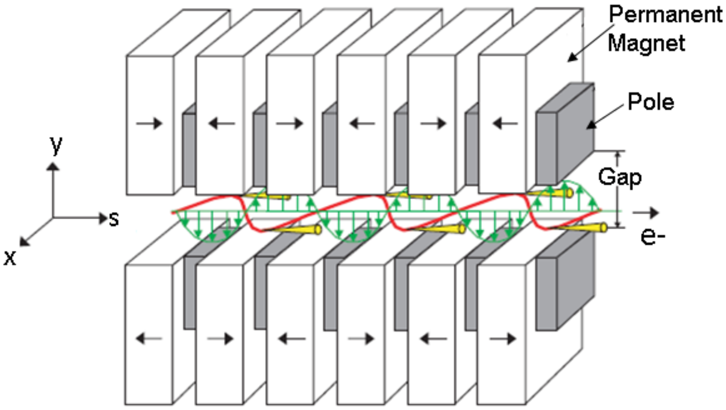

Figure 1.2: Schematic view of a planar undulator magnet with alternating polarity of the magnetic field and of the cosine-like trajectory of electrons. The distance between two equal poles is called the undulator period λ_u. (Figure taken from [24], the co-ordinate along the beam line is s here instead of z).

In the notation used here, the beam travels along the s direction, and the magnetic field (assuming a planar undulator) is in the y (vertical) direction. λ_u is the period of the magnetic field. The x (horizontal) dependence of field can often be neglected, as the width of the undulator pole is normally much larger than λ_u. In vacuum, a static magnetic field in the absence of a time dependent electric field satisfies $\nabla \times \vec{B} = 0$, and hence can be written as the gradient of a scalar potential $\vec{B} = -\nabla\phi$. From Maxwell's equation $\nabla \cdot \vec{B} = 0$, ϕ satisfies Laplace's equation: $\nabla^2\phi = 0$. For a planar undulator, one can write: $\phi(y, s) = f(y)\cos(k_u s)$, where $k_u = 2\pi/\lambda_u$. Substituting into Laplace's equation then gives:

$$\frac{d^2 f}{dy^2} - k_u^2 f = 0. \tag{1.2}$$

The general solution of eqn.(1.2) can be written as:

$$f(y) = a\sinh(k_u y) + b\cosh(k_u y). \tag{1.3}$$

The vertical field is given by:

$$B_y(y, s) = -\frac{\partial\phi}{\partial y} = -k_u\big(a\cosh(k_u y) + b\sinh(k_u y)\big)\cos(k_u s). \tag{1.4}$$

Electrons entering an undulator magnet along the undulator axis ($x = 0$, $y = 0$) are forced to move on an oscillating path in the symmetry-plane $y = 0$. Thus, B_y is symmetric in vertical plane $y = 0$, which gives $b = 0$. Writing $-k_u a = B_0$ (where B_0 is the peak field on-axis):

$$B_y(0, s) = B_0\cos(k_u s). \tag{1.5}$$

For the case where the electron beam is small and confined to the $y = 0$ plane, the magnetic field can be written as a sinusoidal function of s only:

$$\vec{B} = B_0\cos(k_u s)\hat{y}. \tag{1.6}$$

1.2.2 Electron Trajectory in an Undulator

The acceleration by the Lorentz force due to the undulator magnetic field on the electrons is given by

$$\gamma m_e \dot{\vec{v}} = -e\vec{v} \times \vec{B}, \tag{1.7}$$

where m_e and e are the electron rest mass and charge, respectively. $\vec{v}$ is the velocity and γ is the relativistic factor, $\gamma = (1-\beta^2)^{-1/2}$, and $\beta = v/c$ is the scaled velocity with respect to light velocity. In an undulator with pole width large compared to the undulator period, it is possible to assume $B_x = 0$. Resolving for each component, coupled differential equations are obtained as:

$$\begin{aligned} \dot{v}_x &= \frac{e}{\gamma m_e} v_s B_y, \\ \dot{v}_s &= -\frac{e}{\gamma m_e} v_x B_y. \end{aligned} \tag{1.8}$$

Since $v_x \ll v_s$, one can approximate $v_s \sim \beta c$. Thus substituting for B_y from eqn.(1.5),

$$\dot{v}_x \approx \frac{d}{dt} v_x = \frac{e}{\gamma m_e} v_s B_0 \cos(k_u s) \tag{1.9}$$

Using $v_s = ds/dt$,

$$\frac{d}{ds} v_x = \frac{e}{\gamma m_e} B_0 \cos(k_u s). \tag{1.10}$$

Integrating eqn.(1.10) with respect to s gives:

$$v_x = \frac{eB_0}{\gamma m_e k_u} \sin(k_u s). \tag{1.11}$$

Using $k_u = 2\pi/\lambda_u$, a dimensionless “undulator parameter" (also called as the deflection parameter) is introduced as:

$$K = \frac{eB_0\lambda_u}{2\pi m_e c} = 0.9336 B_0[\mathrm{T}]\lambda_u[\mathrm{cm}]. \tag{1.12}$$

The transverse (spatial) velocity component can then be written as

$$v_x = \frac{cK}{\gamma} \sin(k_u s). \tag{1.13}$$

If v_x is small ($v_x \ll c$), v_x/c is approximately equal to the angle of the electron's trajectory to the undulator axis. Hence, K/γ characterises the maximum deflection of the trajectory of the electron (with respect to the undulator axis) as it passes along the undulator. Since the total velocity of the electron must remain constant ($= \beta c$), it is possible to derive the axial velocity component using:

$$v_s^2 = (\beta c)^2 - v_x^2 \tag{1.14}$$

From the definition of relativistic $\beta = \sqrt{1 - \frac{1}{\gamma^2}}$, this becomes:

$$\frac{v_s^2}{c^2} = 1 - \frac{1}{\gamma^2} - \frac{K^2}{\gamma^2}\left(\frac{1-\cos(2k_u s)}{2}\right). \tag{1.15}$$

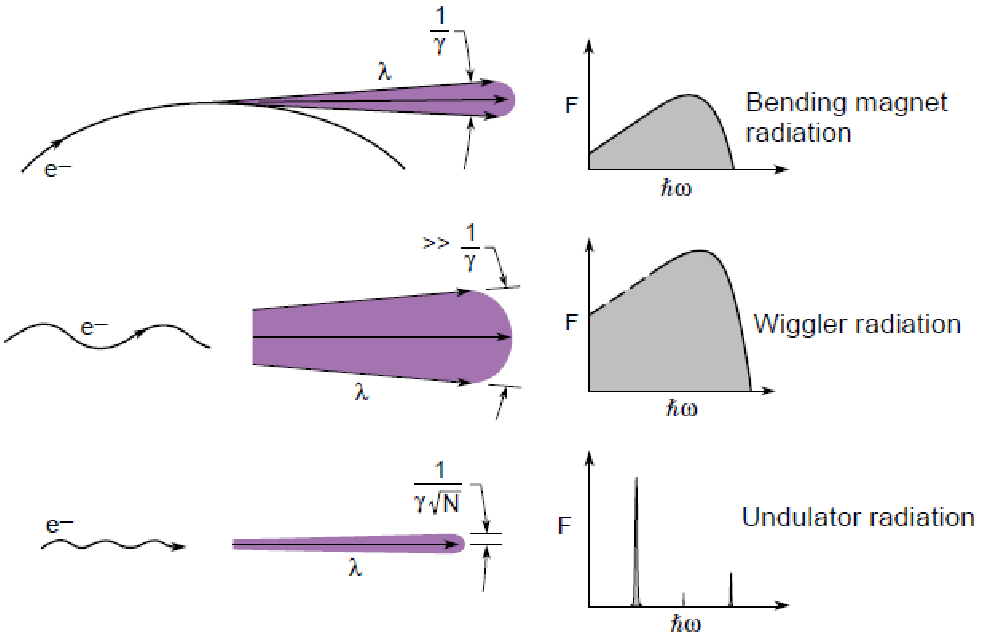

Figure 1.3: Spectrum of synchrotron radiation emitted in a bending magnet, wiggler and an undulator (Figure taken from [25])

.

For $\gamma \gg 1$ and $\frac{K}{\gamma} \ll 1$:

$$\frac{v_s}{c} \approx 1 - \frac{1}{2\gamma^2}\left(1 + \frac{K^2}{2} - \frac{K^2}{2}\cos(2k_u s)\right). \tag{1.16}$$

The axial velocity is modulated at twice the transverse frequency of the undulator field. The axial velocity is maximum at the edges of the electron orbit and is minimum when electrons cross the axis. The average axial velocity inferred from eqn.(1.16) is:

$$\frac{\bar{v}_s}{c} \approx 1 - \frac{1}{2\gamma^2}\left(1 + \frac{K^2}{2}\right) \equiv \bar{\beta}. \tag{1.17}$$

Re-writing eqn.(1.17) using eqn.(1.16), the axial velocity with modulation at spatial frequency $2k_u$ is obtained as:

$$v_s = \bar{v}_s + \frac{K^2}{4\gamma^2}\cos(2k_u s). \tag{1.18}$$

These velocity components are used to explain some important characteristics of undulator radiation in next section.

1.2.3 Characteristics of Spontaneous Undulator Radiation

An electron beam travelling in a curved path at nearly the speed of light emits photons into a narrow cone with opening angle of the order of $1/\gamma$ [26]. As shown in Fig. 1.3, the characteristics of the synchrotron radiation emitted from a wiggler and an undulator differ

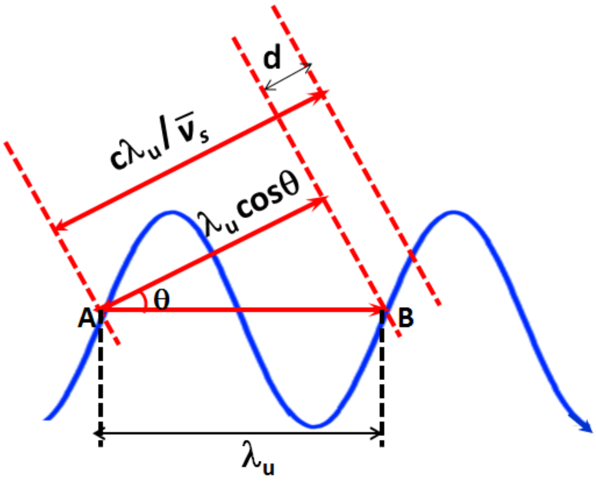

Figure 1.4: Condition for constructive interference in an undulator

significantly from those of the radiation emitted in a bending magnet. In all three, the cone of emitted radiation is centered around the instantaneous tangent to the electron trajectory. In an undulator, the direction of the tangent varies along a sinusoidal trajectory, and the maximum angle with respect to the undulator axis as inferred from eqn.(1.13) is equal to K/γ for relativistic electrons. If this directional variation is less than $1/\gamma$, the radiation field receives contributions from different sections of the trajectory which overlap in space. These contributions then interfere with each other (as explained in the next section) with the result that the radiation spectrum has a narrow spectral line at a well-defined frequency (and the odd higher harmonics; even harmonics are suppressed by destructive interference). This is the case when $K \leq 1$, in other words when the electron trajectory is inside the radiation cone. In a wiggler, on the other hand the trajectory extends beyond the radiation cone, hence $K > 1$ for wigglers.

Undulator Radiation

The radiation properties from an undulator can be explained in terms of the interference of radiation emitted by the same electron at different points in the undulator as shown in Fig. 1.4. In the time it takes the electron to move through one undulator period length λ_u, the radiation emitted from point A is advanced by a distance $c\lambda_u/\bar{v}_s$ and hence is ahead of the radiation emitted at the point B by a distance d where:

$$d = \frac{c\lambda_u}{\bar{v}_s} - \lambda_u \cos\theta \tag{1.19}$$

where θ is the angle of emission with respect to the undulator axis. When this distance is equal to an integer number, n, of radiation wavelengths, there is constructive interference of the radiation from successive points. The condition for constructive interference can be written:

$$n\frac{\lambda}{\lambda_u} = \frac{c}{\bar{v}_s} - \cos\theta. \tag{1.20}$$

Substituing from eqn.(1.17) and using $(1-x)^{-1} = (1+x)$, $c/\bar{v}_s$ is written as:

$$\frac{c}{\bar{v}_s} = \left(1 + \frac{1}{2\gamma^2} + \frac{K^2}{4\gamma^2}\right), \tag{1.21}$$

and using $(1-\cos\theta) = 2\sin^2\theta \simeq \theta^2/2$ for small angles, eqn.(1.20) is written as:

$$\lambda = \frac{\lambda_u}{2n\gamma^2}\left(1 + \frac{K^2}{2} + \gamma^2\theta^2\right). \tag{1.22}$$

Equation (1.22) is known as the undulator equation; it shows that the wavelength of the radiation from an undulator depends not only on the undulator period λ_u and the beam energy, but also on the undulator parameter K and the observation angle θ. The definition of K given by eqn.(1.12) implies that by changing the magnetic field B_0, the wavelength of the emitted radiation can be changed. Note that increasing B_0 increases the wavelength of the undulator radiation. The dependence on θ^2 results in a longer wavelength as one moves away from the axis.

An important property of the undulator radiation is the width of the spectral lines. An electron passing through an undulator with N_u periods produces a wave train with N_u oscillations, with a time duration of $T = N_u\lambda/c$. The electric field of the light wave can be written as:

$$\begin{aligned} E_l(t) &= E_0 e^{i\omega_l t}, && \text{if } -\frac{T}{2} < t < \frac{T}{2} \\ &= 0, && \text{otherwise.} \end{aligned} \tag{1.23}$$

As the electric field is present over a finite period T, the wave train will not be monochromatic. The corresponding frequency spectrum can be found by taking the Fourier transform of the electric field;

$$\begin{aligned} A(\omega) &= E_0 \int_{-\frac{T}{2}}^{\frac{T}{2}} \exp^{-i(\omega_l-\omega)t}\, dt \\ &= 2E_0 \frac{\sin\left((\omega_l-\omega)\frac{T}{2}\right)}{\omega_l-\omega}. \end{aligned} \tag{1.24}$$

The spectral density is given by:

$$\begin{aligned} I(\omega) \propto |A(\omega)|^2 \propto \left(\frac{\sin\xi}{\xi}\right)^2 \\ \text{where, } \xi = \frac{(\omega_l-\omega)T}{2} = \pi N_u \frac{\omega_l-\omega}{\omega_l}. \end{aligned} \tag{1.25}$$

which has a maximum at $\omega_l = \omega$ and a characteristic width of approximately ω_l/N_u.

The angular width of the first harmonic around $\theta = 0$ can be estimated using eqns. (1.22) and (1.25). The radiation frequency as a function of θ can be written as:

$$\omega_l(\theta) = \omega_l(0)\left(\frac{1+\frac{K^2}{2}}{1+\frac{K^2}{2}+\gamma^2\theta^2}\right). \tag{1.26}$$

When $\omega_l(0) - \omega_l(\theta)$ exceeds the bandwidth given by eqn.(1.25) the intensity drops to zero. The rms value of the angular width is approximated as [27]:

$$\sigma_\theta \approx \frac{1}{\gamma}\sqrt{\frac{1 + K^2/2}{2N_u}}. \tag{1.27}$$

For $K \approx 1$, the rms angular width is $\approx 1/\gamma\sqrt{N_u}$. N_u is typically much larger than 1 and the first harmonic of undulator radiation is highly collimated with the typical opening angle of synchrotron radiation γ divided by $\sqrt{N_u}$ (as shown in Fig.1.3).

1.3 Free Electron Lasers

A FEL has two fundamental components: an accelerator to produce an electron beam of certain energy and intensity and an undulator magnet. The mechanism for production of FEL radiation is based on a resonant interaction between the electromagnetic radiation emitted by an electron beam and the electron beam itself as it travels through the undulator magnet. The periodic magnetic field in the undulator forces the electrons to travel on a sinusoidal trajectory (the axis is a straight line path along the undulator) where electrons acquire a velocity component along the direction of the electric field in the radiation. This results in a transfer of energy between the electrons and the electromagnetic radiation. A continuing transfer of energy takes place when a condition of synchronism is satisfied. This energy transfer together with the energy dependence of the electron path through the undulator (as described in Section 1.2.2) results in a density modulation of the electron beam at the resonant radiation wavelength, which in turn results in coherent emission of radiation.

FEL theory is well established in the literature [28, 29, 30, 31]. For the purpose of this thesis, the aim is to understand the constraints on electron beam properties required to drive a FEL. This section summarises the basic principles of operation of FELs, describes different regimes of FEL operation and the scaling of important FEL parameters with electron beam parameters. The material used in the following sections is based on that in references [24, 30, 31, 32, 33].

1.3.1 Types of FELs

Like in conventional lasers, in an FEL there is a phase correlation in the radiation emitted from different electrons. This correlation is obtained by modulating the longitudinal electron beam density on the scale of the radiation wavelength. The density modulation is the result of a process of bunching which starts with the modulation of the electron energy due to the interaction with the radiation field. The length of the path taken by an electron through the sinusoidal field of an undulator depends on the energy of the electron. As a result, a longitudinal density modulation can develop in the electron bunch.

When electrons are bunched over a distance shorter than the radiation wavelength, a situation referred to as "micro-bunching", they radiate in phase and the radiation field intensity increases rapidly. A stronger modulation in the electron density increases the emission level causing stronger bunching. This process continues until the electron density modulation reaches a maximum (i.e. all electrons have same phase of emission and thus the radiation is fully coherent). The length over which the radiation intensity grows by a factor of $e(\approx 2.178)$ is called the "gain length". FELs are usually classified in three different regimes based on the gain length and length of the undulator:

- Low or small gain regime: In this regime, the undulator length is shorter than the gain length. The spontaneous radiation from the undulator is normally captured in the optical cavity, and the FEL gain occurs each time the trapped radiation travels together with an electron bunch. With each electron bunch passage, the light intensity grows by a few percent. The small gain per undulator passage, however, does not prevent the FEL from reaching very high power if the number of passes/electron bunch train length and the quality factor of the optical cavity is high.

- Intermediate gain regime: In this regime, the undulator length is between 1-10 times the gain length. The radiation experiences exponential growth but does not achieve saturation in a single pass. A small amount of feedback using a low quality factor cavity allows the FEL to saturate in a few cavity transit times. This system is known as a Regenerative Amplifier FEL (RAFEL).

- High gain regime: In this regime, the undulator length is several gain lengths. The FEL interaction is a collective, exponential instability and radiation intensity saturates in a single pass through the undulator. No optical cavity is needed for a FEL in this regime.

Depending upon how the micro-bunching is achieved in the FEL, FELs can be categorised as:

- Resonator (or oscillator): The incoherent radiation produced in an undulator is trapped within an optical cavity. Each electron bunch passing through the undulator increases the radiation intensity, which increases the rate at which micro-bunching takes place.

- Amplifier: The intensity of the radiation increases rapidly. There are two ways to achieve this:

1. In a seeded amplifier an external radiation pulse is co-propagated with an electron bunch in an undulator. This initiates the micro-bunching, which grows as the

electron bunch passes through the undulator, leading to exponential growth in the radiation intensity.

2. In a Self-Amplified Spontaneous Emission (SASE) amplifier the micro-bunching process is initiated by inherent fluctuations of the electron distribution at the undulator entrance and the spontaneous radiation emitted in the undulator. The micro-bunching develops rapidly along the undulator as the electrons within each microbunch radiate coherently.

The choice of FEL as per resonator (oscillator), SASE or seeded amplifier depends upon user requirements. A resonator will be suitable if the FEL wavelength is infrared or visible, whereas for short wavelength regime (X-rays), the lack of suitable mirrors leaves an amplifier as effectively the only choice. Though SASE provides good transverse coherence, the longitudinal (temporal) coherence is poor due to the start of FEL amplification from noise. Temporal coherence can be improved by seeding, but at shorter wavelengths it becomes difficult to provide a seed pulse with intensity sufficiently above the noise level in the electron density.

1.3.2 Low Gain FELs

Physics of FELs in Low Gain Regime

In order to understand the energy transfer from electron to radiation, let′s consider the case of an FEL as an amplifier which is seeded by an external laser with wavelength λ_l. The radiation wave co-propagating with the relativistic electron beam can be described by a plane electromagnetic wave given by:

$$E_x(s,t) = E_0 \cos(k_l s - \omega_l t + \psi_0), \tag{1.28}$$

where $k_l = 2\pi/\lambda_l$ and $\omega_l/k_l = c$.

The electric field of the radiation wave exerts a force $\vec{F} = -e\vec{E}$ on the electron. From Newton's second law of motion, one can write:

$$\vec{F} = m_e \frac{d(\gamma \vec{v})}{dt}, \tag{1.29}$$

where m_e and e are the electron rest mass and charge respectively. The rate of energy transfer from an electron to the radiation wave is given by:

$$\dot{W} = \vec{v} \cdot \vec{F} = -e v_x(t) E_x(s,t). \tag{1.30}$$

Using eqns.(1.13) and (1.28) this can be written as:

$$\begin{aligned} \dot{W} &= -\frac{ecKE_0}{\gamma} \cos(k_l s - \omega_l t + \psi_0) \sin(k_u s), \\ &= -\frac{ecKE_0}{2\gamma} [\sin((k_l + k_u)s - \omega_l t + \psi_0) - \sin((k_l - k_u)s - \omega_l t + \psi_0)], \end{aligned} \tag{1.31}$$

This can be simplified as

$$\dot{W} = -\frac{ecKE_0}{2\gamma}\left(\sin\psi - \sin\chi\right). \tag{1.32}$$

where:

$$\begin{aligned} \psi &= (k_l + k_u)s - \omega_l t + \psi_0, \\ \chi &= (k_l - k_u)s - \omega_l t + \psi_0. \end{aligned} \tag{1.33}$$

Energy exchange depends on the phase sum, also known as the pondermotive phase, ψ. The position s of the electron is a function of time t and thus the the term $\psi(t)$ will continuously transfer energy from electron to the radiation if $\psi(t)$ is constant along the undulator independent of time. The condition $\psi = constant$ can be fulfilled at only certain wavelength. Neglecting the longitudinal oscillation, it is possible to use $s(t) = \bar{v}_s t$ and thus obtain:

$$\begin{aligned} \psi(t) &= (k_l + k_u)\bar{v}_s t - \omega_l t + \psi_0 = \text{constant}, \\ \text{giving:}\quad d\psi/dt &= (k_l + k_u)\bar{v}_s - k_l c = 0 \end{aligned} \tag{1.34}$$

Substituting for $\bar{v}_s$ from eqn.(1.17), the radiation wavelength is obtained as:

$$\lambda_l = \frac{\lambda_u}{2\gamma^2}\left(1 + \frac{K^2}{2}\right) \tag{1.35}$$

This condition for sustained energy transfer along the undulator gives the same radiation wavelength as in eqn.(1.22) at $\theta = 0$. This explains why spontaneous radiation from undulator acts as seed radiation in SASE FEL. Using similar treatment for the second term χ in eqn.(1.33):

$$\begin{aligned} \chi(t) &= (k_l - k_u)\bar{v}_s t - \omega_l t + \psi_0 = \text{constant}, \\ \text{giving:}\quad d\chi/dt &= (k_l - k_u)\bar{v}_s - k_l c = 0 \end{aligned} \tag{1.36}$$

Using eqn.(1.17):

$$k_l(1 - \bar{\beta}) = -k_u \bar{v}_s / c \tag{1.37}$$

which implies that $k_l < 0$, indicating that the radiation travels in negative direction, which is non-physical. If ψ is written as a function of $s = \bar{v}_s t$, using eqn.(1.33), the relationship between $\psi(s)$ and $\chi(s)$ can be written as:

$$\chi(s) = \psi(s) - 2k_u s. \tag{1.38}$$

If eqn.(1.35) is satisfied, $\psi(s)$ remains constant and the second term $\sin(2k_u s)$, makes two oscillations per undulator period and thus cancels out over several undulator periods. Taking this into consideration, eqn.(1.32) can be simplified to:

$$\dot{W} = -\frac{ecKE_0}{2\gamma}\sin\psi. \tag{1.39}$$

Low Gain Regime and FEL Pendulum Equations

Considering the low gain regime where the intensity of the radiation is nearly constant, the resonant electron energy $W_r = \gamma_r m_e c^2$ is defined such that:

$$\lambda_l = \frac{\lambda_u}{2\gamma_r^2}\left(1 + \frac{K^2}{2}\right), \tag{1.40}$$

from which it follows that:

$$\gamma_r = \sqrt{\frac{\lambda_u}{2\lambda_l}\left(1 + \frac{K^2}{2}\right)}. \tag{1.41}$$

Electrons with the energy W_r emit undulator radiation whose wavelength is identical to the seed wavelength λ_l.

In general, the electron energy W will be slightly different from W_r, and the relative energy deviation can be defined as:

$$\eta = \frac{W - W_r}{W_r} = \frac{\gamma - \gamma_r}{\gamma_r}. \tag{1.42}$$

The Lorentz factor γ and the pondermotive phase ψ will both change due to interaction with the radiation field. In a low-gain regime where the intensity of the radiation is approximately constant during one passage of the undulator, it is possible to substitute $\dot{E}_0 = 0$ inside the undulator. The time derivative of ψ is no longer zero for $\gamma \neq \gamma_r$; taking the derivative of eqn.(1.33),

$$\frac{d\psi}{dt} = (k_l + k_u)\,\bar{v}_s - \omega_l, \tag{1.43}$$

and substituting for $\bar{v}_s$ from eqn.(1.17) and $\omega_l = k_l c$

$$\frac{d\psi}{dt} \approx k_u c - \frac{k_l c}{2\gamma^2}\left(1 + \frac{K^2}{2}\right). \tag{1.44}$$

By setting $d\psi/dt = 0$ and $\gamma = \gamma_r$:

$$k_u c = \frac{k_l c}{2\gamma_r^2}\left(1 + \frac{K^2}{2}\right). \tag{1.45}$$

Substituting for $k_u c$ from eqn.(1.45) in eqn.(1.44):

$$\frac{d\psi}{dt} = \frac{k_l c}{2}\left(1 + \frac{K^2}{2}\right)\left(\frac{1}{\gamma_r^2} - \frac{1}{\gamma^2}\right). \tag{1.46}$$

Using eqn.(1.45) this is simplified as:

$$\frac{d\psi}{dt} = k_u c\left(1 - \frac{\gamma_r^2}{\gamma^2}\right). \tag{1.47}$$

For small energy difference (i.e. $\gamma \approx \gamma_r$), using eqn.(1.42) one can write (to first order in ψ) :

$$\frac{d\psi}{dt} \approx 2k_u c\eta \equiv \omega' \quad (\omega' \ll k_u c). \tag{1.48}$$

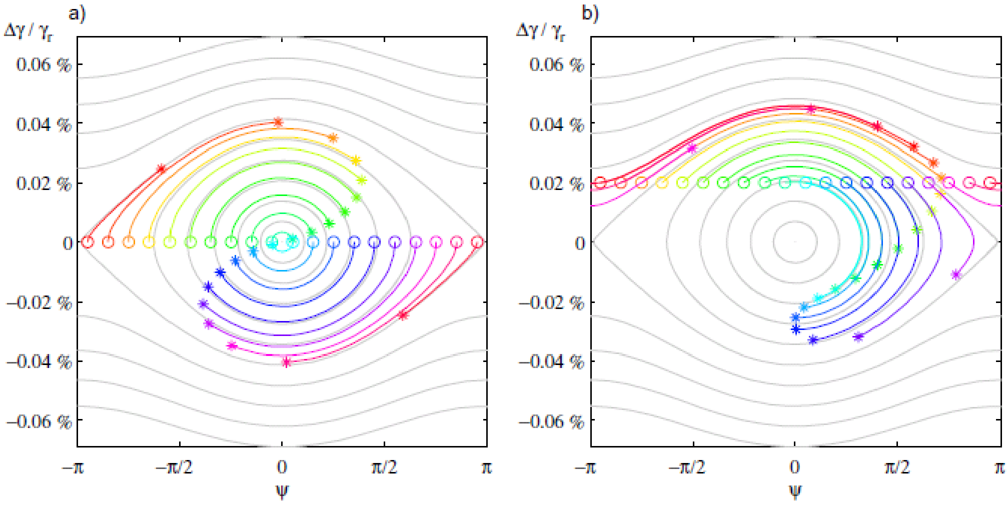

Figure 1.5: Phase space trajectories for 20 electrons of different initial phases. Left: $\gamma = \gamma_r$. The electrons with $\psi_0 < 0$ withdraw energy from the radiation wave while those with $\psi_0 > 0$ supply energy to the radiation wave. The net transfer is zero. Right: $\gamma = \gamma_r$. The net energy transfer is positive. Figure taken from [24].

Using definition of relative energy deviation from eq.(1.42) and eqn.(1.39), the time derivative of energy can be simplified to:

$$\frac{d\eta}{dt} = -\frac{eE_0K}{2m_ec\gamma_r^2}\sin(\psi) \tag{1.49}$$

Combining eqns.(1.48) and (1.49) yields:

$$\frac{d^2\psi}{dt^2} + \Omega^2\sin(\psi) = 0,$$
$$\text{where: } \Omega^2 = \frac{eE_0Kk_u}{m_e\gamma_r^2} \tag{1.50}$$

Because of their similarity to the equations of motion for a pendulum, eqns.(1.48) and (1.49) are known as the FEL pendulum equations. At small amplitude this gives a harmonic oscillation. With increasing angular momentum the motion starts getting non-harmonic. At very large angular momentum one gets unbounded motion. The phase space trajectory of an electron in an FEL can be constructed by solving these two equations. Consider trajectories of few electrons distributed over different initial phases for two cases: Case 1, on resonance $\gamma = \gamma_r$; and Case 2 when $\gamma > \gamma_r$. As shown in Fig. 1.5(a) for Case 1, some electrons lose energy to the radiation and some gain energy from the radiation. Because of the symmetry, there is no net energy transfer. For Case 2, as shown in Fig. 1.5 (b), the symmetry is broken and there is a net energy transfer from the electrons to the radiation.

The FEL theory described by the coupled pendulum equations is a one-dimensional theory. In this theory, dependence on the bunch charge density and the transverse effects (arising due to beam emittance and energy spread) are neglected. It is assumed that the electron bunches are very long compared to the wavelength of the radiation and that the end effects from the head or tail of the bunch can be ignored. The effects of betatron oscillations of the electrons and diffraction of the radiation are also not considered. All these three-dimensional effects generally tend to degrade the quality of the FEL interaction by increasing the gain length and decreasing the saturation intensity in a given length of undulator. The one-dimensional model is therefore the best case model for a given set of parameters.

Low Gain Regime - Madey's Theorem

The radiation wave gains energy from the electrons when η is positive and loses energy to the electrons when η is negative. In order to estimate how much energy will be transferred, a "FEL gain function" is defined as the relative growth of the radiation intensity during one passage of the undulator. The gain function can be derived using the equations derived in previous two sections. The energy (per unit volume) of the radiation field is given by:

$$W_l = \frac{\epsilon_0}{2} E_0^2, \tag{1.51}$$

where ϵ_0 is the permittivity of free space. The energy increase caused by one electron is

$$\Delta W_l = -m_e c^2 \Delta\gamma. \tag{1.52}$$

Thus, the relative gain caused by one electron is

$$G_1 = \frac{\Delta W_l}{W_l} = -\frac{2 m_e c^2}{\epsilon_0 E_0^2} \Delta\gamma. \tag{1.53}$$

Using eqn.(1.48) and considering all electrons in a bunch (n_e):

$$G = -\frac{m_e c \gamma_r n_e}{\epsilon_0 E_0^2 k_u} \langle \Delta\dot{\psi} \rangle, \tag{1.54}$$

where $\langle \Delta\dot{\psi} \rangle$ is the change of the time derivative of the pondermotive phase ψ, averaged over all electrons. This term is obtained by multiplying the pendulum equation (eqn.1.50) by $2\dot{\psi}$ and integrating over time [24]:

$$\dot{\psi}^2 - 2\Omega^2 \cos\psi = \mathrm{const} \Rightarrow \dot{\psi}(t)^2 = \dot{\psi_0}^2 + 2\Omega^2 \left(\cos\psi(t) - \cos\psi_0\right). \tag{1.55}$$

From eq.(1.48):

$$\dot{\psi_0} = \dot{\psi}(0) = 2 c k_u \eta \equiv \omega'. \tag{1.56}$$

which gives:

$$\dot{\psi}(t) = \omega' \sqrt{1 + 2(\Omega/\omega')^2 (\cos\psi(t) - \cos\psi_0)} \tag{1.57}$$

and for weak radiation field this can be expanded up to second order as:

$$\dot{\psi}(t) = \omega' + (\Omega^2/\omega')[\cos\psi(t) - \cos\psi_0] - \Omega^4/(2\omega'^3)[\cos\psi(t) - \cos\psi_0]^2 \tag{1.58}$$

The eqn. (1.58) is solved iteratively. To zeroth order it gives $\dot{\psi}_0 = \omega'$ giving $\Delta\dot{\psi}_0 = 0$. The phase $\psi(t)$ in first order is obtained by integrating zeroth order:

$$\psi_1(t) = \psi_0 + \omega' t. \tag{1.59}$$

Inserting eqn.(1.59) in eqn.(1.58), to first order $\dot{\psi}$ can be written as:

$$\dot{\psi}_1(t) = \omega' + (\Omega^2/\omega')[\cos(\psi_0 + \omega' t) - \cos\psi_0]. \tag{1.60}$$

The flight time through the undulator is T, so the change of $\dot{\psi}_1$ when the electron passes through the undulator is:

$$\Delta\dot{\psi}_1 = (\Omega^2/\omega')[\cos(\psi_0 + \omega' T) - \cos\psi_0]. \tag{1.61}$$

When averaged over initial phases ψ_0, this gives $\langle\Delta\dot{\psi}_1\rangle = 0$, meaning the FEL gain is zero in first order. This is due to the nearly symmetric initial phase space distribution. Integrating eqn.(1.60), ψ in second order can be obtained as:

$$\psi_2(t) = \psi_0 + \omega' t + (\Omega/\omega')^2[\sin(\psi_0 + \omega' t) - \sin\psi_0 - \omega' t\cos\psi_0]. \tag{1.62}$$

Inserting eqn.(1.62) in eqn.(1.58) at $t = T$ and averaging over all initial phases ψ_0 yields:

$$\langle\Delta\dot{\psi}_2\rangle = -(\Omega^4/\omega'^3)[1 - \cos(\omega' T) - \frac{\omega' T}{2}\sin(\omega' T)]. \tag{1.63}$$

Substituting for time of flight through undulator as $T = N_u\lambda_u/c$ and $\xi = \omega' T/2$:

$$\begin{aligned} \langle\Delta\dot{\psi}_2\rangle &= -(\Omega^4/\omega'^3)[1 - \cos(2\xi) - \xi\sin(2\xi)], \\ &= \frac{N_u^3\lambda_u^3\Omega^4}{8c^3}\frac{d}{d\xi}\left(\frac{\sin\xi}{\xi}\right)^2. \end{aligned} \tag{1.64}$$

Using this equation in eqn.(1.54) and substituting for Ω^2 from eqn.(1.50), the FEL gain function is expressed as:

$$G(\omega) = -\frac{\pi e^2\hat{K}^2N_u^3\lambda_u^2n_e}{4\epsilon_0 m_e c^2{\gamma_r}^3}g(\xi), \tag{1.65}$$

where n_e is the number of electrons per unit volume, N_u is the number of undulator periods and $\hat{K}$ is the modified undulator parameter, which takes into account the modulation of the longitudinal velocity of the electrons (which affects the coupling between the electrons and the radiation). The gain function $g(\xi)$ and the dimensionless parameter ξ are defined by:

$$\begin{aligned} g(\xi) &= \frac{d}{d\xi}\left(\frac{\sin^2\xi}{\xi^2}\right), \\ \xi = \xi(\omega) &= \pi N_u\left(\frac{\omega_r - \omega}{\omega_r}\right). \end{aligned} \tag{1.66}$$

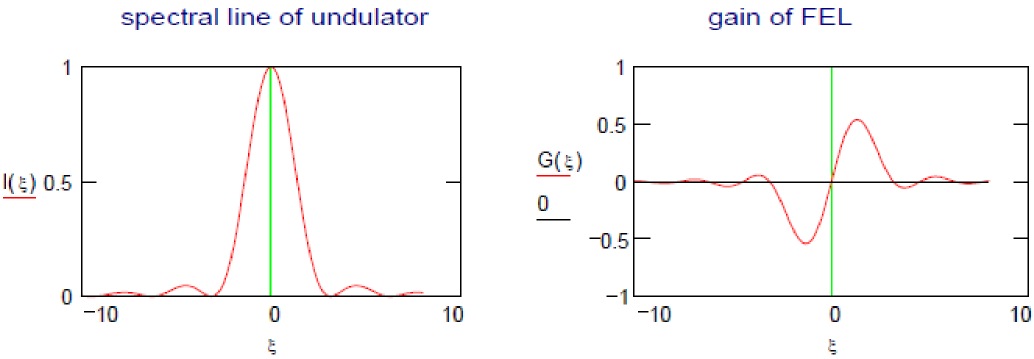

Figure 1.6: The normalised lineshape curve of undulator radiation and the gain curve (in arbitrary units) of low-gain FEL. (Figure taken from [24]).

The variable ξ is a measure of the frequency deviation from the resonant frequency, ω_r, which is the frequency of the “spontaneous" radiation produced in the undulator by electrons with energy $\gamma = \gamma_r$. Equation(1.65), is Madey's Theorem which states that the FEL gain curve is proportional to the negative derivative of the line shape curve of undulator radiation.

The dependence of the gain on the wavelength is described by function $g(\xi)$ as given in eqn.(1.66), the form of which is plotted in Fig. 1.6. $g(\xi)$ is the derivative of $\frac{\sin^2(\xi)}{\xi^2}$ which describes spectral density of the undulator spontaneous radiation as described in eqn.(1.25). For a given electron energy, the gain is a function (through the parameter ξ) of the radiation wavelength. For some wavelengths, the gain is positive; for others, it is negative. Electrons with positive η enhance the intensity of the radiation wave, while those with negative η reduce it. In practice, the gain function determines the frequency and bandwidth of radiation from a low-gain FEL.

1.3.3 High Gain FELs

In high gain FELs, the electron bunch itself is (micro-)bunched on the length scale of the wavelength of the undulator radiation, making it possible for electrons to radiate coherently. The formation of the micro-bunching is a consequence of the interaction between the electrons and the radiation field. Electrons transferring energy to the radiation wave will lose their energy and thus travel a longer sinusoidal path along the undulator, thus falling behind those gaining energy from the radiation field. As this process of micro-bunching continues, an initial weak micro-bunching leads to an increase in emitted radiation, which results in more rapid energy transfer to the radiation wave resulting in a growing modulation. As electrons within each micro-bunch radiate coherently, the increase in radiation power is on the order of total number of electrons in all the microbunches within the coherence length (which is a measure of temporal coherence, expressed as the propagation distance over which the coherence significantly decays). This process is self-sustained and leads to exponentially growing emitted radiation and has three distinct phases (shown in Fig. 1.7): namely an initial start-up period (lethargy), a period of exponential gain and a saturation phase.

In the case of a seeded FEL the micro-bunching process is started by an external radiation pulse in the appropriate wavelength regime. The seed pulse must have sufficient power to initiate the micro-bunching process if the FEL is to operate. For SASE, random fluctuations in the longitudinal distribution of electron bunches at the entrance of the undulator are essential to start off the micro-bunching. On the scale of the radiation wavelength the longitudinal distribution of electrons in the beam is not perfectly smooth, but rather it contains a small degree of local micro-bunching which leads to small variations in the initial longitudinal field intensity. This initial bunching is referred to as the shot-noise. As the electrons travel along the undulator, the emitted radiation field begins to act back on the electrons, initiating the energy exchange and therefore the micro-bunching process. Recalling that the radiation travel with speed of light along the axis, whereas electrons are travelling slower than speed of light on a sinusoidal orbit which is longer than the straight path of radiation, as the field amplitude of the radiation increases, its phase shifts with respect to the electrons, increasing the fraction of energy lost by the electrons to the radiation field. This instability continues until a maximum amount of energy has been extracted and the radiation field is saturated. The growth in radiation power approaches a saturated regime after typically about twenty gain lengths in case of SASE, and is slightly shorter in case of a seeded FEL. Saturation occurs since the emission of radiation leads to a decrease in electron energy and an increase in energy spread, both impeding the FEL process. In the exponential gain regime (after start-up and before saturation) FEL power grows exponentially with distance along the undulator s:

$$P(s) = P_0 \exp(s/L_G). \tag{1.67}$$

The gain length L_G is defined as the distance over which the FEL power grows by a factor $e(\approx 2.718)$. A 1-D model for a monoenergetic beam leads to an expression for the gain length [32]:

$$L_G = \frac{\lambda_u}{4\pi\sqrt{3}\rho_{\text{FEL}}}. \tag{1.68}$$

The parameter ρ_{FEL} is called the Pierce or FEL parameter, which is roughly the ratio of the radiation power at saturation to the beam power, and is given by [34, 35]:

$$\rho_{\text{FEL}} = \frac{1}{4\gamma_r}\left(\frac{I_p}{I_A}\frac{\lambda_u^2 K^2 [JJ]^2}{\pi^2 \epsilon_x \beta_x}\right)^{\frac{1}{3}}, \tag{1.69}$$

where, I_p is the peak beam current and I_A is the Alfvén current (17kA), $[JJ]$ is the undulator radiation coupling factor, which is equal to 1 for a helical undulator and equal to $[J_0(\xi) - J_1(\xi)]$ for a planar undulator where $J_0(\xi)$ and $J_1(\xi)$ are Bessel functions of the first kind with the argument $\xi = \frac{K^2}{4+K^2}$, ϵ_x and β_x are the horizontal beam emittance and

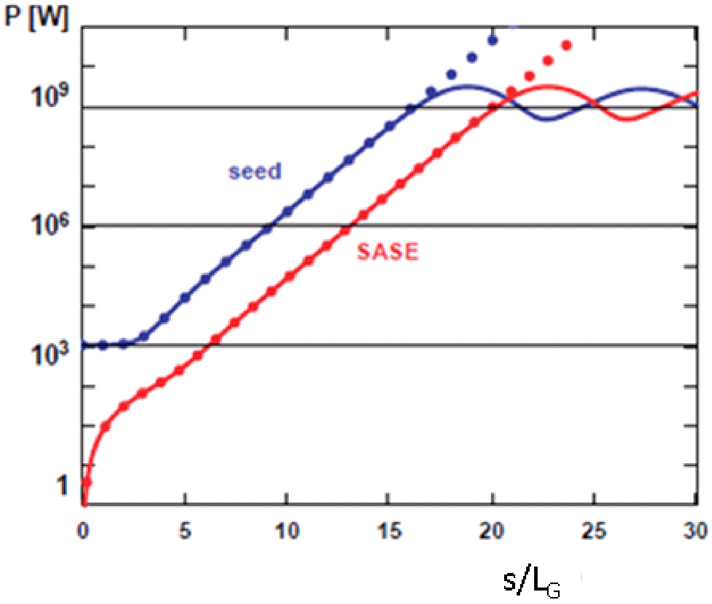

Figure 1.7: Initial start-up period (lethargy), a period of exponential growth and a saturation of the FEL radiation power along the undulator (Figure taken from [32], the x-axis label from the original figure is replaced with s/L_G for consistency with the notation used in this thesis).

lattice amplitude function characterising the beam envelope, (the subscript "x" on ϵ_x and β_x refers to the horizontal plane; however, in the case of FELs the vertical plane behaves in a similar fashion. Whether one uses ϵ_x, β_x or ϵ_y, β_y depends upon the undulator orientation (i.e. horizontal or vertical)).

Only electrons lying within an acceptable energy bandwidth, given by the FEL parameter, contribute to the FEL interaction. During the FEL amplification, energy is transferred from the electron beam to the radiation field. The process of amplification continues until most of the electrons are outside the bandwidth and then this process ceases as the synchronism condition is no longer satisfied. The FEL saturation power is given by:

$$P_{saturation} \approx \rho_{\mathrm{FEL}} P_{beam} \tag{1.70}$$

and is equal in both SASE and the seeded FEL. Thus maximising ρ_{FEL} not only reduces the length of the undulator but also increases the power level of the FEL.

1.3.4 Requirements of Electron Beams for FELs

The realisation of a high gain FEL crucially depends on properties of the electron beam. As seen in Section 1.3.3, the FEL design is usually optimised to maximise the FEL parameter ρ_{FEL}, thus minimising the gain length L_G, and maximising the output radiation power. For chosen undulator parameters, high peak beam current and a smaller value of the product $\epsilon_x\beta_x$ is required to minimise the gain length. The dependence of the gain length on γ_r shows that in order to reach saturation within an undulator of reasonable length, the requirements on the beam become more demanding at higher electron energy. For X-ray FEL, high energy (and short undulator period) are required.

The expressions for gain length L_G and the FEL parameter ρ_{FEL} given in Section 1.3.3 are based on a one-dimensional model, a mono-energetic beam of finite transverse size, which is assumed to be ideally superimposed on the radiation beam along the entire FEL section. When the realistic beam parameters such as electron beam energy spread, transverse emittance and radiation diffraction effects are taken into consideration, the FEL parameter is reduced leading to an increase in the gain length and thus the saturation regime may never be reached in an undulator section or the FEL section of reasonable length. A SASE FEL is usually designed to reach saturation: this makes the length of undulator needed to achieve saturation of fundamental importance in the design of the FEL. In this section, the effects that limit (in practice) the minimum achievable gain length in a FEL are considered.

Beam energy spread prevents bunching of all electrons at the same pondermotive phase. Electrons with different energies have different effective longitudinal velocities and so the bunching is smeared out. For a beam with finite energy spread, only the electrons within a narrow energy window contribute constructively to the FEL gain process. Only if all electrons have the same energy W_r is the power gain length close to the 1D L_G given by eqn.(1.68). For an energy spread,

$$\frac{\sigma_E}{E} \approx \frac{\rho_{\mathrm{FEL}}}{2} \tag{1.71}$$

the gain length is larger by a factor of approximately 1.25 compared to mono-energetic beam. This is conventionally considered as the upper limit for a tolerable increase in gain length [36].

In addition to the requirements on peak current and energy spread, achieving and maintaining an overlap of the transverse size of electron beam with the transverse size of the radiation field in long undulator sections is of great importance for optimum energy transfer. The important parameters ensuring this are the electron beam horizontal emittance ϵ_x and vertical emittance ϵ_y and the diffraction limit of the radiation. The diffraction limit is a characteristic of the radiation beam corresponding to the emittance of a charged particle beam, and is usually defined by the product of the size and divergence with an additional correlation term if appropriate (when away from beam waist). In order to maintain a good overlap between the electron beam and the radiation, the electron beam size and divergence are controlled using focusing magnets in the undulator sections. This focusing leads to betatron oscillations constituting an additional transverse velocity component in addition to the oscillation induced by the undulator field. For the FEL process, this translates in to an effective reduction of the mean electron beam energy and in addition, owing to the difference in betatron oscillation amplitudes, results in effective smearing of the longitudinal velocity, which is equivalent to an energy spread. Taking into account both these effects and using same criterion as in eqn.(1.71), an upper limit for the electron beam emittance is given by [30]:

$$\epsilon_{x,y} < \frac{\langle \beta_{x,y} \rangle}{2\sqrt{2}\gamma_r^2} \rho_{\mathrm{FEL}}, \tag{1.72}$$

where $\langle \beta_{x,y} \rangle$ is the longitudinal average of the Courant-Snyder beta function (explained in Chapter 2).

A good criterion for an optimum overlap of the electron and radiation beams is to equate the electron beam emittance with the equivalent radiation beam emittance. For a diffraction limited radiation beam, assuming the radiation is focussed to a waist, the product of the Gaussian waist size and the half angle divergence at the waist is a constant given by the wavelength of radiation λ_l. The optimum overlap is achieved when both the electron and radiation beam emittances are equal. This leads to a general criterion for the maximum tolerable electron beam emittance as:

$$\epsilon_{x,y} \leq \frac{\lambda_l}{4\pi}. \tag{1.73}$$

For an X-ray FEL, this puts a very demanding requirement on the quality of the electron beam, e.g. 10 keV photon beams (0.125 nm wavelength) will require beam transverse emittance less than 10^{-11}m.rad which in practice cannot be achieved.

Another important effect to consider is diffraction of the radiation beam. As already mentioned, for optimum energy transfer between the electron beam and the radiation, the electron beam size should be properly matched with the radiation beam size. However, the FEL radiation undergoes optical diffraction, which can spoil the good overlap between the electron beam and the radiation, resulting in a reduction of the energy transfer from the electrons to the radiation. However, there is an effect called “gain guiding" [30] that counteracts widening of the FEL beam due to diffraction, allowing the exponential growth in FEL power to continue. To provide efficient gain guiding the FEL amplification has to be large enough so that the radiation intensity overcompensates the losses by diffraction. The characteristic measures for diffraction and FEL amplification are the Rayleigh length Z_R (defined as the distance over which the beam cross section grows by a factor of two from its minimum value at a beam waist) and the gain length L_G. For $Z_R \ll L_G$, the FEL amplification is diffraction limited with a gain length significantly larger than the estimates from the one-dimensional model. For $Z_R \gg L_G$, the one-dimensional model is valid. As a rule of thumb, the Rayleigh length should be twice the gain length or larger.

The three main requirements on the electron beam driving the FEL (namely, a high peak current, very low emittance and very small energy spread) can be satisfied by a specially optimised FEL driver design based on a photoinjector and several linear accelerator modules with suitable bunch compression schemes. In order to provide suitably tailored beams for different and multiple experiments, it is desirable to include so called “beam switchyard" or “beam spreader" as an essential part of the FEL driver. The switchyard or spreader designs need to preserve the above mentioned three requirements and thus need a careful design philosophy.

1.4 Summary

The fourth generation sources based on free electron laser use advances in many fields including ultra-bright electron sources, RF technology, timing and synchronisation, diagnostics etc. Over last decade, few X-ray free electron lasers have come in operation and few more will be in operation in next couple of years. These sources provide several orders higher peak brightness of photons with a larger spectral range than that covered by conventional lasers. The time duration of photon pulses is many orders shorter compared to third generation sources allowing to use it to understand ultra-fast processes in molecules for the first time.

This chapter summarises the basic principles of Free Electron Laser, their types based on gain (low, intermediate and high) and on how micro-bunching is achieved (resonator and amplifier). The three main requirements on the electron beams to drive a high gain FEL are a high peak bunch current, very low emittance and very small energy spread need a specially optimised accelerator design. It is desirable to provide flexibility of FEL configurations and to incorporate multiple FEL beam lines to fully exploit a facility. This is possible by including beam switchyard or beam spreader in the facility. The design of the beam spreader needs to preserve the beam properties. The motivation of the work undertaken in this thesis is discussed.

1.5 Motivation

The electron beam driver for a high-gain amplifier FEL is generally based on a linear accelerator with layout along a straight line in order to maintain the high brightness of the beam from the source. Excluding the beam spreader, the bending in the design of such an FEL driver is essentially restricted to bunch compressors and in case of a seeded FEL, a dogleg for incorporating seeding laser. FELs of this kind serve one experiment at a time with the radiation pulse repetition rate set by the driver linac repetition (or pulse) rate. It is possible to split the FEL photon radiation to multiple experiments, but this has limitations due to optics/mechanics and space constraints. Another option is to use spent beam to drive another FEL, but this is usually only possible for soft X-rays with less demanding beam quality requirements. On the other hand, a third generation light source facility based on a storage ring typically provide some 10’s of beam lines with higher than MHz pulse repetition rates. It is therefore highly desirable that the FEL based fourth generation sources provide many beam lines/user stations to make efficient use of pulsed or continuous wave (CW) linacs as well as to allow for experimental set up and variation in beam properties like in the third generation light source based on storage ring radiation available from the bending magnets and different insertion devices cater for variety of experiments.

The only way to provide multiple beam lines on an FEL is to direct the beam to several beam lines using a beam switchyard or beam spreader. This means either dividing the Linac pulses into different beam lines or switching all the pulses to a particular experiment for some period of time. However whilst doing this, bending the electron beam is unavoidable and the quality of the electron beam (low emittance, low energy spread, high peak current) achieved through a careful design of the accelerator can be completely spoiled if the design of the spreader/switchyard is not chosen and optimised correctly. As described in Chapter 5, a small amount of gradual bending is desirable to maintain the beam properties and this has implications for the length of the spreader which can occupy significant fraction of the total length of the facility. This has a direct impact on the layout and cost of the facility.

The motivation of choosing spreader design as the main topic for this thesis is to develop an understanding of several concepts that could be used to switch the beam with minimum dilution of the beam properties. The aim is to study designs covering different beam energies and parameter regimes. This will guide to propose optimum switchyard design to satisfy the layout constraints; which may be due to site restriction or the facility being built in already existing infrastructure or to propose a suitable layout for a new facility on green field site without any of these constraints. The studies described here cover the beam dynamics issues relevant for an energy range of few GeV with varying bunch parameters. This energy range covers the energy of design studies for UK's New Light Source [37] and a possible future facility in the UK. The research presented here will also be of direct relevance for the delivery of high quality beams from Compact Linear Accelerator for Research and Applications “CLARA" [38] for other applications such as research into plasma wakefield acceleration and dielectric wakefield acceleration.

1.6 Thesis Outline and Author's Contributions

The structure of the thesis is as follows. This Chapter gives a brief history of accelerators as photon sources, outlines the basic theory of how an FEL works and describes the requirements for an FEL driver to deliver a high quality beam for the FEL. Chapter 2 summarises basic beam optics principles and gives definitions of important beam properties used in this thesis. Chapter 3 introduces the beam dynamics challenges in the design of an accelerator as a FEL driver and describes the challenges for each subsystem of the accelerator. Chapter 4 covers the theory of Coherent Synchrotron Radiation (CSR). CSR is one of the most important collective effects detrimental to the electron beam quality and is of particular importance in the spreader/switchyard designs. Techniques to mitigate CSR effects are discussed in this chapter. Chapter 5 addresses spreader designs based on different concepts, covering a range of electron beam energies and beam parameters with recommendations regarding important diagnostics and instrumentation requirements. Chapter 6 describes experimental work on ALICE (Accelerators and Lasers In Combined Experiments, an IR-FEL facility at Daresbury Laboratory). The experiments aim to characterise the beam dynamics in an arc section of the ALICE beam line, with particular emphasis on aspects relevant for the design of spreaders in future FEL facilities. Chapter 7 summarises the work presented in this thesis and its relevance to future national and international facilities, and indicates further work that will need to be done in this area in future.

Major parts of Chapter 1, Chapter 2, Section 3.1 and Chapter 4 include cited works essential to define the context of the work described in this thesis; full citations are provided throughout. All designs, simulation results and figures presented without references are the author's own work. The initial beam spreader design for the UK's New Light Source (NLS) project was built-upon that designed for LBNL's Next Generation Light Source project. This is acknowledged and cited here as well as in the NLS conceptual design report. Improvements in this design and other design options, presented and described in Chapter 5, were completely undertaken by the author. The experimental work on ALICE (Chapter 6) was carried out in conjunction with team members. Where appropriate, full citations of the contributions by these co-workers are provided. The selection of experimental and simulation work relevant to the spreader design included here is almost wholly the author's own work.

Chapter 2

Beam Optics and Beam Parameter Definitions

This chapter introduces the basic concepts used in electron beam transport in a beam spreader and the description of beam parameters used in this thesis. The main references used here are [27, 39, 40, 41].

2.1 Beam Optics

The physical principles by which a beam of electrons is transported and focussed along an accelerator are referred to as the beam optics. Central to the beam optics design is the accelerator lattice, which is the sequence of elements along an assumed ideal reference (design) trajectory that the electrons pass through. The reference trajectory is the path taken by electrons with central momentum equal to p_0, passing through idealised elements (i.e. no errors in positioning and fields). The electron beam is bent and focussed by means of electromagnetic fields ($\vec{E}$ and $\vec{B}$). In the presence of these fields electrons with charge e and velocity $\vec{v}$ experience the Lorentz force given by:

$$\vec{F} = e(\vec{E} + \vec{v} \times \vec{B}). \tag{2.1}$$

At relativistic velocities, a magnetic field $\vec{B}$ can produce the same force on an electron as an electric field $\vec{E}/c$. For example, a magnetic field strength of 1 T is equivalent to an electric field strength of 300 MV/m. In practice however it is easier to produce a magnetic field of 1 T than an electric field of 300 MV/m. Therefore, magnetic fields are generally used to transport a beam of relativistic electrons.

2.1.1 The Co-ordinate System in a Beam Line

It is convenient to describe the motion of individual electrons in terms of co-ordinates with respect to the reference trajectory. The instantaneous position of an electron can be specified by the curvilinear orthogonal co-ordinates (x, y, s), where s is the distance along the reference trajectory from some arbitrary reference point. The horizontal (x) and vertical (y) co-ordinates are the perpendicular distances to the tangent to the reference trajectory at s. The co-ordinates x, y, and s form a local right-handed rectangular co-ordinate system, as shown in Fig. 2.1.

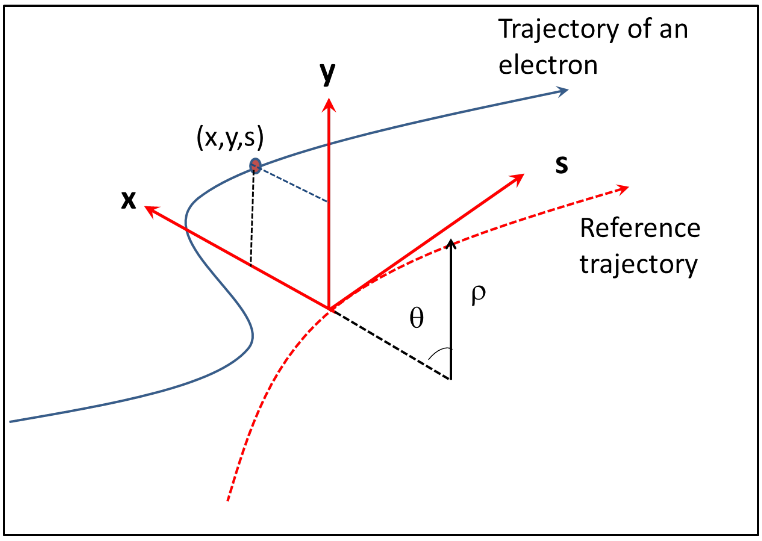

Figure 2.1: Co-ordinate system used to describe electron trajectories in the vicinity of the reference (design) trajectory in a beam transport system.

The transverse momenta are the canonical momenta, normalised by a reference momentum, p_0 which is the momentum of the reference electron which can be chosen arbitrarily:

$$p_x = \frac{1}{p_0}\left(\gamma m_e \frac{dx}{dt} + eA_x\right),$$
$$p_y = \frac{1}{p_0}\left(\gamma m_e \frac{dy}{dt} + eA_y\right), \tag{2.2}$$

where m_e and e are the mass and charge of the electron, γ is the relativistic factor, A_x and A_y are the transverse components of the vector potential. The transverse dynamics of an electron are described by giving (x, p_x) and (y, p_y) as function of s.

As explained later in this chapter, the motion of an electron can be described by Hill's equation (eqn.(2.8)). It is convenient to use the variables x and x' instead of x and p_x. The two variables p_x, p_y given in eqn.(2.2) and $x' = v_x/v_s, y' = v_y/v_s$ are approximately equal only if the angle between the direction of motion of an electron and the reference trajectory is small (i.e. $|x'| << 1, |y'| << 1$). The term "trace space" is used for the co-ordinate space (x, x') and (y, y') as compared to "phase space" which is described by (x, p_x) and (y, p_y).

The longitudinal co-ordinate of an electron is defined by $z = (s/\beta_0) - ct$, where β_0 is the normalised velocity of an electron with the reference energy of $E_0 = \gamma_0 mc^2$, and momentum $p_0 = \beta_0\gamma_0 mc$; t is the time at which the electron of interest arrives at location s. Thus z is approximately the distance along the reference trajectory that an electron is ahead of the reference electron. The final variable to describe the motion of an electron is the energy. It is convenient to use the energy deviation from the reference energy written as:

$$\delta = \frac{E_0}{p_0 c} - \frac{1}{\beta_0}. \tag{2.3}$$

The longitudinal dynamics are described by (z, δ).

2.1.2 Beam Rigidity and Expansion of Magnetic Field Seen by the Beam

Assuming that the reference trajectory lies in the horizontal plane, the magnetic field (including only “normal" multipoles) within the plane of the reference trajectory is purely vertical. An electron with mass m_e following the reference trajectory and being bent through this vertical magnetic field experiences a balance between the Lorentz force $-ev_s B_y$ and the centripetal force $\gamma m_e v_s^2/\rho$, where ρ is the radius of curvature of the reference trajectory. Using this balance of forces and $p_0 = \gamma m_e v_s$ this can be written as:

$$\frac{1}{\rho(x, y, s)} = \frac{e}{p_0} B_y(x, y, s). \tag{2.4}$$

Since the transverse dimensions of the electron beam are small compared to the radius of curvature of its trajectory, it is possible to expand the magnetic field observed by the beam in the vicinity of the reference trajectory as:

$$B_y(x) = B_{y0} + \frac{dB_y}{dx} x + \frac{1}{2!} \frac{d^2 B_y}{dx^2} x^2 + \ldots \tag{2.5}$$

Multiplying both sides by e/p_0, this can be written as:

$$\frac{e}{p_0} B_y(x) = \frac{e}{p_0} B_{y0} + \frac{e}{p_0} \frac{dB_y}{dx} x + \frac{e}{p_0} \frac{1}{2!} \frac{d^2 B_y}{dx^2} x^2 + \ldots \tag{2.6}$$

Using eqn.(2.4) and defining $k_1 = \frac{e}{p_0}\frac{dB_y}{dx}$, $k_2 = \frac{e}{p_0}\frac{d^2 B_y}{dx^2}, \ldots k_n = \frac{e}{p_0}\frac{d^n B_y}{dx^n}$, this can be simplified as:

$$\frac{e}{p_0} B_y(x) = \frac{1}{\rho} + k_1 x + \frac{1}{2!} k_2 x^2 + \ldots \tag{2.7}$$

The terms on the right hand side give the dipole, quadrupole, sextupole and higher order terms, respectively. The magnetic field around the beam can therefore be specified as a sum of multipoles, each affecting the beam in different way, i.e. dipole to bend or steer, quadrupole to focus transversely and sextupole to correct focusing of electrons with deviation in energy and to correct higher order aberrations. If only dipole and quadrupole terms (where the magnetic field is either constant or increases linearly) are used, the optics are described as linear optics. In a beam line (as typically used in a beam spreader design for an FEL), all quadrupole magnets are oriented in such a way that the motion transverse to the direction of motion of electrons on the reference trajectory is in principle decoupled in the horizontal and vertical directions. This orientation of the quadrupoles is consistent with the assumption that $\vec{B}$ is purely vertical in the (horizontal) plane of the magnetic trajectory. In practice however a small coupling will be present due to limitations on the accuracy of alignment of magnets, but the uncoupled transport principles can still be used. Another important assumption is that an electron following the reference trajectory through an idealised magnet experiences a field which begins and ends abruptly at the entrance and exit faces of the magnet (known as the hard edge model). However, in a real magnet, non-zero fields exist (fringe fields) beyond the entrance and exit faces and some approximations are used to take care of these fields e.g. by using a measured magnetic length instead of the physical length of the magnet.

Using the definition of beam rigidity as p_0/e and substituting for momentum ($p_0 = \beta_0 E_0/c$) in eqn.(2.4), where β_0 is the relativistic factor (which is nearly equal to 1 for ultra-relativistic electrons) and E_0 is the energy of a reference electron, the beam rigidity can simply be written as $B_0\rho$ [Tm]=3.33 E_0 [GeV]. This defines the value of ρ in metres given the vertical magnetic field $B_y = B_0$ in Tesla or defines the required magnetic field B_0 to bend the beam with bending radius ρ. E_0 is in the units of giga ($= 10^9$) electron volts (1 eV=energy gained by an electron in passing through a potential of 1 V). The chosen length of a dipole (l_{dipole}) with field B_0 provides a deflection (i.e. a bending angle) of $\frac{l_{dipole}}{\rho} = \frac{l_{dipole}B_0}{p_0/e}$. A dipole can be either a sector magnet, where an electron enters and exits at 90° to the pole face or the entrance and exit faces can be at some angle to the reference trajectory which provides some focusing in the vertical plane as described in Section 2.2.1. Figure 2.2 shows the cross-section of geometry of dipole, quadrupole and sextupole magnets and Fig. 2.3 shows the photograph of these magnets. The magnetic fields are achieved by arranging coils around the poles to provide required fields. The number of turns in these coils, the gap or aperture between the poles will determine the magnetic field experienced by the electrons. The direction of current in the coils and the direction of electrons (into/out of paper) will decide which way electrons are bent and focussed. The main focusing (or defocusing) forces along a beam line are provided by quadrupole magnets which have four iron poles shaped in the form of a

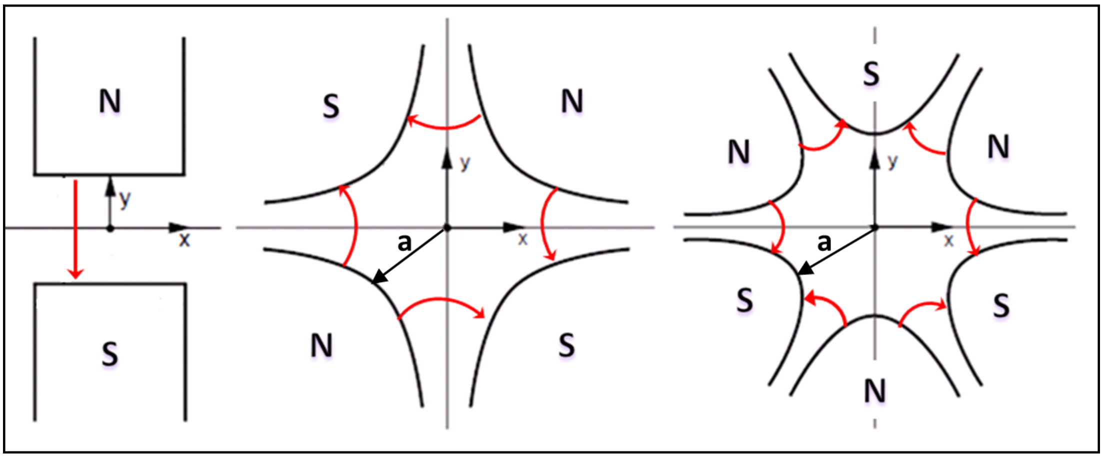

Figure 2.2: Left to right: Illustration of cross-section of dipole, quadrupole and sextupole magnets. Red arrows show direction of the magnetic field.

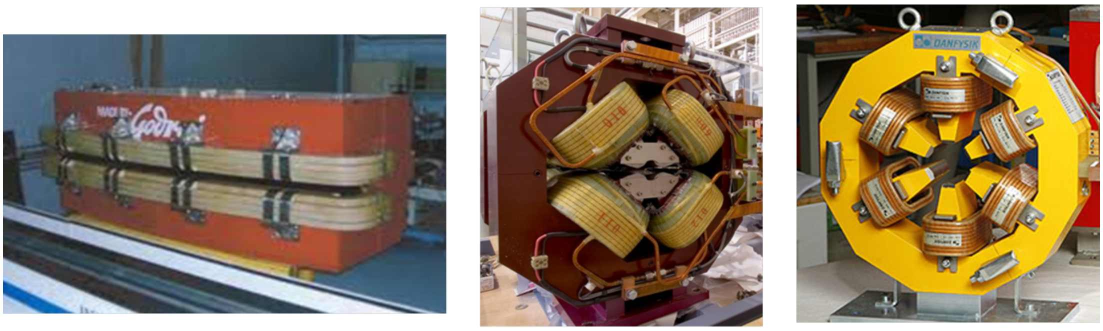

Figure 2.3: Photograph of dipole, quadrupole and sextupoles magnet, taken from [42].

hyperbola $xy = a^2/2$, where a is the radius of circle inscribed between the four poles. The field of the quadrupole magnet is zero on the design axis but it increases linearly with transverse distance. Thus the field components are given by $B_y = gx$ and $B_x = gy$ where $g = dB_x/dy = dB_y/dx$ is the field gradient. Depending upon the direction of motion of electrons, a quadrupole which is horizontally focusing is vertically defocusing and vice versa. In electromagnets, as typically used in the beam transport, the magnetic field depends upon the current passing through the coils of a magnet. The pole shapes and the coils around them are arranged in such a way that the magnetic field increases linearly over the aperture of a magnet from the centre. To keep the same focusing effect from the magnet when beam energy increases, one needs to increase the gradient in the same proportion. In designing the lattice, it is therefore convenient to use a normalised gradient (known as strength) defined by $k_1 = g/B_0\rho$. Higher order multipoles such as sextupoles, octupoles are used for correction of higher order aberrations. The normalised strengths can be written as $k_n = (n!/B_0\rho).(B_{pt}/a^n)$, where n = 0, 1, 2,... for dipole, quadrupole, sextupole, ... etc, B_{pt} is the field at the distance equal to "a" from the centre of the magnet (see Fig. 2.2). Use of these strengths instead of gradients make the lattice design independent of the beam reference energy. The lattice designer has to ensure that the integrated strength values (product of strength and length of a magnet) in the design lattice are practically achievable considering the maximum value of the magnetic field in a given aperture.

2.2 Equation of Motion of an Electron in an Accelerator

For a lattice without coupling and with bending in the horizontal plane, the motion of an electron obeys Hill's equation [41]:

$$\begin{aligned} \frac{d^2x}{ds^2} + \left(\frac{1}{\rho(s)^2} - k(s)\right) x(s) &= \frac{\delta}{\rho(s)}, \\ \frac{d^2y}{ds^2} + k(s)y(s) &= 0. \end{aligned} \tag{2.8}$$

where $k(s)$ is a function of s that characterises the focusing at each point along the beam line in horizontal (x) and vertical (y) planes. $\rho(s)$ is the bending radius of the dipole magnet and δ is the energy deviation from the reference momentum. The homogeneous part of Hill's equations can be written as:

$$u'' + K(s)u = 0, \tag{2.9}$$

where u stands for x or y, assuming K to be constant with $K(s) = (\frac{1}{\rho(s)^2} - k(s))$ and $K(s) = k(s)$ respectively. For $K > 0$, the principle solutions of this differential equation are:

$$\begin{aligned} C(s) &= \cos(\sqrt{K}s) \\ S(s) &= \frac{1}{\sqrt{K}}\sin(\sqrt{K}s) \end{aligned} \tag{2.10}$$

and for $K < 0$ are:

$$\begin{aligned} C(s) &= \cosh(\sqrt{|K|}s \\ S(s) &= \frac{1}{\sqrt{|K|}}\sinh(\sqrt{|K|}s) \end{aligned} \tag{2.11}$$

The general solution of eqn.(2.8) can be written as a linear combination of the two principle solutions as:

$$\begin{aligned} u(s) &= a_1C(s) + a_2S(s) + \delta\eta(s) \\ u'(s) &= a_1C'(s) + a_2S'(s) + \delta\eta'(s) \end{aligned} \tag{2.12}$$

with a_1 and a_2 are the constants determined by the initial conditions. The function $\eta(s)$ is the dispersion function which describes the change in electron trajectory with momentum. Eq.(2.12) can be written in a matrix form as:

$$\begin{pmatrix} u(s) \\ u'(s) \\ \delta \end{pmatrix} = \begin{pmatrix} C(s) & S(s) & \eta(s) \\ C'(s) & S'(s) & \eta'(s) \\ 0 & 0 & 1 \end{pmatrix} \begin{pmatrix} u(s_0) \\ u'(s_0) \\ \delta \end{pmatrix}. \tag{2.13}$$

It is assumed here that the electron energy and energy deviation does not change along the beam line. The trajectory of off-momentum electrons is described by the dispersion function $\eta(s)$ as:

$$\eta(s) = S(s)\int_{s_0}^{s}\frac{1}{\rho(t)}C(t)dt - C(s)\int_{s_0}^{s}\frac{1}{\rho(t)}S(t)dt \tag{2.14}$$

2.2.1 Matrix Formalism

As seen in the previous section, the solutions of equation of motion of an electron can be written using matrix formalism. These can be extended to particular elements in a beam line using 6-D vector, which represents the position and angle of the electron motion in the transverse planes and the longitudinal position and energy of the electron. This 6-D vector is represented as:

$$X = \begin{pmatrix} x \\ x' \\ y \\ y' \\ z \\ \delta \end{pmatrix}. \tag{2.15}$$

The transfer matrices describe the action of a magnetic element and a drift space on the co-ordinates of the electron using linear and higher order terms. The first-order matrix is referred to as R-Matrix, the second-order matrix as T-Matrix, the third-order matrix as U-matrix and so on [43]. The final co-ordinates at location s_1 are then described using the co-ordinates at location s_0 by adding these terms as:

$$X_i(s_1) = \sum_j R_{ij} X_j(s_0) + \sum_{jk} T_{ijk} X_j(s_0) X_k(s_0) + \sum_{jkf} U_{ijkf} X_j(s_0) X_k(s_0) X_f(s_0) \tag{2.16}$$

In a beam line with complex geometries such as arcs and FEL spreader designs, the second order terms can distort the phase space which can affect the beam transport. However, to start with, it is sufficient to use first-order terms to design a beam line. The effect of higher orders are included while tracking the bunch through a beam spreader. We describe the motion of electrons using linear matrices in the following.

The linear R-matrix at location $s = s_0$ is transformed through a R-matrix to give 6-D co-ordinates at location $s = s_1$ given by:

$$\begin{pmatrix} x \\ x' \\ y \\ y' \\ z \\ \delta \end{pmatrix}_{s=s_1} = R(s_1 : s_0) \begin{pmatrix} x \\ x' \\ y \\ y' \\ z \\ \delta \end{pmatrix}_{s=s_0}. \tag{2.17}$$

Assuming a mid-plane symmetry (no coupling between the x and y planes), accelerating cavities are absent (which is the case for a beam spreader) and there is no radiation, the 6×6 R matrix can be simplified as:

$$\begin{pmatrix} x \\ x' \\ y \\ y' \\ z \\ \delta \end{pmatrix}_{s=s_1} = \begin{pmatrix} R_{11} & R_{12} & 0 & 0 & 0 & R_{16} \\ R_{21} & R_{22} & 0 & 0 & 0 & R_{26} \\ 0 & 0 & R_{33} & R_{34} & 0 & 0 \\ 0 & 0 & R_{43} & R_{44} & 0 & 0 \\ R_{51} & R_{52} & R_{53} & R_{54} & 1 & R_{56} \\ 0 & 0 & 0 & 0 & 0 & 1 \end{pmatrix} \begin{pmatrix} x \\ x' \\ y \\ y' \\ z \\ \delta \end{pmatrix}_{s=s_0}. \tag{2.18}$$

By solving the equations of motion for electrons given by eqns. (2.8) in each element in the beam line, one arrives at first order R-matrices as follows:

- A drift space is a field-free region through which the beam passes. It is specified by a single parameter, which is its length l_d:

$$R_{\mathrm{drift}} = \begin{pmatrix} 1 & l_d & 0 & 0 & 0 & 0 \\ 0 & 1 & 0 & 0 & 0 & 0 \\ 0 & 0 & 1 & l_d & 0 & 0 \\ 0 & 0 & 0 & 1 & 0 & 0 \\ 0 & 0 & 0 & 0 & 1 & 0 \\ 0 & 0 & 0 & 0 & 0 & 1 \end{pmatrix}. \tag{2.19}$$

- A quadrupole magnet provides focusing in one transverse plane and defocusing in the other. When the length of a quadrupole is small compared to its focal length (i.e. $l_q << 1/(|k_{x,y}|l_q)$, it can be represented by a thin lens positioned at its centre. In the beam spreader design, this condition is not satisfied and matrices for thick lenses need to be used.

  The R-matrix for a horizontally focusing quadrupole with ($k_x < 0$) and length equal to l_q is given by:

$$R_{\mathrm{quad}} = \begin{pmatrix} \cos\theta & \frac{1}{\sqrt{|k_x|}}\sin\theta & 0 & 0 & 0 & 0 \\ -\sqrt{|k_x|}\sin\theta & \cos\theta & 0 & 0 & 0 & 0 \\ 0 & 0 & \cosh\theta & \frac{1}{\sqrt{|k_x|}}\sinh\theta & 0 & 0 \\ 0 & 0 & \sqrt{|k_x|}\sinh\theta & \cosh\theta & 0 & 0 \\ 0 & 0 & 0 & 0 & 1 & 0 \\ 0 & 0 & 0 & 0 & 0 & 1 \end{pmatrix}, \tag{2.20}$$

  where $\theta = \sqrt{|k_x|}l_q$.

- Vertically focusing quadrupole with ($k_y > 0$) and length equal to l_q:

$$R_{\mathrm{quad}} = \begin{pmatrix} \cosh\theta & \frac{1}{\sqrt{k_y}}\sinh\theta & 0 & 0 & 0 & 0 \\ \sqrt{k_y}\sinh\theta & \cosh\theta & 0 & 0 & 0 & 0 \\ 0 & 0 & \cos\theta & \frac{1}{\sqrt{k_y}}\sin\theta & 0 & 0 \\ 0 & 0 & -\sqrt{k_y}\sin\theta & \cos\theta & 0 & 0 \\ 0 & 0 & 0 & 0 & 1 & 0 \\ 0 & 0 & 0 & 0 & 0 & 1 \end{pmatrix}, \tag{2.21}$$

  where $\theta = \sqrt{k_y}l_q$.

  The matrices are derived assuming that the strength parameter $k_{x,y}$ to be a step function with a constant nonzero value within the quadrupole and zero outside. The strength of a real quadrupole magnet varies smoothly from zero outside to maximum value in the middle of the quadrupole and the integrated value of strength considering this effective length is used in a final lattice design.

- For describing the motion of electrons in a dipole magnet, the simplest case is when the trajectory of electrons is perpendicular to the pole face at the entrance and exit

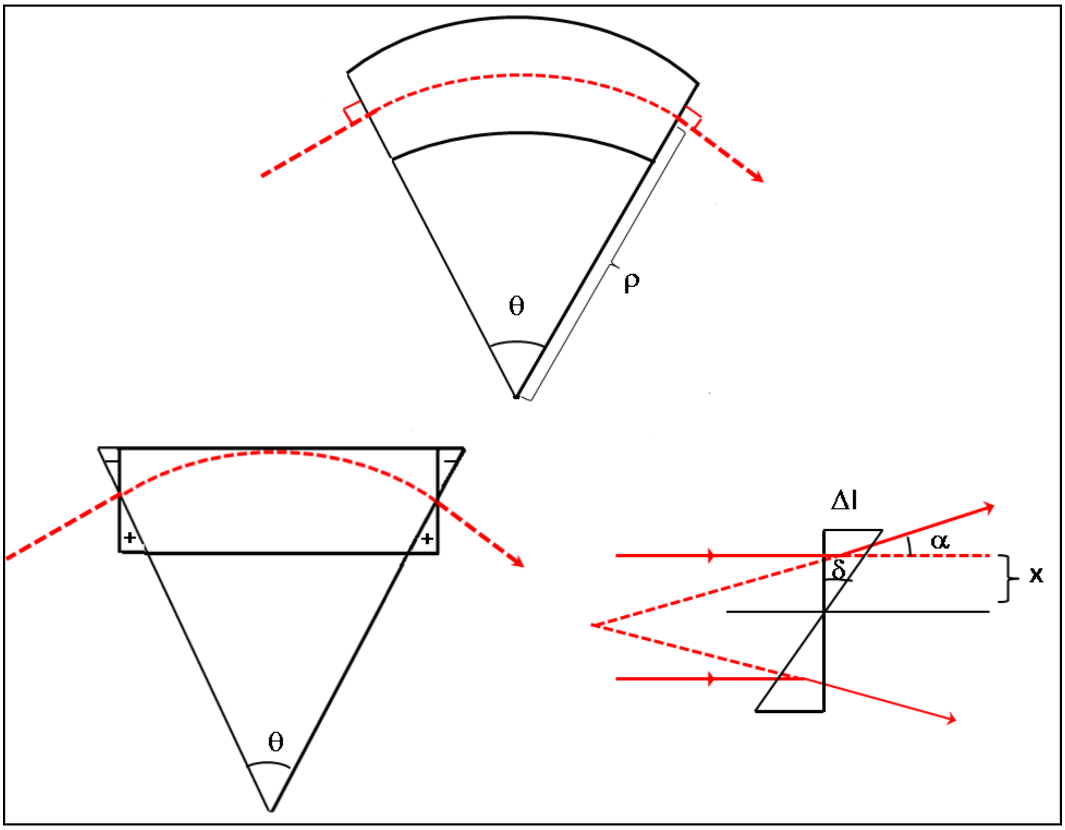

Figure 2.4: Top: Sector dipole magnet. Beam enters and exits at right angle with the pole face edge. Bottom: Rectangular dipole magnet and horizontally defocusing magnetic wedge.

of the magnet as shown in Fig. 2.4. In this case the dipole is known as a sector dipole. The transfer matrix for a sector dipole with length l_{dipole} bending the beam by $\theta = (l_{dipole}/\rho)$ in horizontal plane is given by:

$$R_{\text{dipole}} = \begin{pmatrix} \cos\theta & \rho\sin\theta & 0 & 0 & 0 & \rho(1-\cos\theta) \\ -\frac{1}{\rho}\sin\theta & \cos\theta & 0 & 0 & 0 & \sin\theta \\ 0 & 0 & 1 & 0 & 0 & 0 \\ 0 & 0 & 0 & 1 & 0 & 0 \\ \sin\theta & \rho(1-\cos\theta) & 0 & 0 & 1 & \rho(\theta-\sin\theta) \\ 0 & 0 & 0 & 0 & 0 & 1 \end{pmatrix}. \qquad (2.22)$$

In practice, dipoles magnets are often built with magnet edges not perpendicular to the reference trajectory. A rectangular dipole magnet can be derived from a sector magnet by superimposing at the entrance and exit a “magnetic wedge" of length Δl and angle equal to $\delta = \theta/2$, as shown in Fig. 2.4. At each wedge, the deflecting angle is changed by $\alpha = \Delta l/\rho = x\tan\delta/\rho$. It acts as a thin defocusing lens with focal length $1/f = \tan\delta/\rho$ in the horizontal plane and as a focusing length with the same strength in the vertical plane. The horizontal matrix for a rectangular magnet is written as:

$$R_{\rm dipole} = \begin{pmatrix} 1 & 0 & 0 \\ \frac{\tan\delta}{\rho} & 1 & 0 \\ 0 & 0 & 1 \end{pmatrix} \begin{pmatrix} \cos\theta & \rho\sin\theta & \rho(1-\cos\theta) \\ -\frac{1}{\rho}\sin\theta & \cos\theta & \sin\theta \\ 0 & 0 & 1 \end{pmatrix} \begin{pmatrix} 1 & 0 & 0 \\ \frac{\tan\delta}{\rho} & 1 & 0 \\ 0 & 0 & 1 \end{pmatrix}. \tag{2.23}$$

For $\theta << 1, \delta = \theta/2$, in the bending plane:

$$R_{\rm x} = \begin{pmatrix} 1 & \rho\sin\theta & \rho(1-\cos\theta) \\ 0 & 1 & 2\tan\theta/2 \\ 0 & 0 & 1 \end{pmatrix}. \tag{2.24}$$

In the non-bending plane:

$$R_{\rm y} = \begin{pmatrix} \cos\theta & \rho\sin\theta & 0 \\ -1/\rho\sin\theta & \cos\theta & 0 \\ 0 & 0 & 1 \end{pmatrix}. \tag{2.25}$$

In a rectangular dipole magnet, the weak horizontal focusing of a sector magnet ($1/\rho^2$) is exactly compensated by the defocusing at the entrance and exit faces. A weak focusing is provided in the vertical plane.

The lattice built up of pure dipoles and pure quadrupoles is called separated function lattice. However, it is possible to combine many multipoles in the same magnet, e.g. combining the dipole and quadrupole fields in a single magnet is called as combined function magnet.

The R matrix is symplectic if the beam line does not include dissipative effects such as radiation, scattering etc and thus preserves area in the phase space. Let us consider a small section of a periodic beam line consisting of focusing (F) and defocusing (D) quadrupoles placed at regular intervals separated by a drift space (O). The FODO cells with quadrupole integrated strength equal to $0.5\,\mathrm{m}^{-1}$ and drift length equal to $1\,\mathrm{m}$ are repeated in a beam line. The electron trajectory is plotted in the horizontal plane for a simple case for a lattice with shown in Fig. 2.5. While travelling down this FODO lattice, electrons perform transverse (betatron) oscillations about the reference trajectory. The oscillation amplitude and wavelength of these oscillations will vary along the beam line and is characterised by the quadrupole strengths and the drift lengths (there are constraints on both these parameters for stable motion of electrons in this lattice). It is assumed that there is no coupling between the transverse planes. If the co-ordinates of electrons travelling down this beam line (x, x') are plotted at different s locations in the beam line at corresponding points within each periodic cell, they will trace out ellipses in phase space as shown in Fig. 2.6. The shape of the ellipse defines Courant-Snyder (also known as Twiss) parameters. The area of the ellipse defines the action J_x of the electron.

From the equation of ellipse, it is possible to write:

$$2J_x = \gamma_x x^2 + 2\alpha_x x x' + \beta_x x'^2. \tag{2.26}$$

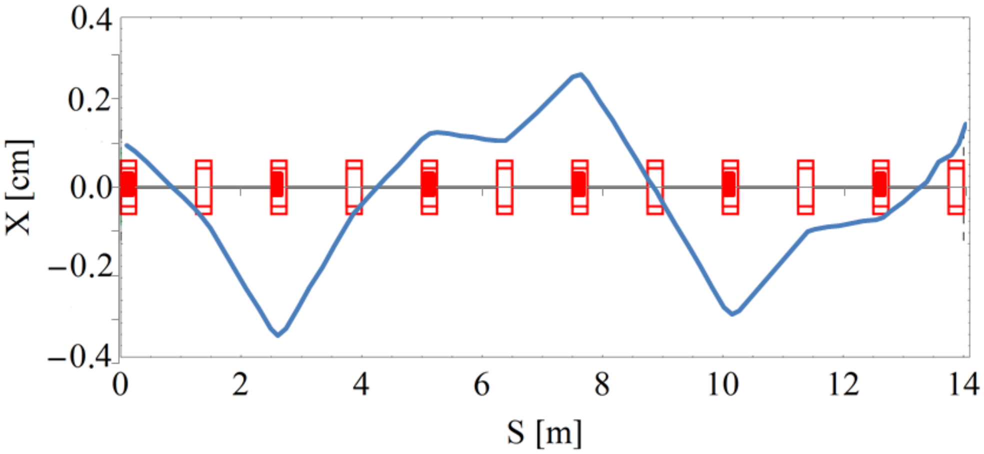

Figure 2.5: Trajectory in horizontal plane of an electron travelling through a FODO beam line consisting of focusing (filled red rectangles) and defocusing (unfilled red rectangles) quadrupoles. The quadrupoles have integrated strengths of 1.4 m^{-1} and drift spaces are equal to 1 m. The initial horizontal co-ordinate and it derivative are x=1 mm and x'=0.

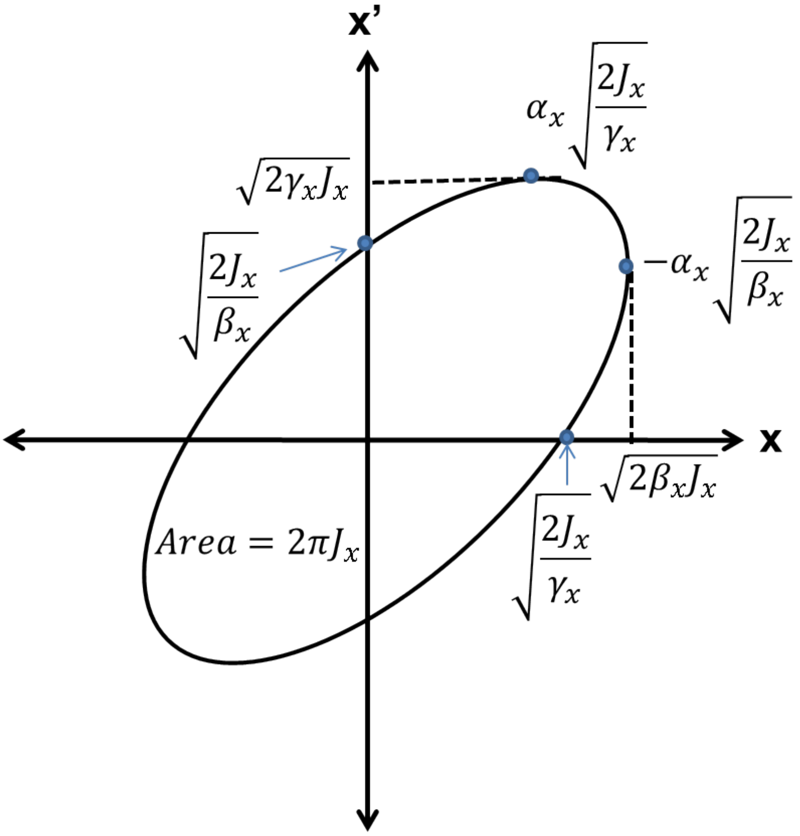

Figure 2.6: The trace space ellipse of electron motion in a beam line.

where α_x, β_x and γ_x are the Courant-Snyder parameters, and satisfy the additional constraint $\beta_x\gamma_x - \alpha_x^2 = 1$. The angle variable ϕ_x is defined as:

$$\tan\phi_x = -\beta_x \frac{x'}{x} - \alpha_x. \tag{2.27}$$

The action-angle variables (ϕ_x, J_x) (J_x is the conjugate momentum) form a canonically conjugate pair. The action variable J_x is used to describe the amplitude of the motion of a single electron [39]. The relationship between these variables and (x, x') is:

$$\begin{aligned} x &= \sqrt{2\beta_x J_x}\cos\phi_x, \\ x' &= -\sqrt{\frac{2J_x}{\beta_x}}(\sin\phi_x + \alpha_x\cos\phi_x). \end{aligned} \tag{2.28}$$

The emittance ϵ_x of a bunch is defined as the average amplitude of all electrons in the bunch:

$$\epsilon_x = \langle J_x \rangle . \tag{2.29}$$

With this relationship between the emittance and the average action, the following relationships for the second-order moments of the electron distribution within the bunch can be obtained:

$$\begin{aligned} \langle x^2 \rangle &= \beta_x\epsilon_x, \\ \left\langle x'x \right\rangle &= -\alpha_x\epsilon_x, \\ \left\langle x'^2 \right\rangle &= \gamma_x\epsilon_x. \end{aligned} \tag{2.30}$$

Combining eqns. (2.29, 2.30) and using the relation $\beta_x\gamma_x - \alpha_x^2 = 1$, the emittance can be expressed in terms of the beam distribution:

$$\epsilon_x = \sqrt{\langle x^2 \rangle \langle x'^2 \rangle - \langle xx' \rangle^2}. \tag{2.31}$$

The transverse emittance is a measure of the trace space area occupied by the electrons in a beam projected onto one transverse plane. This is strictly valid when the electron distribution is centred on the reference trajectory. If there are physical processes involved that produce variable transverse offsets or focusing along a bunch of electrons, the transverse emittance as well as the Courant-Snyder parameters will vary along the bunch. This leads to the concept of slice emittance of electron beam. The overall emittance integrated over the full length of a bunch (the projected emittance) is an important quantity measurable by many diagnostics devices, whereas a special transverse deflecting cavity is required to measure the emittance of individual slices along the bunch.

When electrons are accelerated, the emittance decreases inversely proportional to the momentum. This can be explained by the fact that during the acceleration, only the longitudinal component of the momentum vector is increased while the transverse component stays the same. This results in reduction of the divergence. The term normalised emittance $\epsilon_{Nx,Ny} = \gamma\epsilon_{x,y}$, (where γ is the relativistic factor) is used to describe energy independent emittance, which does not change in a beam line without radiation and other dissipative forces.

2.2.2 Amplitude and Phase Formalism

The second method to solve Hill's equation uses a global function which describes the focusing characteristics of the lattice [39]. Due to the similarity of Hill's equation for simple harmonic motion, it is possible to use the solution of the form:

$$x = \sqrt{2\beta_x J_x} \cos\phi_x, \tag{2.32}$$

where J_x is a constant, and β_x and ϕ_x are functions of s. This equation represents the motion of an electron along a beam line as an oscillation with varying amplitude and wavelength. Substituting eqn.(2.32) in eqn.(2.8) and equating coefficients of $\cos\phi_x$ and $\sin\phi_x$ on either side of equation leads to:

$$\begin{aligned} \beta_x'\phi_x' + \beta_x\phi_x'' &= 0, \\ \frac{\beta_x''}{2\beta_x} - \frac{\beta_x'^2}{4\beta_x^2} - \phi_x'^2 &= -k \end{aligned} \tag{2.33}$$

The first equation in eqn.(2.33) has solution $\phi_x' = \text{constant}/\beta_x$. It is convenient to set this constant equal to 1 (though different values of the constant equally lead to valid solutions, the β_x and ϕ_x will have different interpretation). Substituting this to the second equation gives the differential equation for β_x:

$$\beta_x'' - \frac{4 + \beta_x'^2}{2\beta_x} + 2k\beta_x = 0 \tag{2.34}$$

From the design of the beam line, the value of k is known and thus for given initial values of β_x and β_x' eqn.(2.34) can be integrated to obtain the value of β_x at any position along the beam line.

In the case of a periodic beam line, the focusing strength satisfies the periodicity condition: $k(s + C_0) = k(s)$, where s is any point along the beam line, which has a periodicity C_0. The same periodicity condition can be imposed on the beta functions: $\beta_x(s + C_0) = \beta_x(s)$, $\beta_x'(s + C_0) = \beta_x'(s)$. Similar expressions can be written in the vertical plane.

2.2.3 Transformation of Courant-Snyder Parameters

The trace space ellipse at a point s in a beam line is characterised by the Courant-Snyder parameters $\beta_x(s), \alpha_x(s), \gamma_x(s)$ and the beam emittance ϵ_x in the horizontal transverse plane (and similarly in the vertical transverse plane denoted by y). It is important to know the beam envelope and divergence at different locations along the beam line. This needs transformation of Courant-Snyder parameters through the lattice. As the action is invariant, it is possible to write it at any two points (say s_0 which is a starting point where the Courant-Snyder parameters are known and another point s_1) at which these parameters need to be calculated:

$$2J_x = \gamma_{x_1}^2 x_1^2 + 2\alpha_{x_1} x_1 x_1' + \beta_{x_1} x_1'^2 = \gamma_{x_0}^2 x_0^2 + 2\alpha_{x_0} x_0 x_0' + \beta_{x_0} x_0'^2. \tag{2.35}$$

Using the principal trajectories described in Section 2.2, and taking the inverse of the transformation matrix:

$$\begin{aligned} x_0 &= S'(s)x_1 - S(s)x_1', \\ x_0' &= -C'(s)x_1 + C(s)x_1'. \end{aligned} \tag{2.36}$$

Substituting eqn.(2.36) in to eqn.(2.35) and comparing the coefficients, the Courant–Snyder parameters are calculated as:

$$\begin{pmatrix} \beta_{x1} \\ \alpha_{x1} \\ \gamma_{x1} \end{pmatrix} = \begin{pmatrix} C(s)^2 & -2S(s)C(s) & S(s)^2 \\ -C(s)C'(s) & S(s)C'(s) + S'(s)C(s) & -S(s)S'(s) \\ C'(s)^2 & -2S'(s)C'(s) & S'(s)^2 \end{pmatrix} \begin{pmatrix} \beta_{x0} \\ \alpha_{x0} \\ \gamma_{x0} \end{pmatrix}. \tag{2.37}$$

The transformation of the Courant-Snyder parameters given by eqn.(2.37) not only simplifies the lattice design for periodic lattices (where initial values are known) but is also useful in designing beam transport line where precise initial values of the Courant-Snyder parameters are not known. One can cover a range of starting values of the Courant-Snyder parameters to design the lattice and decide the specifications of lattice elements.

The principal trajectories can be expressed in terms of initial and final Courant–Snyder parameters as:

$$\begin{pmatrix} x_1 \\ x_1' \end{pmatrix} = \begin{pmatrix} \sqrt{\frac{\beta_1}{\beta_0}}(\cos\Delta\phi + \alpha_0 \sin\Delta\phi) & \sqrt{\beta_0\beta_1}\sin\Delta\phi \\ -\frac{(\alpha_1-\alpha_0)}{\sqrt{\beta_0\beta_1}}\cos\Delta\phi - \frac{(1+\alpha_0\alpha_1)}{\sqrt{\beta_0\beta_1}}\sin\Delta\phi & \sqrt{\frac{\beta_0}{\beta_1}}(\cos\Delta\phi - \alpha_1\sin\Delta\phi) \end{pmatrix} \begin{pmatrix} x_0 \\ x_0' \end{pmatrix}, \tag{2.38}$$

where $\Delta\phi$ is the phase advance from s_0 to s_1. Similar matrices can be written in the vertical plane. In a periodic beam line, the same lattice cell is repeated number of times and the Courant–Snyder parameters are the same at the entrance and the exit of each cell. In this case, eqn.(2.38) simplifies to:

$$\begin{pmatrix} x_1 \\ x_1' \end{pmatrix} = \begin{pmatrix} \cos\Delta\phi + \alpha\sin\Delta\phi & \beta\sin\Delta\phi \\ -\gamma\sin\Delta\phi & \cos\Delta\phi - \alpha\sin\Delta\phi \end{pmatrix} \begin{pmatrix} x_0 \\ x_0' \end{pmatrix}, \tag{2.39}$$

where $\Delta\phi$ is the total phase advance in the beam line and $\beta_1 = \beta_0 = \beta$, $\alpha_1 = \alpha_0 = \alpha$ and $\gamma = (1+\alpha^2)/\beta$. From eqn.(2.39), the total phase advance and the Courant–Snyder parameters over a cell are determined as:

$$\begin{aligned} \Delta\phi &= \cos^{-1}\left(\frac{R_{11}+R_{22}}{2}\right), \\ \beta &= \frac{R_{12}}{\sin(\Delta\phi)}, \\ \alpha &= \frac{R_{11}-R_{22}}{2\sin(\Delta\phi)}. \end{aligned} \tag{2.40}$$

2.2.4 Lattice Design Cells

The beam spreader designs described in Chapter 5 consist three basic lattice design cells; FODO, a double bend achromat and an isochronous triple bend achromat. Using previous

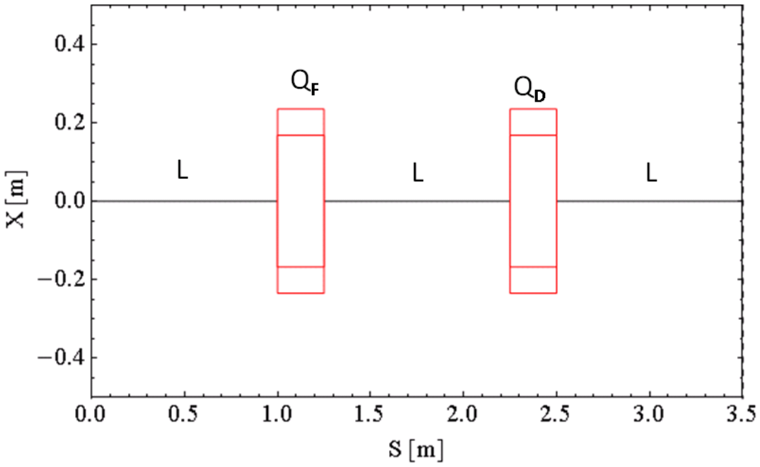

Figure 2.7: Schematic of FODO cell.

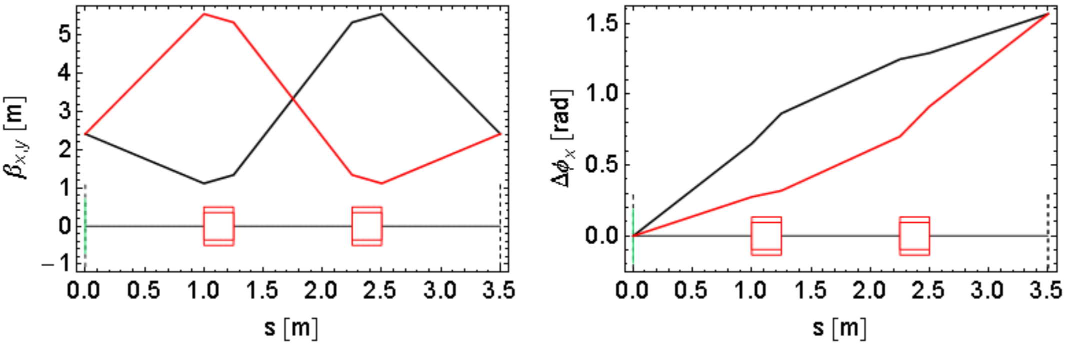

Figure 2.8: Left: Periodic β_x function (red) and β_y function (black) in FODO shown in 2.7. Right: Phase advance in x (red) and y (black) planes.

sections in this chapter, these concepts are briefly described here.

FODO

A FODO lattice consists of two quadrupoles (F and D), each focusing in one plane separated by drift spaces (O). The beam line can be repeated from any point along s. An example of one FODO cell is shown in Fig. 2.7. The F and D in this cell is 0.25 m long and have strength equal to 3.56 m^{-2}. The drift spaces L are equal to 1 m. For the lattice to be periodic, the Courant–Snyder functions β and α in both transverse planes need to be equal at the entrance and exit of this cell as shown in Fig. 2.8. The phase advance in the horizontal and the vertical plane is identical. In this case starting $\beta_x = \beta_y = 2.419$ m and $\alpha_x = 1.111, \alpha_y = -1.111$.

Double Bend Achromat

If a beam line uses dipole magnets to bend the beam, the dispersion is generated and the off-momentum electrons follow different trajectories. For a number of reasons, it is

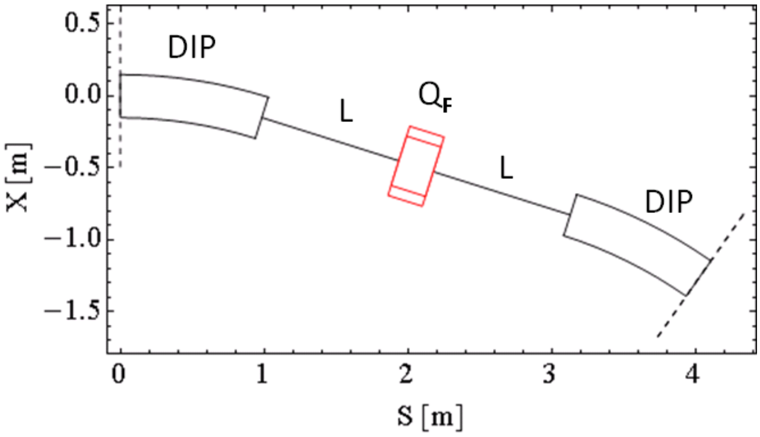

Figure 2.9: Example of achromatic cell with a single focusing quadrupole in the centre.

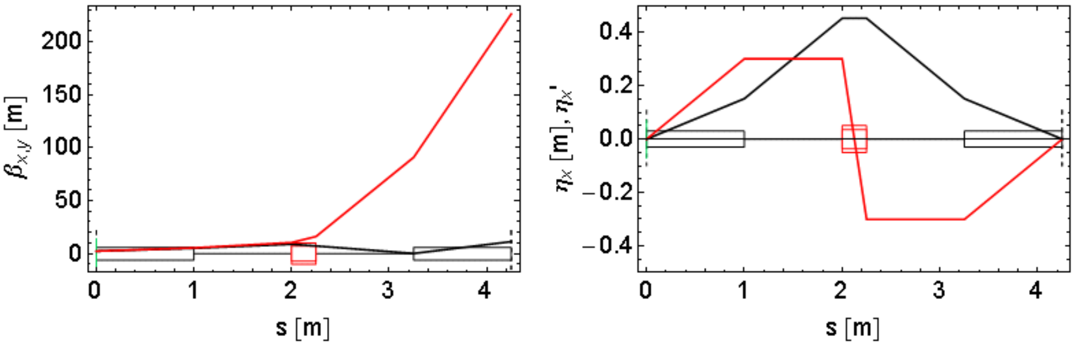

Figure 2.10: Left: β_x function (black) and β_y function (red) in double bend achromat shown in Fig. 2.9. Right: Dispersion (black) and its derivative (red).

preferable to make a beam line "non-dispersive" or "achromatic" after essential bending is acquired. The simplest achromatic cell can be designed using two identical dipoles with a focusing quadrupole (in the plane of bending) placed in the centre as shown in Fig. 2.9. In this example, dipoles are 1.0 m long with bending angle of 0.3 rad. The drift length L is 1 m. Quadrupole is 0.25 m long and has a strength equal to 5.175 m^{-2}. It is assumed that there is no dispersion at the entrance of the achromat. Fig. 2.10 shows the Courant–Snyder parameters, the dispersion function and its derivative. In this design, no focusing is provided in the vertical plane as can be seen from the β_y plot. Adding two more quadrupoles symmetrically placed with ($L_1 = 1$ m and $L_2 = 0.5\,m$) as shown in Fig. 2.11 with strengths of Q_D equal to -5.52 m^{-2} and of Q_F to 6.98 m^{-2} focusing in both planes is possible as shown in Fig. 2.12.

Depending on the beam line design and layout requirements, the design of achromat can be arranged in different ways. For example, the double bend achromat designs used in Chapter 5 insert two dipoles at phase advance of π in a FODO lattice to provide an achromatic design.

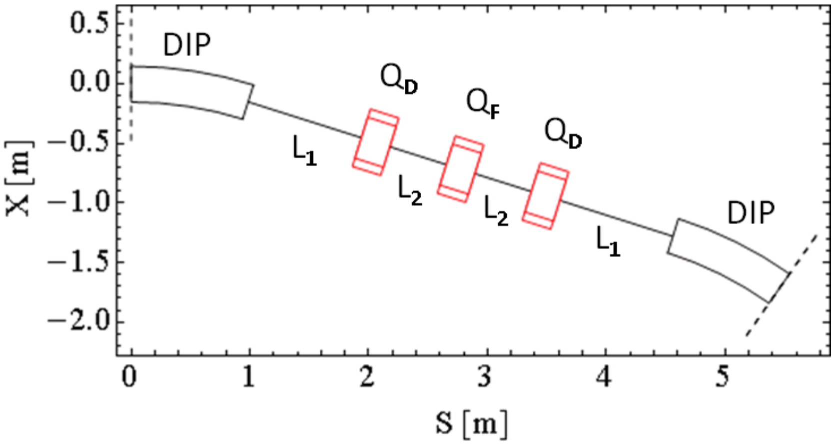

Figure 2.11: Example of achromatic cell with a symmetric quadrupole triplet to provide focusing in both transverse planes.

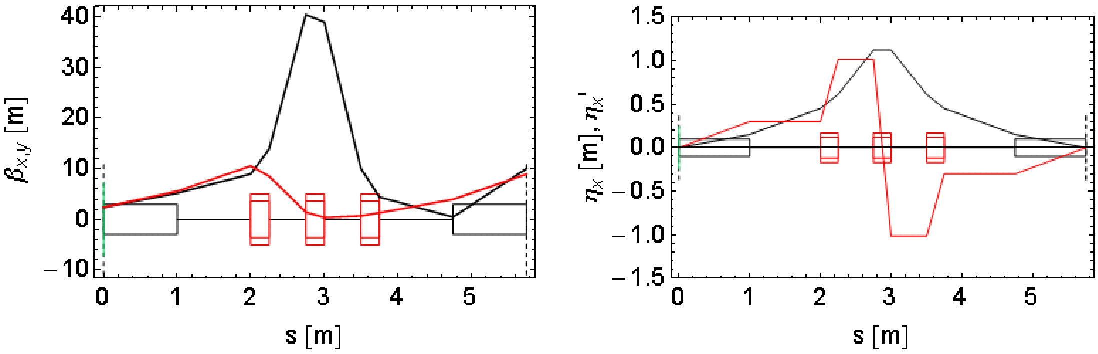

Figure 2.12: Left: β_x function (black) and β_y function (red) in double bend achromat shown in Fig.2.11. Right: Dispersion (black) and its derivative (red).

Achromatic and Isochronous Lattice

A lattice is isochronous if there is no momentum dependence on the total path length. This is achieved by arranging a lattice with dipoles and quadrupoles to manipulate the dispersion function in such a way that the lattice is achromatic as described in previous section and the integral of dispersion function over the lattice is zero. The path length dependence on momentum to first order is given by R-matrix term R_{56}. An example of a triple bend lattice (described in Chapter 5) is shown in Fig. 2.13. Fig. 2.14 shows that the lattice is achromatic and isochronous.

Depending on the beam line design and requirements, the design of triple bend achromat can be arranged in different ways. For example, the ALICE TBA arc described in Chapter 6 and TBA arc designs in beam spreader Chapter 5.

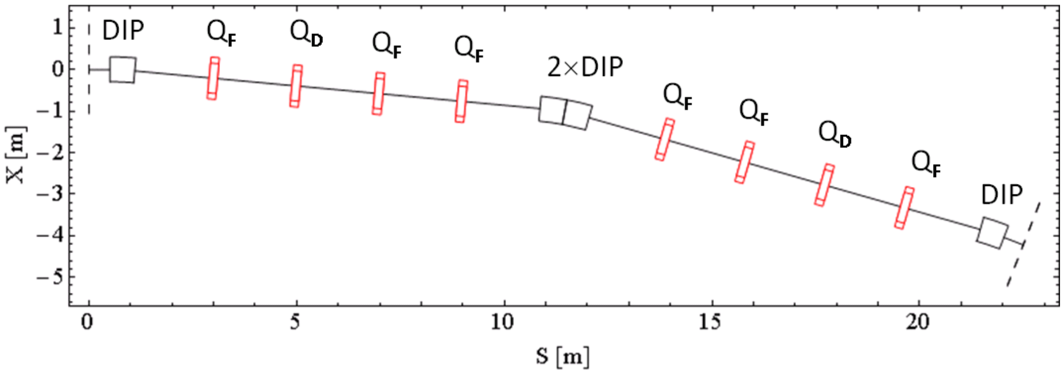

Figure 2.13: Example of triple bend achromat

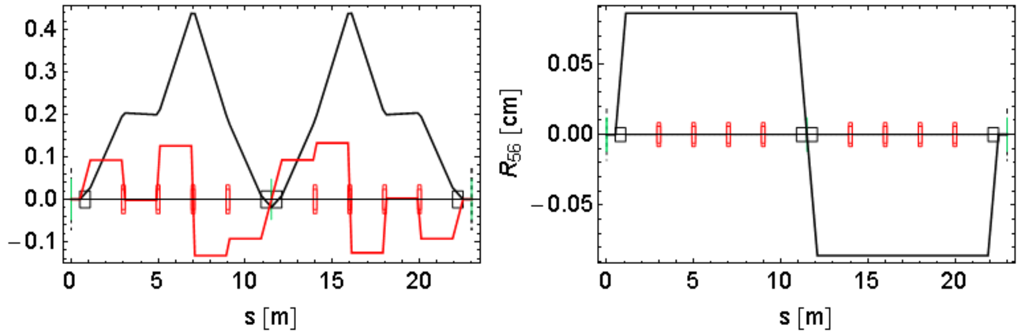

Figure 2.14: Left: Dispersion (black) and its derivative (red) in triple bend achromat shown in 2.13. Right: Path length dependence on momentum shown by a linear matrix term R_{56}.

2.3 Electron Beam Distribution

An electron beam in a beam transport line is described by a six dimensional distribution function (co-ordinates and angles to the reference trajectory) as a function of distance s along the reference trajectory. A commonly used distribution function to represent an electron beam is Gaussian. For example, in horizontal transverse plane, the distribution can be expressed as:

$$f(x, x') = \frac{1}{2\pi\sigma_x\sigma_{x'}} \exp\left(-\frac{x^2}{2\sigma_x^2} - \frac{x'^2}{2\sigma_{x'}^2}\right). \tag{2.41}$$

The standard deviation in x, σ_x when the mean value of the distribution is zero $\langle x\rangle = 0$, is given as:

$$\sigma_x = \langle x^2\rangle^{\frac{1}{2}} = \left(\frac{1}{N_e}\sum_{i=1}^{N_e} x_i^2\right)^{\frac{1}{2}}. \tag{2.42}$$

The summation is over all electrons in a beam and x_i is the horizontal co-ordinate of the i^{th} electron. If the co-ordinate and corresponding angles with respect to the reference trajectory of each electron in a beam are plotted at a given location, it gives the trace space plot in that plane.

A flat-top distribution (in longitudinal as well as transverse planes) is often used in the design of the FEL driver. This alleviates the increase in beam emittance due to space charge at lower energies.

2.4 Errors on Magnetic Elements

In a real accelerator, the assumption of linear transport is not strictly valid as effects such as alignment errors on magnetic elements, deviation in magnetic fields or higher order multipoles arising during magnet design and fabrication as well as requirements to introduce multipole magnets (for example, sextupoles to correct the chromatic effects) are unavoidable. In the design stage of lattice, one often assumes the magnetic elements to be located so that the centre of each element is aligned exactly on the reference trajectory and there is no rotation around the (x, y, s) axes. The field provided by the magnets is an integrated field over the length of the magnetic element which is assumed to be hard edged.

The errors in longitudinal displacement of beam transport elements can usually be dealt with by changing the drift space lengths and by making appropriate changes to magnets providing focusing in most of the cases, except when the symmetry of the periodic lattice could be broken, (for example the centre quadrupole in Fig.2.9).

A dipole magnet providing a bending in the horizontal plane assumes a purely vertical field. Misalignments in the x, y co-ordinates and rotations around the x, y axes cause a change in position and direction of the electron trajectory; to first order these errors do not affect the distribution of electrons about the reference trajectory [44] and so do not affect the beam motion significantly. A rotation around the s axis, however, gives rise to a transverse (horizontal) component in the magnetic field. A rotation about the x axis also gives a horizontal component of the field. This deflects electrons vertically, so that electrons following the reference trajectory on entering the magnet have some vertical displacement and angle, with respect to the reference trajectory on leaving the magnet. A rotation of a dipole around the s axis leads to vertical distortion of the electron trajectories, and also to vertical dispersion.

An ideal quadrupole magnet has a magnetic field that is zero along the axis, assumed to be aligned with the reference trajectory. If the quadrupole of length l_q and strength k_1 is offset horizontally (vertically) by $\Delta x(\Delta y)$, there is a non-zero field seen by an electron following the reference trajectory. This field gives a kick to electron bunch equal to $k_1 l_q \Delta x$ (or $k_1 l_q \Delta y$), where $k_1 l_q$ is the integrated strength of the quadrupole. A rotation of a quadrupole around the s axis gives rise to coupling between the transverse planes (by introducing a skew quadrupole component in the field).

In the case of a sextupole magnet, however, there are different effects from horizontal offsets and vertical offsets. If a sextupole of length l_s and strength k_2 is offset horizontally (vertically) by $\Delta x(\Delta y)$, an electron bunch will receive a kick equal to:

$$\begin{aligned}\Delta x' &= -\frac{1}{2}k_2 l_s(\Delta x^2 - \Delta y^2),\\ \Delta y' &= k_2 l_s \Delta x \Delta y. \end{aligned} \qquad (2.43)$$

A horizontal offset in the sextupole thus generates a quadrupole component, and a vertical offset generates coupling (the same effect as a skew quadrupole). The effects of horizontal offset of the sextupoles in ALICE arc are discussed in Chapter 6.

These undesired effects arising from misalignments and field errors cannot be completely avoided in a real accelerator and once the lattice is designed, it is important to study the sensitivity of the beam properties to these errors to define the level of alignment (and correction) required to maintain the necessary beam quality. In addition to the alignment errors, tolerances on the field uniformity and higher order components (arising from the very nature of magnet design as well as fabrication tolerances) also need to be specified. The systematic errors arising from design and the random errors arising from fabrication need to be considered in deciding the mitigation strategies to achieve close to the design performance.

2.5 Initial Beam Parameters for Beam Line Design

The lattice cells FODO, DBA and TBA as described in Section 2.2.4 are used as basic lattice design cells in beam spreader design described in Chapter 5. At the design stage, it is possible to de-couple the design of beam spreader from the upstream accelerator. A matching section consisting of at least four quadrupoles is sufficient to match the Courant–Snyder parameters from the accelerator exit to the beam spreader entry (assuming that the dispersion and its derivative are zero, which is in general the case). These may be the matched/periodic lattice functions as suited to the beam spreader design.

For tracking the bunch through the spreader, it is easier to start with the 6-D bunch distribution at the entry of the beam spreader (at a later stage, when design of beam spreader is optimised, beam tracking using start-to-end bunch from the upstream accelerator can be used). To generate a bunch distribution at the entry of the spreader, the Courant–Snyder parameters are chosen as appropriate to the lattice cells used. Other beam parameters required for tracking are: bunch charge, energy, beam emittance (normalised or geometric), bunch length, energy spread, chirp in the longitudinal plane (correlated energy spread within bunch) and choice of bunch distribution (Gaussian, flat-top, uniform, parabolic etc.) in the transverse and longitudinal planes. Number of macroparticles can then be used to generate the required bunch distribution for tracking the bunch through the beam line.

2.6 Definition of Beam Time Structure

In the design of a beam spreader, the time structure of the beam driving the FEL has important consequences. This is due to the fact that the same beam is shared between a number of beam lines and the technology choices to switch electron bunches to separate beam lines will depend upon the time separation between consecutive single bunches or burst of macropulses. For example, operating the machine in single shot mode at 100 Hz will lead to bunch separation of 10 msec, whereas a machine operating at 1 MHz will have bunch separation of 1 μsec. This will have implications for the technology used for switching the bunches to different beam lines and hence for the choice of the beam spreader design, as discussed in Chapter 5.

The time structure of the electron beam is an important by-product of the accelerating technology used for the design (or vice-versa - to obtain a specific time structure one may need to choose the appropriate technology). When electrons are accelerated by means of radio frequency (RF) fields (which is the case for an FEL driver), a bunched beam is generated. A pulsed beam consists of a finite number of bunches and it is often required that a FEL driver delivers a beam pulse which is made up of a train of individual bunches. For bunched beams the time period during which the charge is measured can either be shorter than the duration of a bunch or a beam pulse, or it may be longer compared to both. Depending on the time scale, it is appropriate to define the peak current (or bunch current), the pulse current or the average current [27]. The peak current is defined as $I_p = q/\sqrt{2\pi\sigma_\tau}$, where $\sigma_\tau = \sigma_z/\beta_0 c$, σ_z is rms bunch length and β_0 is the scaled velocity factor, q is the bunch charge and τ is the bunch duration. Fig. 2.15 shows the definitions of peak current, pulse current and average current, the pulse current is defined as $I_{pulse} = q/T$, where T is the bunch period. The average current is defined as $\langle I \rangle = N_b q/T_r$, where N_b is the number of bunches in a single pulse duration and $1/T_r$ is the pulse repetition rate.

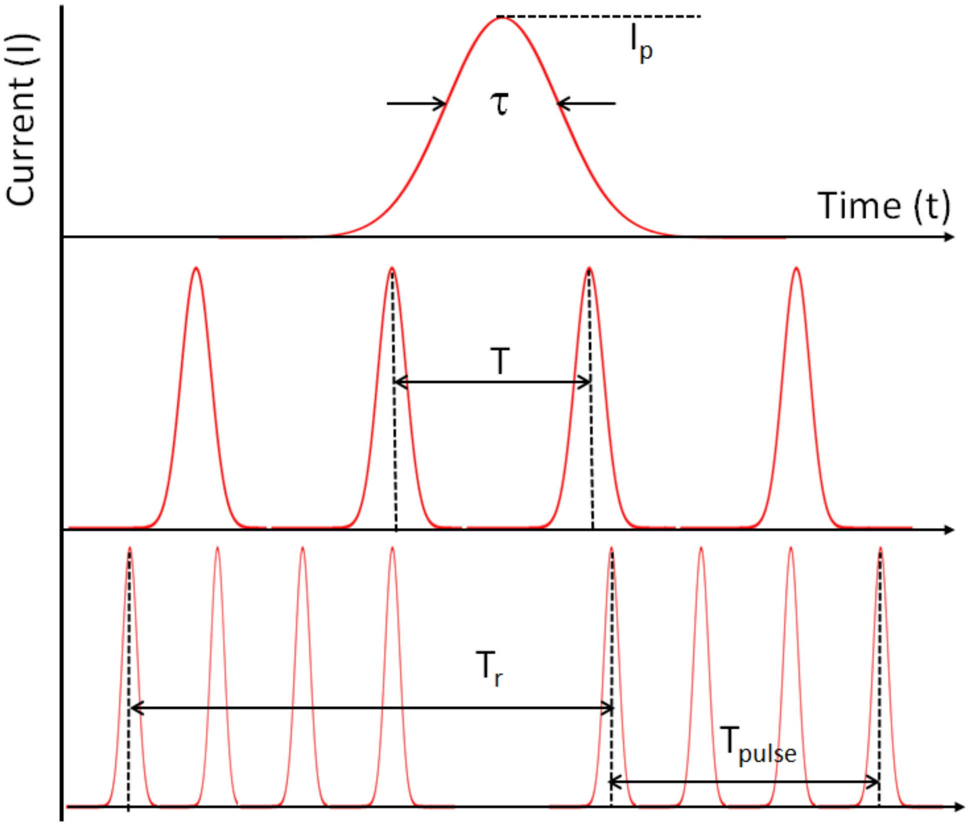

Figure 2.15: Beam time structure definitions

2.7 Summary

This chapter summarises the key principles of beam optics which are well established in designing a beam line. Basic lattice design modules FODO, DBA and TBA described in this chapter form the backbone of first steps in beam spreader lattice designs described in Chapter 5. The key electron beam parameters required for tracking an electron bunch through the beam line and the definition of bunch time structure are described.

Chapter 3

FEL Configurations and Beam Dynamics Challenges

The requirements to deliver high peak bunch current with minimum emittance degradation and low-energy spread for optimum energy transfer from electron bunch to radiation beam are critical to drive a high-gain FEL as described in Chapter 1. The specific beam dynamics and technical requirements are determined by the choice of desirable parameters as dictated by the science case of the FEL under consideration. The fundamental questions that must be answered before deciding the technology and layout configuration choices include: the required single or multiple photon wavelengths, brightness, pulse length and repetition rate of photon pulses, single or multiple FEL beam lines etc. These user requirements translate into accelerator beam specifications which then need to be matched with the choice of available technologies and R&D requirements. This chapter covers the possible layout configurations and the basic challenges that need to be addressed to meet the design goals of an FEL facility. To simplify the description of the facility design, a generic layout of a typical high gain FEL facility capable of delivering photon energies of order of a few keV is described, allowing a discussion of the purpose and the challenges for specific components as well as important beam dynamics effects.

3.1 Potentially Limiting Beam Dynamics Effects

When the intense electron bunch is generated, manipulated and transported down an accelerator, it is subject to various collective and single particle effects. Although the severity with which these can affect the required properties of the electron beam to drive an FEL depends upon the accelerator configuration and beam parameters, there are certain underlying physical processes which will affect the optimisation of the accelerator design and the FEL performance. These processes are described briefly in this section.

3.1.1 Space Charge

Space charge is a collective effect arising due to Coulomb interactions between electrons in a bunch. The self field within a bunch is one of the main limiting factors in achieving the required high peak current to drive an FEL. Space charge manifests itself in both the transverse and longitudinal planes.

For a simplified case of a cylindrical electron bunch with N electrons with charge e, a radius of r_b and a length of L_b, the radial force F_r is given by [30]:

$$F_r(r) = \frac{1}{\gamma^2} \frac{Ne^2}{2\pi\epsilon_0 L_b} \frac{r}{r_b^2}, \text{ with } r \leq r_b, \tag{3.1}$$

where γ is the relativistic factor and ϵ_0 is the permittivity of the free space. This force has a defocusing effect and thus can lead to radial blow up of the bunch. As the force is inversely proportional to γ^2, the force diminishes rapidly as the beam energy increases. The effect of the space charge on the quality of beam is thus critical at low energy (typically few MeV from a RF gun until it is accelerated to few hundreds of MeV in an accelerating section placed immediately after the gun). The defocusing force in eqn.(3.1) is linear with the distance of an electron from the axis of the bunch and thus the space charge induced transverse beam size blow up can be compensated by a solenoid lens with suitable field between the RF gun and the accelerating section [45] .

When a realistic Gaussian electron bunch is considered instead of a cylindrical bunch as assumed above, the expression for F_r changes significantly and the space charge force is given by [30]:

$$F_r(r) = \frac{1}{\gamma^2} \frac{Ne^2}{2\pi\epsilon_0 L_b r} \left(1 - \exp\left(-\frac{r^2}{2\sigma^2}\right)\right), \tag{3.2}$$

where σ is the rms transverse beam size. In this case, the radial force inside a bunch is highly non-linear and thus difficult to compensate by an external magnetic field. Therefore, the beam must be accelerated as rapidly as possible to minimise the effects of the space charge.

The Coulomb repulsion in the bunch in the direction of motion is referred as “longitudinal space charge" (LSC). Although the effects of LSC are stronger at lower energy, it continues to have an impact on beam dynamics through much higher energies. There is no LSC force if the bunch current profile is uniform. However, in a bunched beam, the LSC force tends to push electrons away from each other, accelerating the front electrons and decelerating the back electrons to give rise to an energy modulation. The main effect of the LSC is to introduce an energy chirp along a bunch as the head of the bunch is pushed forward and the tail decelerated. It can also cause micro-bunching as explained later in this chapter as any density modulation in the bunch can induce an energy modulation through longitudinal space charge, and the energy modulation can (in certain circumstances) enhance the density modulation.

3.1.2 Wake Fields

The electromagnetic fields generated by a moving bunch exert forces on the electrons in a bunch (or the following bunches - depending upon the bunch separation) due to the impedance of the surrounding vacuum vessel. Interaction of short electron bunches with the vacuum chamber determined by the shape of the chamber (geometric wakes) and chamber material (resistive wakes) cause energy modulation along the bunch. The longitudinal wake fields affect the total energy and energy spread of the bunch whereas the transverse wakes kick the bunch transversely causing emittance growth. The strength of the wake fields strongly depends on the beam pipe geometry and choice of material. Even though generally the wake fields can affect the beam quality adversely, in case of Free Electron Laser, the wake fields in the accelerating structures are useful in reducing the correlated energy chirp in the bunch. If the accelerator design does not provide enough wake fields to remove the energy chirp, additional structure known as "dechirper" needs to be included in design [46, 47]. The dechirper provides additional wake fields to meet the requirements on energy chrip in the FEL. The important effects in FEL design are wake fields from Higher Order Modes (HOMs) from the accelerating as well as higher harmonic structures, the narrow gap vessels in the undulator sections and narrow collimator gaps.

3.1.3 Coherent Synchrotron Radiation

When a very short electron bunch travels through a dipole magnet, it emits coherently at wavelengths that are comparable to (or larger than) the bunch length and can propagate in the vacuum chamber. As electrons traverse the dipole on an arc of a circle, radiation from one part of the arc can catch up with electrons on another part of the arc. The effect of this coherent synchrotron radiation (CSR) on the smooth electron density function can be explained [48, 49] with reference to Fig. 3.1. An electron bunch with total charge q travelling in a dipole with bending radius R and bending angle θ can be divided into two parts, a "tail" and, a "head", each with charge $q/2$, separated by distance L_b, where L_b is the characteristic length of the bunch. The CSR emitted from the tail of the bunch can affect the electrons at the head of the bunch only if the CSR is emitted by the tail electrons less than a slippage length behind head. The slippage length s_l is the difference in length between the chord AB (that the radiation takes) and the path length along the arc from A to B (that the electron bunch takes):

$$s_l = \mathrm{arc(AB)} - \mathrm{chord(AB)} = R\theta - 2R\sin\left(\frac{\theta}{2}\right) \approx \frac{1}{24}\theta^3 R \tag{3.3}$$

which gives:

$$\begin{aligned} \theta &= 2\left(\frac{3s_l}{R}\right)^{1/3}, \\ d &= \mathrm{chord(AB)}\sin(\theta/2) \approx 2R\sin^2(\theta/2) = 2(3s_l)^{2/3}R^{1/3}, \end{aligned} \tag{3.4}$$

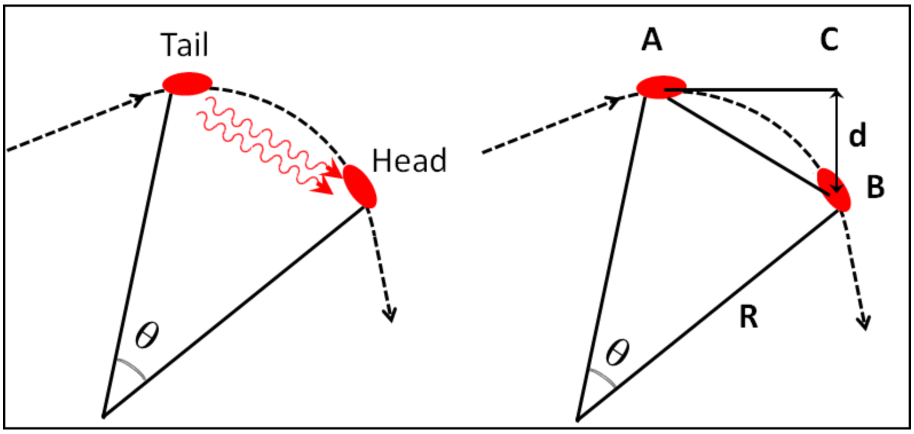

Figure 3.1: Inside a bending magnet the radiation which is emitted from electrons in the tail of a bunch can catch up with electrons in the head of a bunch which are less than a slippage length $s_l = \mathrm{arc(AB)} - \mathrm{chord(AB)}$ ahead of the tail. The head and the tail of a bunch can only interact if the magnet is long enough.

where d is the perpendicular distance between point C to point B. The magnitude of the transverse electric field acting on the electrons in the head of the bunch can be estimated as:

$$E_\perp \cong \frac{1}{4\pi\epsilon_0}\frac{2q\lambda_z}{d}, \tag{3.5}$$

where λ_z is the longitudinal electron density, $\lambda_z = N/L_b$. This field is radiated at A, its direction at B is perpendicular to the line(AC) and the electrons in the head will experience an accelerating force due to this field given by:

$$F_\parallel \cong eE_\perp\theta = \frac{2eq\lambda_z\theta}{4\pi\epsilon_0 d} = \frac{2eq\lambda_z}{4\pi\epsilon_0\sqrt[3]{3s_l R^2}}. \tag{3.6}$$

When a bunch is short ($L_b \leq s_l$) and the length of the bending magnet is long ($\gamma\theta >> 1$), the “Steady State" approximation can be applied, where the transient effects when bunch enters and leaves the magnet are not important. In this case, substituting a uniform density distribution $\lambda_z = N/L_b$, where N is the number of electrons per bunch (with $N/2$ electrons in the head and $N/2$ in the tail) and $s_l = L_b$, the rate of energy loss per unit length of the magnet can be written as:

$$\frac{dE}{dz} = -\int_{-\infty}^{\infty}\lambda_z(s)F_\parallel(s)ds = -\frac{1}{4\pi\epsilon_0}\frac{N^2e^2}{\sqrt[3]{3R^2L_b^4}}. \tag{3.7}$$

The “long magnet" condition ensures that radiation from the electrons in the tail overtakes electrons in the head before leaving the magnet. This energy loss, together with the fact that the radiation is coherent and at a wavelength comparable to the bunch length, results in a modulation of the energy along the bunch. This is similar to a wakefield but unlike wakefields, CSR affects the electrons ahead of the emitting electrons rather than behind. The change in energy of the electrons thus depends upon their longitudinal position in the bunch and (combined with dispersion) results in the transverse displacement of longitudinal slices of the electron bunch. This leads to an increase in the projected transverse emittance in the bending plane.

3.1.4 Incoherent Synchrotron Radiation

Incoherent synchrotron radiation (ISR) is emitted when the trajectories of electrons are bent in a dipole. When a photon is emitted it changes the energy of the electron resulting in a change of its transverse co-ordinate moving on a new dispersive trajectory. This phenomenon known as quantum excitation causes betatron oscillation around a new dispersive orbit. This causes transverse emittance growth and an increase in the energy spread. This is a well known phenomenon in storage rings, however, in a storage ring the restoration of beam energy by the RF cavities leads to damping of the emittance. In a transfer line, only excitation of the emittance occurs. Estimates for the emittance degradation are based on storage ring excitation formulae [50], but can be modified to reflect a more rigorous treatment of the excitation effects in a transport system [51]. For example, the growth in rms momentum spread and emittance generated by quantum excitation during 180° of bending (as required in some accelerator configurations described later in this chapter) at energy $\gamma m_0 c^2$ are given as follows [52]:

$$\begin{aligned}
\sigma_E^2 &= 1.18 \times 10^{-33}[\mathrm{G}eV^2 m^2]\frac{\gamma^7}{\rho^2}, \\
\delta\epsilon &= 7.19\pi \times [\mathrm{m}^2 rad]\frac{\gamma^5}{\rho^2}\langle H_x \rangle, \\
\text{where:} & \\
< H_x > &= \frac{1}{L}\int \frac{ds}{\beta_x}\left(\eta^2 + \left(\beta_x\eta' - \frac{1}{2}\beta_x'\eta\right)^2\right), \qquad (3.8)
\end{aligned}$$

is the average of the quantum excitation function H_x in the dipoles given by $\gamma_x\eta^2 + 2\alpha_x\eta\eta' + \beta_x\eta'^2$; β_x, α_x and γ_x are the Courant-Snyder parameters, η and η' are the dispersion and derivative of the dispersion function, L is the orbit length, and ρ the orbit radius in the bends. The parameters of the arc and the optics in the dipoles need to be chosen to minimise the function H_x in order to keep the emittance degradation to a minimum.

3.2 Facility Configuration Options

The science case of the facility under consideration is important in defining the desired range of photon characteristics. But since the cost to build and run a facility depends upon the parameter regime and the technology choices, the decision on facility configuration is likely to be influenced by it. For example, the fundamental requirement of the wavelength reach defines the choice of energy (for a practical range of undulator parameters) which heavily influences the cost. The additional requirements such as repetition rate of electron bunches, spacing between the bunches/macropulses, photon pulse length, temporal coherence, variable polarisation, multiple, simultaneous users etc. are important to decide the choice of accelerator technology. Some of these requirements have implications for both the construction and the operating costs of the facility and thus several iterations of various configuration choices are often needed before the final selection is made.

The accelerator system driving a FEL is typically based on an RF linear accelerator (linac) with electrons produced from a photocathode gun. A given bunch of electrons remains in the accelerator only briefly, for times that are short compared to most emittance growth or damping times from radiation effects (with the exception of CSR effects). If a laser-driven photocathode gun is used as the electron source, it is relatively easy to change the time structure and the beam current delivered to users by controlling the duration and power of the lasers that stimulate electron production at the injector. The transverse emittance of the electron beam tends to be set by the laser spot size on the cathode and by beam dynamics in the low-energy electron source region, and this emittance may be well preserved during the acceleration to higher energy. The pulse duration, and more generally the longitudinal phase space distribution, is manipulated by using beam-RF and electron beam optics techniques. There are several possibilities for the configuration of an FEL driver, capable (in principle) of meeting the requirements on the photons from the FEL. Fig. 3.2 shows some of the basic possibilities: single pass linac, re-circulating linac with linac in one/two arms and energy recovery linac. Extensions of these concepts (e.g. to have more than one re-circulation loop) is possible in some cases. The beam switchyard/spreader is not shown in these configurations and if multiple FEL beam lines are required, this additional requirement needs to be considered separately in each configuration.

3.2.1 Single Pass Linac

The single pass linac configuration is based on a linear geometry with the exception of the use of dipoles for compressing the bunch longitudinally and spectrometer beam lines for characterising the beam energy and energy spread. This configuration is less complex in terms of beam dynamics compared with the other configurations shown in Fig. 3.2, which depend heavily on bending the beam with dipoles. The dipoles add complexity due to coherent and incoherent synchrotron radiation (CSR and ISR) as well as chromatic terms. The single pass configuration also has flexibility for future upgrade especially if there are no constraints to extend the length of the facility. In this configuration, it is easy to choose different energies either by operating the linacs and magnetic components at a set energy (lower than the allowable maximum accelerating gradients in linacs) or by extracting beams at several locations along the accelerator. The rate at which electrons will be delivered to FEL beam lines will ultimately be decided by the repetition rate of bunches/macropulses

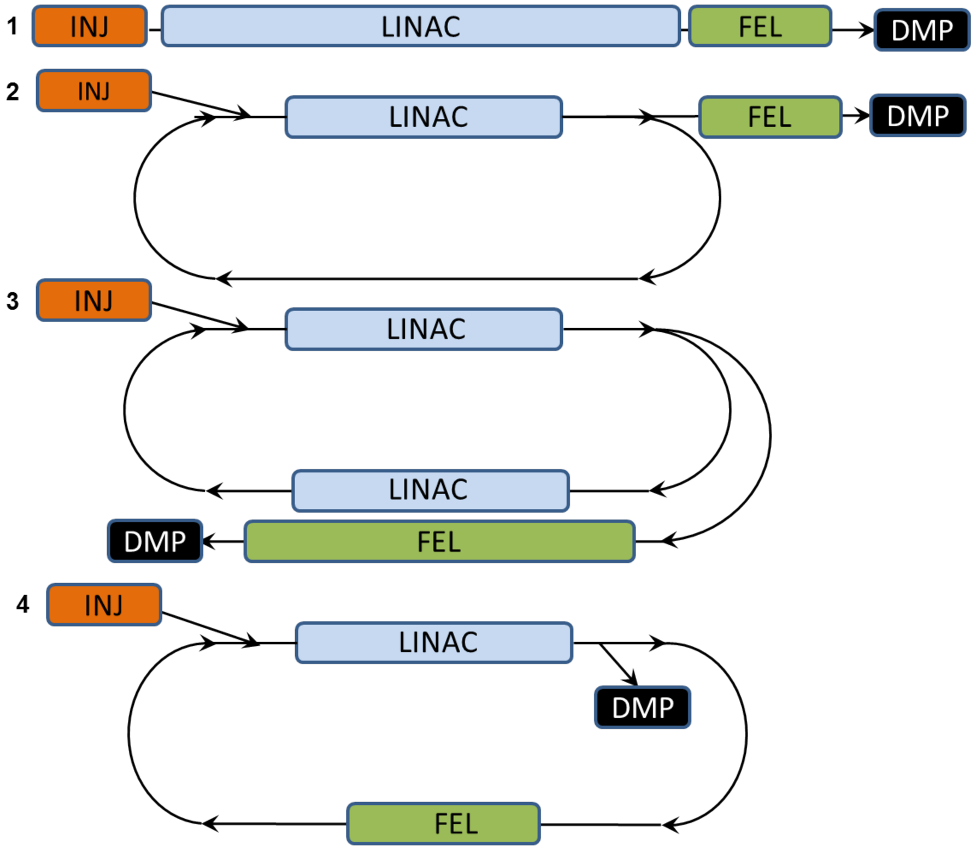

Figure 3.2: Accelerator configurations for FEL facility: 1.Single pass linac 2. Re-circulating linac with linac in one arm 3. Re-circulating linac with linacs in two arms 4. Energy recovery linac. INJ - Injector, LINAC - Accelerating structures, FEL - Free electron laser, DMP - Dump for electron beam.

from the photoinjector. The possibility of tuning the facility for a particular experiment is relatively easy compared to other configurations described in the next two sections. However, the length of the facility is relatively large in this configuration and there is a need for a large number of accelerating cavities and substantial RF infrastructure which is a major cost driver of FEL facilities. If electron bunches are extracted at multiple energies, one may need multiple beam dumps and this could have implications for the layout and cost of the facility particularly for higher beam powers (i.e. in the range of few kW to sub-MW). A single pass linac configuration will be considered later in this chapter to describe different subsystems and associated beam dynamics issues.

3.2.2 Re-circulating Linac

In order to reduce the significant costs for large number of accelerating cavities and their RF infrastructure (especially if the facility is based on a superconducting RF technology to deliver high repetition rate photon pulses), it is important to consider whether a re-circulating linac configuration could meet the FEL specifications. Re-circulating linacs are accelerators in which electron bunches pass through the linac cavities multiple times. This arrangement allows one accelerator to feature some advantages of both the ring and the linac based configurations. The re-circulating linac configuration is considered to potentially save both construction as well as operating costs of the facility (as fewer accelerating structures and associated RF sources means that the power and cryogenics requirements significantly reduce). In principle, one is able to extract beams of different energies from one location, enabling FELs resonant at different wavelengths to operate efficiently (provided the FEL designs allow this flexibility). The length of the facility is reduced as the beam passes through a shorter linac multiple times instead of making just one pass and as a consequence, the radiation shielding is required for a shorter (but somewhat wider) machine. A final advantage is that a natural upgrade path (to higher beam energies, allowing shorter FEL wavelengths) is established without the need to add accelerating modules; instead, additional recirculation paths can be constructed. The re-circulation configuration however needs additional design issues to be considered compared to a single pass machine, such as: combining and separating beams of different energies, bending the beam using arcs by 180° (at least) two times, adjusting path lengths so that electron bunches enter the linac on the correct phase on subsequent passes, etc. These issues lead to more complex beam transport systems and optics. The bunch compression and linearisation scheme are restricted as the compression cannot be done in sections with multiple beam energies. Incoherent and coherent synchrotron radiation (ISR and CSR) within the arcs leads to emittance degradation. All these issues make it more difficult to produce required high quality electron bunches for FEL operation. Due to extra beam transport, jitter tolerances also become more stringent.

3.2.3 Energy Recovery Linacs

Energy recovery as a concept dates back half a century [53]. As with many innovative accelerator ideas the practical realisation of the concept took more than two decades to materialise. The first demonstration experiments were conducted initially at the SCA FEL machine at Stanford [54, 55]. With the advances in superconducting RF technology and the successful demonstration at Jefferson Lab of DEMO-FEL [56], various groups throughout the world were inspired to explore the potential of energy recovery for various applications. This included pushing the boundaries of existing technology to deliver highly advanced light sources encompassing both FELs and spontaneous sources. Energy Recovery Linac (ERL) accelerators have significant advantages over storage rings as in ERLs the electron beam characteristics are determined by the injector; the technological developments allow to produce shorter bunches with a flexible bunch pattern. ERL accelerators also have advantages over single pass linac based machines as they offer improvements in efficiency, and potentially large increases in average currents and light source power as well as reduced dump activation. The energy recovery principle allows the construction of electron linear accelerators that can accelerate average beam currents similar to those provided by storage rings, but with the superior beam quality typical of linacs [57].

The idea of energy recovery in a re-circulating RF linac is based on the fact that RF fields, by proper choice of the time of arrival of the electron bunches in the linac, may be used to both accelerate and decelerate the same beam. As in a re-circulating configuration, a beam is injected into the linac and synchronised with the RF to accelerate on the first pass through the linac. If the re-circulation path is chosen to be precisely an integer plus half of RF wavelengths, then on the second pass through the linac, the beam is decelerated by the same RF cavities that accelerated it on the first pass. For cavities within the re-circulation loop, energy is transferred, via the RF field, from the decelerating beam to the accelerating beam. A key point is that after an initial acceleration step for the first bunches in a machine pulse, the RF power system does not need to provide the energy to accelerate the later bunches. Furthermore, in an ERL, the final energy at the beam dump is the same as the injection energy which simplifies the beam dump design.

In re-circulating linacs and ERLs, in addition to the complexity of designing additional beam transport there are other important beam physics issues which need to be considered. Beam instability resulting from ion trapping is one example. The ionisation of the residual gases in the vacuum chamber is caused by collision of electrons with the residual gas as well as by synchrotron radiation. Depending upon the bunch separation and parameters of the electron bunches, positively charged ions can get trapped in the chamber, in a similar way to that in which ions can become trapped by the beam in the storage rings. At every passage of an electron bunch, the ions can be focussed due to the potential of the electron bunches and as a result accumulation of ions may take place. The accumulated ions in turn can affect the properties of electron lattice and beam parameters. The remedies adopted usually are either to leave a gap between long trains of electron bunches to allow for ions to escape or/and to use ion clearing electrodes.

Another important issue to consider when the accelerating configuration is based on a multiple pass re-circulating linac is an instability known as beam breakup (BBU) which can limit the beam current [58]. In an accelerating cavity, a number of higher-order modes (HOMs) are excited by a bunched electron beam. If a HOM has a dipole field, it will kick an electron bunch in a transverse direction. When the kicked electron bunch returns to the same accelerating cavity after re-circulation with position and phase that further excites the HOM, its amplitude can grow exponentially and the beam is eventually lost due to the finite transverse aperture of the beam pipe. Estimates of threshold currents required to initiate the instability can be made using an analytical formula [59] and provide guidelines for the appropriate choice of RF parameters to maintain a safe margin.

3.2.4 Comparison of Issues in Different Configurations

The choice of accelerator configuration is based on the required FEL parameters and can vary significantly depending upon the FEL wavelength regime (IR, UV, soft X-ray, hard X-ray etc.). For example, a requirement on high average current to deliver high flux and brightness will need an ERL configuration. The possibility to incorporate a multi-pass option in an ERL configuration may be required to reach higher energy. The single pass and single shot (one bunch in an RF pulse operating at order 100 Hz) will typically have low average current but the higher energy reach will be easier to achieve by adding more accelerating structures.

Depending upon the choice of configuration, several considerations need to be addressed. For example, an injector merger is not required on a single pass machine unless there is a plan for two different injectors to be used on the facility to deliver beam parameters in two different regimes, (for example, different pulse repetition rates as was foreseen in New Light Source [37]). Whereas in the ERL or re-circulation linac, a merger is necessary to bring the beam from the injector into the main loop. As explained later, a higher harmonic cavity is necessary to linearise the phase-space in the case of a single pass linear machine, whereas there is a possibility of linearising in the arcs in case of a re-circulating linac and ERL. It is also possible to compress bunches in arcs instead of using dedicated bunch compressor chicanes, although such a scheme is much more restricted due to implications of CSR in the arc and better control of linearisation in a dedicated system. Due to typically long lengths (several meters) of the linac, there is usually a requirement to include focusing quadrupoles between the accelerating modules. In case of a re-circulating linac, these quadrupoles have to provide appropriate beam optics correct for two different beam energies and can add more complexity if the number of passes is more than two. There is a requirement to match the optics correctly to the arc in both re-circulating linac and ERL. This has implications for both the cost and footprint of the facility, even though the number of accelerating modules is reduced due to re-circulation. When entering the linac second time, it is required that the correct RF phase is seen by the beam, which needs additional means to adjust the path length between passes.

All three configurations have limitations due to CSR, ISR, space charge, wakefields and microbunching but there is additional beam transport to be factored in the design optimisation for the re-circulation and the ERL. There can be multiple locations of beam dumps for single pass and re-circulation linac at the end of every beam line, which could be combined into one if required. In case of an ERL, the used beam will have to combined and brought back into the main linac for energy recovery. This will involve additional beam transport and full energy recovery may be difficult due to beam disruption after the FEL (typically, there is a large increase in energy spread).

The design issues to consider in the beam spreader design are independent of the linac configuration. The factors which need consideration include maintaining achromaticity (dispersion and its derivative is equal to zero) and isochronicity (there is no path length dependence on energy, a condition R_{56}=0), perturbations to the beam phase space due to higher order terms, CSR, ISR, microbunching. The separation between multiple beam lines to accommodate the magnets and diagnostics also needs consideration. The issues to consider in the choice of design configuration are summarised in Table 3.1. It should be noted that at higher electron beam energies (typically above a few GeV and higher bunch charge), the complexity of passing the beams through spreaders, combiners and arcs and the dilution of emittance due to synchrotron radiation adds more restrictions on re-circulation and ERL options but these options are worth considering at a design stage to see whether they are viable for the required beam parameter regime. For example, a re-circulating linac option was studied in detail for the UK New Light Source and was shown to deliver similar performance to a single pass design [60]. The cost comparison in this case demonstrated that the construction cost would be lower by $\sim$ 30% [61] and operating costs would also be significantly reduced.

3.3 Subsystems of Single Pass Linac

For the purpose of the work related to the spreader design in this thesis (for FELs covering photon wavelengths in the hard X-ray regime) a generic single pass linac layout is used as a basis to describe the various subsystems. The layout is shown in Fig. 3.3. The design incorporates an injector (consisting of an electron source and acceleration to energies of typically a few hundred MeV), several accelerating modules to reach higher energies, a few stages of bunch compressors, a higher harmonic cavity for linearisation of the longitudinal phase space, a laser heater to control the amount of energy spread (which can help to suppress some beam instabilities), collimation in the injector as well as in a dedicated section at full energy, several diagnostics sections, a spreader/switchyard to direct electron bunches to different FEL lines, FEL undulators, photon transport to experimental stations and beam dumps for electrons. Each system is briefly discussed below.

3.3.1 Injector

The type of injector used for most fourth generation light sources is the RF photoinjector [1] (also known as an RF gun) based on RF technology and laser driven photocathode. The RF gun [63] provides a low emittance beam at high charge, typically less than a nC. In this gun, electrons are produced in a strong accelerating field from a photocathode driven by a suitable laser system. A critical issue for the generation of ultralow emittance beams is the minimisation of the beam degradation due to space charge forces. This is achieved by increasing the accelerating field strength and optimising the laser pulse length, profile and transverse size on the photocathode [64]. The initial normalised thermal emittance

---

[1] although a thermionic gun is used at SACLA [62]

Table 3.1: Design issues to consider in single pass and re-circulation/energy recovery linacs.

Machine Area	Single Pass Linac	Re-circulation Linac/ERL
Injector merger	Not required unless two injectors are considered.	Merger required. Need to consider ratio of injection and final energies. Additional beam transport - injection line including injection merger is required.
Phase space lineariser	Higher harmonic cavity required.	Possible to use sextupoles in the arcs in some cases, though the scheme may be restricted.
Bunch compressor	Dedicated chicanes for magnetic compression.	Possible to compress in arcs. Bunch compressor chicanes cannot be located in the region where multiple beams traverse together.
Linac	Additional focusing may be required.	Requirement of focusing to deal with different energy beams.
Additional beam transport	Not required	Additional/complex beam transport required for matching into/from the arcs, path length corrector.
Beam dump	More than one for beam energy diagnostics and if there are multiple FEL lines	More than one if multiple FEL lines in re-circulation option. Multiple beam dump option in ERL configuration may be difficult with energy recovery.
Beam dynamics issues	Space charge, CSR, ISR, wakefields, microbunching	Space charge, CSR, ISR, wakefields, microbunching, ion trapping, BBU thresholds.
Beam switchyard/ spreader	Achromaticity, isochronicity, higher order beam transport terms, CSR, ISR, microbunching, layout, timing, beam line separation, future upgrades, possibility to extract at different energies.	Achromaticity, isochronicity, higher order transport, CSR, ISR, microbunching, layout, timing, separation and beam lines, future upgrades. Possibility to extract at different energies slightly restricted. Need to combine spent beam from multiple beam lines for energy recovery in ERL.

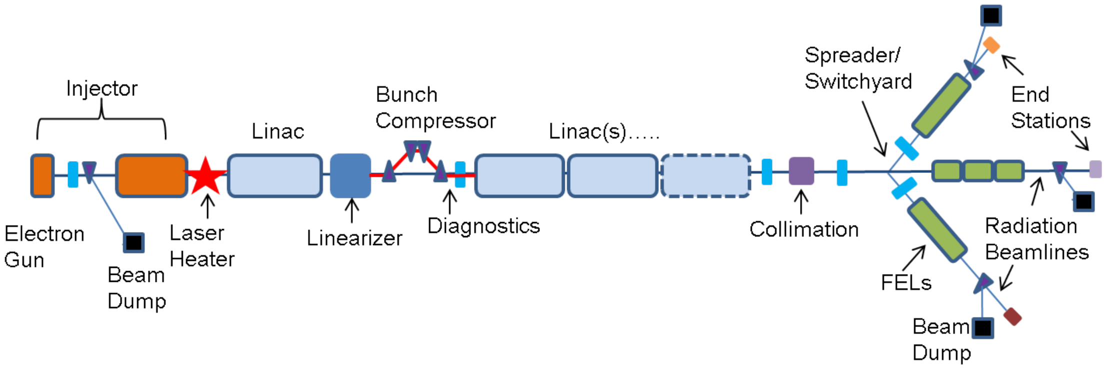

Figure 3.3: Schematic layout of generic FEL facility based on a single pass linac configuration.

(the emittance of the electrons as they are extracted from the cathode surface) for photoemission from a metal photocathode is given [65] as:

$$\gamma\epsilon_{th} = \sigma_{laser}\sqrt{(\hbar\omega - \phi_{eff})/3m_0c^2}, \tag{3.9}$$

where σ_{laser} is the transverse rms laser beam size on the cathode, $\hbar\omega$ is the laser photon energy, ϕ_{eff} is the effective work function of the metal and m_0c^2 is the rest mass energy of electrons. The initial thermal emittance can be minimised by proper choice of the photocathode material and the transverse size of the laser beam on the cathode. The longitudinal profile of the electron pulse is equal to the profile of the laser pulse. However, due to space-charge effects (the Coulomb interaction between the electrons), a high density electron bunch soon increases in both length and transverse dimensions, leading to an increase in emittance and a decrease in peak current (see section 3.1.1). It is therefore essential to accelerate the short electron bunches as fast as possible.

A typical RF gun consists of half an RF cell followed by one or more full cells. Most commonly used RF guns operate at S-band (3 GHz) or L-band (1.3 GHz) frequencies (see Appendix B for exact RF frequencies). The photocathode (metal or semiconductor) is placed at the center of the back plane of the gun cavity and a drive laser with suitable power synchronised with the RF field is used to extract the required charge from the photocathode. Photocathodes and laser systems are chosen to meet the specific requirements of the FEL. Single shot FELs with low repetition rate (single shot in the range of 100's Hz) use copper photocathodes which have low quantum efficiency and thus require a high power laser in the ultra violet (e.g. LCLS [66] FERMI [67], CLARA [38]). These photocathodes have long lifetimes and require relatively low maintenance. For a high repetition or burst mode FELs (kHz to MHz), where the number of bunches in a single machine pulse is three orders of magnitude higher than in single shot FELs, high quantum efficiency cathodes and lasers in the visible range are used (e.g. FLASH [68], X-FEL [69]).

As an example, Fig. 3.4 shows the electron gun on the Versatile Electron Linear

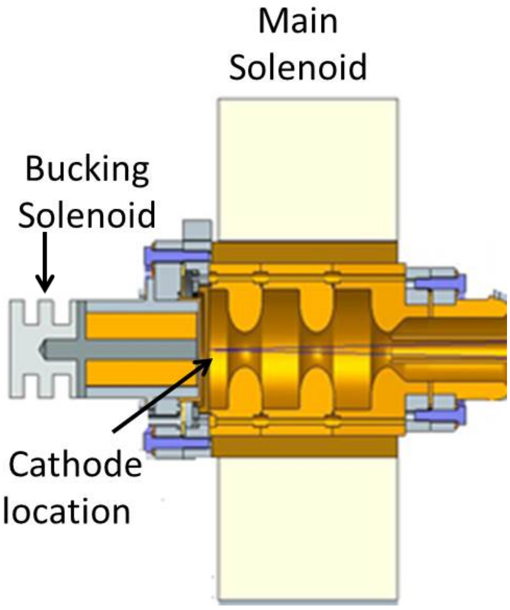

Figure 3.4: Schematic of 2.5 cell S-band VELA RF photoinjector operating at Daresbury Laboratory.

Accelerator (VELA) photoinjector accelerator operating at Daresbury Laboratory [70]. The electron gun for VELA is a 2.5 cell S-band normal conducting RF gun with coaxial coupler originally designed for the ALPHA-X project [71]. A main solenoid surrounds the gun cavity with a bucking coil close to the cathode to cancel the magnetic field on the cathode plane. The design gradient is 100 MV/m, which equates to a maximum beam momentum at the exit of the gun of 6.5 MeV/c. The gun is driven by a frequency-tripled Ti:Sapphire laser system with a pulse energy of 1 mJ at 266 nm. For electron beam dynamics simulations, a laser spot diameter of 1 mm and a measured Gaussian longitudinal laser profile of 76 fs rms have been used. This short pulse length allows the gun to operate in the so-called “blow-out" regime, where the bunch length expands due to space-charge [72]. A 250 pC bunch expands to 1.3 ps rms bunch length during acceleration in the gun and then further expands after the gun as there are no further accelerating sections.

In addition to the beam dynamics issues involved in delivering the required bunch parameters for FEL operation, there are additional challenging technical issues to be addressed if the gun is operated at high repetition rate (higher than few 10’s of Hz). In this case, the gun cavity temperature needs to be maintained within a fraction of a degree to maintain the resonant frequency and a high quality factor in the presence of high RF power. This requires an effective temperature stabilisation system. Other important factors which need to be considered [73] are the choice of photocathode material, surface quality (smoothness and purity) of the photocathode, temporal and transverse profile and power of the drive laser pulse, peak and average RF power, synchronisation of laser and

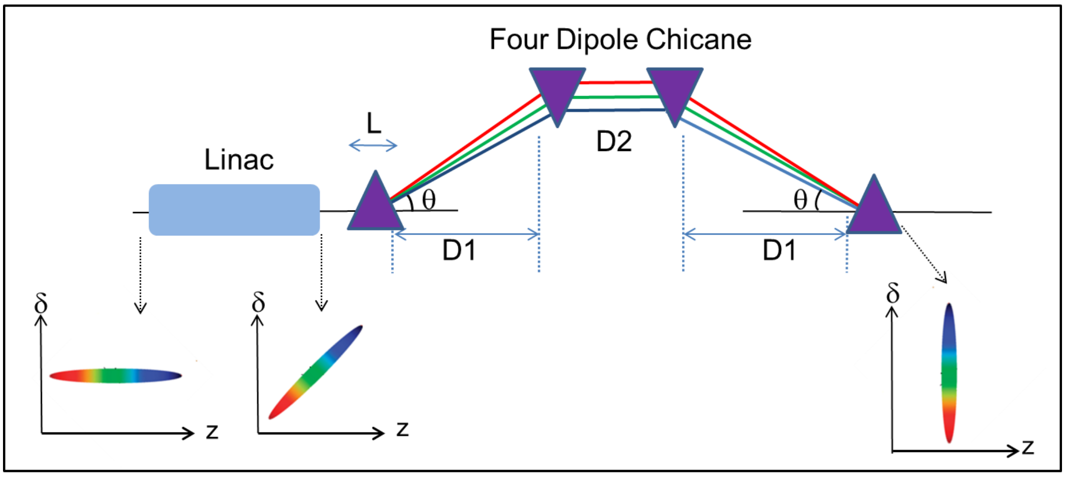

Figure 3.5: Principle of bunch compression. High energy electrons shown in blue and low energy electrons are shown in red.

RF pulses, and the vacuum in the gun.

3.3.2 Bunch Compressor

In order to achieve the high peak bunch currents required for an FEL, the bunch length produced from the injector is reduced by some factor using a “bunch compressor". The principle of bunch compression is based on the processes shown in Fig. 3.5. Firstly, a time-energy correlation or “chirp" is imprinted onto the bunch by passing it through a linac which is operated off crest so that the front (head) of the bunch sees a different gradient than the back (tail) of the bunch. Secondly, this chirped bunch is passed through a non-isochronous beam transport section making use of different path lengths for different energy electrons. The high energy electrons in the tail of the bunch travel on a shorter path and low energy electrons at the head of the bunch travel on a longer path. As a result, the bunch length at the exit of the chicane is shorter compared to the bunch length at the entrance. The net effect of this process is a rotation in longitudinal phase space which increases the energy spread by the same factor by which the bunch length is reduced, so the longitudinal emittance is conserved.

To describe these processes in more detail, the transformations of the longitudinal phase space variables in each step need to be considered. The first step is to pass an electron bunch in an RF cavity at an off-crest phase. This does not change the longitudinal position of an electron with respect to the bunch center, but it changes the energy deviation by an amount depending upon its position in the bunch. The energy of a given electron in a bunch changes from initial E_i to final E_f. At the same time, the initial and final energies of the reference electron change from E_0 and E_1 due to acceleration as follows:

$$
\begin{aligned}
E_i &= E_0(1+\delta_0), \\
E_f &= E_1(1+\delta_1) = E_i + eV_{\mathrm{rf}}\cos(k_{\mathrm{rf}}z_0 + \phi_{\mathrm{rf}}), \\
E_1 &= E_0 + eV_{\mathrm{rf}}\cos(\phi_{\mathrm{rf}}),
\end{aligned} \tag{3.10}
$$

where $k_{rf} = 2\pi f_{\mathrm{rf}}/c$ is the wave number. From these equations, an expression for the energy deviation δ_1 can be writen as:

$$
\delta_1 = \frac{E_0(1+\delta_0) + eV_{rf}\cos(k_{rf}z_0 + \phi_{rf})}{E_0 + eV_{rf}\cos(\phi_{rf})} - 1. \tag{3.11}
$$

To first order in $eV_{rf}/E_0 \ll 1$, the position and energy deviation after the linac are:

$$
\begin{aligned}
z_1 &= z_0, \\
\delta_1 &= \left(1 - \frac{eV_{rf}}{E_0}\cos(\phi_{rf})\right)\delta_0 + \frac{eV_{rf}}{E_0}[\cos(\phi_{rf} - k_{rf}z_0) - \cos(\phi_{rf})].
\end{aligned} \tag{3.12}
$$

In a linear approximation for the RF, the above equations can be expressed in terms of a matrix:

$$
\begin{pmatrix} z_1 \\ \delta_1 \end{pmatrix} \approx \begin{pmatrix} 1 & 0 \\ R_{65} & R_{66} \end{pmatrix} \begin{pmatrix} z_0 \\ \delta_0 \end{pmatrix}, \tag{3.13}
$$

where:

$$
\begin{aligned}
R_{65} &= -\frac{eV_{\mathrm{rf}}k_{\mathrm{rf}}}{E_0}\sin(\phi_{\mathrm{rf}}), \\
R_{66} &= 1 - \frac{eV_{\mathrm{rf}}}{E_0}\cos(\phi_{\mathrm{rf}}).
\end{aligned} \tag{3.14}
$$

The non-linear chirp arising due to the RF waveform seen by the bunch can be written as:

$$
\delta(z) = \delta_0 + h_1 z + h_2 z^2 + h_3 z^3 \ldots \tag{3.15}
$$

where h_1 denotes the first order chirp which is equal to (R_{65}) as shown above, h_2 the second order chirp and h_3 the third order chirp.

The second stage is to pass this chirped bunch through a non-isochronous section of beam line (such as a four dipole chicane) thus creating a path length difference for the head and tail of the bunch. The path length deviation is described by the matrix terms R_{56} and higher order matrix terms T_{566} etc. These terms depend upon the dispersion and the parameters of the chicane dipoles (length, bending angle and radius) and the distance D_1 between the first and second (and between the third and fourth) dipoles. The distance D_2 between second and third dipoles does not affect R_{56} and is chosen on the requirements of other considerations such as diagnostics, energy collimation etc. After passing through this dispersive section, the longitudinal co-ordinate (relative to the bunch centre) and the energy deviation of an electron can be written as:

$$
\begin{aligned}
z_2 &= z_1 + R_{56}\delta_1 + T_{566}\delta_1^2 + U_{5666}\delta_1^3 + \ldots, \\
\delta_2 &= \delta_1.
\end{aligned} \tag{3.16}
$$

In a linear approximation, this can be written in the matrix form as:

$$\begin{pmatrix} z_2 \\ \delta_2 \end{pmatrix} = \begin{pmatrix} 1 & R_{56} \\ 0 & 1 \end{pmatrix} \begin{pmatrix} z_1 \\ \delta_1 \end{pmatrix}. \tag{3.17}$$

The total transformation is product of two matrices given by eqns. (3.13) and (3.17):

$$\begin{pmatrix} z_2 \\ \delta_2 \end{pmatrix} = \begin{pmatrix} 1 + R_{65}R_{56} & R_{56}R_{66} \\ R_{65} & R_{66} \end{pmatrix} \begin{pmatrix} z_0 \\ \delta_0 \end{pmatrix}. \tag{3.18}$$

Assuming an upright ellipse in the longitudinal phase space (i.e. no final energy chirp, so that $\langle z_2\delta_2\rangle$=0), the rms bunch length at the end of the chicane is given by:

$$\sigma_{z,f} = \sqrt{(1 + R_{56}R_{65})^2\sigma_{z,i}^2 + R_{56}^2 R_{66}^2 \sigma_{\delta,i}^2}. \tag{3.19}$$

Thus the final bunch length depends upon the RF chirp, initial energy spread and matrix terms R_{56} and R_{66}.

In order to deliver the high peak bunch current required to drive an FEL and to avoid potential degradation of the beam due to CSR, the bunch compression is usually done in multiple stages along the beam transport at different energies of the beam. The linacs between these stages accelerate the electron beam to higher energy and thus prepare it for the next stages of compression. In such a way, the compression factor (ratio of bunch lengths after the compression to the bunch length before the compression) from each individual bunch compressor can be reduced so mitigating effects from nonlinearities and CSR, and resulting in an overall lowering of emittance growth. In addition, the phase and strengths between different stages can be tuned for optimal performance. The number, locations and strengths of the bunch compressors are optimised to achieve the required longitudinal bunch parameters at the entrance of the FEL. The transverse optics of the bunch compressor are optimised using quadrupoles placed before the chicane so as to minimise the horizontal beta function and H-function at the fourth dipole of each bunch compressor. This mitigates the effects of coherent synchrotron radiation emission in particular the increases in energy spread and transverse emittance, as explained in Chapter 4.

3.3.3 Lineariser

In a facility where bunch compression is carried out in several stages, generally the first stage of the bunch compressor is located after the injector where the bunch length is typically long. When this long bunch passes off-crest in the linac before compression, it experiences the curvature of the RF waveform. As a result the longitudinal phase space of the compressed bunch is non-linear as shown in Fig. 3.6. This can generate local current density spikes which consequently cause detrimental effects due to CSR. The chirp given in eqn.(3.15) contains linear and higher-order terms. The RF curvature can be cancelled

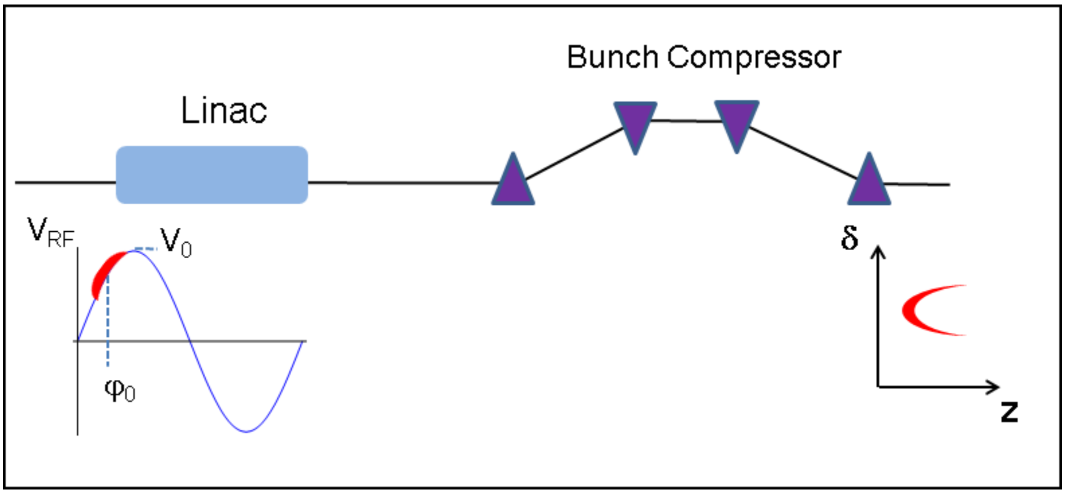

Figure 3.6: Effect of RF curvature on longitudinal phase space after bunch compressor.

by using a higher harmonic cavity close to 180° in phase. In presence of this cavity, the total voltage seen by the beam before entering the bunch compressor is given by:

$$V(z_0) = V_s \cos(k_s z_0 + \phi_s) + V_x \cos(k_x z_0 + \phi_x), \tag{3.20}$$

where s, x denote linac and harmonic cavity respectively. $k_{s,x} = 2\pi/\lambda_{s,x}$ are the RF wave numbers, with relationship equal to $k_x = hk_s$. z_0 is the longitudinal position of the electron with respect to the reference electron. The second derivative of eqn.(3.20) at $z_0 = 0$, is:

$$V''(z_0 = 0) = -k_s^2 V_s \cos(\phi_s) - k_x^2 V_h \cos(\phi_h). \tag{3.21}$$

In order to cancel the second order chirp from the RF, the expression for V" in eqn.(3.21) needs to be equated to zero and $\phi_h = 180°$. This gives the required voltage on the harmonic cavity:

$$V_h = V_s \cos(\phi_s)/h^2. \tag{3.22}$$

Operating the harmonic cavity at 180°, causes a slight reduction in the electron energy, which can be compensated by upstream linacs. The principle of linearisation using a higher harmonic cavity is shown in Fig. 3.7.

The above approach is simplistic without considering the non-linear terms arising from the bunch compression chicane. A detailed consideration of the non-linear effects are considered in [74] which gives the required higher harmonic voltage to compensate the compression transformation up to second order, thereby maintaining the initial temporal bunch profile and avoiding unnecessary amplification of undesired collective effects.

It is also possible to compensate the phase space curvature using sextupoles in a bunch compressor, but this creates problems with higher order dispersion and complicates other aspects of the beam dynamics. In dipole-based chicanes, higher order dispersion is cancelled without the need for sextupole, by ensuring appropriate symmetry in the design.

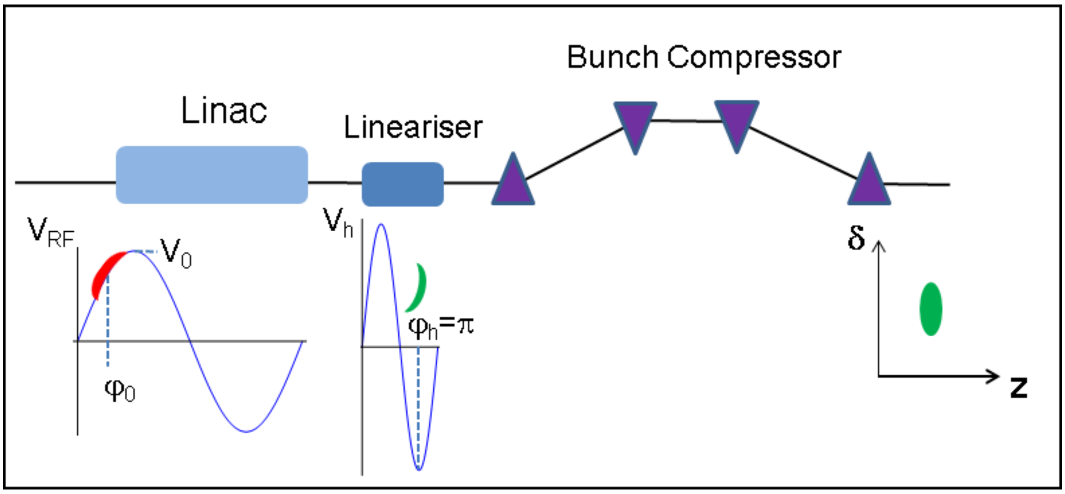

Figure 3.7: Principle of higher harmonic RF correction to remove effect of RF curvature on longitudinal phase space.

In the later stages of bunch compression, as the bunch length is already relatively short compared with the main RF wavelength, the nonlinear curvature from the sinusoidal RF wave has a much smaller impact and hence no harmonic RF linearisation is generally required.

3.3.4 Example of Bunch Compression, Linearisation, CSR and Wakefields

In order to illustrate bunch compression, the effect of a lineariser and how wakefields and CSR may affect the transverse and longitudinal parameters of the bunch, the results of the simulations for a beam line shown in Fig. 3.8 are described. The beam line consists of a 4 m long S-band linac, 1 m long fourth harmonic lineariser and a bunch compressor chicane giving R_{56}= -6.26 cm. A Gaussian bunch of 100 MeV beam energy, 1 nC bunch charge with normalised beam emittances of 1 mm.mrad in both transverse planes and uncorrelated energy spread of 0.001, rms bunch length of 650 μm (2.16 psec) is tracked through this beam line using code elegant [75]. The simulations are done with and without CSR and wakefields in the linac. The linac is operated off-crest by -17° to provide a correlated energy spread. Fig. 3.9 shows the longitudinal phase space and the corresponding peak current at the entrance of the linac, at the exit of the linac and at the exit of the bunch compressor chicane. In this case, CSR and wakefields are not included and there is no lineariser (i.e. no higher harmonic RF). The effects of non-linearities can be seen in the longitudinal phase space at the exit of the chicane.

A fourth harmonic of the S-band RF (X-band) is used in this example to linearise the longitudinal phase space. The optimised voltage and phases are 4.0 MV/m and +165° with respect to the crest. Fig. 3.10 shows the longitudinal phase space, slice current, slice energy spread and slice transverse emittance in the horizontal plane (the vertical emittance is not of significance in this case as the bunch compressor bends the beam in the horizontal

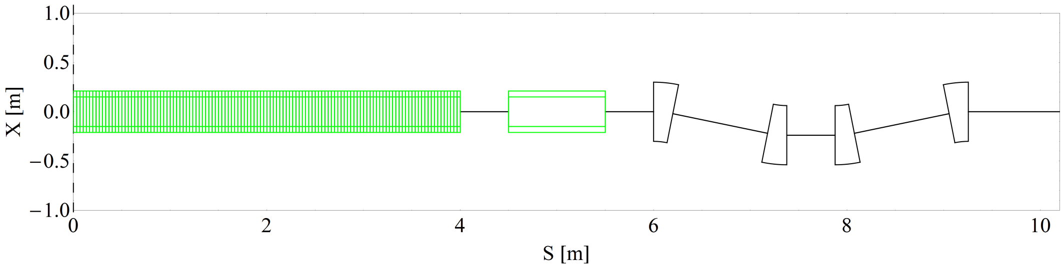

Figure 3.8: Bunch compressor beam line used for tracking through (Left to right) off-crest linac, a lineariser and a magnetic chicane.

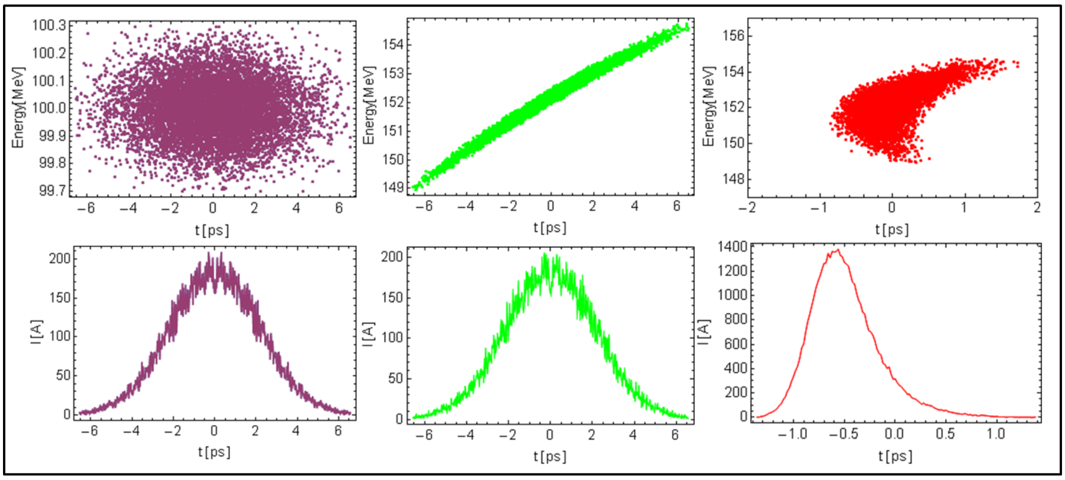

Figure 3.9: Left to right: Longitudinal phase space (top row) and slice current (bottom row) at linac entry, linac exit, bunch compressor exit. Wakefields and CSR not included; no lineariser.

plane). Four different cases are shown: lineariser off, lineariser optimised to cancel the curvature, including linac wakefields and optimisation of lineariser in the presence of the wakefields. Fig. 3.11 shows the same quantities but now with CSR turned on, resulting in a marginal reduction in slice current and increase in horizontal slice emittance. This illustrates that optimisation of the system should include all the possible wakefields and collective effects, otherwise the final beam parameters could be far from the required values.

3.3.5 Laser Heater

A collective instability known as microbunching is known to occur in linacs driving an FEL. A high-brightness electron beam with a small amount of longitudinal density modulation can create self-fields that lead to beam energy modulation. When this energy modulated bunch passes through a dispersive region such as bunch compressor, which introduces a path length dependence on energy, the induced energy modulation is then converted to additional density modulation that can be much larger than the initial density modulation. This amplification process characterised by the increase in density modulation can be

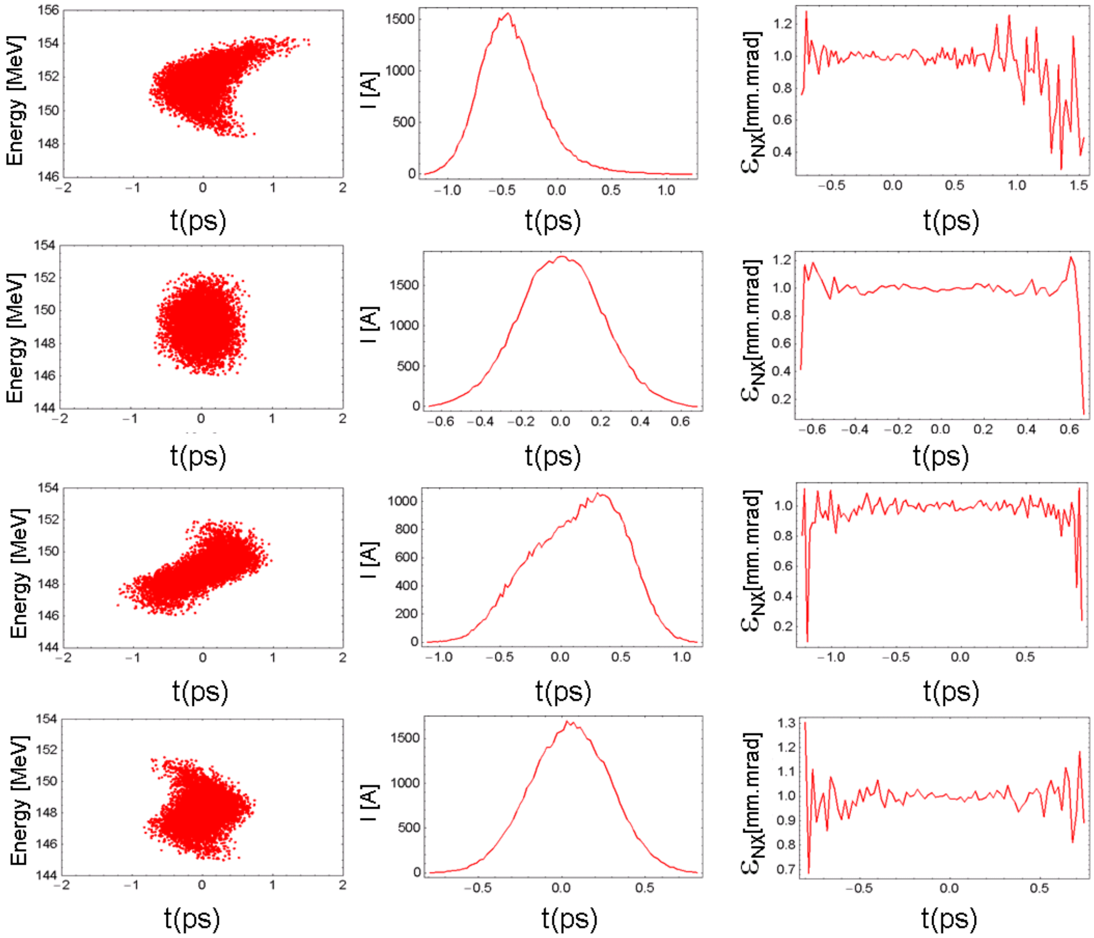

Figure 3.10: Left to right: Longitudinal phase space, slice current, slice horizontal emittance. Top to bottom: Lineariser off, wakefields off. Lineariser on, wakefields off. Lineariser on, wakefields on. Lineariser optimised with wakefields on. CSR off in all cases.

accompanied by a growth of emittance if significant energy modulation is induced in a dispersive region. This instability can be harmful to short-wavelength FEL performance by degrading the beam quality.

The microbunching instability is presumed to start at the photoinjector exit growing from a density and/or energy modulation caused by shot noise and/or unwanted modulations in the photoinjector laser temporal profile. As the electron beam travels along the linac to reach the bunch compressor, the density modulation leads to an energy modulation via longitudinal space charge. The resultant energy modulations are then transformed into higher density modulations by the bunch compressor. This increased density modulation leads to further energy modulations in the rest of the linac. Coherent synchrotron radiation in the bunch compressor can also contribute to enhance the energy and density modulations and can even increase the beam emittance directly. The microbunching instability can severely deteriorate the quality of the electron beam affecting the FEL. When more than one bunch compressor is present, the overall gain in energy and density

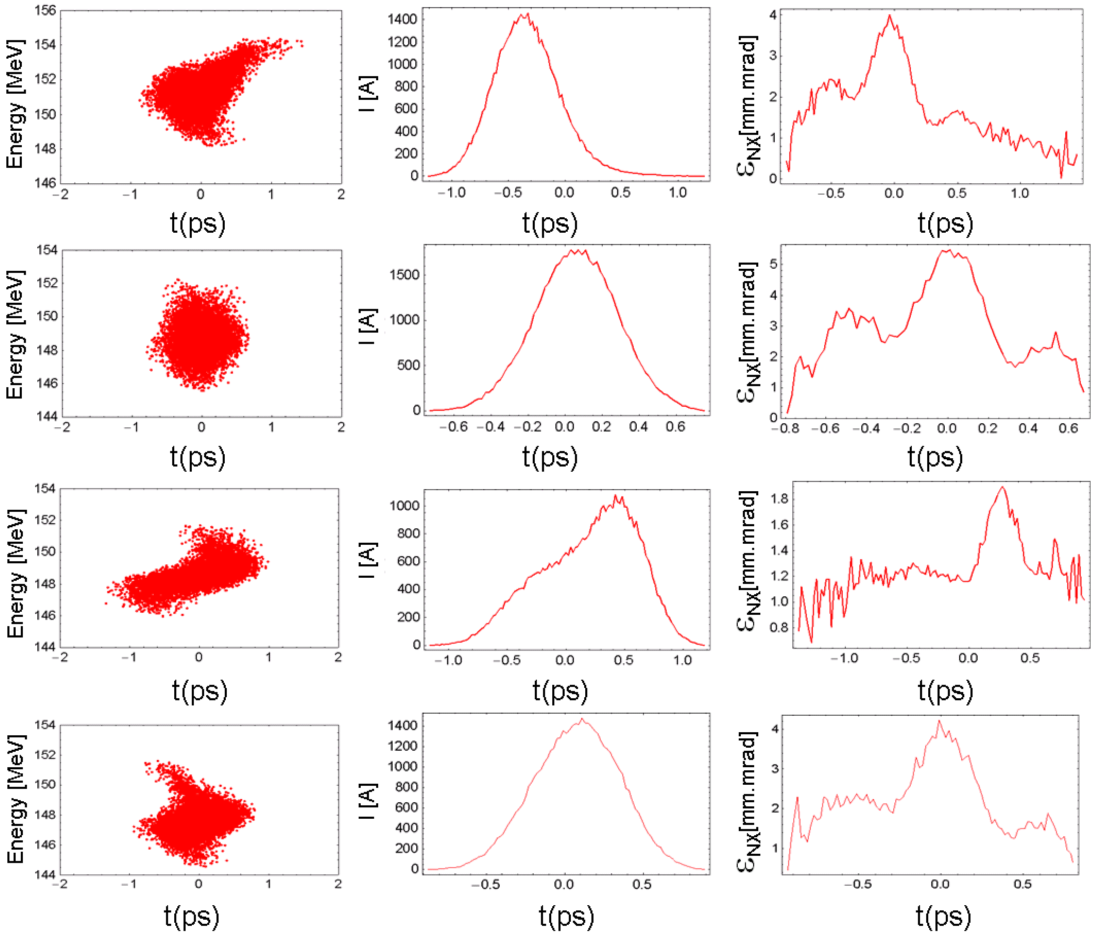

Figure 3.11: Left to right : Longitudinal phase space, slice current, slice horizontal emittance. Top to bottom: Lineariser off, wakefields off. Lineariser on, wakefields off. Lineariser on, wakefields on. Lineariser optimised with wakefields on. CSR on in all cases. Note the change in scale for slice emittance.

modulation is the product of individual compressor gains, including longitudinal space charge, CSR and linac wakefield effects [76].

A laser heater [76] provides an effective way to control the uncorrelated energy spread with the ability to increase it beyond the very low energy spread coming from the photoinjector. This provides a way to suppress the microbunching instability. A laser heater system as shown in Fig. 3.12 makes use of resonant laser-electron interaction in a short undulator magnet to induce energy modulation at the optical frequency [76]. The resulting interaction within the undulator produces a modulation of the mean electron beam energy on the scale of the optical wavelength. The transverse dynamics in the last half of the chicane time-smears the energy modulation leaving only an effective energy spread increase. The energy spread causes non-reversible mixing in the longitudinal phase space (Landau damping), which suppresses the gain of the micro-bunching instability. It is most effective if the laser heater is located before the first bunch compressor.

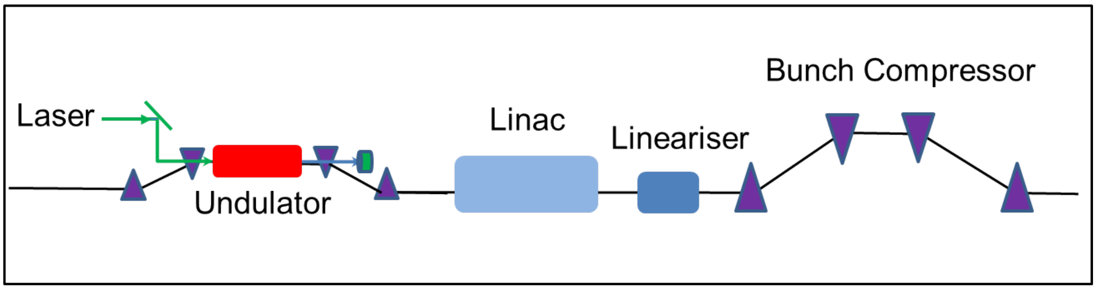

Figure 3.12: Schematic of laser heater and its location in the beam line for a X-ray FEL.

Measurements at the LCLS demonstrate the ability of a laser heater to suppress the microbunching instability, mitigating its impact on the X-ray FEL performance [77].

3.3.6 Linac

The linear accelerator consists of a series of resonant structures which provide an electric field along the direction of motion of the electrons to accelerate them. Electromagnetic plane waves in free space have electric fields that are transverse to the direction of the wave. In order to accelerate electrons co-propagating with the electromagnetic wave, a resonant cavity is used which has transverse magnetic modes; such modes have axial electric fields that can be used for acceleration. The cavity structure is also arranged in such a way that it slows down the phase velocity of the electromagnetic wave to below the speed of light. This allows the acceleration of electrons travelling at a speed less than the speed of light.

The capital and operating cost of an FEL facility is largely determined by the chosen technology and options for RF acceleration and power. The two major technical approaches for RF acceleration are normal conducting accelerators and superconducting accelerators. Each of these have different capabilities and technical issues. Reliable power sources to power the linac exist at many frequencies, including the L, S, C and X bands [78]. It is possible to reach accelerating field, upto 25 MV/m at S-band, up to 35 MV/m at C-band and 100 MV/m at X-band [79]. The repetition rate of facility based on normal conducting RF are however limited to less than 1 kHz. They also have greater potential for wakefield effects due to smaller beam apertures. The superconducting technology offers accelerating gradients upto 35 MV/m [80] and can be optimised to operate at higher repetition rates (upto 1 MHz CW) albeit at lower gradients, for example, maximum design gradient in X-FEL is 23.6 MV/m operating in long pulse mode (650 μsec at 10 Hz repetition rate). Achieving higher accelerating gradients in the linac allows for reducing the length, and is thus attractive for a FEL facility, even though raising the accelerating field requires an increase of the installed RF power (in proportion to the square root of the gradient). The choice for technology of the injector and the linac depend on the requirements for the FEL pulses (repetition rate and separation between macropulses).

The high-gain FEL facilities in operation or planned use normal conducting 3 GHz S-band (LCLS-I [66], FERMI@ELETTRA [48]), 5.7 GHz C-band (SACLA [62], SwissFEL [81]) and superconducting 1.3 GHz L-band (FLASH [22], European X-FEL [82]) RF systems. There are a number of studies in progress to investigate whether X-band (12 GHz) will provide suitable beam for FEL facilities [78, 83, 84]. The challenges in X-band are the strong wakefields, lack of availability of higher harmonic cavities for the lineariser and expensive RF power sources. Other important factors to consider are the non-linearity in phase space, the tolerances on phase jitter and impact of misalignment at different RF frequencies. A detailed comparison of S, C and X-band X-FEL design [78] demonstrates that even though it is possible to increase the accelerating gradient from S to X band, the higher frequency structures will be less tolerant to jitter, and mis-alignments. As there are four times difference in RF frequency and RF wavelength between S-band RF and X-band RF, a same timing jitter measured in absolute time in S-band RF would have a much larger impact on X-band RF based FEL.

3.3.7 Collimation

A collimation system is required in an FEL driver to limit the beam halo. The beam halo is mainly generated due to dark current from the injector (caused by field emission in the gun cavity in the presence of high electromagnetic fields) but can also result from scattering with residual gas particles and off-energy beam tails caused by CSR. If these halo electrons are not collimated before they enter the FEL sections (consisting typically of permanent magnet undulators), they can de-magnetise the undulator magnets over a period of time, cause Bremsstrahlung co-axial with the photon beam lines and activate the beam line components. Dark current also adds complexity in characterising the electron beam and can pose significant challenges for low charge operation modes of the facility. Collimating the halo electrons as near as possible to the various sources (before the halo can be accelerated with the beam) is normally preferable as this reduces the overall radiation level in the facility. The amount of damage to undulators and the level of radiation in the facility depends on the average beam power and energy. It is estimated [85] that halo from beams with kW beam power may cause serious damage to undulators within hours or even minutes, if not collimated. In addition to removing the beam halo continuously, the collimation system must also provide protection against mis-steered beam or element failure scenarios in high power/high energy facilities.

It is important to collimate beam halo in both transverse and longitudinal planes. A dedicated lattice design needs to be included in the FEL driver for transverse collimation with correct phase advances between different collimators to ensure that the entire phase space is covered [86, 87]. Collimation in the longitudinal plane can be achieved by having collimators in a region with non-zero dispersion. The necessary collimator gaps are determined by tracking a beam halo down the lattice ensuring that no beam halo particles reach the undulators at the start of the FEL sections. The undulator gaps and optics then define the apertures required in the collimators. Since the FEL design often strives to achieve small (5 - 7 mm) undulator gaps, smaller gaps are required in the collimators compared to the available transverse aperture in the rest of the machine (typically in the range of 20 - 40 mm diameter). Thus, the wakefields of the collimators need to be included in the tracking simulations to make sure that the bunch properties do not deteriorate significantly. However, reliable theoretical estimates and simulations of collimator wake fields are difficult to establish for short bunches. If collimator wakefield effects become a severe concern it is possible to redesign the system to mitigate these effects. For example, energy (longitudinal) collimation could be relocated to the spreader where there are higher levels of dispersion and the betatron (transverse) collimation section could be lengthened to give larger beta functions at the collimators. It is possible to reduce the wakefields by designing collimators with smooth transitions, but this has implications for space and facility length.

3.3.8 Beam Spreader/Switchyard

The beam spreader allows the electron beam to be sent through different FEL lines which may have different configurations (as well as beam parameters). The design of the spreader should be transparent to the beam, i.e. should not deteriorate the quality of the beam designed to meet the FEL requirements. However, because the very concept of spreading or switching is based on bending the beam to direct the beam to different beam lines, spreaders can degrade the beam quality due to CSR, ISR and chromatic effects. In order to maintain the required properties, the design of the spreader generally needs to be achromatic and preferably isochronous and should include strategies to minimise the emittance growth caused by CSR.

In single shot, low repetition rate facilities, one can share the beam using beam lines based on DC dipoles (that need to be turned on/off depending on the path selected for the electron beam) and a combination of focusing and defocusing quadrupoles with a proper phase advance or a design based on isochronous arcs. For facilities with high repetition rates, it is possible to divide the beams by using a fast pulsed dipole magnet (known as a kicker) deflecting the beam in a specially designed beam line, or by using an RF deflector where a subharmonic of the main RF cavities can provide the same effect of deflecting the beam. The spreader design should include a flexibility to add more beam lines at a later stage if required. The choice of the spreader design is critical in the facility construction and can have significant implications for the cost and for the overall facility footprint.

As an example, the beam spreader design for NLS, shown in Fig. 3.13, consists of a long FODO “take-off" section with a series of extraction points for various FEL lines. Bunches which are not diverted to a particular FEL line continue to pass on-axis through the FODO beam line. Each extraction section consists of two Triple Bend Achromat

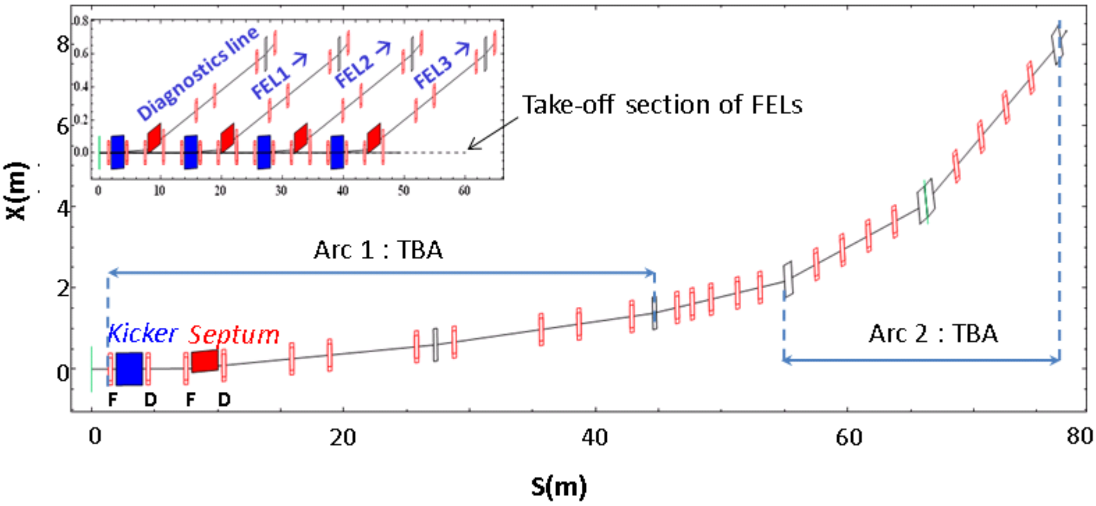

Figure 3.13: Schematic of NLS spreader showing one beam line. Quadrupoles are shown in red and dipoles are shown in black.

(TBA) arcs, where the kicker and the septum replace the first dipole of the first TBA arc. This spreader design will be discussed in detail in Chapter 5. The design allows a different configuration of FEL in each branch and can be easily upgraded to include more FEL lines.

3.3.9 FELs

As discussed in Chapter 1, a FEL design requires a perfect overlap of the electron beam with the radiation. The challenges for maintaining the quality of the electron beam in the FEL sections are described in this section. The specific challenges involved in the FEL designs which depend upon the schemes chosen for the FEL layouts (SASE, seeding schemes) are not discussed.

A SASE high gain amplifier FEL consists of several undulator sections to reach the saturation. These sections can be hundreds of meters long and thus require some periodic focusing for the electron beam to maintain optimum overlap with the radiation beam. This is typically done by having a FODO configuration in between the undulator modules. The second important requirement comes from the tolerances of FEL designs to beam trajectory through the undulators. This needs ensuring that the electron beam deviation from the reference trajectory is as small as possible (typically few microns). Both these requirements need high resolution beam diagnostics in these sections such as cavity beam position monitors.

In a seeded FEL, there is a need to bring in a seed into the FEL section and this may need a suitable arrangement in the layout. Depending upon the scheme of modulation, the FEL section incorporates modulators (undulators tuned at a certain wavelength), chicanes and radiators (undulators tuned at another wavelength). The requirements of optimum electron beam overlap and the trajectory correction are important similar to the SASE schemes.

For compact hard X-ray FELs, permanent magnet in-vacuum undulators with variable gap are currently the technology of choice because they give the best combined performance in terms of short period, field strength, gap width, field quality and flexibility. The gaps in these undulators are smaller (typically $6-8\,\mathrm{mm}$) to reach higher wavelengths for a given electron beam energy and thus pose several challenges in terms of incorporating the focusing quadrupoles, diagnostics and vacuum devices whilst keeping the optimised short distances between the undulator modules. The small aperture requirements need a careful consideration for machine protection. It is essential to keep the beam losses in the FEL sections to avoid loss of magnetisation in the permanent magnets as described in the collimation section.

At the end of undulator sections, it is necessary to transport the electron beam to the beam dump. The FEL radiation is transported to the experimental stations. The experience at LCLS [88] shows that it is useful to characterise the electron beam after the FEL as it provides a key information on electron beam properties to optimise the lasing process.

3.3.10 Diagnostics

FEL operation depends upon an electron beam with low emittance, low energy spread and high peak current. Dedicated diagnostics sections are essential to make sure that the photoinjector and other sections of the facility are optimised to achieve and deliver close to design beam parameters, during the initial commissioning as well as normal running of the facility. In order to fully characterise the 6D phase space for both projected and slice parameters, the facility should include numerous dedicated diagnostics devices as listed in Table 3.2, at key locations throughout the facility. Dedicated diagnostics sections are needed for measuring slice and projected 6D beam parameters. Use of diagnostics devices throughout the facility ensures that the design trajectory is followed, and that the beam is transported without losses and with the required properties to the FEL entrance.

3.3.11 Beam Dump

At the end of the FEL driver it is necessary to provide a beam dump for safe disposal of the electron beam. The design of the beam dump is determined by the average beam power at the dumps and thus depends on the beam energy, bunch charge and the time structure. The beam power could vary between several watts to hundreds of kilowatts. The power density can be a more difficult issue than the total power. The thermal considerations are important for high power beam dumps as extracting the heat from the power deposited by the beam is a major constraint in the beam dump design. The choice of material and the stress due to steady state heating and the transients need to be carefully evaluated

Table 3.2: Measured properties of electron bunches and the associated diagnostics devices.

Property	Diagnostics devices
Bunch charge	Wall current monitor, Faraday cup, integrated current transformer.
Dark current	Wall current monitor, Faraday cup.
Bunch position	Beam position monitor, optical screen monitor, synchrotron radiation monitor.
Projected transverse emittance	Optical screen monitor, pepperpot, wire scanner, slits.
Courant-Snyder(Twiss) parameters	Optical screen monitor, wire scanners.
Bunch length	Electro-optical sampling, transverse deflecting cavity.
Bunch slice properties	Transverse deflecting cavity + optical screen monitor.
Electron energy	Spectrometer dipole + beam position monitor/optical screen monitor.
Bunch energy spread	Spectrometer dipole + optical screen monitor.
Bunch arrival time	Beam arrival monitor.
Bunch transmission efficiency	Wall current monitor, Faraday cup, integrated current transformer, Beam Position Monitor.

in designing the high power beam dump. In order to maintain the radiation level in the facility within acceptable limits (set by the relevant regulations), the design of the beam dump needs to ensure that the beam is completely contained within the beam dump and that adequate shielding is provided.

3.4 Summary

The main beam dynamics challenges to provide ultra-bright electron beam to drive an X-ray FEL are space charge, coherent and incoherent synchrotron radiation, wake fields and micro-bunching. These challenges are briefly discussed in this chapter considering different accelerator configurations such as single pass linac, re-circulating linac and energy recovery linac. The differences in these different configurations have been discussed briefly. The choice of accelerator configuration is dictated by the photon requirements from the users. A generic layout of a single pass facility is used to describe the functions of different subsystems. The design and technological challenges are mentioned where appropriate (e.g. facility operating at high repetition rate). To a large extent, the beam spreader design options are independent of accelerator configuration as the beam spreader starts at the exit of the accelerator.

Chapter 4

Coherent Synchrotron Radiation

4.1 Introduction

Electromagnetic radiation is always emitted when electrons are accelerated. When electrons are accelerated parallel to their direction of motion, as in the linac, the radiation power is negligible. But when electrons experience transverse acceleration while passing through bending magnets, the radiation power is high. As discussed in Chapter 1, three generations of synchrotron radiation sources exploit this radiation. In a single pass machine for X-ray FEL, there are three sections where radiation is important to consider; namely bunch compression chicane, a spreader or switchyard and the FEL sections.

For an electron bunch in a circular motion, three regimes of synchrotron radiation are distinguished (neglecting transition regimes) [89, 90] as shown in Fig. 4.1. The abscissa of the figure is normalised to $\sigma_0 = R/\gamma^3$, where R is the bending radius and γ is relativistic Lorentz factor. As long as all electrons radiate individually, only incoherent synchrotron radiation (ISR) is emitted and the total radiated power scales linearly with the number of electrons:

$$P_0 = \frac{1}{6\pi\epsilon_0}\frac{Ne^2c\gamma^4}{R^2}, \tag{4.1}$$

where N is number of electrons, e is electron charge and c is speed of light.

As an example, an electron bunch with charge 200 pC and 500 MeV beam energy passing through a dipole with a bending radius of 5 m the incoherent power is $\approx$ 2 W. At beam energy of 2 GeV, the incoherent power loss is 540 W. Thus, the ISR is negligible at lower energies but at higher energies (like in beam spreader), ISR cannot be neglected.

As briefly discussed in Section 3.1.3, when a short electron bunch travels through a dipole magnet, it emits coherently at wavelengths that are comparable to (or larger than) the bunch length and can propagate in the vacuum chamber. As electrons traverse the dipole on an arc of a circle, radiation from one part of the arc can catch up with electrons on another part of the arc. If the longitudinal range of electron bunch is much smaller than σ_0, they radiate coherently. In this regime of fully coherent synchrotron radiation

(CSR), all electrons radiate as one point charge with a power of:

$$P_{coh} = \frac{1}{6\pi\epsilon_0}\frac{N^2 e^2 c\gamma^4}{R^2}, \tag{4.2}$$

which is N times the power of the incoherent radiation. For the bending magnet located at 500 MeV with bending radius of 5 m, the coherent radiated power for a bunch charge of 200 pC is 2.6 GW and at 2 GeV it is 675 GW. The bunch length has to be of the order of $\approx$ 600 nm which is far from typical bunch lengths (few to tens of microns at 200 pC) as described in Chapter 5.

In between these two extreme regimes, is the regime of where the radiation power is proportional to N^2 and depends upon the rms bunch length σ_l but not on the energy γ [89]. The power in this regime is given by:

$$P_{CSR} = \frac{1}{\epsilon_0}\frac{N^2 e^2 c x}{R^{2/3}\sigma_l^{4/3}}, \quad \text{with} \;\; x = \frac{\Gamma(5/6)}{4\pi^{3/2}}\frac{1}{\sqrt[3]{6}} \approx 0.0279. \tag{4.3}$$

Using the same example, for a bunch charge of 200 pC and bunch length equal to 25 μm passing through a dipole of radius 5 m, the radiated coherent power is $\approx$ 17 kW independent of energy.

Comparing above three equations, it can be seen that the three radiation regimes transition to fully coherent at $\sigma_l \approx \frac{2}{3}\sigma_0$ and at $\sigma_l \approx N^{3/4}\sigma_0$ transition to fully incoherent.

For the beam spreader designs presented in Chapter 5, the beam energies considered are 2.2 GeV and 6.6 GeV and the values of bending radii lie between 6-15 m (except for kicker and septum magnets, where the bending radii are very large). For the bunch charge of 200 pC considered, the transition to incoherent regime at 2.2 GeV happens at $\approx\sigma_l$ of 500 μm (R=6 m) and 1.25 mm (R=15 m). At 6.6 GeV this is much lower at $\approx\sigma_l$ of 18 μm (R=6 m) and 46 μm (R=15 m). Therefore, a bunch length of 25 μm used in beam spreader designs, is very close to the partially coherent regime close to the ISR transition. This explains the need to optimise the beam spreader designs to minimise the ISR as explained in Chapter 5.

This partially coherent part of the radiation at a wavelength comparable to the bunch length, results in a modulation of the energy along the bunch. This is similar to a wakefield, but the main difference is that the CSR affects the electrons ahead of the radiating electron rather than behind (as in the classical wakefield effects). Due to the dependence of the CSR power on the bending radius and the bunch length, it is important to reduce the bending angles (short magnet lengths and large bending radius) to minimise its detrimental effects on beam as explained later in this chapter.

The power loss due to CSR described above does not reduce the total energy uniformly across the bunch (which could be corrected) but this energy loss is distributed along the bunch. The main relevant results from the well known paper by Saldin *et al* [91] which presents the CSR theory for a bunch of any length moving in an arc of a finite angle and

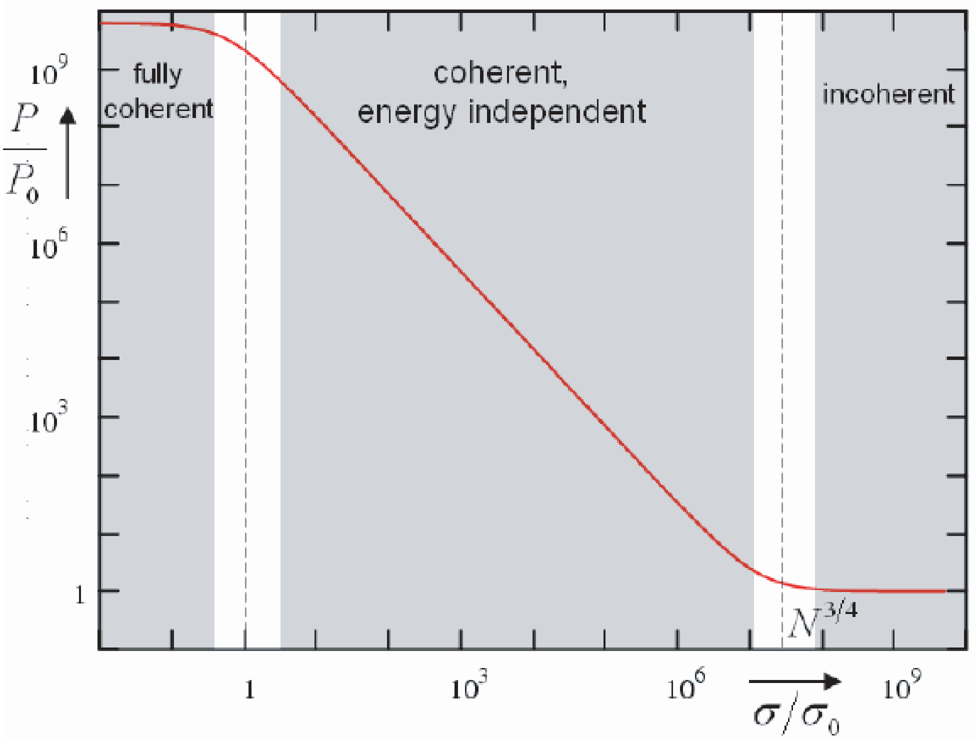

Figure 4.1: Regimes of fully coherent, energy independent coherent and incoherent radiation. Figure taken from [90].

analyses the radiative interaction of the electrons in the bunch for a line charge distribution are summarised. When the wavelength of the coherent radiation is of the order of the bunch length $'L_b'$, a scale length of the process known as slippage length (defined as $s_l = \frac{R\theta}{2\gamma^2} + \frac{R\theta^3}{24}$, where θ is the bending angle, R is the bending radius and γ is relativistic Lorentz factor) is useful to describe the interaction of electrons and photons during the emission. The CSR emission depends on the details of the charge distribution and on the geometry of the electron path and it causes a variation of the electron energy along the bunch. As this happens in a dispersive region and that different slices of the bunch are subject to a different energy variation, they start betatron oscillating around new, different dispersive orbits during the emission, thus increasing the projected beam emittance in the plane of bending. This is analogous to emittance growth from incoherent synchrotron radiation as described in Section 3.1.4.

Following [91], the energy change per distance travelled inside a bending magnet of finite length can be evaluated by means of the CSR wake potential. In the "steady state" (radiation does not depend upon azimuthal position and transient effects at the dipole entry and exit are neglected) approximation ($R/\gamma^3 \ll L_b \leq s_l$), the wake potential can be written as:

$$W_{CSR}^{SS}(z) = -\frac{1}{4\pi\epsilon_0}\frac{2e}{\sqrt[3]{3R^2}}\int_{-\infty}^{z}\frac{1}{(z-z')^{1/3}}\frac{d\lambda_z(z')}{dz'}dz'. \tag{4.4}$$

The energy loss of electron per unit distance through a dipole due to the radiation emission of the entire bunch $(dE/dz)_{CSR}$ is given by $eNW^{SS}_{CSR}(z)$. For short bunch length ($L_b \leq s_l$ and long magnet $\gamma\theta >> 1$), using eqn.(4.4) and Gaussian line charge distribution of electrons given by:

$$\lambda(s) = \frac{N}{\sqrt{2\pi}\sigma_l}\exp\left(-\frac{s^2}{\sigma_l^2}\right). \tag{4.5}$$

The energy loss per unit length of the reference electron due to CSR emission is given by:

$$\left(\frac{dE}{dz}\right)_{CSR} = -\frac{1}{4\pi\epsilon_0}\frac{2Ne^2}{\sqrt{2\pi}\sqrt[3]{3R^2\sigma_l^4}}F\left(\frac{s}{\sigma_l}\right), \tag{4.6}$$

where the function F is given by:

$$F(\xi) = \int_{-\infty}^{\xi}\frac{d\xi'}{(\xi-\xi')^{1/3}}\frac{d}{d\xi'}\exp^{-(\xi')^2/2}. \tag{4.7}$$

Using the energy loss per electron, the total CSR power can be calculated as:

$$P_{csr} = -\int_{-\infty}^{\infty} ds\lambda(s)\left(\frac{dE}{dz}\right)_{CSR}. \tag{4.8}$$

While leading electrons gain energy, the trailing electrons lose energy. Averaged over the entire bunch, the electrons loose energy. The total CSR power is given by [91]:

$$P_{csr} \approx \frac{1}{4\pi\epsilon_0}\frac{3^{1/6}N^2e^2}{2\pi\sqrt[3]{R^2\sigma_l^4}}\left(\Gamma\left(\frac{2}{3}\right)\right)^2 \approx \frac{0.352\ c}{4\pi\epsilon_0}\frac{N^2e^2}{\sqrt[3]{R^2\sigma_l^4}}. \tag{4.9}$$

The mean fractional energy offset ($\delta = (p-p_0)/p_0$) due to CSR and the standard deviation of the energy offset are obtained [92] from results given by Saldin et al:

$$\begin{aligned} <\delta> &= -0.3505\ r_e\frac{N}{\sqrt[3]{R^2\sigma_l^4}}\frac{R\theta}{\gamma}, \\ (\delta)_{s.d.} &= 0.2459\ r_e\frac{N}{\sqrt[3]{R^2\sigma_l^4}}\frac{R\theta}{\gamma}, \end{aligned} \tag{4.10}$$

where r_e is the radius of electron.

This change in energy spread increases the projected emittance which can be explained using a simple model. This assumes that the phase space of the longitudinal beam slices are unperturbed, but as a result of CSR their centroids $(x_c(s), x'_c(s))$ have shifted. The second moments of the full bunch can then be expressed as superpositions of the second moments of the centroids and those of the unperturbed distribution, which are described by the Courant–Snyder parameters α_x and β_x, and the initial emittance as ϵ_{x0} as:

$$\begin{aligned} <x^2> &= <x_c^2> + \epsilon_{x0}\beta_x, \\ <xx'> &= <x_c x'_c> - \epsilon_{x0}\alpha_x, \\ <x'^2> &= <{x_c}'^2> + \epsilon_{x0}\gamma_x. \end{aligned} \tag{4.11}$$

Assuming a CSR induced bunch length correlated energy spread $\sigma_{\delta,CSR}$ is generated in a short single dipole (e.g. last dipole of bunch compression chicane) with bending angle θ, the increase in angular spread is $\Delta x'_{rms} = \theta(\delta)_{s.d.}$. The increase in projected emittance caused due to this additional angular spread is:

$$\frac{\Delta\epsilon_x}{\epsilon_{x0}} \approx \frac{1}{2}\frac{\beta_x}{\epsilon_{x0}}(\theta(\delta)_{s.d.})^2. \tag{4.12}$$

This formula gives an estimate of increase in projected emittance when beam passes through the dipole. The validity of this formula with *elegant* simulations is shown in an example used in Section 4.3.3.

The dependence of the increase in emittance on the Courant–Snyder parameter β_x has important implication to the lattice design of beam spreader. A lattice design minimising this parameter where bunch length is shortest (e.g. last dipole of bunch compression chicane) can help to reduce the impact of CSR on emittance growth. However, when different parts of electron bunch get different CSR kicks the mismatch of bunch slices can still increase the projected emittance. The optics system can be designed to minimise this increase in emittance as discussed later in this chapter which form a basis of design for the beam spreader designs discussed in Chapter 5.

4.2 Shielding due to the Vacuum Chamber

The electromagnetic fields generated by an electron bunch interact with the conducting walls of the vacuum chamber. If the wavelengths of these electromagnetic fields are larger than the size of the vacuum chamber, they cannot propagate inside the chamber. This suppresses (shields) the low frequency part of the spectrum and decreases the radiation power compared to that in a free space. There are number of publications on theory of shielding of CSR. An exact expression for the CSR power radiated by a bunch in steady state, written as a summation over all harmonics of the radiated power is emitted by a Gaussian line charge on a circular orbit centred between two infinite parallel conducting plates is presented in [93]. The expression for the shielded CSR power for beam and machine parameters is presented in [94]. The analysis is further modified in [95] to include strong shielding regime in which the threshold harmonic (which satisfies the boundary conditions at the plates) exceeds the characteristic frequency of the bunch. The ratio of coherent power to free-space steady state CSR is given by [95]:

$$\frac{P_{coh}}{P_{freespace}} \approx 4.2\left(\frac{n_{th}}{n_c}\right)^{5/6} \exp\left(-\frac{2n_{th}}{n_c}\right), \; n_{th} > n_c, \tag{4.13}$$

where $n_{th} = \sqrt{2/3}(\pi R/\Delta)^{3/2}$ is the threshold harmonic number for propagating radiation, Δ is the vacuum chamber total gap, $n_c = R/\sigma_l$ is the characteristic harmonic number for a Gaussian longitudinal density distribution with the rms value of σ_l and bending radius R. The spectral component of the radiation with harmonic numbers beyond n_c is incoherent.

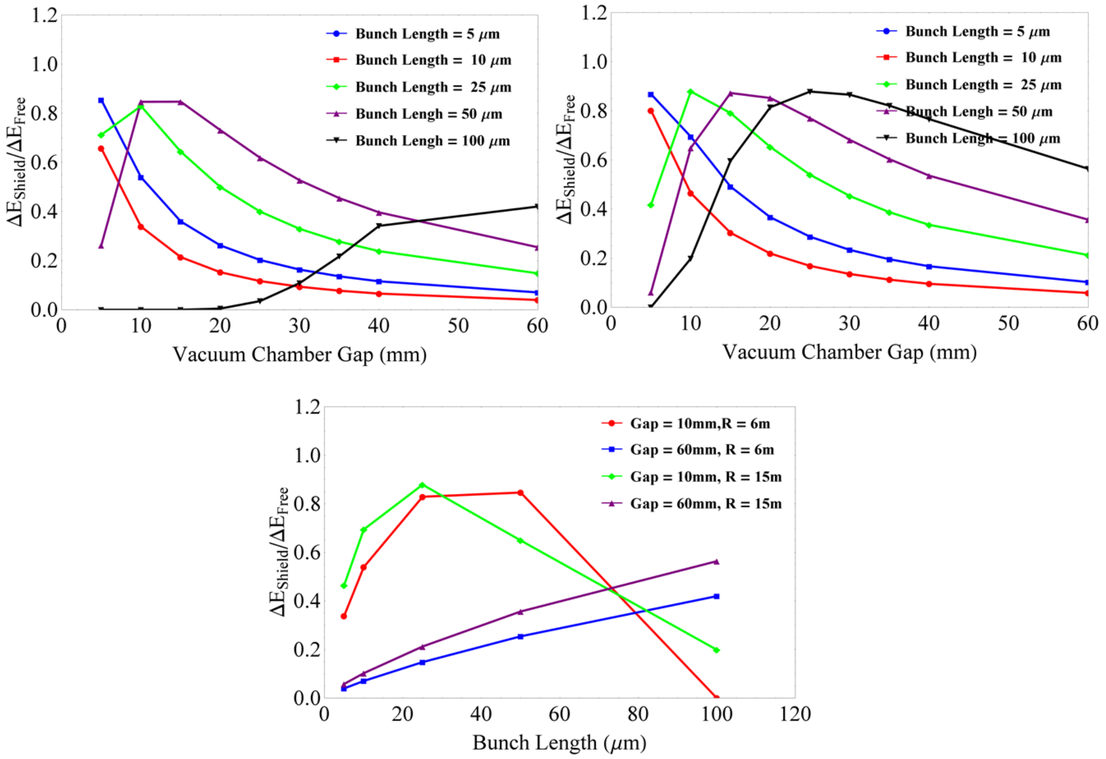

Figure 4.2: Suppression of CSR by vacuum chamber shielding for different bunch lengths. Top: Left: Bending radius =15 m, Right=6 m, Bottom: Comparison of two bending radii for two vacuum chamber gaps (10 mm and 60 mm) as a function of bunch length.

Fig. 4.2 shows the effect of shielding for different bunch lengths for two values of bending radii 6 m and 15 m, respectively (corresponding to the beam spreader designs presented in Chapter 5). From these figures it can be seen that for shorter bunch lengths (of the order of 10-20 μm as in the case of beam spreader designs) and typical vacuum gap of the order of 30 mm there is small level of shielding. In order to provide significant shielding, the required vacuum gaps will be very small. Reduction in vacuum chamber gap will have other consequences such as very tight tolerances on beam trajectory, effects of wakefields etc.

4.3 Tracking Including CSR

In many optics and tracking codes normally used for lattice design such as MAD [96], TRANSPORT [97] etc, the bunch self interaction due to synchrotron radiation (and also due to space charge fields which is not necessary to consider due to energy regime of beam spreader considered in this thesis) are neglected. Several special codes have been developed (such as TraFic4 [98], CSRTrack [99]) and/or existing codes have been expanded (such as *elegant* [75]) to include this effect. An overview of the existing codes and benchmarking of several codes can be found in [100, 101].

The simplest and fastest method to calculate the CSR fields is the so called 1-D or the projected method. It neglects transverse beam dimensions and calculates the longitudinal self-field of a one dimensional beam that is obtained by a projection of the real three-dimensional beam to a reference trajectory. For the field calculation at a certain instant, it is assumed that the longitudinal distribution is rigid and has not changed at retarded times (the earlier time when radiation is emitted which reaches head of the bunch).

The CSR model in *elegant* is based on the analytical formulae derived in [91] for the energy change of an arbitrary line-charge distribution as a function of the position in the bunch and in a dipole magnet. Effects of changes in the longitudinal distribution within a dipole are included but it does not include the effect of the transverse distribution of the beam on the CSR and the variation of the CSR across the beam. The model includes the effect of the transverse beam distribution on the amount of emittance growth due to change in energy. The 1-D model can be applied when Derbenev criterion [49] $\frac{\sigma_x}{\sigma_z} << (\frac{R}{\sigma_z})^{1/3}$ is satisfied (where σ_x is the horizontal beam size and σ_z is the longitudinal beam size). For the beam parameter regime considered for the beam spreader designs discussed in Chapter 5, this criterion is satisfied and so the simulations using *elegant* are adequate. The validity of *elegant* simulations has also been experimentally verified at few FEL facilities [102, 103] where the criterion for using 1-D code is applicable. The code *elegant* includes CSR in drift spaces by propagating the final CSR wake in each dipole through the drift spaces after the dipoles. It is important to define the drift spaces after the dipoles as “CSRDRIFT" to consider this.

When the Derbenev criterion is not satisfied, the full three-dimensional integration of the retarded Lienard-Wiechert potentials is required. This is computationally highly intensive. An approach followed in codes TraFic4 [98] and CSRTrack [99] is to use Gaussian sub-bunches to represent the 3-D distribution of the whole bunch and use a convolution method to reduce the field calculation of 3-D sources to 1-D integrations [104].

4.3.1 Implementation of 1-D CSR model in *elegant*

Following [91], the rate of change of energy in the bunch can be split in two terms given by:

$$\frac{dE}{cdt} = T_1(s, R, \theta) + T_2(s, R, \theta), \tag{4.14}$$

where R is the bend radius, θ is the angle into the bend, s is the position within the bunch, c is speed of light and t is time. T_1 is responsible for most of the CSR effect and transitions into the steady state result as described with eqns.(4.4, 4.6) and is given by:

$$T_1 = \frac{-2e^2}{\sqrt[3]{3R^2}} \int_{s-s_l}^{s} \frac{d\lambda}{dz} \left(\frac{1}{s-z}\right)^{1/3} dz, \tag{4.15}$$

where $\lambda(z)$ is the linear charge density, s_l is the slippage length. The term T_1 physically implies that an electron will be affected by the radiation from the charge following behind it by a distance up to the slippage length. As the bunch travels through the dipole magnet, the slippage length increases and thus each electron in the bunch is affected by radiation from a larger number of electrons behind it. The second term T_2 represents a transient at the entrance of the dipole which dies out if the dipole is sufficiently long and is given by:

$$T_2 = -\frac{2e^2}{\sqrt[3]{3R^2}}\frac{\lambda(s-s_l)-\lambda(s-4s_l)}{s_l^{1/3}}. \tag{4.16}$$

For a long dipole, s_l will become large enough so that T_2 becomes zero. The code *elegant* implements these results by splitting each dipole into a specified number of slices, for each slice, it propagates the entire bunch using a second or fourth-order canonical integrator, computes the CSR wake and applies the CSR kicks. Computation of CSR wakes is performed as follows: (1) arrival times of electrons at the end of the dipole piece are binned. (2) the density histogram is smoothed using Fast Fourier Transform convolution with appropriate filter (3) the same filter is used to take the derivative of the smoothed density distribution. (4) The T_1 and T_2 functions are computed for each bin. (5) energy of each electron is changed by $\Delta(s)(dE/cdt)$ for the bin it occupies, where $\Delta(s)$ is the central path length of the dipole piece ($=c\Delta t$ where Δt is the time taken for an electron to pass through the slice of dipole). In order to decide the number of bins and number of macroparticles to be used in simulations, convergence tests were performed as described in next section.

4.3.2 Convergence Tests for CSR in *elegant*

In the beam spreader designs presented in Chapter 5, one of the important parameter to optimise is the transverse emittance in the plane of bending. To ensure that the number of macroparticles, bins and kicks assumed for beam tracking simulations of CSR in *elegant* are appropriately chosen, the convergence tests were carried out for three different cases.

1. A single dipole magnet of length 0.5 m and bending angle of 3°. Beam energy 2.2 GeV, bunch charge 1 nC and normalised projected transverse emittance 0.3 mm. mrad at two different bunch lengths 25 μm and 50 μm. It should be emphasised that these small emittance numbers at high charge are not possible to achieve practically. These parameters are considered only to see the convergence in simulations.

2. A single dipole magnet of length 0.2 m and bending angle of 11.5°. Beam energy 150 MeV, bunch charge 1 nC, normalised projected transverse emittance 1.0 mm. mrad and rms bunch length of 100 μm. This corresponds to the dipole and beam parameters used in four dipole chicane used for example of CSR tracking in Section 4.3.3.

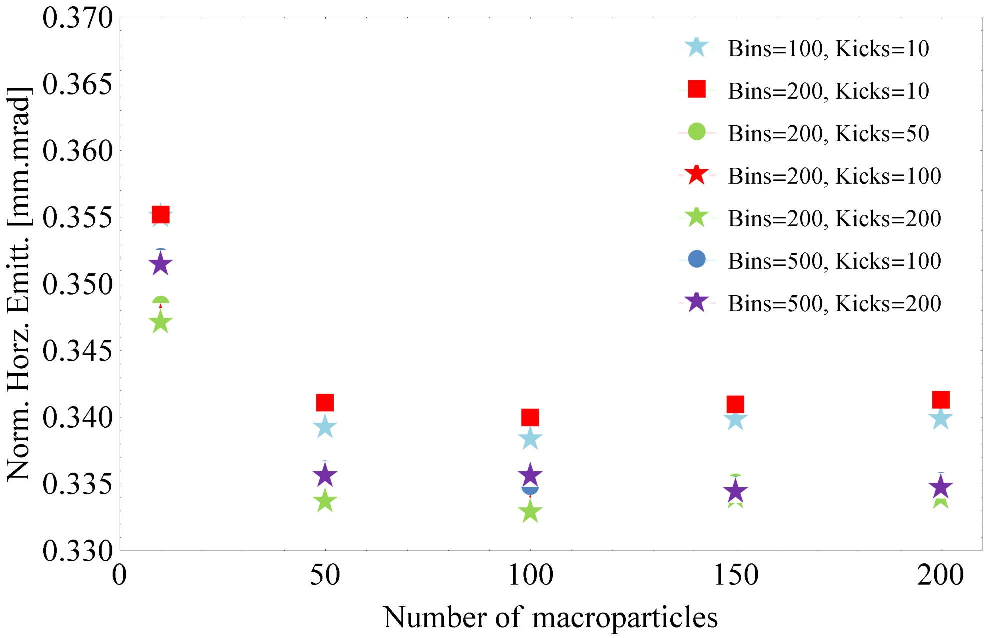

Figure 4.3: Convergence tests for CSR induced emittance growth for a single 3° dipole with length 0.5 *m*. Beam energy 2.2 GeV, bunch charge 1 *nC*, normalised horizontal emittance of 0.3 mm.mrad. Bunch length 25 *µm*.

3. A single dipole magnet of length 0.8 m and bending angle of 6°. Beam energy 2.2 GeV, bunch charge 200 pC, normalised projected transverse emittance 0.3 mm. mrad and rms bunch length of 25 μm. The dipole and beam parameters are taken from beam spreader design from Chapter 5.

In all above three cases, the simulations are repeated for 10000, 50000, 100000, 150000 and 200000 macroparticles, for number of kicks equal to 10, 50, 100, 150, 200 and number of bins equal to 50, 100, 150, 200, 500. The results for (1) are shown in Fig. 4.3, Fig. 4.4, for (2) in Fig. 4.5 and for (3) in Fig. 4.6, respectively.

It is possible to conclude from these results that for cases 1 and 2, the horizontal emittance value converged (to third to fourth decimal point in units of mm.mrad) for 100000 macroparticles, 500 bins and 100 kicks (the results are exactly same as 500 bins and 200 kicks and overlap in the figures). However, for case 3, where small emittance value of 0.3 mm.mrad, bunch length of 25 μm and a dipole angle of 6° is used the spread in emittance values for more than 100000 macroparticles, 500 bins changes the emittance to second decimal in units of mm.mrad. Based on these studies, 100000 macroparticles, 500 bins and 100 kicks are used in beam spreader chapter in general but when looking at small changes in emittance (to second decimal), the simulations are repeated with higher number of kicks.

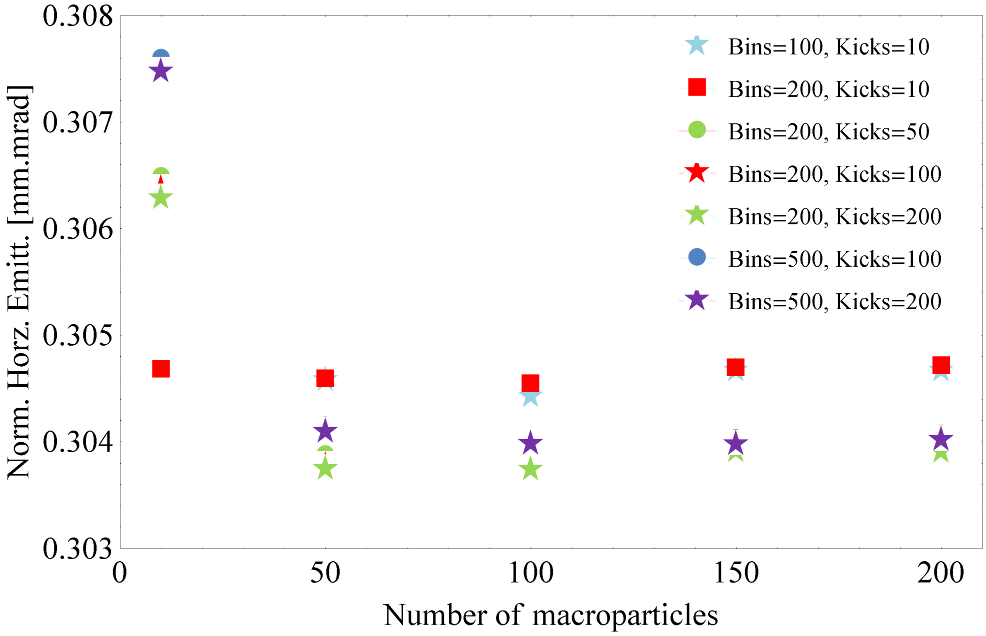

Figure 4.4: Convergence tests for CSR induced emittance growth for a single 3° dipole with length 0.5 m. Beam energy 2.2 GeV, bunch charge 1 nC, normalised horizontal emittance of 0.3 mm.mrad. Bunch length 50 μm.

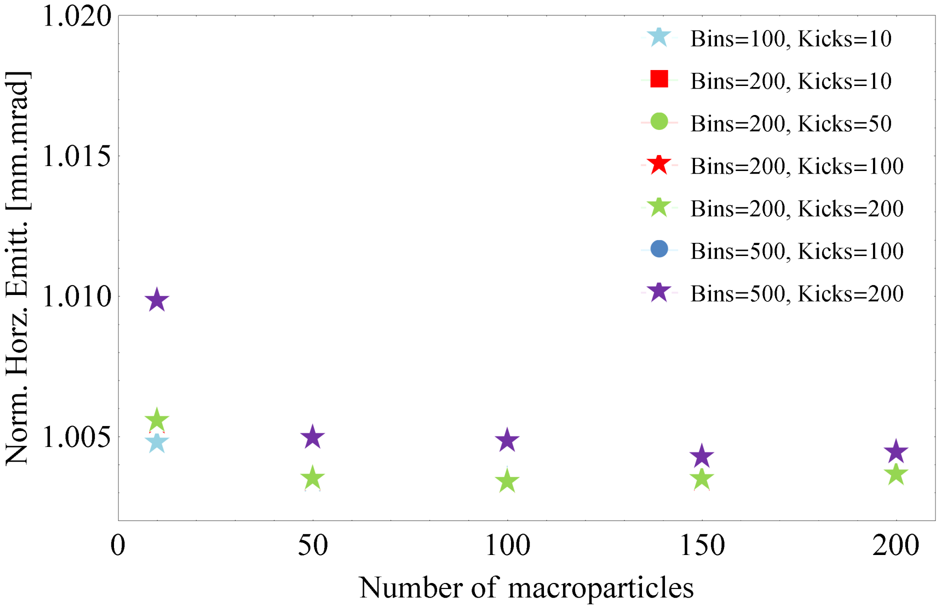

Figure 4.5: Convergence tests for CSR induced emittance growth for a single 11.5° dipole with length 0.2 m. Beam energy 150 MeV, bunch charge 1 nC, Normalised horizontal emittance of 1.0 mm.mrad, bunch length 100 μm. The single dipole and beam parameters used here are for four dipole chicane simulations included in Section 4.3.1.

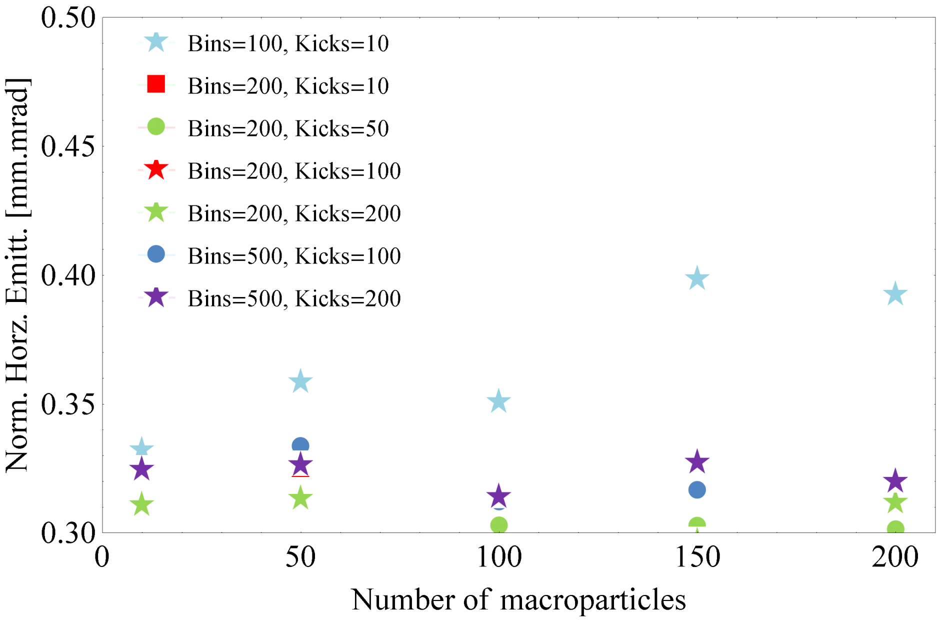

Figure 4.6: Convergence tests for CSR induced emittance growth for a single 6° dipole with length 0.8 m. Beam energy 2.2 GeV, bunch charge 200 pC, normalised horizontal emittance of 0.3 mm.mrad, bunch length 25 μm.

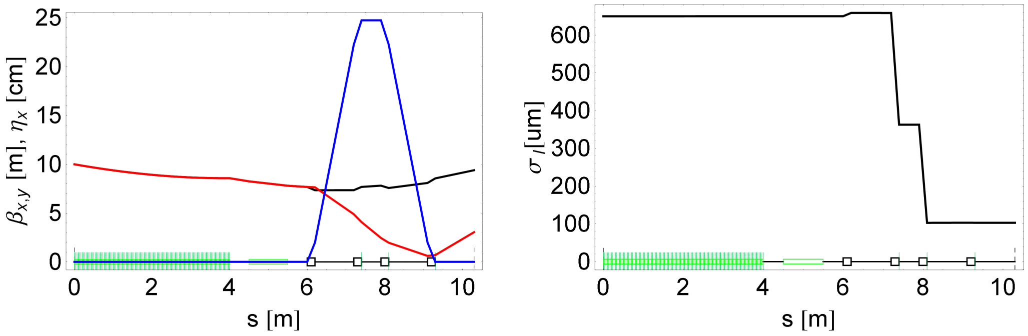

Figure 4.7: Left: Courant–Snyder parameters and dispersion, Right: Bunch length along the beam line (Section 3.3.4) used in for CSR tracking shown in Section 4.3.3.

4.3.3 Example of Simulation of Coherent Synchrotron Radiation

To show the difference in results of simulations using only steady state wake as well as steady state along with the transient effects, the results of CSR simulations shown for a beam line described in Section 3.3.4 are presented in details. The beam line consists of a 4 m long linac, 1 m long fourth harmonic lineariser and a bunch compressor chicane. A Gaussian bunch of 100 MeV beam energy, 1 nC bunch charge with normalised emittance of 1 mm.mrad in both transverse planes and uncorrelated energy spread of 0.001, rms bunch length of 650 μm (2.16 psec) is used. Fig. 4.7 shows the Courant–Snyder parameters, dispersion and bunch length along the beam line.

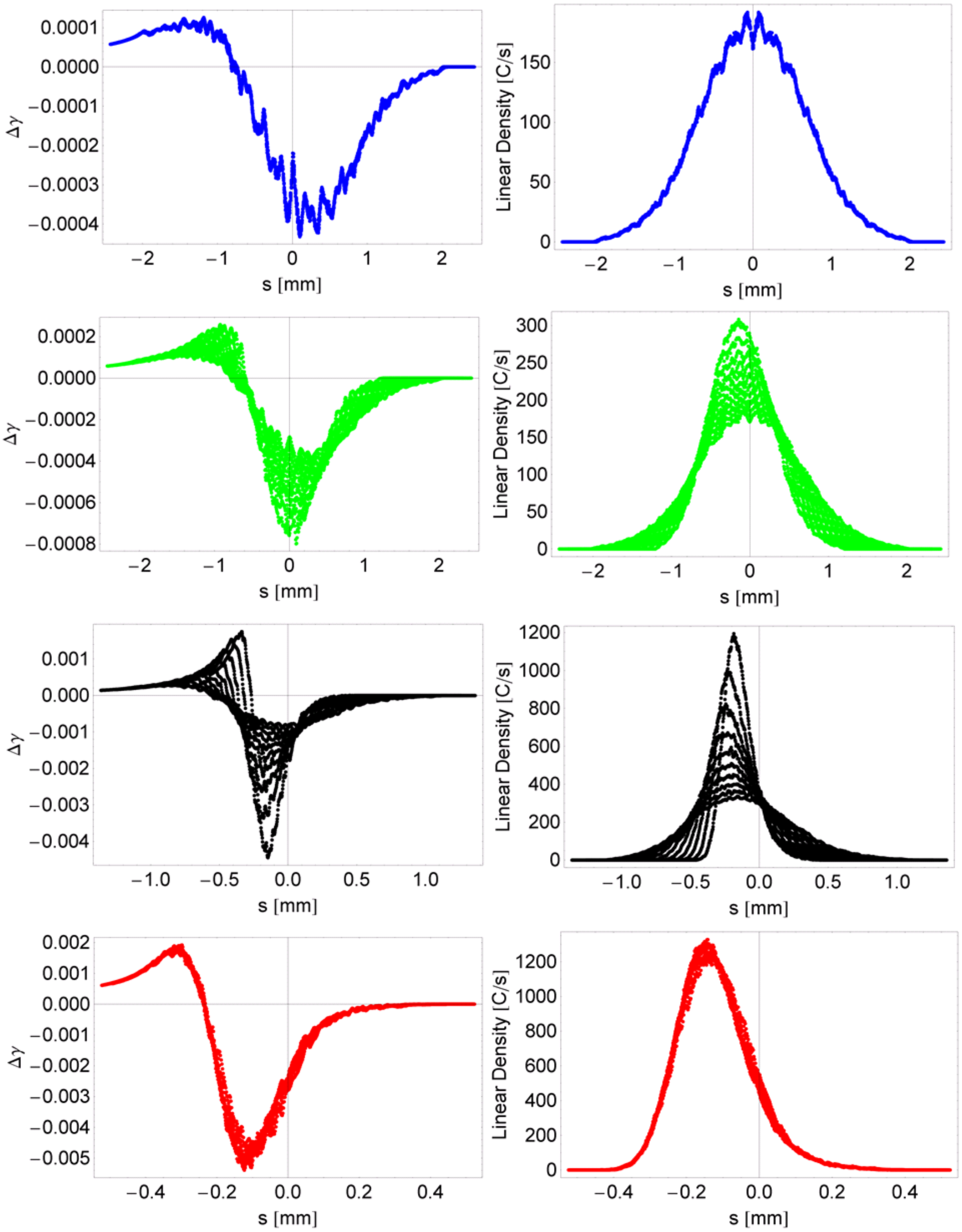

Figure 4.8: Left: Change in γ in the last piece of a dipole due to steady state CSR wake field. Right: Linear density of electrons in successive pieces of a dipole. Number of kicks are equal to 100 (but only every 10^{th} one is plotted), so the change in γ with 100 kicks is 100 times larger. Top to bottom: DIP-01, DIP-02, DIP-03, DIP04.

The energy change ($\Delta\gamma$) due to terms T_1 and T_2 and the linear charge density are plotted inside each dipole for two cases. The results using steady–state CSR wakes are shown in Fig. 4.8 and the results including transients are shown in Fig. 4.9. The effect of finite dispersion in successive pieces of dipole on change in energy and linear density is

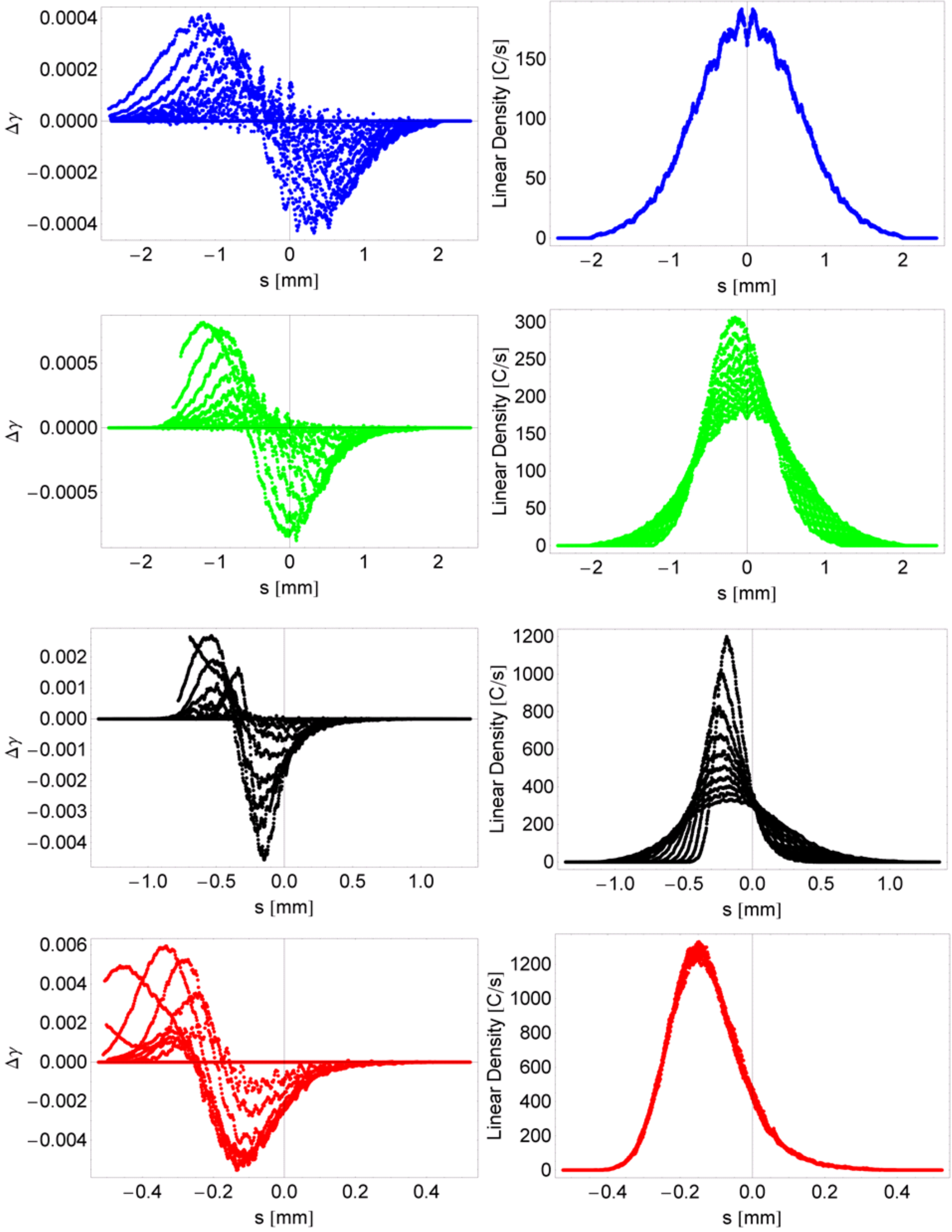

Figure 4.9: Left: Change in γ in the last piece of a dipole due to steady state and transient CSR wake fields. Right: Linear density of electrons in successive pieces of a dipole. Number of kicks are equal to 100, so the change in γ with 100 kicks is 100 times larger. Top to bottom: DIP-01, DIP-02, DIP-03, DIP04.

seen in dipoles 2 and 3. The mean energy offsets are -3.78$\times10^{-3}$ and -3.18$\times10^{-3}$ for steady–state and steady–state including transients CSR wakes, respectively. This energy spread increases the projected emittance which can be estimated using eqn.(4.12). The energy offset and the normalised projected horizontal emittance are shown in Fig. 4.10.

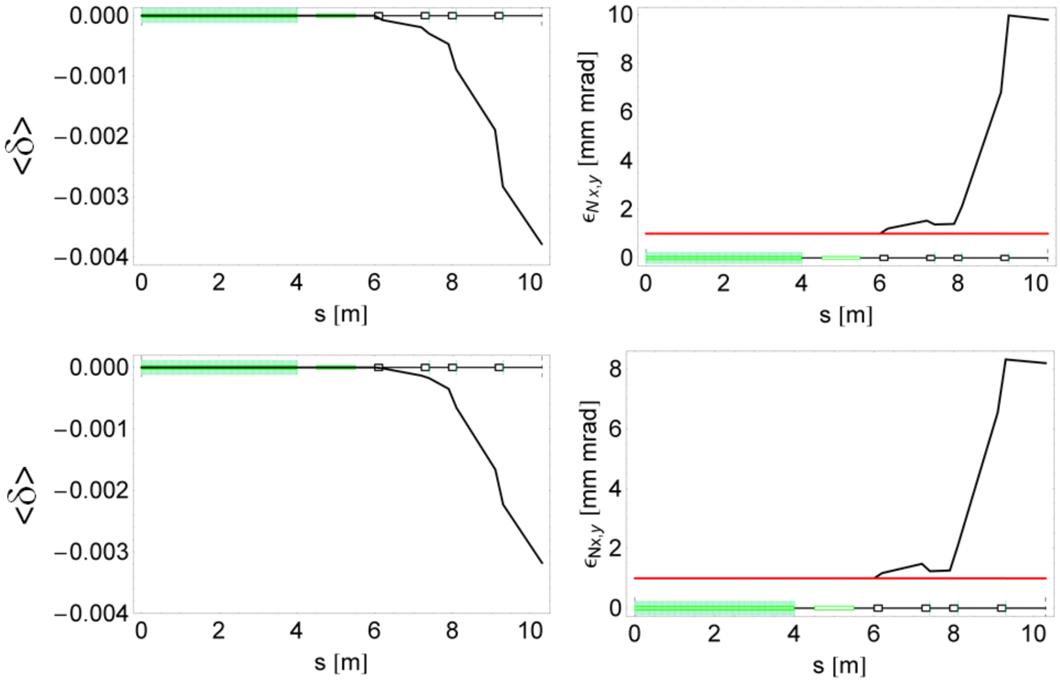

Figure 4.10: Left: Mean fractional momentum offset due to CSR. Right: Projected normalised horizontal emittance. Top: Steady–state CSR. Bottom: Steady–State including transient effects.

As mentioned earlier and demonstrated in Chapter 5, shorter dipole magnets are used to keep the CSR to minimum in beam spreader designs and thus the transient effects of CSR need to be considered. For this reason, effect of transients are included in tracking for beam spreader designs.

4.4 Coherent Synchrotron Radiation Mitigation Techniques

4.4.1 Introduction

The CSR field affects the electron transverse motion due to changing of the electron energy in the dispersive beam line (as in the case of beam spreader). When energy is changed, the electron starts a betatron oscillation around a new reference trajectory. As a result different slices of bunch have different spatial and angular offset, which results in misalignment of different bunch slices increasing the projected emittance. This transverse offset varies with longitudinal position within the bunch and in principle the emittance growth can be completely suppressed if this transverse offset can be removed by optics design as explained in [105].

An electron which loses energy $\delta(s)$ at location s within the system with bending magnets is transported to its end through the chromatic transfer functions, R_{16} and R_{26}, which map an off-energy electron from the point of energy loss in to transverse phase space at the end of the bending magnet system. Since the energy loss can be different for different electrons, the resulting energy spread can potentially dilute the transverse emittance in the bending plane depending upon the coherence of the process. A random process results in an intrinsic emittance dilution (as in the case of incoherent synchrotron radiation) which is not correctable, on the other hand a coherent energy spread generates a transverse offset which varies with longitudinal position. Thus, it is possible to reverse this process.

For the horizontal phase space described by $\vec{x} = [\vec{x}.\vec{x'}]^T$, the rms emittance ϵ is defined by ϵ^2=$|\langle\vec{x}.\vec{x}^T\rangle|$. The energy spread coupled with the chromatic transfer functions can change the on-energy phase space as:

$$\vec{x_s} = \vec{x_0} + \Delta\vec{x}(s) + \begin{pmatrix} R_{16}(s) \\ R_{26}(s) \end{pmatrix} \delta(s). \tag{4.17}$$

Starting with initial emittance of ϵ_0 and for simplicity, defining the coordinates such that $\langle x\rangle = \langle\Delta x\rangle = 0 = \langle\delta\rangle$ the final emittance at the exit of the bending system is given by:

$$\epsilon^2 = \epsilon_0^2 + \epsilon_0 \left[\beta_x\langle\Delta x'^2\rangle + 2\alpha_x\langle\Delta x\Delta x'\rangle + \gamma_x\langle\Delta x^2\rangle\right] + \langle\Delta x^2\rangle\langle\Delta x'^2\rangle - \langle\Delta x\Delta x'\rangle^2, \tag{4.18}$$

where β_x, α_x and γ_x are the nominal Courant–Snyder parameters in the bending system. The last two terms of eqn.(4.18) give increase in emittance even for beam with initial zero emittance.

When the energy loss is uncorrelated (incoherent), the variance of $\Delta x(\Delta x')$ due to incremental energy spread generated at each location is added in quadrature and summed over the bending system.

$$\begin{aligned} \langle\Delta x^2\rangle_{incoh} &= \int_{path} R_{16}(s)^2 \frac{d\sigma_\delta^2}{ds} ds, \\ \langle\Delta x'^2\rangle_{incoh} &= \int_{path} R_{26}(s)^2 \frac{d\sigma_\delta^2}{ds} ds. \end{aligned} \tag{4.19}$$

When the energy loss is a function of longitudinal position along the bunch, the transverse coordinate shifts at each location and can be added linearly and is given by:

$$\begin{aligned}\langle \Delta x^2 \rangle_{coh} &= \left(\int_{path} R_{16}(s) \frac{d\sigma_\delta}{ds} ds \right)^2 , \\ \langle \Delta x'^2 \rangle_{coh} &= \left(\int_{path} R_{26}(s) \frac{d\sigma_\delta}{ds} ds \right)^2 . \end{aligned} \tag{4.20}$$

Due to coherence, the correlation $\langle \Delta x^2 \Delta x'^2 \rangle = \langle \Delta x^2 \rangle \langle \Delta x'^2 \rangle$ and the last two terms in eqn.(4.18) cancel out.

The incoherent terms in eqn.(4.19) are always positive and thus cannot be nullified. Whereas the sign of the coherent parts in eqns.(4.20) can change along the beam path and can be nullified at the end of the beam path with a choice of proper lattice design. If the bunch length is constant, then the CSR induced $\frac{d\sigma_\delta}{ds}$ is constant and can be factored out from the integrations in eqn.(4.20). Therefore if the beam line lattice is designed to satisfy $\int_{path} R_{16}(s) ds = 0$ and $\int_{path} R_{26}(s) ds = 0$, then there is no net emittance increase. This principle is used to cancel the CSR kicks using certain optics conditions in the spreader design as explained in next section.

4.4.2 Optics Balance

A way to cancel the CSR perturbations to the transverse emittance by imposing certain symmetric optics conditions on the electron transport system was suggested in [106] for the special case of identical CSR kicks along the beam line. It is in principle possible to impose certain symmetric optics conditions in beam spreader designs. As the beam manipulations are completed before entering the beam spreader, the energy spread is small and the bunch length is approximately constant and, consequently (in the ideal case), CSR emission can be formulated by assuming identical beam parameters at all source points (i.e. dipole magnets). As presented in details in Chapter 5, the beam spreader typically includes several identical dipole magnets and quadrupole magnets for focusing and control over dispersion and its derivative. The idea is that successive CSR kicks separated by π betatron phase advance (in the bending plane) add with opposite sign, and thus cancel the slice transverse mismatch with no or negligible emittance growth. The slice of the bunch starts oscillating around a new dispersive trajectory defined by the dispersion function at the kick location and the CSR-induced energy shift. If the lattice functions and the parameters of this bunch slice remain identical by the time it reaches the second dipole placed at π betatron phase advance, it receives CSR kick in the opposite direction and thus cancels out the action induced by the first one. Thus after passing through two dipoles, the bunch slice returns to previous off-momentum trajectory and as a consequence there is no (or minimum) emittance growth [107, 108].

The beam spreader layout could be arranged in two different ways [109] satisfying the phase and optics constraints as shown in Fig. 4.11. The one in the upper diagram gives

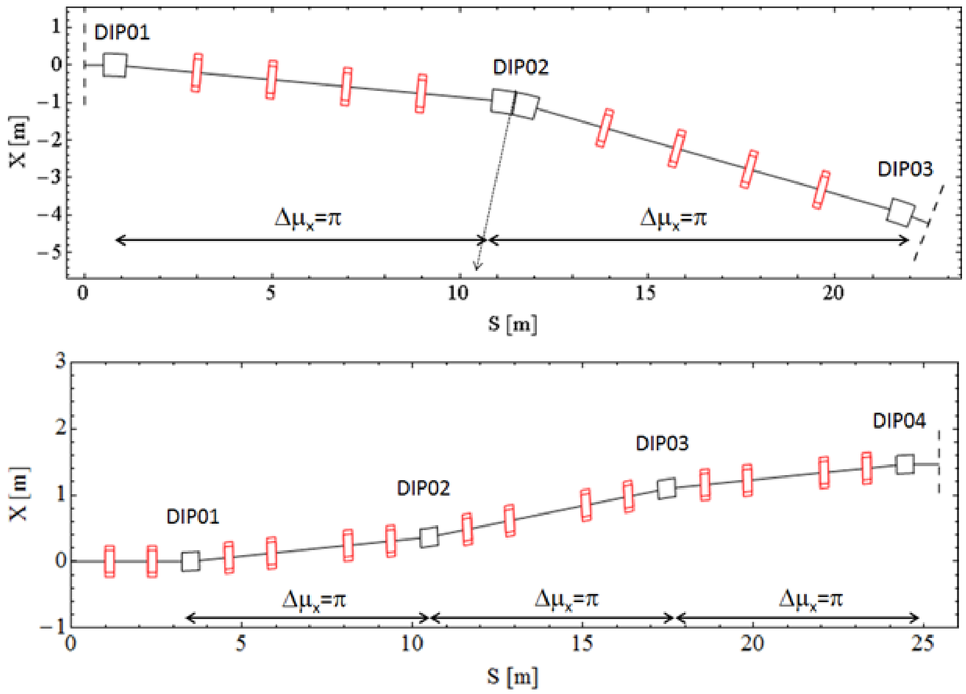

Figure 4.11: Possible spreader design options [Top] An arc providing an angular separation and [Bottom] a dogleg configuration providing parallel separation. Phase advance between consecutive dipoles is maintained at π for cancellation of CSR kicks.

an angular separation between beam lines. In this case, the CSR kicks are canceled if the central dipole is twice as large as the one on either side, and the phase advances between first and the centre of the second dipole and from the centre of the second dipole to the third dipole is arranged equal to π. All dipoles bend the beam in same direction and thus this configuration (TBA) gives an angular separation between the beam lines. The one in the lower diagram of Fig. 4.11 uses two DBA cells bending the beam in opposite directions and thus bringing it parallel to the line at the start of the beam spreader. Both these configurations are used in Chapter 5 as basic building blocks of proposed lattice designs.

The ideal design conditions mentioned above are however not achievable in a real machine (due to optical mis-match, alignment and magnet field errors etc) and could only partially compensate the emittance growth. In a real machine with finite bunch dimensions, there are several factors that can affect the cancellation; the very condition of fixed phase advance and lattice functions at dipole locations depend upon electron energy offset, so any chromatic aberrations will affect the degree of cancellation of CSR kicks, the cancellation of kicks also assumes a single kick at each dipole, which is not the case for long dipole magnets followed by long drifts (which may be limited due to cross-coupling between energy shifts along the spreader beam line), non-zero values of the R-matrix terms (R_{51}, R_{52}) combined with a finite emittance beam can change the path length between the two kick points resulting in to change in longitudinal position of an electron, which can lead to different CSR driven energy shifts.

4.4.3 Example of Optics Balance

To illustrate the cancellation of CSR kicks by choosing a suitable lattice design, based on design and experimental studies carried out at FERMI@ELETTRA [107] a beam line using FODO cells (more details of choice of the FODO are described in Chapter 5) where identical dipoles are incorporated to have a betatron phase advance of π between each consecutive pair of dipoles is considered. The lattice shown in Fig. 4.11 (bottom) consists of two DBA cells with all four identical dipoles (DIP01, DIP02, DIP03, DIP04). The values of dispersion function and its derivative $|\eta_x|$ and $|\frac{d\eta_x}{ds}|$ are exactly the same at all dipoles. Each DBA ensures $\Delta\mu = \pi$ between the dipoles and symmetric β_x and α_x values. Two DBAs are separated by four quadrupoles again tuned to provide a phase advance of π between them. The Courant–Snyder parameters β_x, α_x, dispersion function η_x and its derivative η'_x and the phase advance $\Delta\mu_x$ in the bending plane (horizontal in this case) are shown in Fig. 4.12. This optics arrangement with completely identical optics conditions at all four dipoles with correct phase advance between consecutive dipoles provides a basis for compensation of emittance change due to CSR generated in the dipoles.

To explain this, let′s start with an electron having an initial co-ordinates as ($x_0 = 0$ and $x'_0 = 0$) and assume that the CSR in DIP01 causes a change in energy for this electron by δE. The gradient of the dispersion is η'_x, $\Delta x' = \eta'_x \delta E$. At the entrance of DIP02 after passing the lattice with phase advance of π from DIP01, the angle of the trajectory of electron is -$\eta'_x \delta E$. Assuming that there is no mixing of longitudinal co-ordinates within the bunch while transporting from DIP01 to DIP02, the energy change experienced by the same electron in DIP02 due to the CSR is the same as in DIP01. The sign of η'_x in DIP02 is opposite to that in DIP01, thus the total change in angle of the trajectory of the electron at the exit of DIP02 is $-2\eta'_x \delta E$. After passing through one more section with phase advance of π the trajectory angle at the entry of DIP03 is $+2\eta'_x \delta E$. Considering the sign of η'_x in DIP03, the angle at the exit of DIP03 is $2\eta'_x \delta E - \eta'_x \delta E = \eta'_x \delta E$. After phase advance of π, at the entry of DIP04, it is equal to $-\eta' \delta E$. Again considering the sign of η'_x in DIP04, the trajectory angle at the exit of DIP04 is $-\eta'_x \delta E + \eta'_x \delta E$, which is equal to zero. This shows that assuming no mixing of longitudinal positions of electrons inside the bunch, the spreader design with identical lattice and bunch parameters at every dipole as described here should not increase the projected beam emittance due to energy changes due to CSR. This principle is used for the beam spreader designs in Chapter 5.

This model has been extended further for asymmetric optics in [107, 108] and has been experimentally verified on beam spreader design at FERMI by intentionally breaking the optics balance in the second DBA [107, 108].

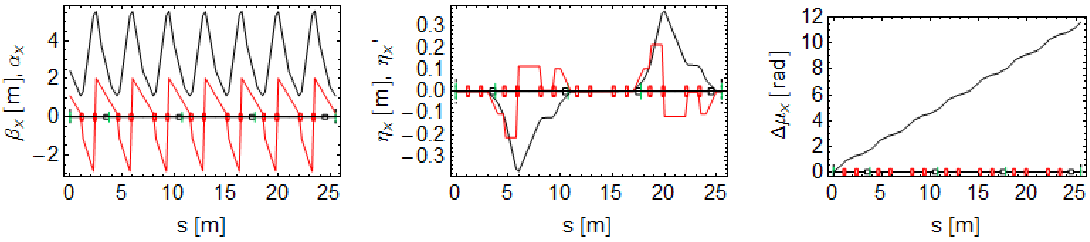

Figure 4.12: Left: Courant–Snyder parameters β_x (black), α_x (red), Middle: Dispersion function (black) and its derivative (red). Right: Betatron phase advance in the horizontal plane along the beam line shown in bottom figure from Fig. 4.11.

4.4.4 Matrix Approach

A first order matrix approach proposed [110, 111] for a TBA arc used in an Energy Recovery Linac minimises the CSR-induced emittance growth by matching the beam envelope to the net CSR kick at the exit of a single achromatic cell. When the electron energy is much larger than the CSR induced energy spread, a linearised approximation can be adopted to describe the electron dynamics. The CSR induced energy spread results in the displacement of bunch slices in (x, x') phase space at the end of the TBA arc. In the linear regime (weak CSR), it can be assumed that all bunch slices align on a single line as shown in Fig. 4.13. The projection of emittance depends on the orientation of the CSR kick and the phase space ellipse which can be minimised if TBA is designed to match the orientation to the CSR kick. An achromatic cell design to achieve this is described by Hajima in [110, 111] as follows.

A first-order equation of motion in the horizontal plane given in Section 2.2 can be modified to include additional terms from CSR as:

$$x'' + \frac{x}{\rho^2} = \frac{1}{\rho}\left(\delta_0 + \delta_{CSR} + k(s - s_0)\right), \tag{4.21}$$

where δ_0 as initial fractional momentum deviation. The last two terms on the right hand side are due to CSR terms, the first one δ_{CSR} is the normalised momentum deviation caused by CSR in upstream path $(0 < s < s_0)$. The entrance of the dipole starts at $s = s_0$. The CSR effect in a dipole is given by the normalised CSR potential given by $k = W/E_0$, where W is CSR wake potential and E_0 is the reference energy. It is assumed that each electron experience a constant CSR wake through the entire bending path. This assumption is valid if all the dipoles have the same bending radius, the longitudinal prfoile of the bunch does not change and the transient CSR effects are not large. With these assumptions eqn.(4.21) can be solved analytically. A 5×5 transfer-matrix representing a solution to eqn.(4.21) is used to describe the motion in terms of a vector $\vec{x}(s_0) = (x, x', \delta_0, \delta_{CSR}, k)^T$ and to evaluate the "CSR dispersion" (correlation between x and k). The matrix for a sector dipole is given by [110]:

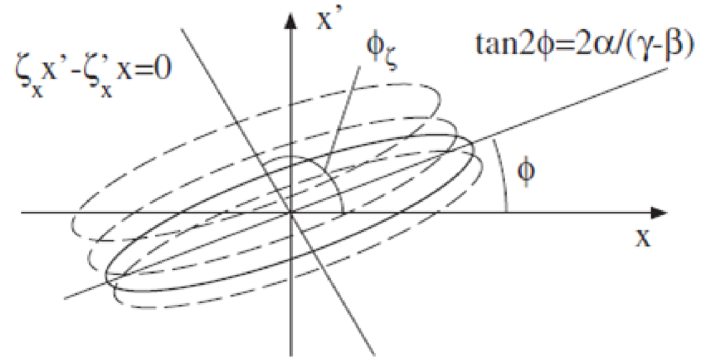

Figure 4.13: Two-dimensional phase space ellipse in horizontal plane, and displacement of beam slices due to the CSR kick. (α, β, γ) are Courant–Snyder parameters. Figure taken from [110].

.

$$R_{\text{bend}} = \begin{pmatrix} \cos\theta & \rho\sin\theta & \rho(1-\cos\theta) & \rho(1-\cos\theta) & \rho^2(1-\cos\theta) \\ -\frac{1}{\rho}\sin\theta & \cos\theta & \sin\theta & \sin\theta & \rho(1-\cos\theta) \\ 0 & 0 & 1 & 0 & 0 \\ 0 & 0 & 0 & 1 & \rho\theta \\ 0 & 0 & 0 & 0 & 1 \end{pmatrix}. \tag{4.22}$$

Writing similar transfer-matrices for a drift and a quadrupole, the motion of an electron can be tracked through the achromatic beam line. As mentioned in Chapter 2, the off-axis motion of an electron caused by the initial momentum error is expressed in terms of the momentum dispersion function η:

$$\left(\eta(s_1)\ \eta'(s_1)\ 1\ 0\ 0\right)^T = R_{s_0\to s_1}\left(\eta(s_0)\ \eta'(s_0)\ 1\ 0\ 0\right)^T. \tag{4.23}$$

In a similar manner, the CSR wake dispersion function (ξ, ξ') can be defined as :

$$\left(\xi(s_1)\ \xi'(s_1)\ 0\ L_b(s_1)\ 1\right)^T = R_{s_0\to s_1}\left(\xi(s_0)\ \xi'(s_0)\ 0\ L_b(s_0)\ 1\right)^T. \tag{4.24}$$

where $L_b(s_1)$ is the total bending path length for $0 < s < s_1$. The displacement of electron is given by $(k\xi, k\xi')$ in the (x, x') phase space. In an achromatic lattice, η and η' are zero at the exit, but the dispersion and its derivative due to CSR (ξ, ξ') are non-zero. This residual dispersion results in the growth of the projected emittance. Since the deviation of the trajectory of a electron due to CSR is expressed as $(k\xi, k\xi')$ in the first-order approximation, each slice of bunch aligns on the line given by $\xi x' - \xi' x = 0$ in the (x, x') phase space as shown in Fig. 4.13.

The method suggested here can be used to optimise an achromatic cell to minimise the CSR effect by adjusting the quadrupoles so that ξ and β have the same envelope after the cell. The CSR wake dispersion function is calculated using the transfer-matrices, giving the value of ϕ_ξ as shown in Fig. 4.13 and the Courant–Snyder parameters are optimised to match the angle ϕ equal to ϕ_ξ. The method described here assumes the conditions: all dipoles have the same bending radius, the electron bunch does not change its longitudinal profile, and the transient CSR effect at the entrance and exit of the magnet is not large.

The transfer matix method has been further extended for double-bend achromat in [112] together with optimisation of the phase advance to cancel the CSR kicks. The extension includes transfer-matrix analysis to achromats with dipoles of different radii and angles, based on a assumption that $\delta_{CSR} \propto \rho^{2/3}$, it includes the transfer-matrix for the quadrupole section between dipoles in terms of betatron phase advance and Courant–Snyder parameters and a point-kick model of the CSR effect in dipoles. These studies illustrate the equivalence between the optical balance used in Section 4.4.1 and the transfer-matrix analysis. The application of the transfer-matrix method described in this section is applied to TBA arc design in Chapter 5.

4.5 Summary

CSR in the beam spreader design has the potential to damage the quality of bunch in both the longitudinal and the transverse planes. In order to simulate the effect of CSR, several simulation codes have been extended or developed. The beam parameters and dipole configurations used in the beam spreader design satisfy the Derbenev criteria and thus 1D CSR model is considered for the studies undertaken in this thesis. Following convergence studies for different beam parameter and dipole settings for the studies presented in this thesis it seems appropriate to use number of macroparticles equal to 100,000, number of CSR kicks in each dipole equal to 100 and number of bins equal to 500 for simulations.

The comparison of change in energy offset due to CSR and the transverse projected emittance increase for steady state CSR and steady state with transients show that for short dipole lengths (as used in beam spreader), it is important to include transients in order not overestimate the emittance growth.

Due to the fundamental difference in effect of incoherent and coherent radiation on electron bunch properties, it is possible to arrange the beam line design to effectively cancel out the CSR emittance growth in the plane of bend. This needs a careful optics design maintaining similar bunch parameters at subsequent dipole locations in addition to betatron phase advance of π between a consecutive pair of dipoles. To what extent this cancellation works is explored further in Chapter 5.

Chapter 5

Beam Spreader Designs

5.1 Introduction

As described in Chapters 1 and 3, the electron beam driver for an X-ray FEL is based on a linear accelerator with layout along a straight line in order to maintain the high brightness of the beam from the photoinjector. The bending of the beam is restricted essentially to bunch compressors and in the case of a seeded FEL, a dogleg for incorporating the seeding laser. Unlike the third generation light sources, which deliver photon beams to a few tens of beam lines, X-ray FEL facilities are restricted to a few experiment beam lines. FELs of this kind serve one experiment at a time with the radiation pulse repetition rate set by the driver linac repetition (or pulse) rate. It is possible to split the FEL photon radiation to multiple experiments, but this has limitations from optics/mechanics and space constraints [113]. Another option is to use the spent beam to drive another FEL, but this is usually only possible for soft X-rays with less demanding beam quality requirements. X-ray FEL facilities are expensive and considering the high demand from users, more beam lines and user stations are both desirable and beneficial. As well as providing more capacity for users, switching electron bunches to different beam lines also allows for flexibility of the experimental set up and variation in photon properties.

The only way to provide multiple electron beam lines on an X-ray FEL is to direct the beam after the linac to several beam lines using a beam switchyard or a beam spreader. This means either dividing the linac pulses into different beam lines or switching all the pulses to a particular experiment for some period of time. However, in doing this, bending the electron beam is unavoidable and the quality of the electron beam (low emittance, low energy spread, high peak current) achieved through a careful design of the accelerator can be completely spoiled if the design of the spreader/switchyard is not chosen and optimised carefully.

In order to keep the deterioration of the beam properties to a minimum, the bending of the electron beam in a spreader needs to be done gradually. This, however, means that to get a practicable transverse offset between the beam lines, the longitudinal distance increases significantly as the beam energy increases. The longer beam line thus makes the overall facility footprint bigger, increasing the construction cost. The length of the accelerator part of the facility is mainly dictated by the choice of RF frequency and significant R&D is being pursued to achieve higher gradients to make the facility footprint more compact. Even though this helps to reduce the footprint of the acceleration part of the facility, one consequence is that the length of the spreader and the experimental halls become a dominating factor of the total cost.

In single shot, low repetition rate facilities, the easiest way to share electron bunches between different beam lines is to use beam spreaders based on DC dipoles (that need to be turned on/off depending on the path selected for the electron beam) and a combination of focusing and defocusing quadrupoles with a proper phase advance or a design based on isochronous arcs. For facilities with high repetition rates, it is possible to select the required number of bunches in each beam line by using an appropriate device (pulsed magnet, kicker magnet, RF deflector) to deflect the bunches to different beam lines. The spreader design should include the flexibility to add more beam lines at a later stage if desired. The choice of the spreader design is critical in the facility construction and can have significant implications for the overall facility footprint, and hence for the cost of the facility.

This chapter starts with a brief introduction and overview of X-ray FELs that are either already operating, under construction or have been proposed (for the UK) recently. Particular attention is given to the beam spreaders in the different facilities. The beam spreader design studies described in this thesis are carried out at two different energies; 2.2 GeV and 6.6 GeV. The 2.2 GeV was the design energy for UK's New Light Source project [37] and 6.6 GeV is within the likely energy range of a possible future UK X-ray FEL facility [114]. The concepts described in Chapter 4 to minimise the effects of CSR are used for these designs. Experimental studies carried out on the ALICE arcs are presented in Chapter 6. On the basis of the results from the ALICE studies, as well as studies carried out for NLS, generic diagnostics requirements are proposed for the spreader designs described here.

5.2 Survey of Beam Spreader Designs

A small number of X-ray FEL facilities have come into operation over the past decade, but there are several more which will be in operation in next few years. Table 5.1 summarises the facilities which are already operating or under construction around the world, with key machine parameters and year of first operation. Table 5.2 summarises details of beam spreader designs for these facilities. The facilities proposed or under consideration in the UK during the duration of this thesis are also listed. In addition to the operating facilities and the facilities presently under construction, several projects have been proposed worldwide for which in-depth studies have been carried out leading to conceptual or detailed technical design reports. However, due to the high construction as well as operational costs of these facilities, many proposals do not transition to real projects. It is worth noting that the technological developments achieved for high energy particle physics projects (such as the linear collider projects like TESLA [115], JLC [116], NLC [117] and ILC [80]) have been crucial for the success of the existing high energy X-ray FELs such as LCLS, SACLA and FLASH (leading to European X-FEL).

As regards developments in the UK over the past decade, there have been two detailed studies for medium energy FELs: 4GLS based on the energy recovery principle [118] and NLS based on a single pass linac (with a re-circulation option studied for comparison) [37]. Both of these projects were developed to the conceptual level but did not transition to construction. The recent strategic FEL review published by the Science and Technology Facilities Council [114] outlines the need for an X-ray FEL in the UK. Even though the parameters of UK X-FEL are not yet decided, the report mentions the need for hard X-rays and high repetition rate. For the purpose of the comparison of spreader designs presented in this thesis, it is assumed that the UK X-FEL beam energy will be three times higher than the energy that was proposed for NLS.

5.2.1 Linac Coherent Light Source - LCLS-I and LCLS-II

The Linac Coherent Light Source (LCLS) [66] at SLAC National Accelerator Laboratory in the USA was the world's first X-ray FEL. The idea of building such a facility was initiated in 1992 and first experiments using this FEL took place in 2009.

The accelerator schematic is shown in Fig. 5.1. LCLS-I is comprised of a high brightness S-band photoinjector, booster linac, laser heater, a dogleg bringing the beam from injector into the main linac (last third of the old SLAC S-band linac which accelerates the beam to 14 GeV) and dedicated beam diagnostics sections. Two bunch compressors located at 250 MeV and 4.3 GeV reduce the bunch length. An X-band RF structure is used for linearisation. The high energy beam from the linac is transported through a second dogleg to a 121 m long undulator section. The design of the dogleg needs to satisfy a number of requirements: incorporating diagnostics for beam energy, energy spread and emittance measurements, maintaining an achromatic and isochronous beam transport as well as flexibility in the matching optics to the undulator beam line at different beam energies. After exiting the undulator, the electron beam is deflected onto a beam dump, while the photon beam enters the experimental areas, and feeds into seven experimental beam lines (not shown in the schematic).

Many challenges of high energy single pass linacs were addressed for the first time at LCLS-I, including saturation of optical screens due to coherent synchrotron radiation [119], operation of a laser heater for control of the energy spread and suppression of instabilities [77], beam based alignment to achieve micron level orbit tolerances in the undulator sections [120], self-seeding using a crystal in the soft X-ray regime [121], and

Table 5.1: Operational and under construction X-ray FEL facilities. Proposed or under consideration facilities in the UK during the period of this thesis are also included. NC: normal conducting, SC: Superconducting. See Appendix B for details of RF frequencies.

Facility (Year of first operation)	Shortest wavelength (nm)	Max beam energy (GeV)	Max RF Repetition rate (Hz)	FEL Pulses/ RF pulse	Max Bunch charge (nC)	Facility Length (km)	RF Frequency & Technology
LCLS-I (2009)	0.15	13.6	120	1	0.25	1.7	S-band, NC
SACLA (2011)	0.1	8	60	1	0.2	0.8	C-band, NC
FERMI (2010)	4	1.5	50	1	0.5	0.5	S-band, NC
FLASH (2005) & FLASH II (2016)	4	1.2	10	2700	1	0.32	L-band, SC
European X-FEL (2017)	0.05	17.5	10	2700	1	3.4	L-band, SC
LCLS-II (2017)	0.25	4	10^6	CW	1	0.32	L-band, SC
SwissFEL (2017)	0.1	5.8	100	2	0.2	0.7	S,C-band, NC
SINAP SXFEL (2017)	9	0.84	10	1	0.5	0.6	S-band, NC
PAL XFEL (2017)	0.1	10	60	1/2	0.2	1	S-band, NC
NLS	1.24	2.2	$10^3 - 10^6$	CW	0.2	0.7	L-band, SC
Future UK X-FEL	TBD	TBD	TBD	TBD	TBD	TBD	TBD, TBD

use of bunch slice measurements post-undulator for tuning the FEL [88], to name just a few.

The LCLS-II [123] project under construction at SLAC is a high repetition rate, high average brightness FEL based on LCLS-I and existing facilities at SLAC. A schematic of LCLS-II is shown in Fig. 5.2 and schematic showing both LCLS-I and LCLS-II is shown in Fig. 5.3. The facility includes a new high repetition rate (MHz) injector [124] and a continuous wave (CW) superconducting 4 GeV linac. Two bunch compressor chicanes are used to compress the electron bunches. The electron bunches are transported through the existing 2 km long bypass line to the beam switchyard, where a new 3-way spreader system will be installed. This will provide the flexibility to deflect the beam bunch-by-bunch

Table 5.2: Beam spreader details for FEL facilities described in Table 5.1.

Facility	Switchyard design based on	Number of beam lines	Comments
LCLS-I and LCLS-II	Kickers or RF deflectors	2	Complex combinations of beams from S and L-band entering same FEL beam lines.
European X-FEL	Kicker and septum	2+1 dump line + provision for one additional beam line	Selection of required bunch patterns to each beam line, unwanted bunches send to beam dump.
SACLA	Kicker and septum	3	Plan to upgrade to 5.
SwissFEL	Kicker and septum	2	Two bunches in one RF pulse, one being transported to each beam line.
SINAP SXFEL	-	1	-
PAL XFEL	Kicker	2	Simultaneous or independent operation of soft X-ray FEL beam line.
FERMI	DC dipole	2	
FLASH	Kicker and septum	2	Separate bunch train to FLASH and FLASH II.
NLS	Kicker and septum	3	Possibility to add more beam lines.
UK FEL	TBD	TBD	TBD

into either a soft X-ray undulator (SXU) or hard X-ray undulator (HXU), or towards a beam dump. New SXU and HXU variable gap undulators will be installed in the existing experimental hall. The LCLS-I beam will also be delivered to the HXU undulator. Options based on either magnetic kickers [125] or RF deflecting cavities [126] are being considered for the 3-way beam spreader as shown in Fig. 5.4.

5.2.2 FERMI at Elettra

FERMI [129] is a single-pass linac-based seeded FEL at the Elettra Laboratory in Italy. The facility was proposed in 2002 and first FEL light was obtained in 2010. A general layout is shown in Fig. 5.5. The accelerator and FEL complex comprises a photoinjector and two short linac sections generating a bright electron beam of ~100 MeV, the main linear accelerator in which the beam is compressed using two bunch compressors and accelerated up to ~1.5 GeV and the beam spreader to transport the beam to the undulators. The beam spreader design (Fig. 5.6) is based on DC dipole magnets arranged at phase advance of π between the consecutive pairs of dipoles as described in Chapter 4.

The FERMI facility includes two separate coherent radiation sources, FEL-1 and

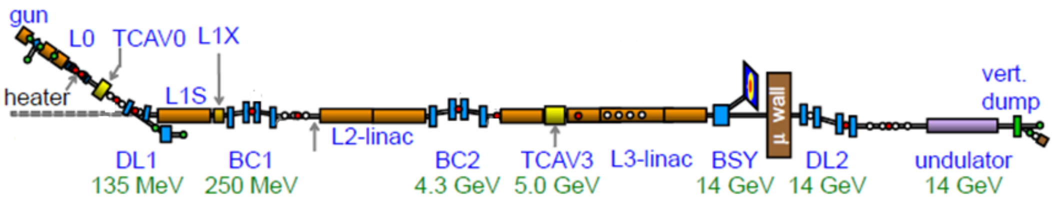

Figure 5.1: Schematic of LCLS-I facility at SLAC National Accelerator Laboratory. Figure taken from [122].

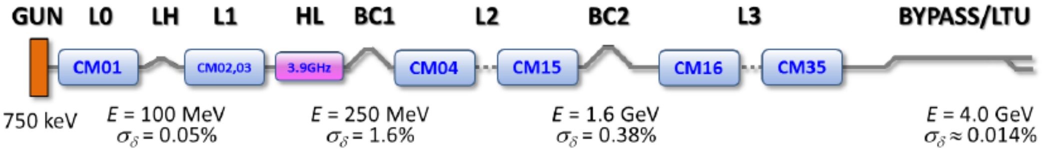

Figure 5.2: Schematic of LCLS-II facility at SLAC National Accelerator Laboratory. Figure taken from [125].

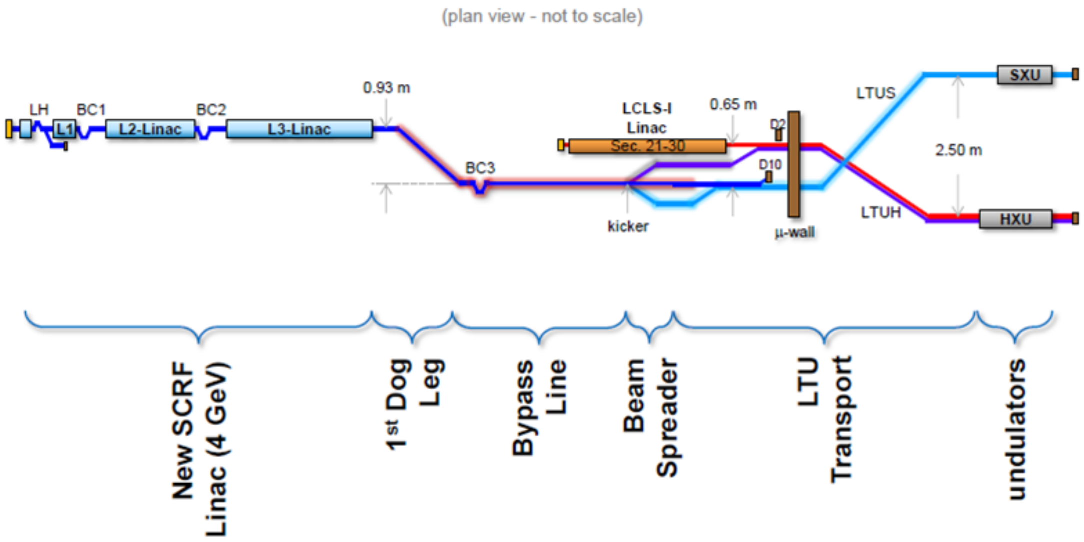

Figure 5.3: Schematic of LCLS-I and LCLS-II at SLAC. Figure taken from [127].

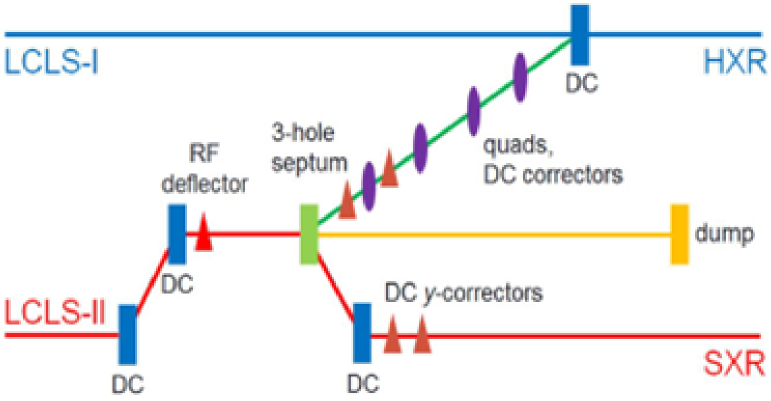

Figure 5.4: Schematic of proposed three way spreader for LCLS-II. Figure taken from [126].

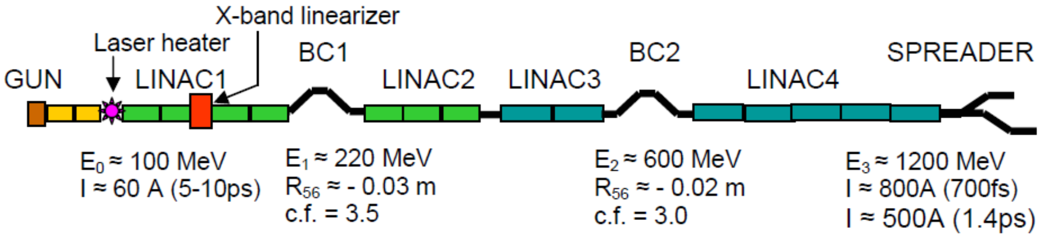

Figure 5.5: Schematic of FERMI at Elettra. Figure taken from [48].

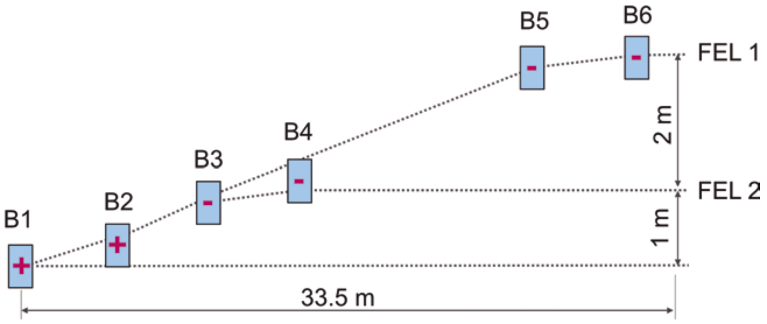

Figure 5.6: Schematic of the beam spreader at FERMI at ELETTRA. Figure taken from [128].

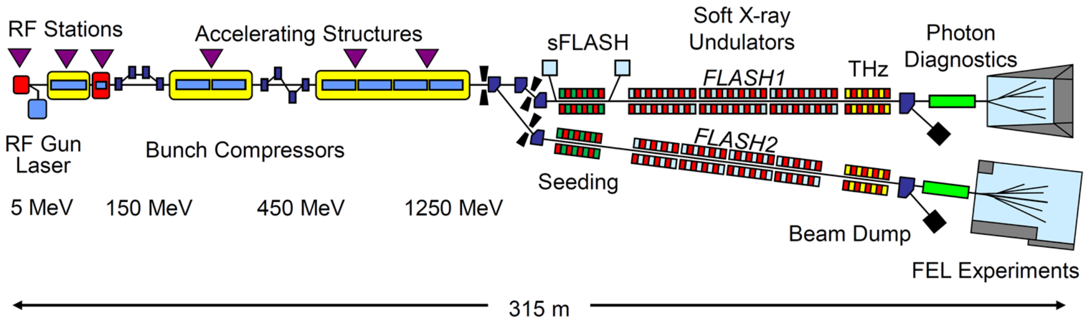

Figure 5.7: Schematic of FLASH facility at DESY. Figure taken from [22].

FEL-2, that are being brought online sequentially. FEL-1 operates in the wavelength range between 20 and 100 nm, while the FEL-2, operates at shorter wavelengths between 4 to 20 nm.

5.2.3 FLASH Facility at DESY

FLASH (Free Electron Laser in Hamburg) [22], was the world's first FEL designed and constructed for operation in the extended ultraviolet and soft X-ray spectral range (XUV). The facility is located at the Deutsches Elektronen-Synchrotron (DESY) laboratory in Hamburg, Germany. FLASH has also served as a pilot facility for the European X-FEL which has been under construction in Hamburg since 2009 and is based on the same accelerator technology.

A schematic of the FLASH facility is shown in Fig. 5.7. The electron bunches are produced in an L-band photoinjector and accelerated by a superconducting linear accelerator. The electron bunches are longitudinally compressed at energies of 150 MeV and 450 MeV. The beam is then accelerated to $\sim$1.25 GeV, passing through a collimation section to remove unwanted beam halo. The undulator section is approximately 27 m long and consists of permanent magnets.

Since 2012, a major upgrade has been undertaken at FLASH, with the construction of a second undulator tunnel and a new experimental hall with the aim of doubling the capacity for experiments. A fast kicker is installed immediately after the last superconducting accelerator module, enabling distribution of the accelerated and compressed electron beam to both of the FEL undulator lines, i.e. FLASH1 (first beam line) and FLASH2 (new). FLASH2 covers essentially the same spectral range as FLASH1; however, its variable-gap undulator enables two experiments to take data at two distinct wavelengths quasi-simultaneously. In addition to the SASE mode used in FLASH1, seeding options are considered for FLASH2 to improve beam quality.

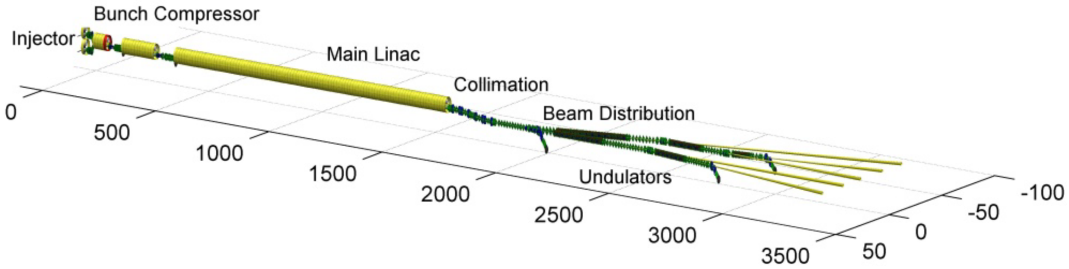

Figure 5.8: Schematic of European X-FEL at DESY. Figure taken from [130].

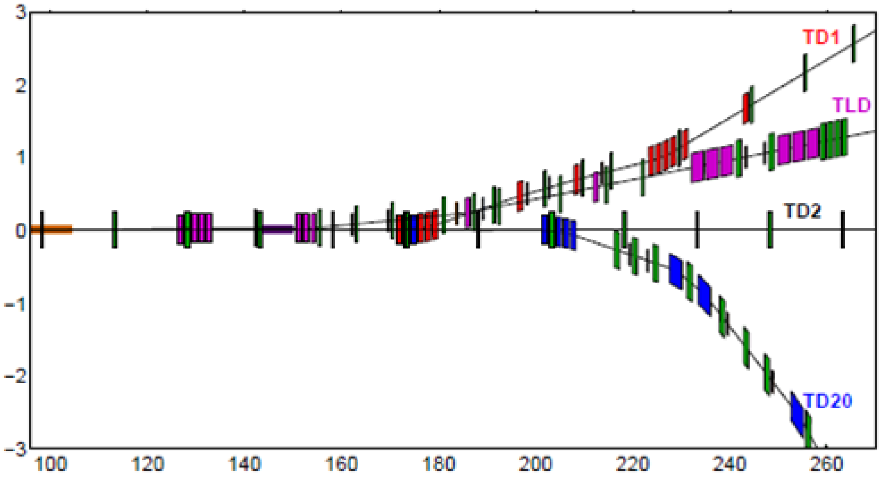

Figure 5.9: Top view of the beam separation area for European X-FEL spreader. Red, magenta and blue colours mark septa and dipoles of beam lines TD1, TLD (dump line) and TD2. Horizontal and vertical distances are in meters. Figure taken from [131].

5.2.4 European X-FEL

The European X-FEL [82] under construction at DESY in Germany will be world's first hard X-ray FEL based on superconducting RF. A schematic of the facility is shown in Fig. 5.8. The European X-FEL will generate 27000 photon pulses per second (unlike the 100 photon pulses per second at similar energy machines), which offers a significant advantage for photon users. The superconducting driver linac of the FEL can deliver electron bunch trains up to 600 μs long with a repetition rate of 10 Hz and a maximum energy of 17.5 GeV. Civil construction of the facility started in early 2009 and the user operation is planned to start in 2017.

The accelerator is based on the superconducting TESLA technology, which has been developed by DESY and its international partners within the TESLA Technology Collaboration. Since 2005, DESY has been operating the free-electron laser FLASH (Section 5.2.3), which is a prototype of the European X-FEL.

The facility has been planned as a multiuser facility with the possibility to distribute electron bunches of one bunch train to either of the two photon beam lines (a third beam

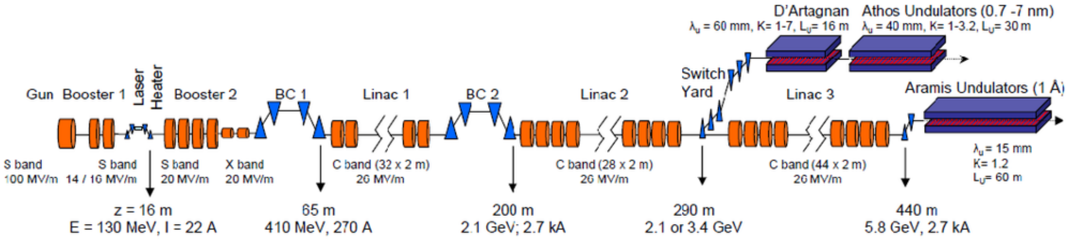

Figure 5.10: Schematic of SwissFEL at PSI. Figure taken from [81].

line 'TD20' is planned to be added later), each with its own set of undulators. This is achieved by means of a combination of slow and fast switching magnets [131, 132, 133], which allows generation of different bunch patterns as required by different experiments. A fast kicker selects the bunches from the trains to be kicked into the respective beam line and a slow kicker (which is ramped while fast kicker is operating) removes the unwanted bunches towards the beam dump. The dump beam line also serves as a commissioning beam line. This scheme allows the operation of the upstream accelerator at a constant bunch frequency and thus increases the stability of the overall system.

The beam spreader is located after the beam collimation and trajectory feedback systems. It uses a scheme of kickers and a Lambertson septum with a geometry that generates dispersion in both horizontal and vertical planes. The layout of the separation area is shown in Fig. 5.9. The extraction magnets are integrated into the FODO lattice with 90° phase advance between the cells, which provides optimum positions for the kicker and septum. The extraction beam dump line TLD lies between two beam lines TD1 and TD2 and is in the vertical plane to allow more space between TD1 and TD2. The optics designs of the separation areas of the beam lines need to satisfy a number of constraints such as the suppression of dispersion in both horizontal and vertical planes, suitable Courant–Snyder parameters to match to the downstream design, correction of chromatic terms and physical separation of components in adjacent beam lines. Though the beam quality in the beam dump line is not an issue, the optics in two undulator beam lines need to provide a large energy acceptance (up to $\pm 1.5\%$ from the nominal energy) without any noticeable deterioration in transverse or longitudinal bunch properties. The design uses sextupoles and octupoles to correct for higher order chromatic terms [134, 135].

5.2.5 SwissFEL at PSI

The SwissFEL facility [81] was officially approved in 2012 to be constructed at the Paul Scherrer Institute in Switzerland. The facility is based on S-band and C-band normal conducting RF accelerating structures providing a maximum electron beam energy of

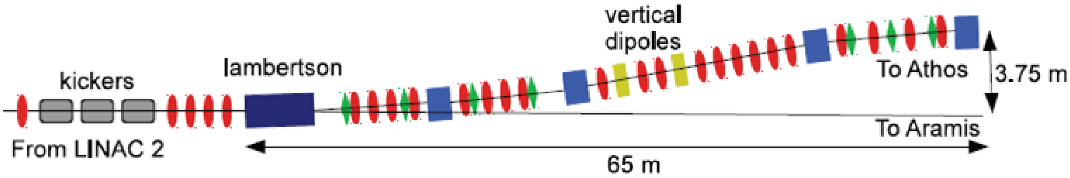

Figure 5.11: Schematic layout of SwissFEL Athos Switchyard. Horizontal dipoles and Lambertson magnet are shown in blue, vertical dipoles are shown in yellow, quadrupoles are shown in red and sextupoles in green. Figure taken from [136].

5.8 GeV. The FEL will cover a photon wavelength from 0.1 nm to 0.7 nm on a hard X-ray beam line ("Aramis") with three experimental stations. The commissioning of the facility started in 2016 and user operation is planned for 2017. Phase 2 of the project will deliver a soft X-ray beam line ("Athos") covering a photon wavelength from 0.7 nm to 7 nm and is expected to deliver photon beam in 2020. Figure 5.10 shows a schematic of the facility.

The facility is designed to work in double bunch mode with a bunch time separation of 50 ns and a repetition rate of 100 Hz. In order to provide electrons to the soft X-ray beam line, a beam spreader located at an energy of $\sim$ 3 GeV will direct it to the Athos beam line. A set of 3 fast resonant kickers [137] followed by a Lambertson septum will divert the second of the two bunches from the linac [136]. This second bunch will then be further transported through the spreader while the first bunch continues straight towards the Aramis beam line. In order to allow some flexibility for different configurations, the beam spreader design allows variation of R_{56} over a range of values.

The beam spreader [136, 138] shown in Fig. 5.11 has a total length of 65 m and the separation between the beam lines is 3.75 m. The incoming beam is co-linear with the Aramis beam line. The spreader includes one Triple Bend Achromat (TBA) section and one Double Bend Achromat (DBA) section. The TBA section allows adjustment of R_{56} by varying the dispersion in the central dipole. The kicker deflects the beam in the vertical direction. A set of two vertical dipoles and four quadrupoles after the TBA bring the beam back to the horizontal plane. The optics are designed to make the system achromatic in the vertical plane. Five quadrupoles located after this section are used to change the phase advance between the TBA section and the DBA section. This choice of optics design minimises the kicks due to CSR. The DBA section also accommodates the energy collimators. The beam line includes a number of sextupoles for correcting the chromatic terms.

5.2.6 SPring-8 Angstrom Compact free electron LAser (SACLA)

The SPring-8 Angstrom Compact free electron LAser (SACLA) is located adjacent to the SPring-8 synchrotron source and was the first X-ray FEL to be built in Japan. The Spring-8 Compact SASE Source (SCSS) project was started in 2001 [139] in order to

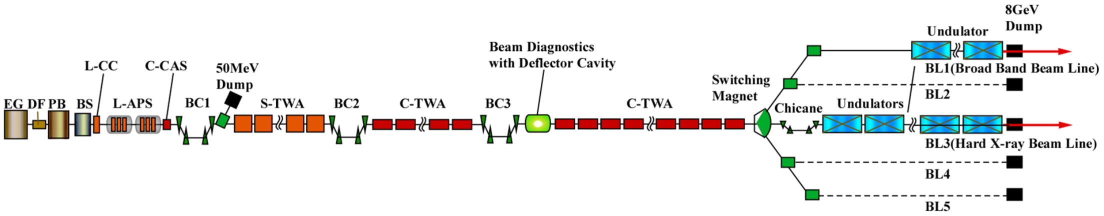

Figure 5.12: Schematic of SACLA. Figure taken from [140].

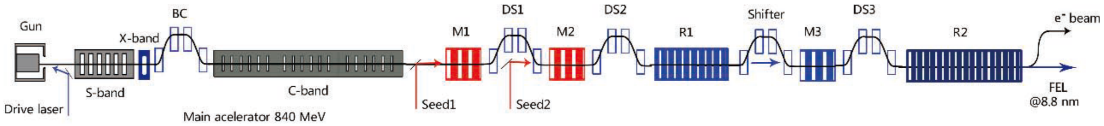

Figure 5.13: Schematic of SINAP SXFEL at Shanghai. Figure taken from [141].

develop the technology for an X-ray SASE-FEL. Construction of SACLA was funded in 2006 and the first FEL light was obtained in 2011.

SACLA uses short period (18 mm compared to 30 mm at LCLS-I) in-vacuum undulators. This reduces the electron beam requirement to 8 GeV to obtain 0.1 nm photon wavelength compared to other projects (14 GeV in LCLS and 17.5 GeV in European X-FEL). SACLA is the first X-ray FEL to use a normal conducting accelerating system at C-band, which allows an accelerating gradient as high as 35 MV/m to be achieved. These unique features allow lasing at a relatively short distance of 0.7 km, compared to other similar X-FELs such as LCLS (2 km) or the European X-FEL (3.4 km).

Another unique feature of the machine is the use of a thermionic injector instead of a photoinjector as used in other X-FEL facilities. The accelerator schematic is shown in Fig. 5.12. A beam spreader located at the end of the accelerator deflects the electron beam horizontally in three directions using a kicker magnet and a DC twin septum magnet [140]. BL3 is the undulator beam line in the centre, where the beam travels straight (without deflection) from the accelerator. BL2 is the second undulator, where the kicker and septum magnets first deflect the beam horizontally by +3°, and then a DC dipole bends the beam back by -3° to make it parallel to the BL3 undulator line. Two small dipoles placed in between the dogleg cancel the R_{56}. As reported in [140], the operation of BL2 has been demonstrated recently. The CSR effects in the dogleg are currently limiting the peak current. To cancel out the CSR effects, it is planned to re-arrange the beam optics, to replace the existing layout with four identical dipoles bending the beam by 1.5° with horizontal phase advance of π between two pairs.

5.2.7 Shanghai X-FEL

The Shanghai X-ray FEL (SXFEL) test facility has been constructed in preparation for a hard X-ray FEL in China [141]. The SXFEL project is under construction at the Shanghai Synchrotron Radiation Facility campus. The test facility is based on an 840 MeV electron

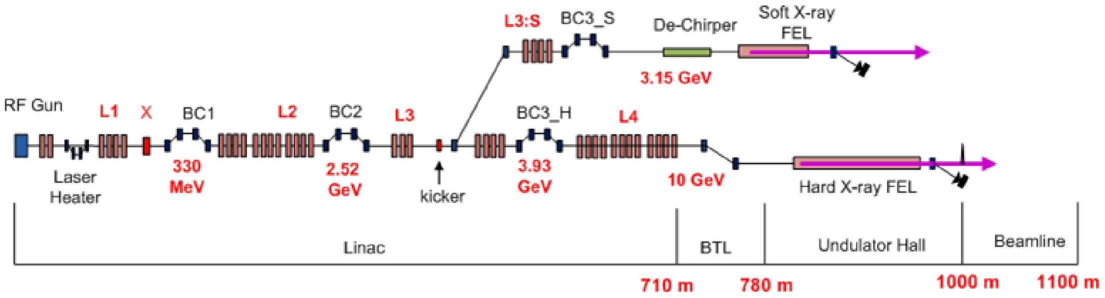

Figure 5.14: Schematic of PAL X-FEL in Korea. Figure taken from [142].

linac and generates 8.8 nm FEL radiation using seeded schemes. The project was approved in 2011 and the installation was due to be completed by the end of 2016. There is the potential to upgrade the beam energy to 1.6 GeV by adding more C-band RF accelerating structures. The layout of the facility is shown in Fig. 5.13.

5.2.8 PAL X-FEL

The Pohang Accelerator Laboratory X-ray Free Electron Laser (PAL-XFEL) in Korea began construction in 2011. The facility is planned to open for users in 2017 with soft X-ray FEL radiation in the range of 1 to 4.5 nm using a 3.15 GeV electron beam. A shorter wavelength range from 0.1 to 0.6 nm will be covered with the hard X-ray undulator beam line at an electron energy of 10 GeV. The layout of the facility is shown in Fig. 5.14. The facility uses S-band accelerating technology and the bunches are compressed using three bunch compressors.

A switch line for the soft X-ray FEL is located at $\sim$3 GeV point with a kicker and a Lambertson type septum. The switch line consists of two double bend achromats with a bend angle of each dipole equal to 3°. The beam line for soft X-rays has its own bunch compressor (BC3-S). A de-chirper system (consisting of a corrugated pipe) is installed to reduce the correlated energy spread to within the limit required for a soft X-ray FEL.

5.2.9 New Light Source (NLS) Project in the UK

The UK's New Light Source project started in April 2008 to explore the prospects for a UK FEL facility with unique capabilities. The first phase of the project undertook a broad-based consultation on the science drivers. The results of this consultation were reported [143] in October 2008. The second phase of the project led to the production of a conceptual design for the proposed facility, which was completed in May 2010 [37]. The project was highly rated scientifically. However, due to financial constraints the project was put on hold.

The schematic layout of NLS is shown in Fig. 5.15. It was proposed to achieve the baseline specification for the facility by providing three FEL beam lines covering a wavelength range from 0.124 nm to 24.8 nm. To provide the required tunability, an

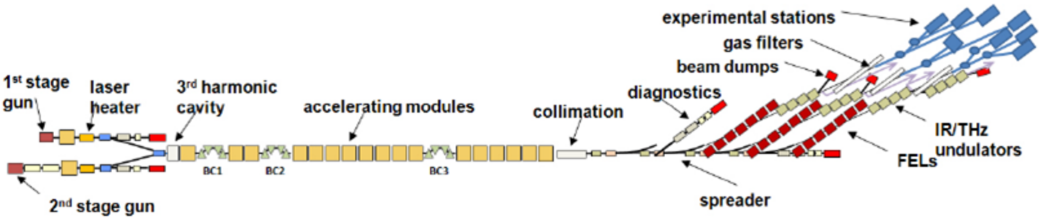

Figure 5.15: Schematic of NLS. Figure taken from [37].

electron beam energy of 2.2 GeV with variable gap undulators was chosen. The repetition rate of the facility was set to 1 kHz initially, increasing up to 1 MHz subsequently. This drove the choice for superconducting technology for the accelerating structures operating in CW mode.

For the first stage of operation, it was planned to use an injector based on a modified version of the DESY FLASH/XFEL gun. Several options such as a very high frequency gun and superconducting gun were considered for the second stage injector. The injector consisting of photoinjector and a short linac raised the beam energy to 135 MeV. A laser heater was included to introduce the required energy spread to mitigate microbunching instability before transporting the electron beam through a merger section. The merger section was designed to integrate the beam from both injectors and also to provide diagnostics for characterisation of the electron beam. A third order harmonic cavity was included for the linearisation of longitudinal phase space before compressing the bunch. Three bunch compressors were to be located at 205 MeV, 460 MeV and 1.5 GeV along the 2.2 GeV superconducting linac. A dedicated beam collimation section was proposed at the exit of the linac before the electron beam enters the beam spreader.

The beam spreader design was adapted from that of NGLS [144] and was based on a kicker magnet located in a FODO lattice, followed by a septum. This kicker-septum pair formed the first bend in the first Triple Bend Achromat. To provide enough transverse separation between the beam lines the first TBA was followed by another TBA. Both these TBA sections were designed to be achromatic and isochronous. Four such beam lines were planned to be included after the collimation section on a matched straight line incorporating a FODO lattice. A take-off section where the beam was deflected to a separate beam line consisted of a kicker-septum pair inserted in the FODO lattice.

One of these four beam lines was proposed to be used for characterising the beam entering the FEL beam lines. Three FEL beam lines were planned to incorporate different undulator configurations. After passing through the FEL lines the electron beam was deflected and transported to the high power (450 kW at 1 MHz repetition rate) beam dump. A straight on (non-deflected) diagnostics beam line was planned for commissioning and characterisation. The layout thus had a clear path for future upgrades to include additional beam lines. The design of the spreader, as it was presented in the conceptual design report and the subsequent design improvements studied as part of the studies undertaken here are described in detail later in this chapter.

5.3 Beam Spreader Design Considerations

In order to arrive at the optimum beam spreader design the following points need to be considered:

- Layout constraints due to existing infrastructure, components etc: the design of the facility to fit into existing infrastructure (e.g. LCLS in existing tunnel) and components may limit the choices available for the facility footprint.

- Number of the electron beam lines post spreader and upgrade path: the design choices made for the beam spreader will essentially dictate the flexibility in the FEL beam lines. Future options to include beam lines without affecting the existing footprint are important to consider.

- Flexibility of changing undulator configuration in beam lines post spreading: if there are different beam dynamics requirements in the FEL beam lines, such as variability of FEL configuration with different bunch parameters (variability of R_{56}, chirp, peak bunch current etc.), the optics design of the spreader needs to accommodate this.

- Repetition rate of the upstream accelerator and time separation between the bunches including flexibility of changing the bunch structure at the photoinjector: the choice of technology to switch bunches to different beam lines is decided by the repetition rate and bunch time structure generated at the photoinjector.

- Stability and jitter tolerances: switching the required bunches to a particular beam line needs precise timing to trigger the kicker, septum and other pulsed magnets. The temporal properties of these devices decide the stability of the beam in the beam line in addition to jitter (random noise) from these devices.

- Beam parameters: the design should be “transparent" in the sense that it should minimise the deterioration of bunch parameters such as peak bunch current (thus bunch length), transverse (projected and slice) emittances and energy spread and should provide dispersion free beam optics matching to the undulator sections.

- Combining additional requirements such as energy and transverse collimation and diagnostics in each beam line: the dispersive regions in the beam spreader may provide suitable locations for energy collimation, and non–dispersive regions with correct phase advances can be used for collimation in the transverse planes.

Table 5.3: Possible options for beam spreader designs, adapted from [145].

Method	Pros	Cons	Comment
DC magnet	Easy	Only one beam line at a time	Useful for commissioning and studies etc.
Pulsed magnets	Stable and not so hard	Reduces duty factor	Hard for many beam lines.
High-Q resonant kicker at $f_{bunch}/2$	Conventional, stable and safe	Same structure for beams unless change at source	Suitable for multi-user operation.
High-Q RF deflector and optical delay at gun	Stable and flexible regarding time structures	More than 2 beam lines complicated	$>$ 2 beam lines possible?
Fast, high repetition rate kicker	Allows arbitrary pattern to be picked out	Challenging with stability & safety issues	Ideal solution for optimum flexibility.

- Ruggedness of technical solutions: the technical solutions chosen for switching the beam should provide fail-safe operation serving precise number of bunches as required by the experiments.

- Implications for the construction and the operating costs: the design choices made for the beam spreader can have significant impact on the facility footprint driving both the construction and the operating cost.

5.3.1 Options for Beam Switching

The first important decision in the choice of beam spreader design is the technique used to switch/divert electron bunches to different beam lines. This is very closely related with the available repetition rate of the facility. Table 5.3 (adapted from [145]) summarises the options available with their pros and cons. Some details of each of these options are discussed below:

- DC magnet: a DC dipole magnet placed at the entrance of the beam spreader switches the beam to the required beam line. Being a DC magnet, it is possible to switch the beam for any required length of time to a particular beam line. This is suitable typically in a low repetition rate machine when all the pulses can be sent to a particular beam line. Even though it can also be used for high repetition facilities, it does not offer particularly effective use of the facility. The time required for the DC magnet to turn on is typically of the order of few msec and the beam can be switched off at the injector while the dipole is being fully powered. In high energy machines, switching off one dipole and turning on another should provide only negligible kick due to the remnant field in the dipole but at medium energies, it will be necessary to de-gauss the dipole.

- Pulsed magnets: a pulsed dipole magnet can be switched on and off at a certain rate and thus makes it possible to divert the beam to a particular beam line. The pulsed magnets provide a stable solution and are not hard to build. The rate of changing makes this option useful for few beam lines and it needs to be weighed against an easy solution using a DC dipole as described above.

- High Q resonant kicker at $f_{bunch}/2$ frequency: The high Q resonant kicker [146] divides the bunch structure symmetrically (unless there is a change at the source) as shown in Fig. 5.16. This provides high stability, reliable and fast bunch separation.

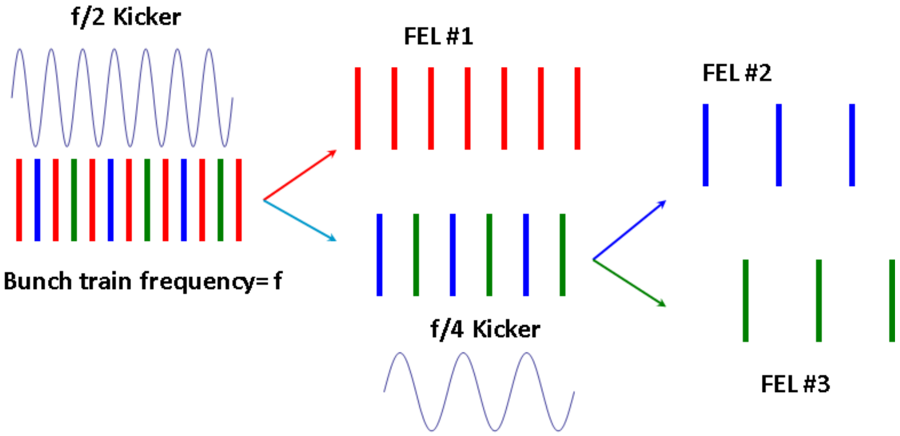

Figure 5.16: Beam distribution based on resonant kicker at half of RF frequency. Figure adapted from [145].

- High-Q RF deflector and optical delay at gun: A transverse deflecting RF cavity operates in a mode where the center of the bunch experiences a finite integrated transverse Lorentz force. Cavities operating in this mode were originally proposed at SLAC [147] and at the Jefferson Laboratory [148] as tools for beam separation and bunch length diagnostics. The use of transverse RF deflectors in a beam spreader allows distributing electron bunches with on-demand repetition rates in each beam line (Fig.5.17) with repetition rates well above the few hundred kHz limit from fast kickers. The steady state nature of the transverse fields provides higher deflection stability and shot-to-shot reproducibility as compared to those achievable with fast kickers where deflecting pulses are created at every bunch passage [149]. Incorporating a delay line for the photoinjector laser system allows customised filling patterns [150].

- Fast, high repetition rate kicker: A fast kicker allows to divert individual bunches (or a selected number of bunches in a bunch train) to different beam lines (Fig.5.18). The fast kicker consists of a fast, high power pulser and stripline electrodes [151].

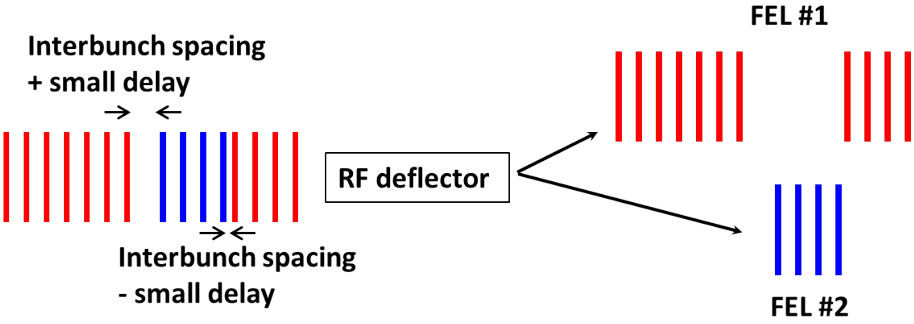

Figure 5.17: Beam distribution based on high-Q RF deflector and optical delay at gun. Figure adapted from [145].

The required rise and fall time depends upon the separation between the bunches as well as the macropulses. For example, for European X-FEL the separation between the bunches is 100 ns and thus the fast kicker needs to have a rise/fall time less than this spacing, whereas a CW machine with 1 MHz repetition rate has bunch separation of 1 μs. The stability of the kicker needs to be very high as it directly impacts the stability of bunches provided to a specific beam line. The most challenging rise and fall time (~ 1 ns) kicker has been developed for the International Linear Collider damping rings [151].

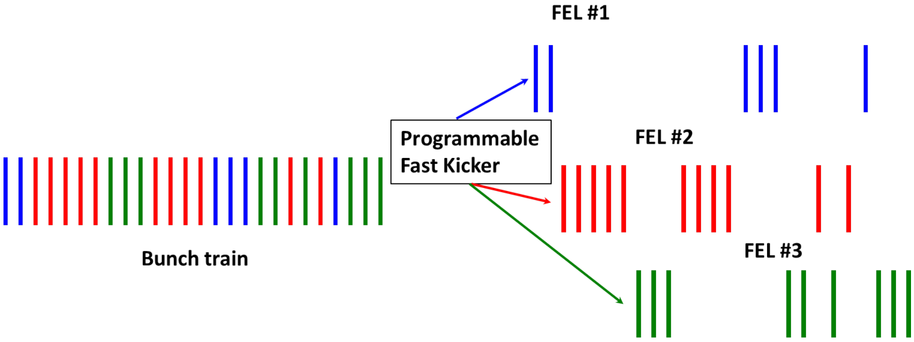

Figure 5.18: Beam distribution based on high repetition rate kicker. Figure adapted from [145].

Kicker and Septum

As shown in Table 5.2, a combination of kicker and septum is generally used in beam spreader designs. Both kicker and septum magnets provide a dipole kick to the beam. Kicker magnets provide fast rise and fall times but are restricted to relatively weak fields. Thus the kickers provide possibility of time selection allowing to choose the number of bunches to be kicked into a specific beam line. The septum on the other hand provides slower rise and fall times, but a stronger magnetic field than kicker magnets. A septum used in an accelerator provides a partition which separates two field regions; the region with homogeneous field provides a transverse space separation from the diverted and non-diverted beams [152].

The main sub-systems of a kicker system consist of a pulse forming network, kicker magnet, fast, high power switches, resonant charging power supply, coaxial cables and terminators. Each one of these has complex design issues to address for achieving the challenging requirements of fast rise times required for beam spreaders with MHz repetition rates.

The main difference between a dipole magnet and a magnetic septum is that the magnetic septum has a homogeneous magnetic field and a zero (or negligible) field region, separated by a relatively thin septum, whereas a dipole magnet has only a homogeneous field region. This often leads to having a high current density in the septum conductor and associated cooling problems. The septum can be DC, pulsed or Lambertson type (where magnetic material is used to separate the field free region instead of an electric current as is the case in a DC or pulsed septum).

5.3.2 Lattice Design Options

The beam spreader lattice design options need to satisfy the list of criteria discussed in the introduction of Section 5.3. The two important aspects of the design are the choice of the take-off region and the lattice to transport the beam to different beam lines. Two design concepts, one based on Triple Bend Achromat (TBA) arcs and another one based on Double Bend Achromat (DBA) (obtained by incorporating dipoles magnets in FODO lattice at phase advance of π) are well suited as discussed in Section 4.4.2. The TBA provides achromatic and isochronous solution whereas the DBA one is achromatic but not isochronous. In principle, both these designs can have take-off sections based on kicker/ septum magnets or deflecting cavities or DC dipole magnets. The studies presented in this thesis propose and compare the layouts of beam spreaders based on these different concepts and highlight the differences where appropriate. The beam energies used are 2.2 GeV (as in NLS studies) and three times this energy at 6.6 GeV (based on the assumption that UK X-ray FEL energy will be in the energy range of $6 - 7$ GeV). However, the proposed designs could in principle be scaled to any other energy.

The studies of the beam spreader design at both these energies assume similar bunch parameters (taking into account their energy dependence) to make the comparisons as fair as possible. Since every facility uses a different set of bunch parameters, the advances made at several facilities to reach the minimum projected transverse emittance values have been reviewed as shown in Table 5.4. On the basis of this review, a single set of parameters have been chosen for the beam spreader designs. A bunch charge of 200 pC was chosen as it provides the required peak current (following compression) with acceptable impact from the collective effects. A challenging value of normalised projected emittance of 0.3 mm.mrad in the transverse planes has been chosen as this will maximise

Table 5.4: Bunch parameters at undulators at some X-ray FEL facilities

Facility	Bunch charge (pC)	Projected normalised emittance (mm.mrad)	Bunch length (rms) (μm)	Comment
LCLS-I	20 - 250	0.3 - 1.0	1 - 20	Measured slice emittance of 0.4 mm.mrad at 250 pC at LCLS injector.
LCLS-II	10 - 300	0.2 - 0.7	0.6 - 52.0	
SwissFEL	10 - 200	0.25 - 0.65	1.8 - 9.0	Measured projected emittance of 0.3 mm.mrad at 200 pC at the test facility.
NLS	200	<1.0	23	Bunch length FWHM
European X-FEL	1000	1.4	24	Measurements at PITZ injector facility demonstrated 0.6 mm.mrad at 1 nC.
FERMI @Elettra	800 - 1000	<1.5	210 - 420	Bunch length FWHM.

the deterioration due to CSR which is being analysed in a beam spreader design. A Gaussian longitudinal bunch distribution with a rms bunch length of 25 μm (83 fs) has been chosen as this is a moderate number to compare the effects of CSR. However, it is useful to have a flat-top longitudinal distribution (to minimise the impact of space charge at lower energies) to achieve the required low emittance values without spikes in the slice beam emittance. Following the single pass and two pass recirculation studies for NLS, the longitudinal phase space at the entry of the spreader is as shown in Fig. 5.19. A small energy chirp is assumed at the start of the spreader to evaluate its impact on beam spreader design. It will be shown later that if the beam spreader lattice is not isochronous, the residual chirp can de-compress/compress the bunch further depending upon the sign of the chirp and the sign of R_{56}.

The tracking results presented in this chapter mainly use the bunch parameters given above. However, in order to show the relative differences, the results of tracking without energy chirp, with a higher projected emittance ($\approx$1 mm.mrad) with energy chirp and a flat-top longitudinal beam distribution are included in a few selected cases.

5.4 Beam Spreader Design Based on Triple Bend Achromat

5.4.1 Beam Spreader at 2.2 GeV

A spreader design based on a TBA lattice was suggested in the conceptual design report for NLS as shown in Fig. 5.20. It should be noted that the sign convention used here bends

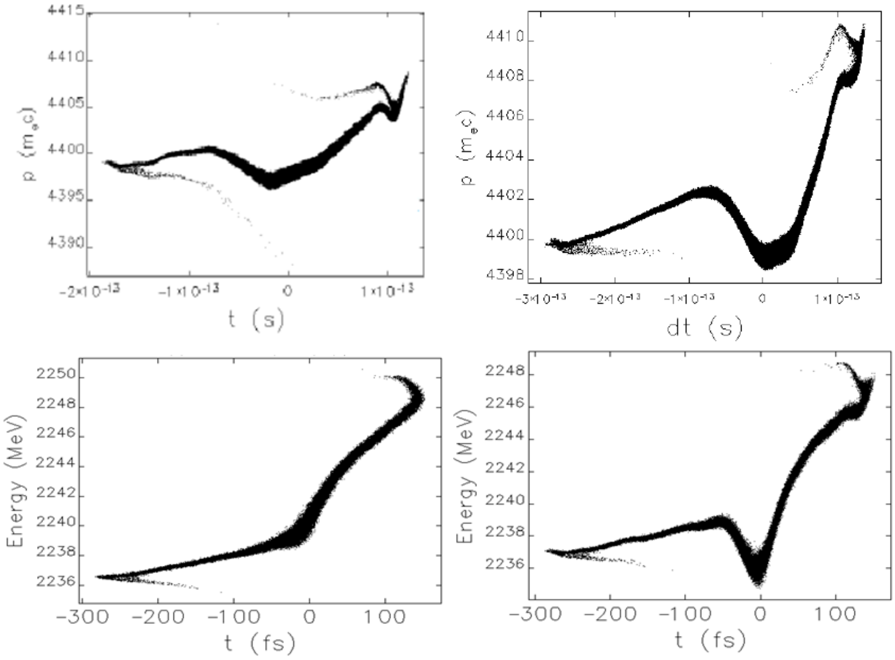

Figure 5.19: Top: Longitudinal phase space in single pass linac at the exit of linac (left) and exit of the beam spreader (right)[37] (See schematic Fig. 5.15). Bottom: Longitudinal phase space at the entry of the spreader (left) and exit of the spreader (right) for re-circulation linac option [153].

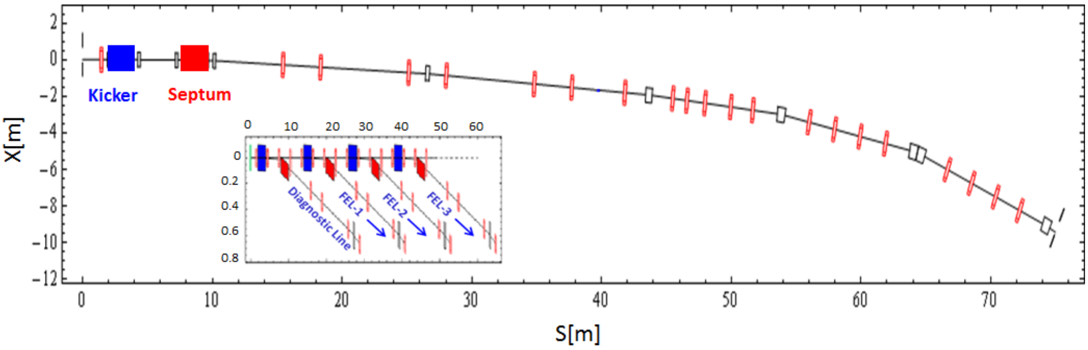

Figure 5.20: Schematic of NLS spreader based on LBNL design [144] showing one beam line. The inset on the bottom shows the start of the different FEL beam lines and the main figure shows details of the complete lattice for one spreader line with a take-off line starting with a kicker and a septum. The quadrupole after the kicker and on either side of the septum are modeled as combined function magnets to take into consideration an off-axis kick. Quadrupoles are shown in red and dipoles in black in rest of the line.

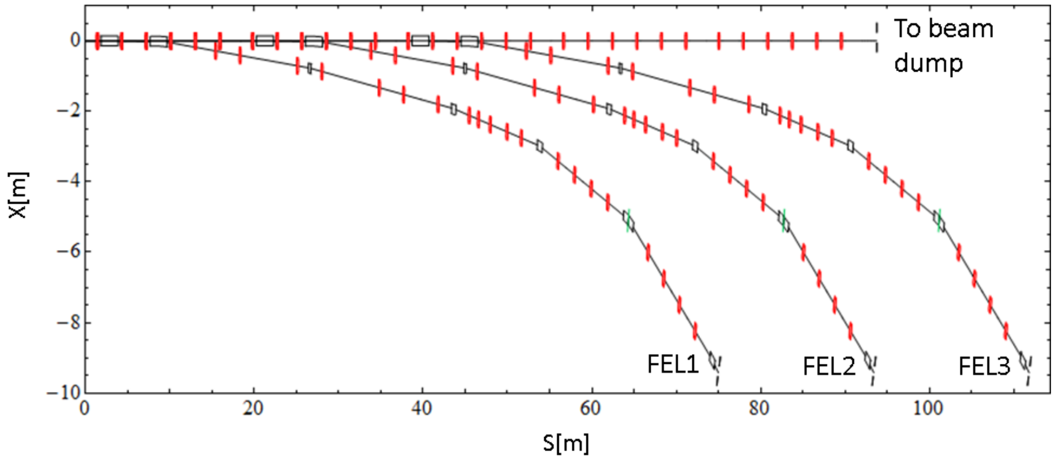

Figure 5.21: Schematic of multiple FEL beam lines using the TBA spreader design shown in Fig. 5.20.

the beam in positive *x* and if signs of bending are reversed, the beam is bent in negative *x* direction (as was shown in the CDR). Thus the sign can be chosen as appropriate for the facility footprint; the direction of bending does not affect the final properties of the electron bunches. The spreader consists of a long FODO take-off section (where the beam is separated first time from the straight-on facility axis) with a series of extraction points for various FEL lines. Fig. 5.21 shows the layout of multiple FEL beam lines using the lattice shown in Fig. 5.20. This design keeps open the possibility for including more beam lines in future. Bunches that are not diverted to a particular FEL line continue to pass on-axis through the FODO lattice. Each extraction section consists of two Triple Bend Achromat (TBA) arcs, where the kicker and the septum together replace the first dipole of the first TBA arc. A 2 m long kicker placed between the first F and D quadrupole provides a kick of 3 mrad. The beam passes off-axis by ∼4 mm in the centre of the D quadrupole immediately after the kicker giving an additional kick of 1.43 mrad and by ∼16 mm in the centre of the F quadrupole before the septum giving a kick of -5.3 mrad. The beam is thus nearly parallel to the straight-on facility axis at the entrance of the septum. The septum kicks the beam by 27 mrad. The beam passes off-axis by ∼53 mm through the D quadrupole after the septum giving an additional kick of 17.5 mrad, thereby reducing the required strength of the septum magnet. The beam is finally separated from the incoming beam after the D magnet after the septum. The first TBA arc “arc1" is then completed with two additional dipoles and seven quadrupoles. The total bending angle provided by kicker, septum and off-axis quadrupoles is 43.6 mrad and can be represented as the first dipole of the arc. The second dipole bends the beam by 24 mrad and the third dipole by 36 mrad. The total bending angle coming from the first arc is 103.6 mrad (∼5.9°). Arc1 ends at s=45 m and is followed by matching quadrupoles to match the beam into second TBA arc. The second arc “arc2" starting at s=53 m is also a TBA but

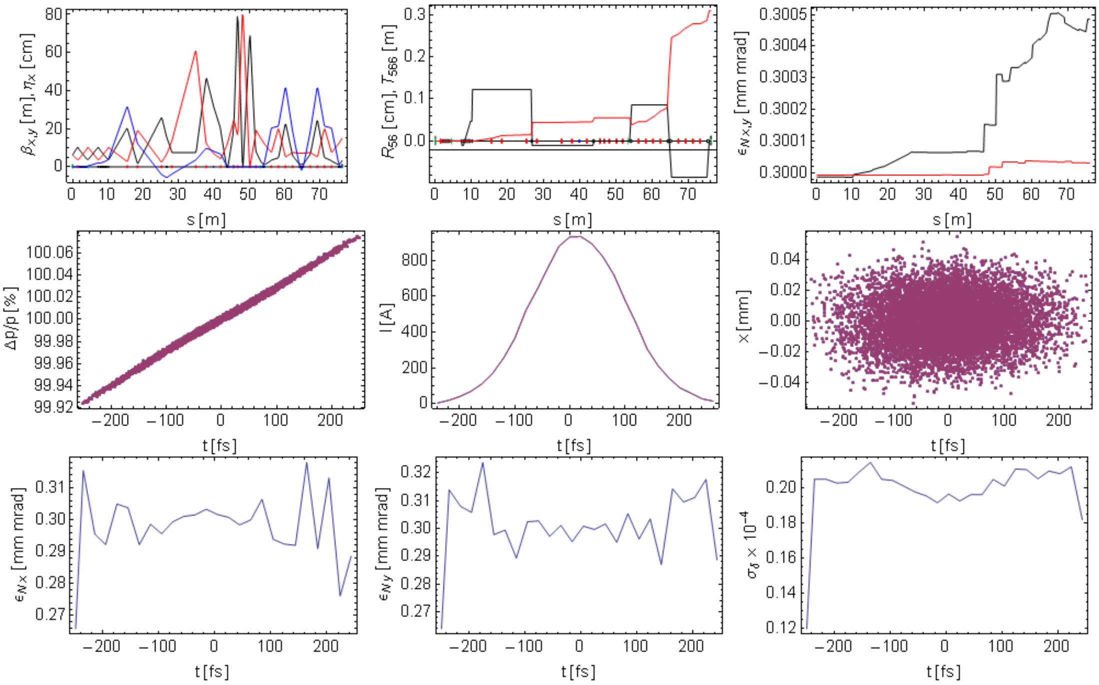

Figure 5.22: Optics and tracking of Gaussian bunch through the spreader shown in Fig. 5.20. CSR is off and ISR is on. Top (left to right): β_x in black, β_y in red, η_x in blue; R_{56} in black, T_{566} in red; Normalised horizontal emittance in black and normalised vertical emittance in red. Middle (left to right): longitudinal phase space, slice current, horizontal co-ordinates of macroparticles as a function of longitudinal position within the bunch. Bottom (left to right): slice normalised horizontal emittance, slice normalised vertical emittance, slice energy spread. The length of the slice is 20 fs.

bends the beam more strongly, with the first and third dipoles giving a kick of 92.7 mrad each, and the middle dipole a kick twice of this value. The total bending angle provided by this arc is thus 278.1 mrad (∼21°), stronger by a factor of 2.5 compared to the first arc. Four quadrupoles on each side of the middle dipole are used to give achromatic and isochronous conditions outside the arc. Both arcs are independently achromatic and isochronous.

The optics and results of tracking a Gaussian bunch through the beam spreader (shown in Fig. 5.20) with CSR off and ISR on are shown in Fig. 5.22. Results with both CSR and ISR on are shown in Fig. 5.23. The figures show the lattice functions, first and second order dispersions (R_{56} and T_{566}), normalised projected horizontal and vertical emittances along the spreader lattice, longitudinal phase space, slice current and horizontal co-ordinates of electrons along a bunch, the slice horizontal and vertical emittances and slice energy spread. Comparing these two figures, the differences in bunch properties as a result of CSR are clearly seen in the projected normalised horizontal emittance (note the change in scale), longitudinal phase space and bunch slice properties. The bunch peak current is not affected because of the isochronicity of the design. The projected normalised horizontal emittance increases to 0.36 mm.mrad at the end of the beam spreader as a

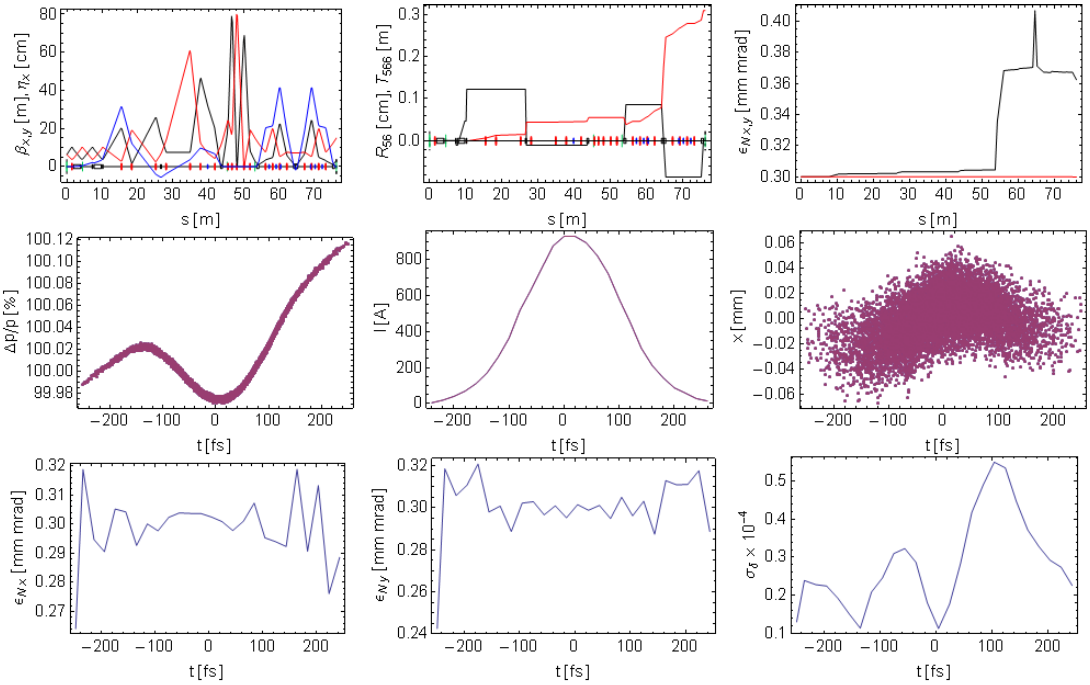

Figure 5.23: Optics and tracking of Gaussian bunch through the spreader shown in Fig. 5.20. CSR and ISR on. Top (left to right): β_x in black, β_y in red, η_x in blue; R_{56} in black, T_{566} in red; Normalised horizontal emittance in black and normalised vertical emittance in red. Middle (left to right): longitudinal phase space, slice current, horizontal co-ordinates of macroparticles as a function of longitudinal position within the bunch. Bottom (left to right): slice normalised horizontal emittance, slice normalised vertical emittance, slice energy spread. The length of the slice is 20 fs.

result of CSR kicks to different parts of the bunch. The resulting horizontal kick to the bunch and its effect on slice energy spread are also noticeable. The slice emittances however are not increased. The second order terms in the spreader, namely the horizontal and vertical chromaticities (second order matrix terms T_{162} and T_{364} and the second order dispersion T_{566} are shown in Fig. 5.24. It was found during NLS studies that these terms can adversely affect the performance of a single spike operation [37] due to a large energy spread. It was found that by correcting these higher order terms, it was possible to maintain a high bunch peak current. It was therefore decided to include sextupoles in the spreader as additional tuning knobs. In case of a beam energy error (with respect to the spreader dipole magnet settings), the T_{566} term generates a lower order feed-down term, resulting in a non-zero value of R_{56}. As described in Chapter 6, the sextupole magnet position alignment can cause R_{56} errors and linear dispersion errors in both transverse planes, as well as x-y coupling and beta-mismatch errors. Since the optimisation of sextupole scheme (location, number and strengths) depends upon the optimised settings for a particular FEL mode, these are not included in design and tracking in this chapter. However, from NLS studies as well as from spreader designs for SwissFEL and European X-FEL it is important to note that sextupoles and octupoles may be required in the beam

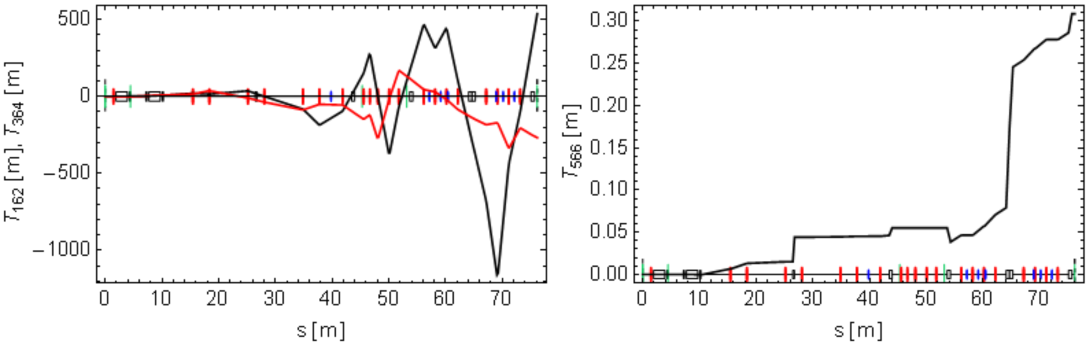

Figure 5.24: Left: horizontal (in black) and vertical (in red) chromaticities (second order matrix terms T_{162} and T_{364} respectively). Right: second order dispersion (T_{566}) in spreader design Fig. 5.20.

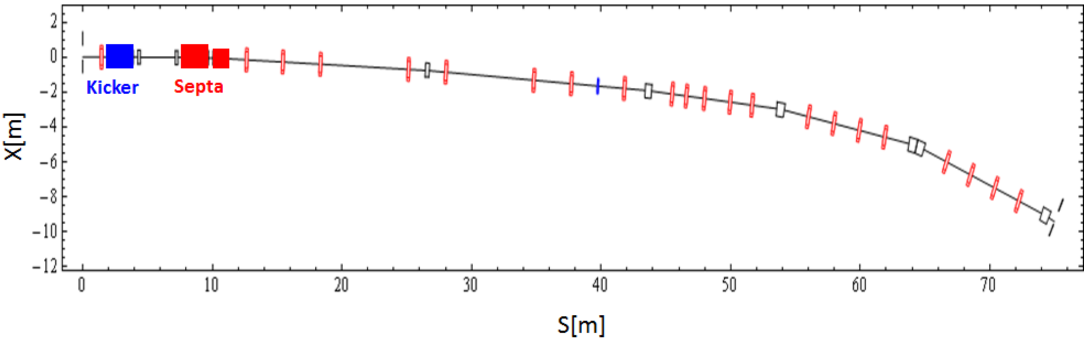

Figure 5.25: Schematic of modified design of NLS spreader. The large aperture quadrupole in Fig. 5.20 after the septum is replaced with one more septum. The quadrupoles after the kicker and before the septum are modeled as combined function magnets to take into consideration an off-axis kick. Quadrupoles are shown in red and dipoles in black in rest of the line.

spreader, and the experimental results presented in Chapter 6 are important to consider.

Initially the spreader design used a large beam offset of ∼53 mm in the quadrupole after the septum. However, achieving the required gradient in such a large aperture quadrupole is challenging and increasing the length of this magnet (to obtain the required integrated strength) increases the length of FODO take-off section. In addition to this, there may be additional undesirable beam dynamics effects due to such a large beam offset. The proposed solution is to replace this quadrupole with a nominal aperture quadrupole as in rest of the spreader and include an additional septum providing a kick of ∼17.5 mrad after the 25 mrad septum as shown in Fig. 5.25. Optics studies show that the quadrupole term can be absorbed in the original lattice while keeping the isochronous and achromaticity conditions as before. The betatron phase advance between dipoles is optimised further to cancel the CSR kicks. As a result of this the betatron functions in arc2 are significantly different than in Fig. 5.23. The results of beam tracking through the spreader design shown in Fig. 5.25 with CSR and ISR on are shown in Fig. 5.26. The

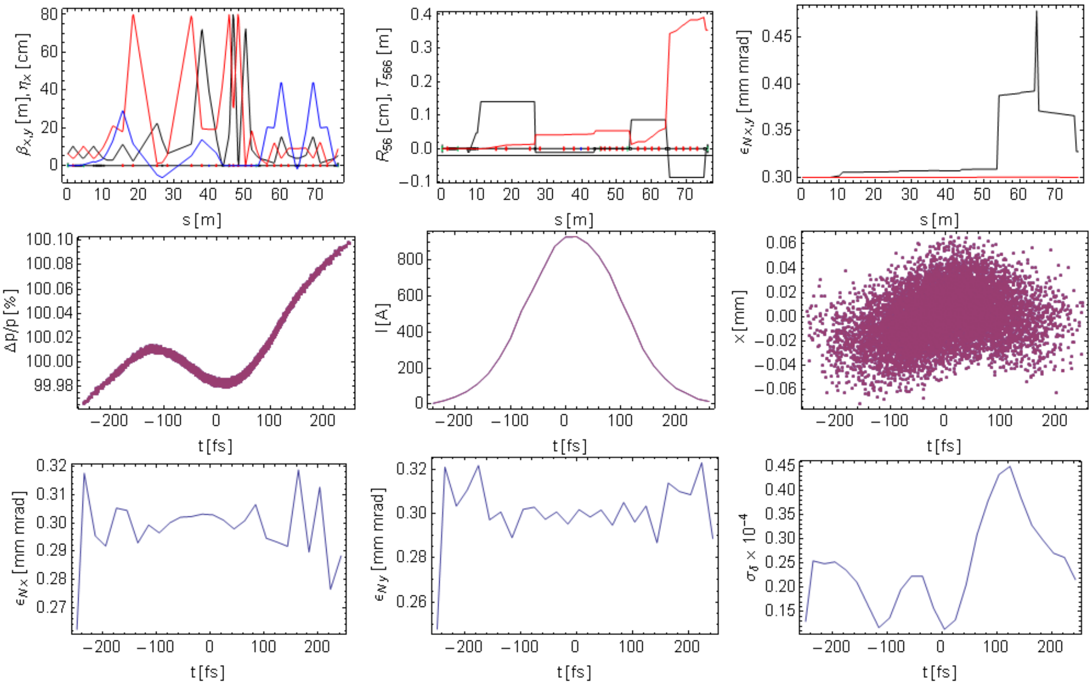

Figure 5.26: Optics and tracking of Gaussian bunch through the spreader shown in Fig. 5.25. CSR and ISR on. Top (left to right): β_x in black, β_y in red, η_x in blue; R_{56} in black, T_{566} in red; Normalised horizontal emittance in black and normalised vertical emittance in red. Middle (left to right): longitudinal phase space, slice current, horizontal co-ordinates of macroparticles as a function of longitudinal position within the bunch. Bottom (left to right): slice normalised horizontal emittance, slice normalised vertical emittance, slice energy spread. The length of the slice is 20 fs.

projected horizontal emittance has reduced to 0.32 mm.mrad compared to the CDR design which gave 0.36 mm.mrad. The reduced effect of CSR on the horizontal co-ordinates as a function of longitudinal position the bunch and on the bunch slice properties is also noticeable. Even though in practice this small change in emittance would be difficult to measure, it shows the importance of maintaining phase advance close to π between the dipoles.

As shown in tracking studies, CSR in arc2 increases the horizontal projected emittance from an initial value of 0.3 mm.mrad to 0.32 mm.mrad when the phase advance is adjusted. To see how the bending in arc2 affects this, the bending angle in each dipole of arc2 was reduced by factor of 2 and then by a factor of 4 from the original dipole angle of 92.7 mrad. Fig. 5.27 shows the projected normalised horizontal emittance (left) and the transverse offset (right) as the arc2 dipole angles are changed. The projected emittance at the spreader exit reduces from 0.327 mm.mrad to 0.315 mm.mrad and 0.312 mm.mrad when angles are reduced by half and a quarter. The transverse offset is reduced from 9.5 m to 7.5 m and 6.5 m, respectively. It is therefore possible to conclude that an optimum choice of angle can be made to achieve the required transverse offset without degradation to beam quality through the spreader. In this particular example, there is very little advantage

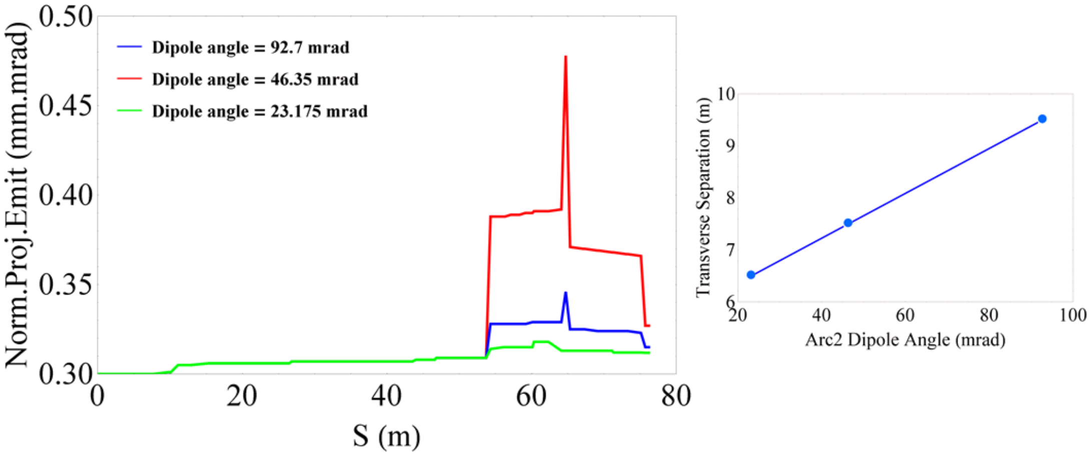

Figure 5.27: Projected horizontal emittance (left) and transverse offset (right) for TBA spreader at 2.2 GeV for different dipole angles in arc2 of the configuration shown in Fig. 5.25.

obtained by reducing the bending angles and so achieving 7.5 m transverse offset with halved bending angles is probably preferable.

5.4.2 CSR Matrix Compensation Method

The matrix compensation method [110] described in Chapter 4 is applied to NLS CDR arc2 design. As seen in Section 5.4.1, the projected normalised horizontal emittace increased from 0.3 mm.mrad to 0.36 mm.mrad at the exit of the spreader as shown in Fig. 5.23.

It should be noted that the arc2 design has not been optimised using the R-matrix method (by optimising quadrupole strengths to match ξ_x and β_x envelope at the exit of arc, while maintaining the chromaticity and isochronicity conditions). Instead the design of arc2 as presented in Section 5.4.1 is used and an extended transfer matrices are written for arc2 as explained in Section 4.4.4. Multiplying these matrices the dispersion and its derivative due to CSR (ξ, ξ') at the exit of arc2 is obtained as (-1.072 m^2, -0.1197 m). This gives the angle of CSR kick (angle made by line $\xi_x x' - \xi'_x x = 0$ in (x, x') phase space, as shown in Fig. 4.15) equal to $\phi_\xi = 0.110$.

In order to match the Courant-Snyder parameters at the exit of arc2 to match the orientation of phase space with ϕ_x, the Courant–Snyder parameters at the entry of the arc2 are scanned (-6.0 $< \alpha_x <$ +8 and 0.25 $< \gamma_x <$ 7). Fig. 5.28 shows the variation of projected horizontal normalised emittance at the exit of the arc2 as α_x values are changed for fixed value of γ_x. For each of these Courant–Snyder parameter, the value of angle ϕ (the angle made by phase space ellipses (Fig. 4.15)) is calculated. The minimum emittance of 0.338 mm.mrad correspond to the curve γ_x=0.5, α_x=+1.5 and β_x=6.5 m and ϕ_x=0.115 as shown in Fig. 5.29. This demonstrates the method of minimisation of emittance using the matrix approach. Using these optimised Courant–Snyder parameters

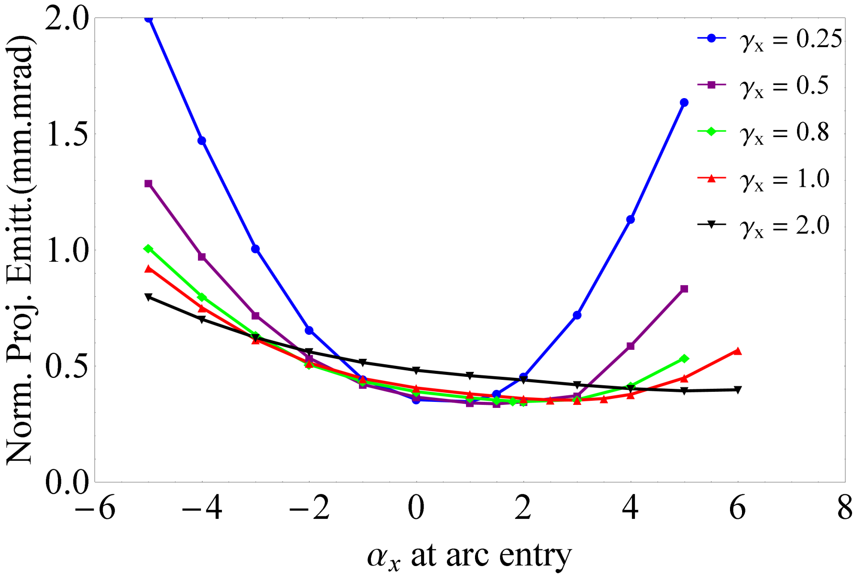

Figure 5.28: Projected emittance at the end of arc2 for a fixed γ_x as a function of α_x.

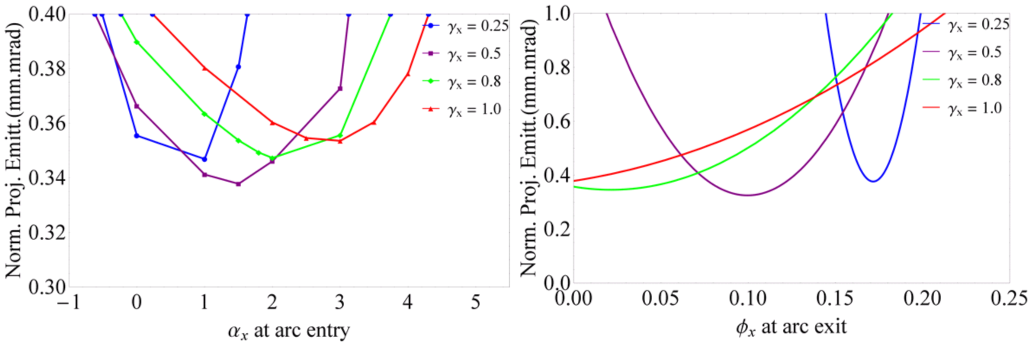

Figure 5.29: Left: Magnified region of interest from Fig. 5.28. Right: Projected emittance at the end of arc2 as a function of ϕ_x for the curves on the left.

at the entry of arc2, the tracking results confirm achieving this value of emittance at the exit of the spreader as shown in Fig. 5.30. As shown in Section 5.4.1, the minimum emittance can be brought down to 0.32 mm.mrad by adjusting the betatron phase advance between the arc dipoles Fig. 5.26 and thus one can use any of these methods by optimising the arc design from the start.

5.4.3 Beam Tracking With Different Initial Beam Parameters

The tracking results shown in the previous sections assume a Gaussian bunch distribution in transverse and longitudinal planes and uses extremely challenging normalised transverse emittances. In this section, the tracking is repeated for the lattice shown in Fig 5.25 with different initial beam parameters. Fig. 5.31 shows the bunch length (left) and normalised emittance (right) along the beam line and the longitudinal phase space at the exit of

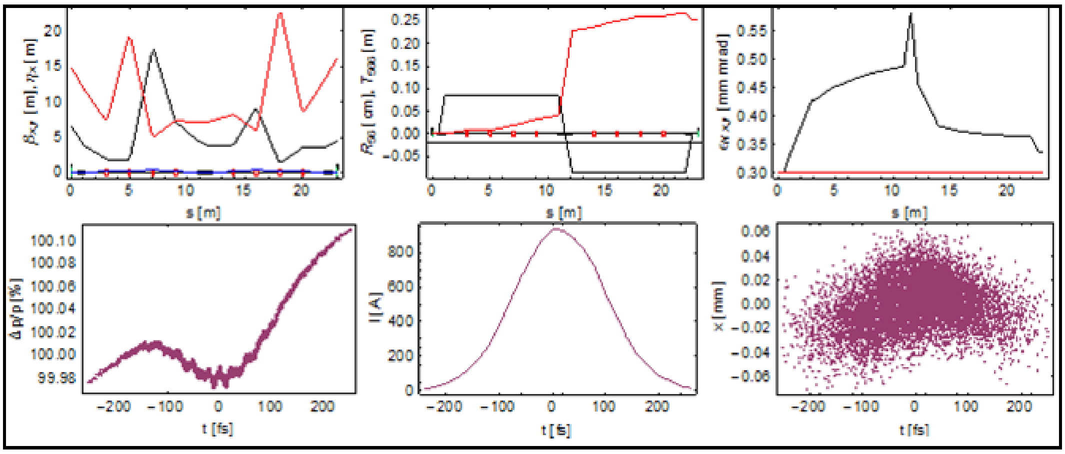

Figure 5.30: Tracked bunch in NLS CDR lattice of arc2 with R-matrix optimisation of CSR kicks, from left to right (Top) - lattice functions, R_{56} and T_{566} and projected horizontal emittance; (Bottom) - longitudinal phase space, slice current and horizontal co-ordinates of macroparticles as a function of longitudinal position within the bunch.

the spreader (middle) from tracking a bunch with a Gaussian distribution in all three planes. The cases with and without a chirp with initial emittance of 0.3 mm.mrad (top and middle) and with a chirp and initial emittance of 1 mm.mrad (bottom) are compared. The increase in normalised emittance at the end of the spreader in each case is 9.2 %, 1 % and 3 %, respectively. The differences can be attributed to small changes in bunch length in the first two cases. In the third case the relative change in bunch emittance is smaller due to a higher starting transverse projected emittance.

Instead of using a Gaussian longitudinal distribution at the start of the spreader, it may be advantageous to have a flat-top distribution. A flat-top distribution at lower energies helps to reduce the increase in projected/slice beam emittance due to space charge. Also, sometimes there is a requirement to have a flat-top longitudinal profile in the FEL (for example for seeding, as was specified in NLS). In order to keep the bunch peak current similar to the Gaussian case, it is necessary to reduce the total bunch length to $\sim 20\,\mu$m. For a Gaussian distribution, $\pm 3\sigma$ is used. The results from tracking this bunch (through the lattice used in Fig 5.25) with chirp and 0.3 mm.mrad beam emittance is shown in Fig. 5.32. The slice emittance and energy spread show peaks at the start and end of the bunch, but in contrast to the Gaussian distribution, the slice energy spread is uniform between the peaks. This may be desirable for certain FEL schemes with seeding.

Fig. 5.33 shows the bunch length (left) and normalised emittance (right) along the beam line and the longitudinal phase space at the exit of the spreader (middle) from tracking a flat-top bunch with chirp and without chirp with initial emittance of 0.3 mm.mrad (top and middle), and with chirp and initial emittance of 1 mm.mrad (bottom). The increase in normalised emittance at the end of the spreader in each case is 20.3 %, 14.1 % and 7.8 %, respectively. Compared with the corresponding cases with Gaussian

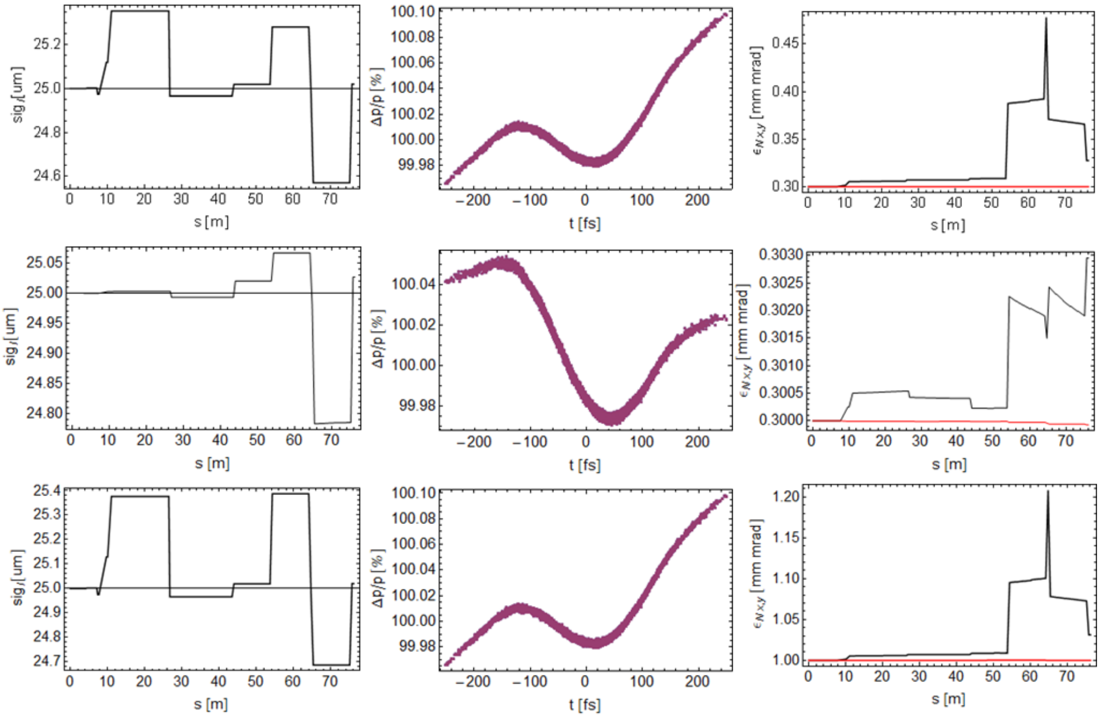

Figure 5.31: Results of beam tracking with Gaussian bunch in all three planes for beam spreader Fig. 5.25, Left: bunch length along the spreader, Middle: longitudinal phase space, Right: projected normalised emittances along the beam line. Top: beam emittance 0.3 mm.mrad, Gaussian bunch with chirp, Middle: beam emittance 0.3 mm.mrad, Gaussian bunch without chirp, Bottom: beam emittance 1.0 mm.mrad, Gaussian bunch with chirp.

distribution, it is clear that the longitudinal flat-top distribution increases the projected emittance by noticeable factor. This is expected as the bunch length is reduced to get similar bunch peak current and thus the tail of the bunch has a larger number of electrons compared to the Gaussian distribution, resulting in higher CSR kicks to the electrons in head. However, the slice energy spread is uniform over the length of the bunch (except from the peaks at the start and end of the bunch), which may be advantageous for an FEL.

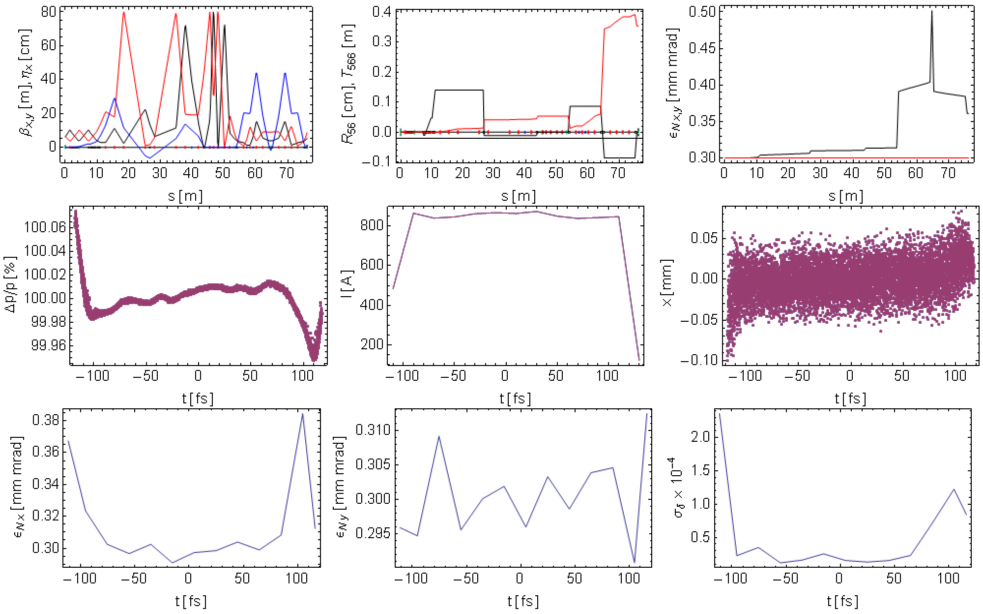

Figure 5.32: Optics and tracking of flat-top bunch in longitudinal plane bunch through the spreader shown in Fig. 5.25, CSR and ISR on. Top (left to right): β_x in black, β_y in red, η_x in blue; R_{56} in black, T_{566} in red; normalised horizontal emittance in black and normalised vertical emittance in red. Middle (left to right): longitudinal phase space, slice current, horizontal horizontal co-ordinates of macroparticles as a function of longitudinal position within the bunch. Bottom (left to right): slice normalised horizontal emittance, slice normalised vertical emittance, slice energy spread. The length of the slice is 20 fs.

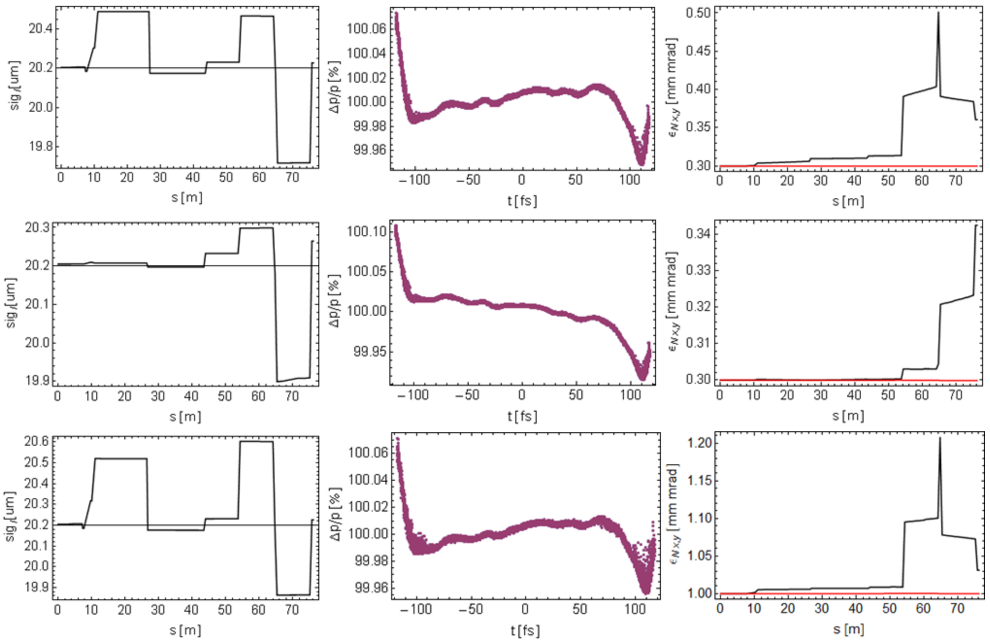

Figure 5.33: Results of beam tracking with flat-top longitudinal distribution with bunch length 20 μm for the beam spreader shown in Fig. 5.25. Left: bunch length along the spreader. Middle: longitudinal phase space. Right: projected normalised emittances along the spreader. Top: with chirp and transverse normalised emittance of 0.3 mm.mrad. Middle: without chirp and transverse normalised emittance of 0.3 mm.mrad. Bottom: with chirp and transverse normalised emittance of 1.0 mm.mrad.

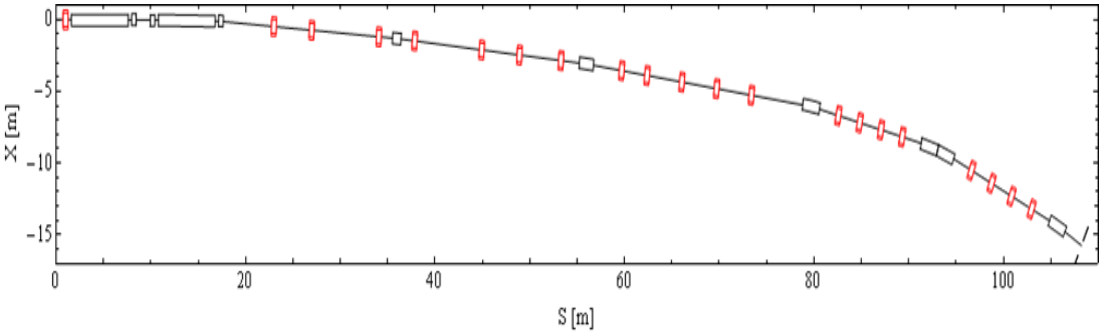

Figure 5.34: Schematic of TBA spreader at 6.6 GeV. The quadrupoles after the kicker and before the septum are modeled as combined function magnets to take into consideration an off-axis kick. Quadrupoles are shown in red and dipoles in black in rest of the line.

5.4.4 Beam Spreader Design at 6.6 GeV

The 2.2 GeV beam spreader design described in earlier sections has been scaled for a 6.6 GeV beam spreader. The kicker and septum lengths are increased by a factor of three to keep the same bending angle (as the maximum field in the septum and the kicker will be limited by technology). This increase in length needs another FODO lattice to be designed to allow the 6 m long kicker and septum magnets to fit within the drift space between an F-quadrupole and a D-quadrupole. The FODO has been chosen to give a 7 m drift between the quadrupoles, the distance between the cells is set to 0.75 m to keep the Courant-Snyder β functions in both transverse planes below 20 m. The beam offsets in the quadrupoles become larger due to the longer drifts between quadrupoles. The beam passes off-axis by ∼11.2 mm in the centre of the D quadrupole immediately after the kicker giving an additional kick of 4.3 mrad and by ∼26 mm in the centre of the F-quadrupole before the septum giving a kick of ∼ -9 mrad. The beam is thus nearly parallel to the straight-on facility axis at the entrance of the septum. The septum kicks the beam by 27 mrad. The beam passes off-axis by ∼115 mm through the D quadrupole after the septum giving an additional kick of ∼39 mrad, thereby reducing the required strength of the septum magnet. The beam is finally separated from the incoming beam after the D quadrupole following the septum. The first TBA arc is then completed with two additional dipoles and seven quadrupoles. The total bending angle provided by the kicker, septum and off-axis quadrupoles is ∼ 64 mrad and can be represented as the first dipole of the arc. The second dipole bends the beam by 24 mrad and the third (final) one bends the beam by 36 mrad. The total bending angle coming from the first arc is thus 124 mrad (∼7° as compared to ∼5.7° for 2.2 GeV spreader). Scaling the arc2 dipoles to keep the dipole field similar to 2.2 GeV case gives a total angle of ∼ 21°. A transverse separation of ∼15 m is then achieved in ∼110 m, as shown in Fig. 5.34.

For the same beam parameters (except energy) the beam optics and the tracked beam parameters are shown in Fig. 5.35 with CSR and ISR on, Fig. 5.36 with CSR on and ISR

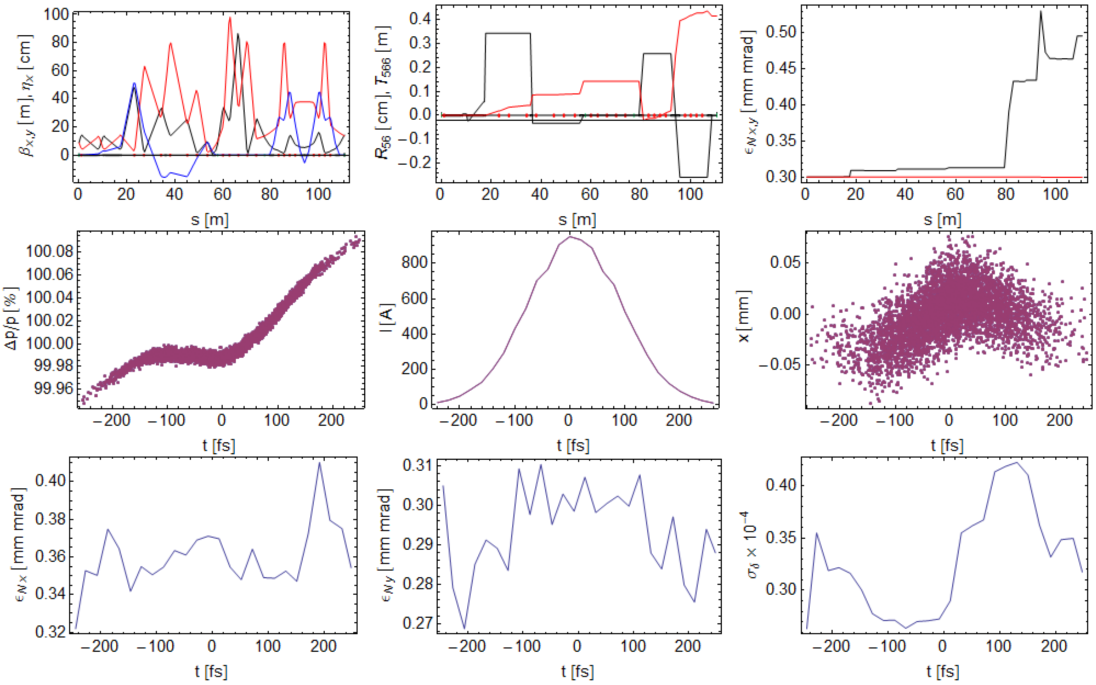

Figure 5.35: Optics and tracking of Gaussian bunch through the 6.6 GeV spreader shown in Fig. 5.34. CSR and ISR on. Top (left to right): β_x in black, β_y in red, η_x in blue; R_{56} in black, T_{566} in red; normalised horizontal emittance in black and normalised vertical emittance in red. Middle (left to right): longitudinal phase space, slice current, horizontal co-ordinates of macroparticles as a function of longitudinal position within the bunch. Bottom (left to right): slice normalised horizontal emittance, slice normalised vertical emittance, slice energy spread. The length of the slice is 20 fs.

off and Fig. 5.37 with CSR off and ISR on. Unlike the 2.2 GeV case, the effect of ISR at high energy in both arcs contributes to the final emittance of 0.50 mm.mrad. The final emittance from only ISR is 0.36 mm.mrad.

As the CSR and ISR emittance growth mainly occurs in arc2, the effect of the dipole angles used in arc2 as the CSR and ISR emittance growth is evaluated further. The original angle of 92.7 mrad was halved and quartered. A comparison of the projected horizontal emittances for these cases is shown in Fig. 5.38. Reducing the bending angle in arc2 reduces the transverse separation by a few meters as shown on the right. The reduction in bending angle by a quarter reduces the final projected emittance from 0.5 mm.mrad to 0.32 mm.mrad with both CSR and ISR on, and results in a reduction in transverse separation from 15 m to 11 m.

This scheme however requires very large aperture quadrupoles to accommodate the beam offset of 115 mm. To achieve the required gradient in a quadrupole with such a large aperture in the given length is not practical (in addition, the external dimensions of such a quadrupole will need more transverse space). The academic exercise carried out here was mainly to highlight the effect of ISR at the higher energies. Alternative options such as first bending the beam in the vertical plane and then bringing it back to

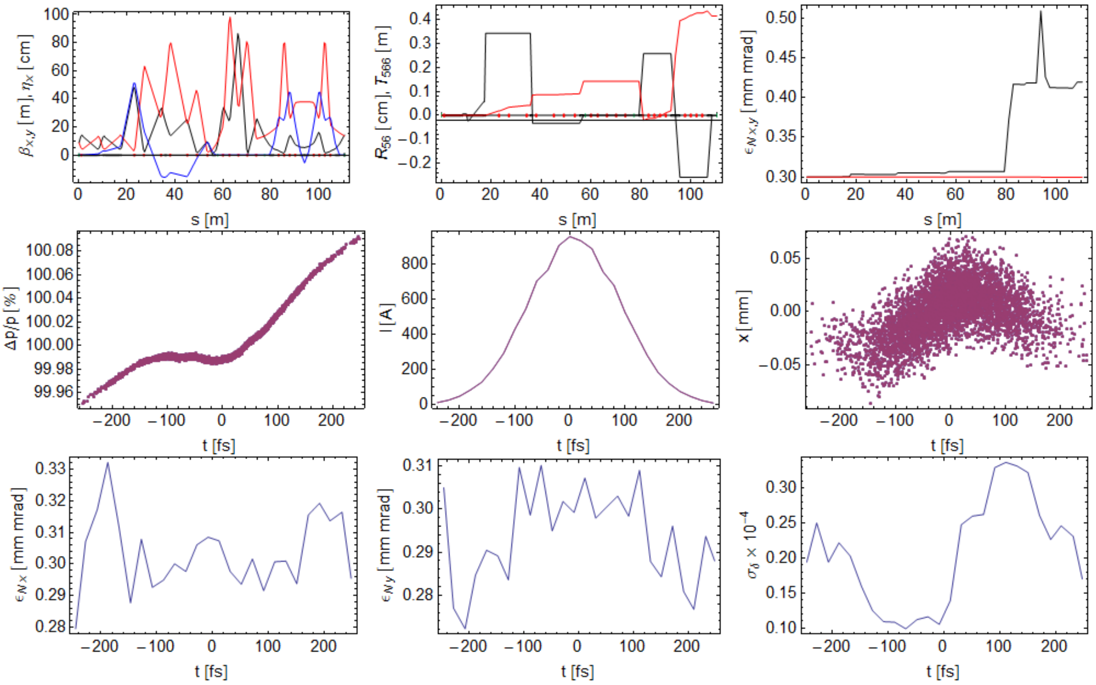

Figure 5.36: Same as Fig. 5.35 but with CSR on and ISR off

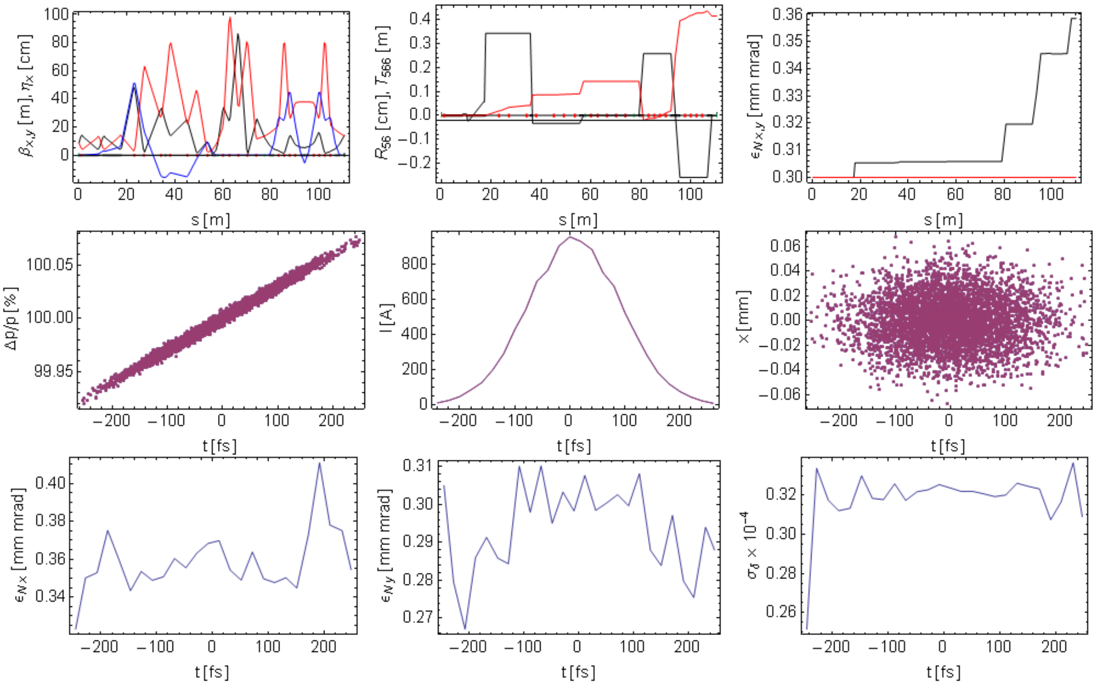

Figure 5.37: Same as Fig. 5.35 but with CSR off and ISR on

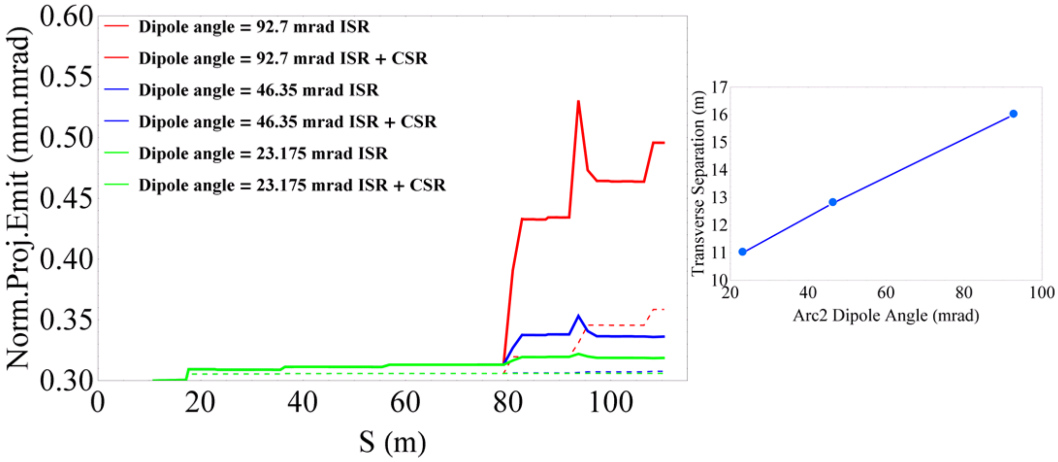

Figure 5.38: Projected horizontal emittance (left) and transverse offset (right) with only ISR and with ISR and CSR on for TBA beam spreader at 6.6 GeV for different dipole angles in arc2.

the horizontal plane after the required separation is achieved will be better solution (as adopted at European X-FEL [132, 131] and SwissFEL [136], for example.)

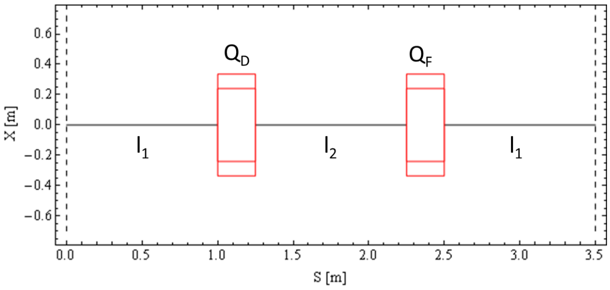

Figure 5.39: Schematic of single cell of FODO lattice.

5.5 Beam Spreader Design Based on Double Bend Achromat

The lattice design based on a FODO lattice uses optics symmetry and an appropriate phase advance between the dipoles as described in Chapter 4. A betatron phase advance of π in the bending plane between two consecutive dipoles cancels the dispersion and its derivative (hence the name double bend achromat) as well as the CSR kicks, provided that the bunch and lattice parameters are approximately the same at these two locations. The spreader design based on this concept [107, 108] has experimentally been demonstrated to preserve the normalised horizontal emittance. The beam line based on a FODO lattice can be achromatic (with the correct phase advance between the dipoles) but is not isochronous and thus the cancellation of CSR kicks can work perfectly only with certain beam parameters and lattice design.

In this section, beam spreader designs based on DBA lattices based on FODO lattices at both 2.2 GeV and 6.6 GeV are presented. The tracking simulations use the same starting parameters as were used in the previous sections on beam spreader designs (based on TBA) to allow a direct comparison of the final beam parameters in both these configurations.

5.5.1 Beam Spreader design at 2.2 GeV

In order to decide the correct phase advance between the locations in FODO lattice where dipoles can be inserted, it is important to consider specific FODO lattices. FODO lattices are periodic lattices with properties described in Chapter 2. The drift spaces used should be of sufficient length to incorporate dipoles and the beta functions and dispersions along the line should be reasonable to avoid higher order perturbations to beam. The FODO cell shown in Fig. 5.39 consists of F and D quadrupoles each with length equal to 0.25 m. The drift lengths at the start of the FODO and end of the FODO are equal to l_1 and the drift length between the between the quadrupoles is equal to l_2. The phase advances and maximum beta functions in horizontal and vertical planes for different values of drifts and quadrupole strengths are shown in Fig. 5.40.

If two dipoles bending in the same direction are inserted in the FODO lattice with the phase advance between them equal to π, the dispersion (and its derivative) close at the

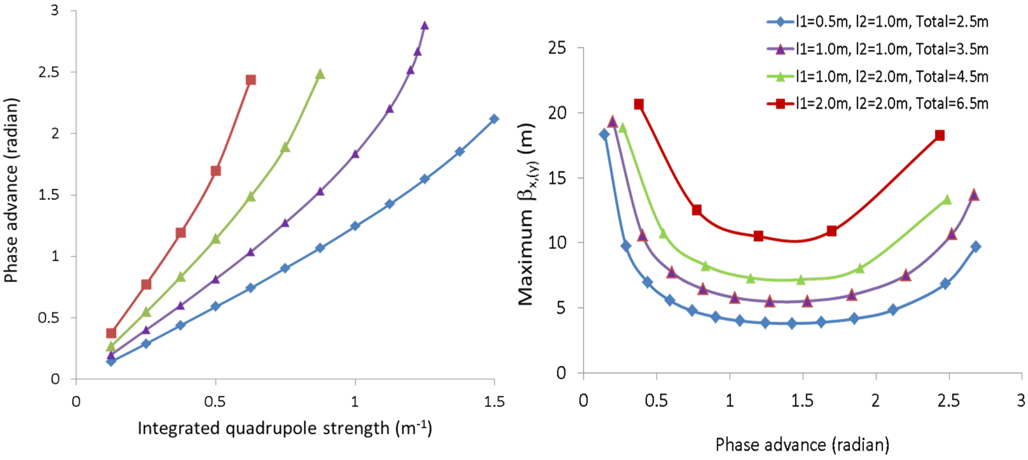

Figure 5.40: Left: phase advance over a FODO cell as a function of integrated quadrupole strength for different drift lengths l_1 and l_2 from Fig. 5.39. Right: maximum value of Courant–Snyder beta function in the FODO cell as a function of phase advance.

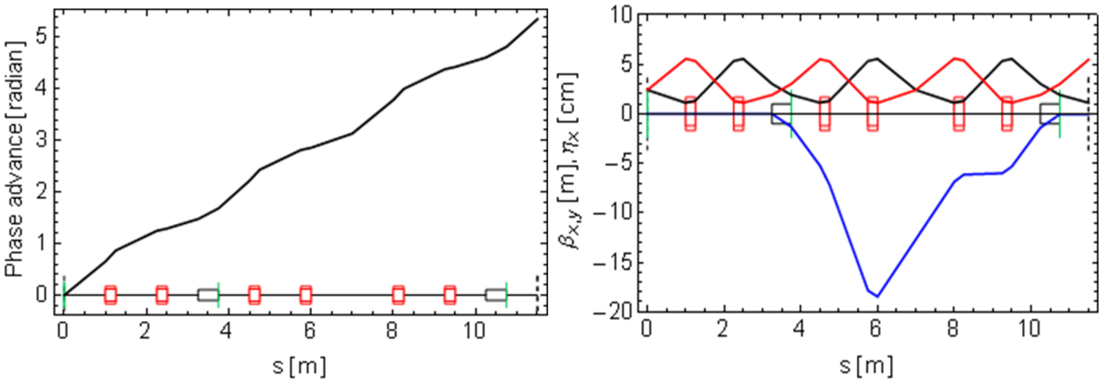

Figure 5.41: Left: phase advance of π between two dipoles for the FODO lattice using three FODO cells with total length equal to 3.5 m from Fig. 5.40. Right: Courant–Snyner beta functions (horizontal in black and vertical in red) and dispersion (in cm) (in blue) along the lattice.

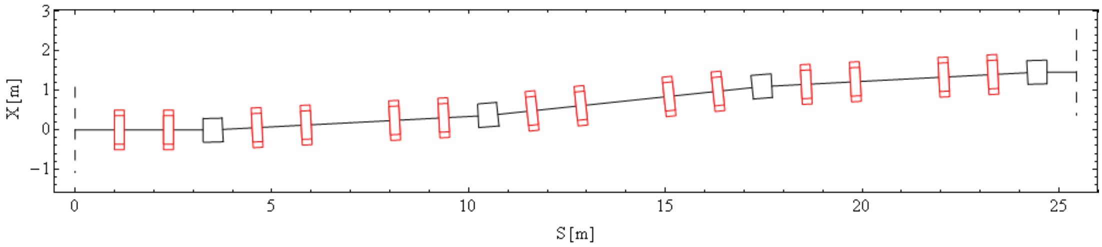

Figure 5.42: Schematic of a beam spreader based on 3° bending angle dipoles embedded in a FODO lattice. The phase advance per cell (each cell 3.5 m long) of FODO is $\pi/2$.

exit of second dipole, thus satisfying the achromatic condition. As shown in Fig. 5.40, the maximum phase advance in a FODO cell is less than π, thus at least two FODO cells (each with phase advance of $\pi/2$) are needed to construct an achromat. The separation of the beam spreader from the straight on beam line depends upon the angles of the dipoles and distance between the dipoles. A beam spreader design with four dipoles can bring the beam line parallel to the linac for FEL line. Fig. 5.42 gives an example of this scheme. In principle, a final decision on the FODO design to use is taken considering not only the maximum betatron function and the phase advance but also considering the number of magnets and their power supplies (which affect the cost of the facility). For no specific reason, FODO cell lengths of 3.5 m and 6.5 m are used for the lattices described here. All the lattices with FODO cell length from 3.5 m to 6.5 m have a maximum value of betatron functions less than 25 m. The variation in betatron function as a function of the phase advance becomes narrower as the length of the FODO increases.

As explained in Section 4.4.2, if successive CSR kicks are separated by a betatron phase advance equal to π in the bending plane, there is no or negligible emittance growth. In the first example, a dipole with a bending angle of 3° embedded in a FODO cell with each having $\pi/2$ phase advance is used, as shown in Fig. 5.41. The beam then passes through two more FODO cells and then enters FODO cells incorporating two dipoles bending in the opposite direction to the first pair of dipoles by $-3°$. This brings the beam line parallel to the accelerating linac as shown in Fig. 5.42. The optics and results of tracking through this beam line are shown in Fig. 5.43. The projected normalised beam emittance in the horizontal plane is almost unchanged at the exit compared to the emittance at the start.

To illustrate the effect of not maintaining the phase advance of π between second and third dipole, two more FODO cells are added in the middle as shown in Fig. 5.44, making the phase advance between the second and third dipoles equal to 2π, which adds the CSR kicks instead of cancelling out. The effect of this on the projected emittance, slice emittances and energy spread are shown in Fig. 5.45.

By adding two more FODO cells in the middle section, the phase advance between the dipoles is equal to 3π which again maintains the normalised projected horizontal emittance

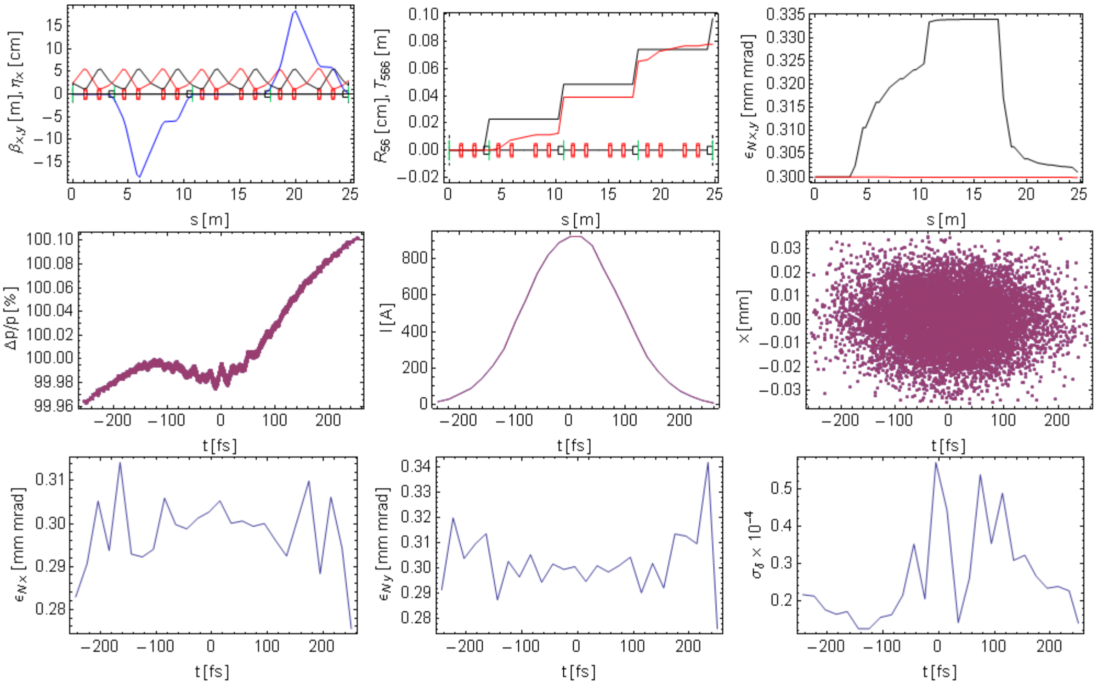

Figure 5.43: Optics and tracking of Gaussian bunch through the 2.2 GeV FODO spreader shown in Fig. 5.42. CSR and ISR on. Top (left to right): β_x in black, β_y in red, η_x in blue; R_{56} in black, T_{566} in red; Normalised horizontal emittance in black and normalised vertical emittance in red. Middle (left to right): longitudinal phase space, slice current, horizontal co-ordinates of macroparticles as a function of longitudinal position within the bunch. Bottom (left to right): slice normalised horizontal emittance, slice normalised vertical emittance, slice energy spread. The phase advances between each pair of dipoles is π.

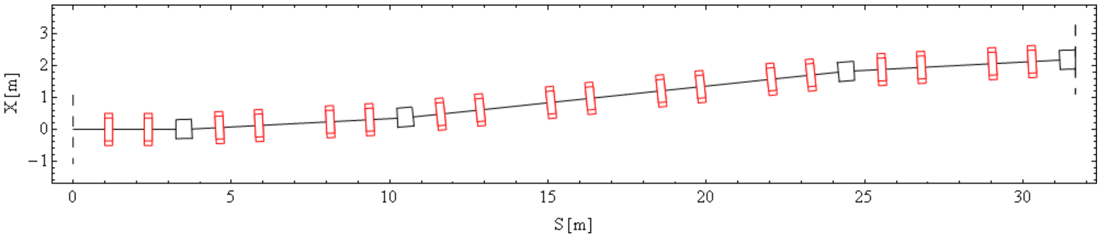

Figure 5.44: Schematic of a beam spreader based on 3° bending angle dipoles embedded in FODO lattice. The phase advance per cell (each cell 3.5 m long) of FODO is $\pi/2$. The phase advance between dipoles 2 and 3 is equal to 2π.

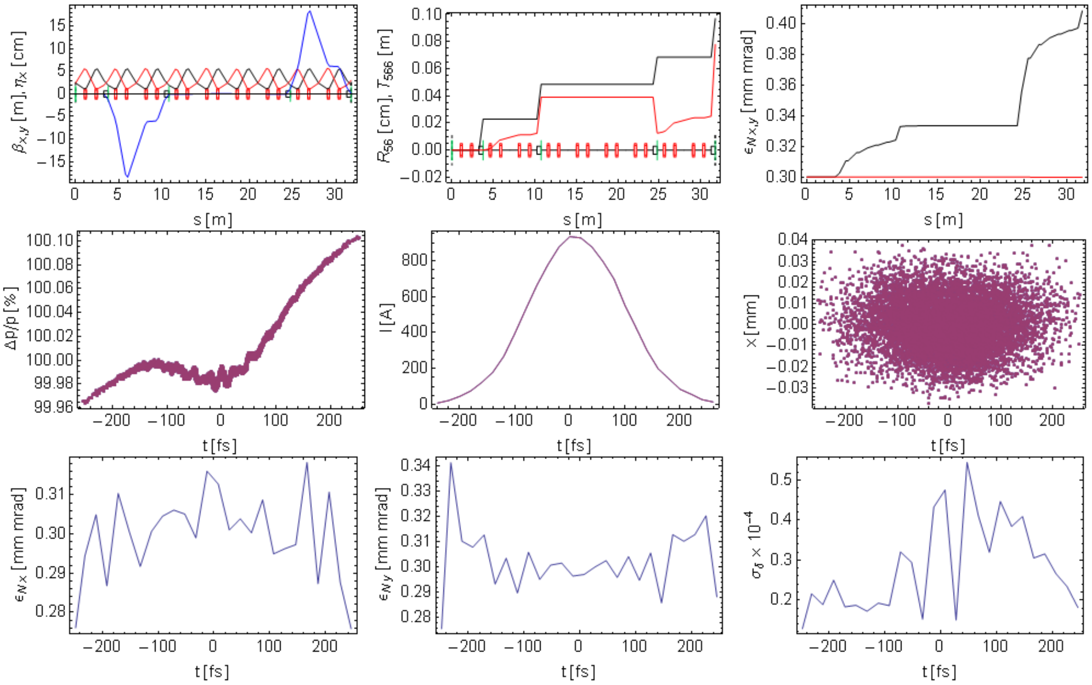

Figure 5.45: Optics and tracking of Gaussian bunch through the 2.2 GeV FODO spreader shown in Fig. 5.44. CSR and ISR on. Top (left to right): β_x in black, β_y in red, η_x in blue; R_{56} in black, T_{566} in red; Normalised horizontal emittance in black and normalised vertical emittance in red. Middle (left to right): longitudinal phase space, slice current, horizontal co-ordinates of macroparticles as a function of longitudinal position within the bunch. Bottom (left to right): slice normalised horizontal emittance, slice normalised vertical emittance, slice energy spread. The phase advance between second and third dipoles is equal to 2π.

Table 5.5: Comparison of FODO based DBA spreader lattices. *includes 8 dipoles instead of 4.

Dipole angle	No. of FODO cells	X (m)	Total length (m)	FODO cell length (m)	Dipole length (m)	R_{56} (cm)	T_{566} (m)	bunch length (μm)	ϵ_{Nx} (mm. mrad)
3°	7	1.5	25.5	3.5	0.5	0.10	0.08	25.3	0.3010
4°	7	1.9	25.5	3.5	0.5	0.10	0.08	25.5	0.3031
6°	7	3.0	25.5	3.5	0.5	0.41	0.32	25.7	0.3099
9°	7	4.2	25.5	3.5	0.8	1.40	0.64	27.4	0.3783
12°	7	5.8	25.5	3.5	0.8	2.50	1.25	29.2	0.5661
15°	7	6.4	25.5	3.5	0.8	3.90	2.00	31.8	0.9437
3°	11	3.0	39.5	3.5	0.5	0.10	0.08	25.3	0.3005
3°*	19	9.0	66.0	3.5	0.5	0.19	0.15	25.4	0.3086
6°	11	5.9	39.5	3.5	0.5	0.39	0.31	25.7	0.3099
6°	11	5.9	39.5	3.5	0.8	0.61	0.31	26.1	0.3100
12°	7	10.2	44.0	6.5	0.8	2.30	2.40	28.8	0.7763
15°	7	13.0	44.0	6.5	0.8	3.90	2.00	31.8	1.3702
12°	7	10.2	44.0	6.5	1.5	4.40	2.30	32.0	1.1978
15°	7	13.0	44.0	6.5	1.5	7.00	3.60	38.0	2.3682

almost unchanged.

In order to obtain more separation between spreader beam lines to avoid any physical clash between the straight on beam line components and adjacent beam lines (if more than one spreader beam line is required), it is possible to add more FODO cells in between dipoles two and three (still maintaining odd multiple of π betatron phase advance). However this will need more quadrupoles and associated power supplies (hence the cost will increase). Thus it is useful to study how far the dipole angle can be increased while still maintaining the beam quality (i.e. bunch length, normalised projected and slice emittance, slice energy spread etc.). Table 5.5 gives the results for several dipole angles. When the bending angle is increased, the dipole field has to increase unless the length of the dipole is increased. To accommodate an increased length of dipoles, longer FODO cells are required.

From the results presented in Table 5.5, it can be inferred that if the dipole angles are kept below 6°, the compensation of CSR works almost perfectly. Fig. 5.46 shows the possible layout of a beam spreader for multiple (in this case 3) FEL beam lines using 6° dipoles.

For dipole angles higher than 6°, the maximum projected emittance along the line increases as noted in Table 5.5. As the dipole angle increases, R_{56} increases and as the FODO lattice is not isochronous, if the bunch enters the spreader with an energy chirp, then the bunch length will change. This affects the exact cancellation of CSR kicks. For the extreme case of 15° dipole angle, the length of a dipole has significant effect

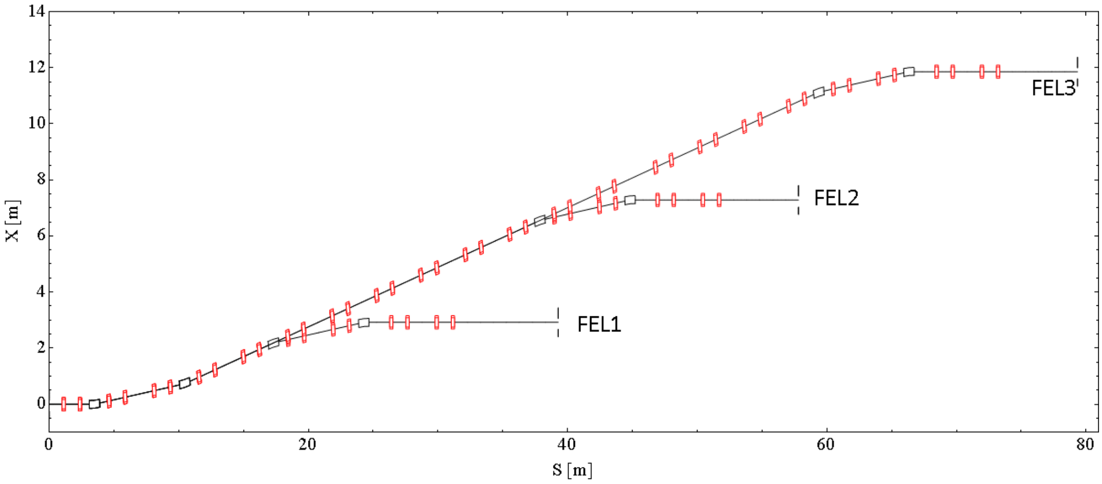

Figure 5.46: Schematic of multiple FEL beam lines using FODO spreader design using 6° dipoles inserted at correct phase advances.

on the projected as well as the bunch slice parameters. Fig. 5.47 and Fig. 5.48 show tracking results from a FODO lattice with cell length 6.5 m case with dipole length 0.8 m compared with a case with dipole length 1.5 m corresponding to 2.4 T (too high for normal conducting electromagnet) and 1.28 T magnetic field on the dipoles, respectively. The tracking results through longer dipoles demonstrate no cancellation of CSR kicks. The CSR kicks result in a strong spike in slice peak current, slice horizontal emittance and slice energy spread.

It is also interesting to see the “bow-tie" shape in the horizontal phase space in both these cases as a consequence of the effect of CSR on the horizontal variables (x, x') in the dipoles, because of the non-zero dispersion. In the first pair of dipoles, electrons lose energy depending on their longitudinal co-ordinate within the bunch. Because of the dispersion in the dipoles, when the bunch exits the second dipole and enters a region with zero (linear) dispersion, there is still some net change in the horizontal variables: this effect is analogous to quantum excitation from incoherent synchrotron radiation. This means that electrons enter the second pair of dipoles with horizontal co-ordinate (and momentum) depending on their longitudinal co-ordinate. But now there is further energy loss from CSR, affecting electrons in the same way as before according to their longitudinal positions, and resulting (at the exit of the final dipole) in a further change in the horizontal variables, depending on the longitudinal co-ordinate of the electron. But because the horizontal variables at the entrance to the second pair of dipoles already had a dependence on the longitudinal co-ordinate, the net effect is a change in horizontal variables depending on the initial values of the horizontal variables.

These results show that for CSR cancellation to work, it is necessary to keep dipole lengths and angles to reasonably low values.

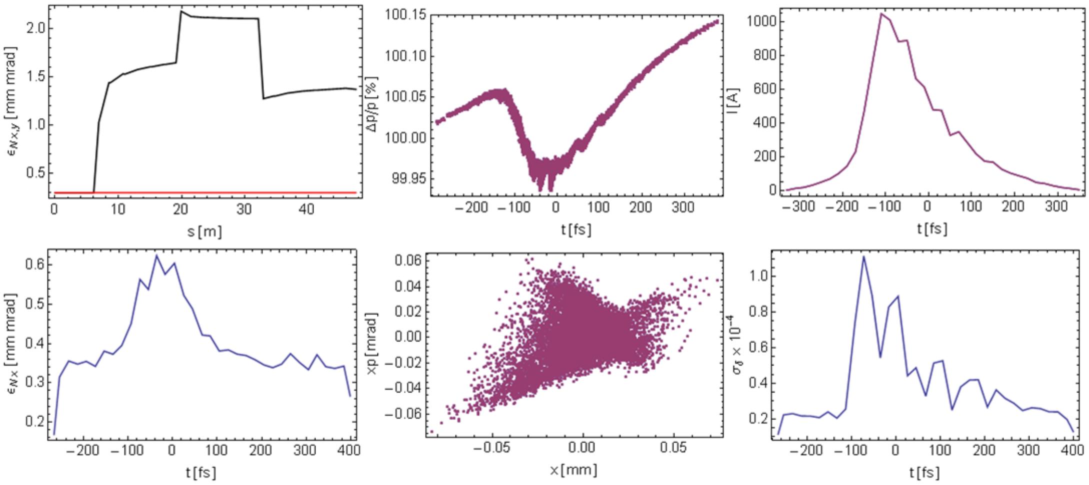

Figure 5.47: Tracking results through DBA based on FODO (cell length 6.5 m) with 0.8 m long 15° dipoles. Left to right: normalised horizontal emittance in black, longitudinal phase space, slice current; slice normalised horizontal emittance, phase space in horizontal plane, slice energy spread.

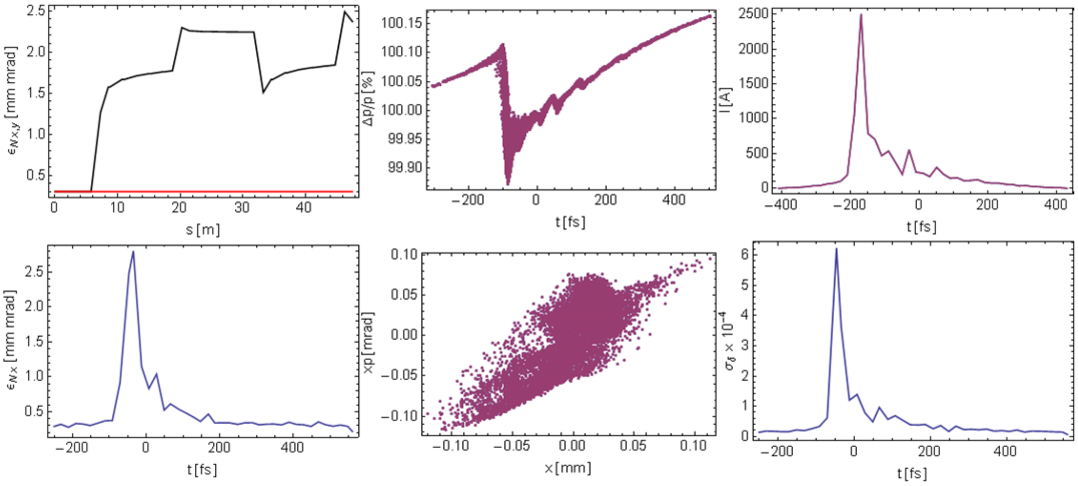

Figure 5.48: Tracking results through DBA based on FODO (cell length 6.5 m) with 1.5 m long 15° dipoles. Left to right: normalised horizontal emittance in black, longitudinal phase space, slice current; slice normalised horizontal emittance, phase space in horizontal plane, slice energy spread.

5.5.2 Beam Tracking With Different Initial Beam Parameters

The tracking results shown in previous section assume a Gaussian bunch distribution in transverse and longitudinal planes and are done for extremely challenging normalised transverse emittances. An initial correlated energy spread (chirp) is also assumed. In this section, the tracking for a similar lattice to the one shown in Fig 5.42 but with 6° dipoles is repeated with different initial beam parameters. Fig. 5.49 shows the bunch length (left) and normalised emittance (right) along the beam line and the sliced longitudinal phase space at the exit of the spreader (middle) from tracking a Gaussian bunch in all three planes with chirp and without chirp with initial emittance of 0.3 mm.mrad (top and middle), with chirp and initial emittance of 1 mm.mrad (bottom). The increase in normalised emittance at the end of the spreader is 6.1 %, 7.1 % and 1.9 %, respectively. The differences can be attributed to a small change in the bunch length in the first two cases. In the third case the relative effect in bunch slice emittances is smaller due to higher starting transverse projected emittance. Fig. 5.50 shows the bunch length (left) and normalised emittance (right) along the beam line and the slice longitudinal phase space at the exit of the spreader (middle) from tracking a flat-top bunch in the longitudinal plane with chirp and without chirp with initial emittance of 0.3 mm.mrad (top and middle), with chirp and initial emittance of 1 mm.mrad (bottom). The bunch length was reduced in flat-top mode to obtain a similar peak bunch current to the case of a Gaussian distribution. The increase in normalised emittance at the end of the spreader is 42.4 %, 46.5 % and 15.8 %, respectively. The difference in emittances using chirped and unchirped bunch may be attributed to small differences in longitudinal phase space at the final dipoles. The large increase in the projected emittance can be attributed to more electrons in the tail compared to a Gaussian distribution (as the amplitude of the flat-top distribution is the same as the peak in the Gaussian) but also due to a higher energy loss due to CSR for shorter bunch length. This process can thus change the bunch parameters at subsequent dipoles, affecting cancellation of CSR kicks. The increase in emittances is significantly higher than the TBA lattice.

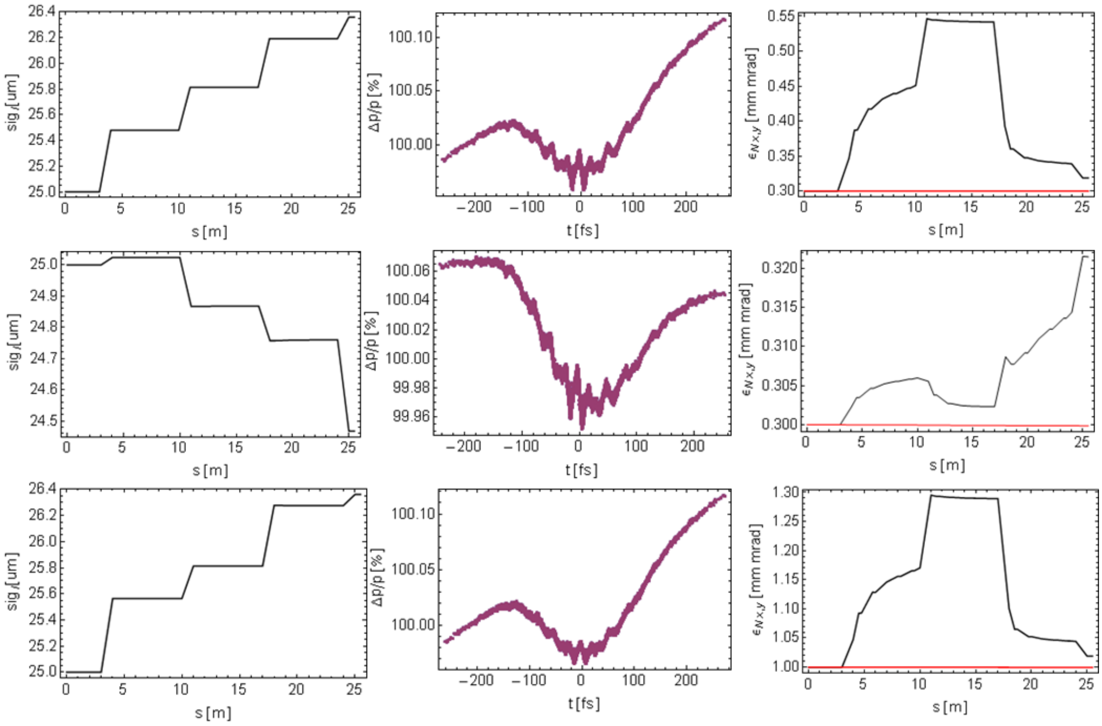

Figure 5.49: Results of beam tracking with Gaussian bunch in all three planes for beam spreader shown in Fig. 5.42 with 6° dipoles, Left: bunch length along the spreader, Middle: longitudinal phase space, Right: projected normalised emittances along the beam line. Top: beam emittance 0.3 mm.mrad, Gaussian bunch with chirp, Middle: beam emittance 0.3 mm.mrad, Gaussian bunch without chirp, Bottom: beam emittance 1.0 mm.mrad, Gaussian bunch with chirp.

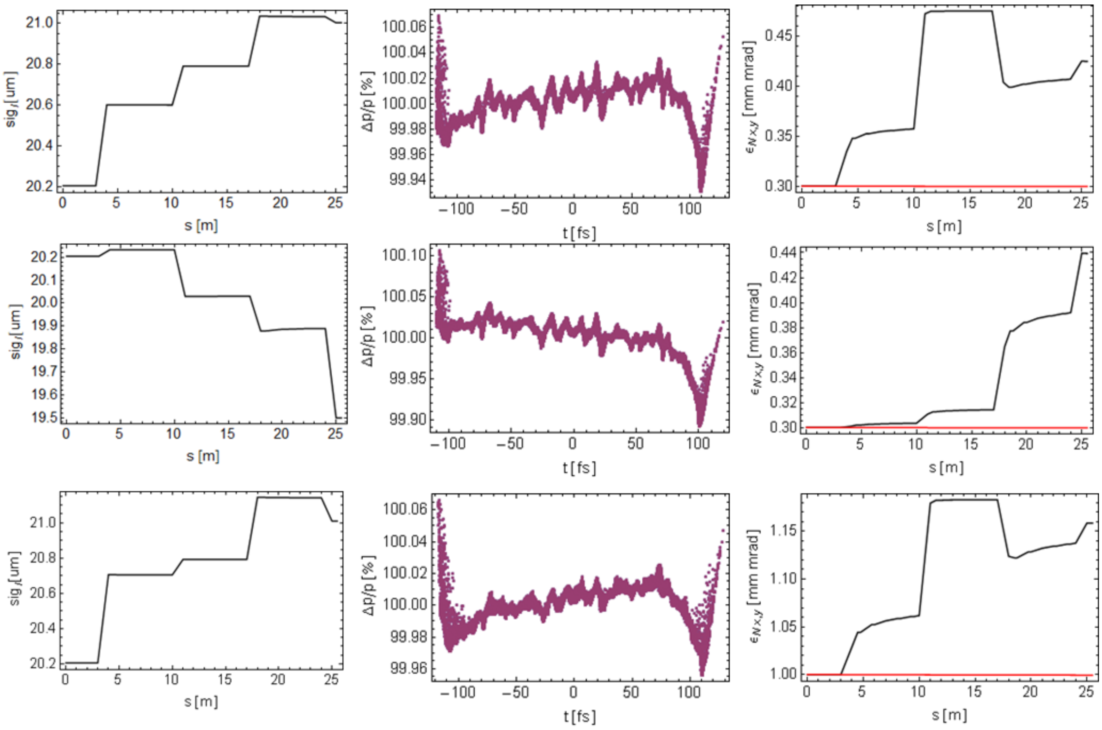

Figure 5.50: Same as Fig. 5.49 but with flat-top bunch in the longitudinal plane.

5.5.3 Beam Spreader Design at 6.6 GeV

To design a DBA beam spreader at 6.6 GeV, the 2.2 GeV DBA beam spreader designs based on FODO lattices can be scaled to see their performance at higher energy. From the results presented in section 5.5.1, the dipole angles of 6° and 12° are considered to achieve enough transverse separation in moderate beam line length and these angles are taken as starting angles. If these angles are proved to deteriorate the beam quality, lower than 6° angles can be used.

Due to three times higher energy, it order to keep the magnetic field below ∼1 T, it is necessary to increase the dipole length from 0.8 m to 2.4 m. For 6° bending, needing a dipole field of 0.96 T. The length of the FODO cell is increased to 6.5 m to accommodate these longer dipoles. The increase in the dipole angle to 12° with 2.4 m length gives a dipole field of 1.92 T; it is necessary to increase the dipole length further to reduce the dipole field to ∼1.5 T (a reasonable upper limit on the field strength in a normal-conducting electromagnetic dipole). For the sake of comparing the major differences with respect to 2.2 GeV spreader design qualitatively, the dipole length is kept to 2.4 m. The important effect at this higher energy comes from the incoherent synchrotron radiation. Figs. 5.51, 5.52 and 5.53 show the effect of ISR off and on in addition to the CSR using 6° dipole. The ISR marginally increases the normalised projected horizontal emittance (from 0.3 mm.mrad to 0.34 mm.mrad) and the CSR kicks are almost cancelled.

Whereas if the bending angle is increased to 12°, as shown in Figs. 5.54, 5.55 and 5.56 with ISR on and CSR off, ISR off and CSR on and both ISR and CSR on, respectively, it is evident that the effect of ISR leads to a large increase in projected as well as the slice emittance, and also increases the slice energy spread. This result is significantly different compared to the TBA lattice at 6.6 GeV (as described earlier in Section 5.3.5). The TBA lattice is optimised for minimum ISR (lattice functions and dispersion functions are smaller in dipoles) compared to the DBA lattice.

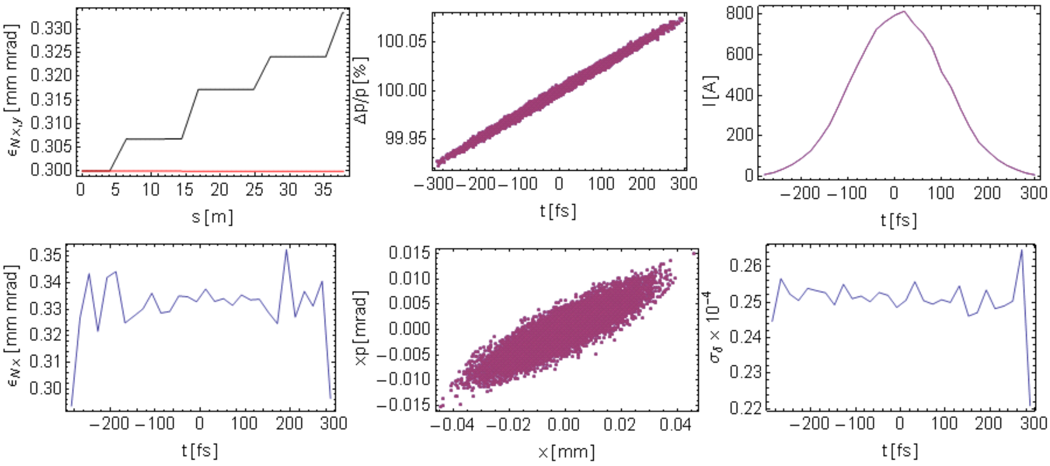

Figure 5.51: Tracking results through 6.6 GeV beam spreader based on FODO (6.5 m) with 6° dipoles, ISR on and CSR off. Left to right: projected normalised horizontal emittance (black),longitudinal phase space, slice current, slice horizontal normalised emittance, horizontal phase space and slice energy spread.

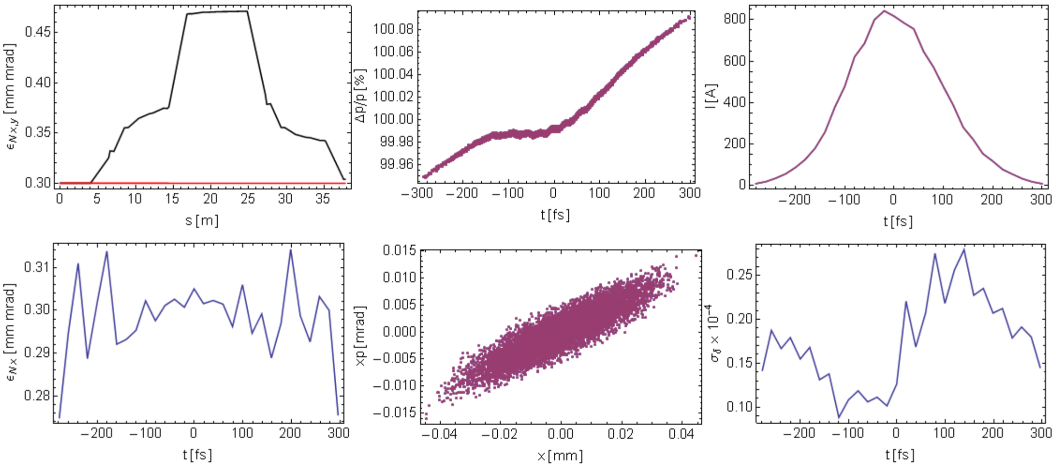

Figure 5.52: Same as Fig.5.51 but with ISR off and CSR on.

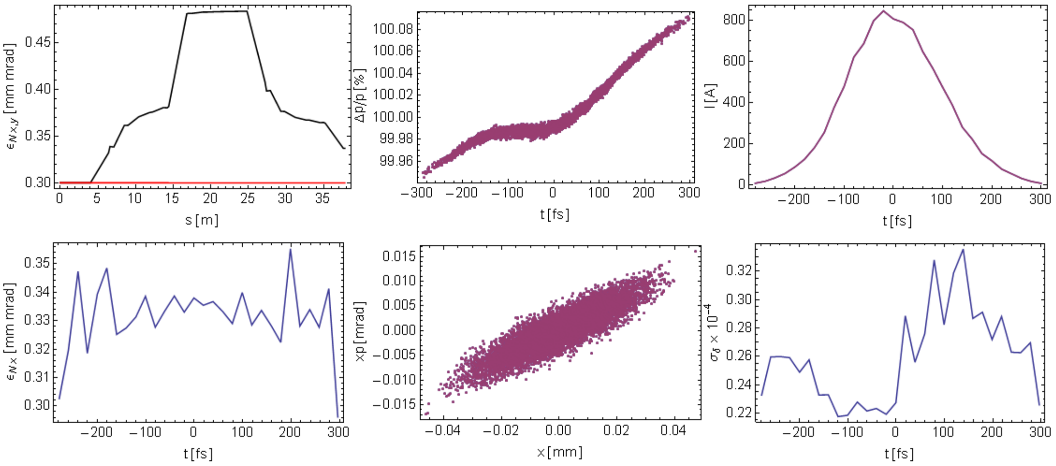

Figure 5.53: Same as Fig. 5.51 but with both ISR and CSR on.

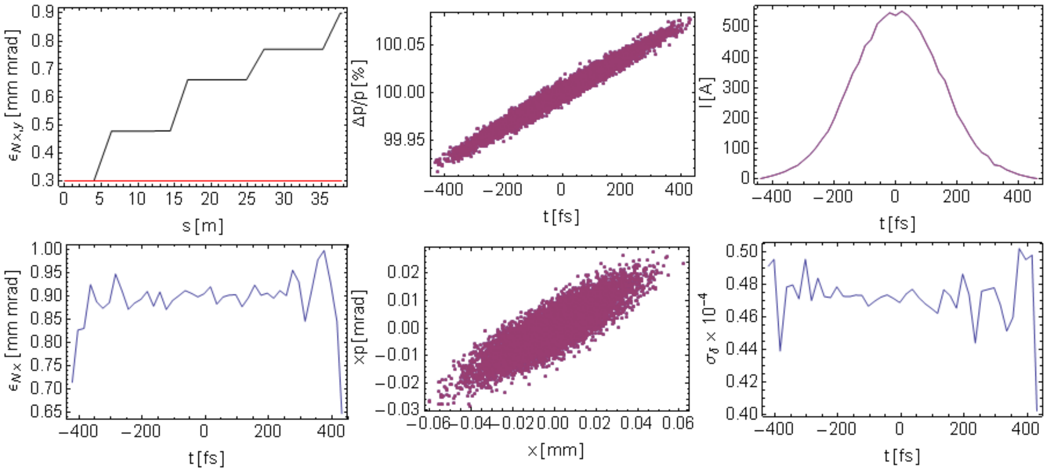

Figure 5.54: Tracking results through 6.6 GeV DBA beam spreader based on FODO (6.5 m) with 12° dipoles with ISR on and CSR off. Left to right: projected normalised horizontal emittance (black), longitudinal phase space, slice current, slice horizontal normalised emittance, horizontal phase space and slice energy spread.

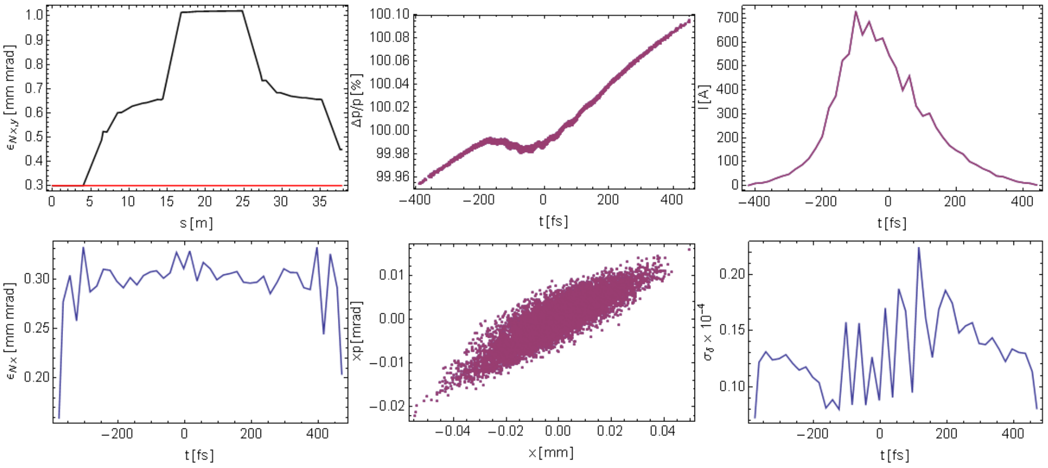

Figure 5.55: Same as Fig. 5.54 but with ISR off and CSR on.

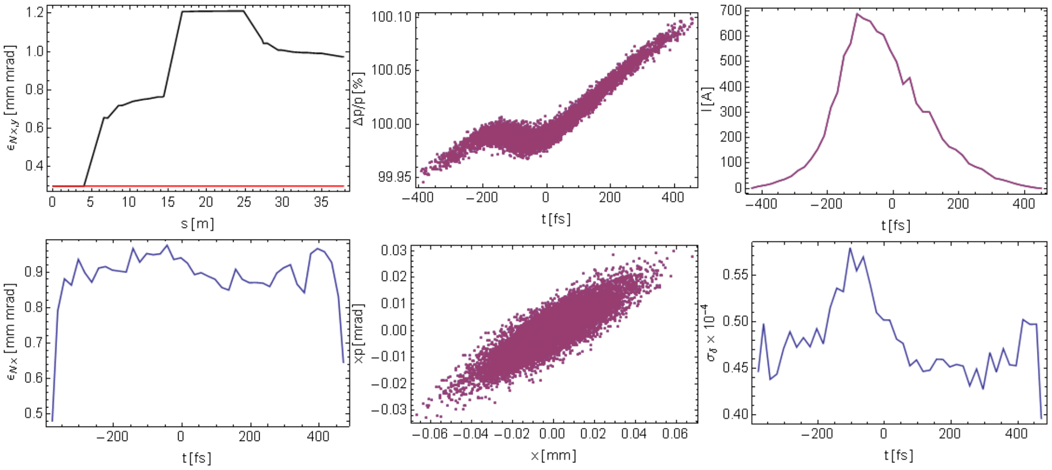

Figure 5.56: Same as Fig. 5.54 but with both ISR and CSR on.

5.6 Lattice Tolerances

As described in Section 2.4, the magnets in an accelerator can be aligned only to a certain accuracy, and the field in the magnet is limited by the stability of the power supplies which power the magnets. With sophisticated laser alignment techniques and accurately marked fiducials, the magnets (specifically quadrupoles) can be aligned within 100 μm with respect to their magnetic centers in transverse directions (DX and DY in the notation used here) and the rotation around the s-axis (referred to as TILT) of 1 mrad. The fractional strength error (FSE) is the deviation from the ideal strength (or bending angle) due to magnet fabrication errors and/or achievable power supply stability. Field strength errors of less than 0.1% are typically required to keep the machine parameters close to the design values. If a lattice uses identical dipoles, it is often possible to power these dipoles in series (all identical dipoles powered using a same power supply) and the same is true for the quadrupoles. This reduces the cost and makes the operation of the facility simpler (but leads to the requirement for better matching in to these sections, as independent control of each magnet is not possible or is restricted). Where magnets are powered in series, this leads to correlations between errors, which must be taken into account in simulations.

5.6.1 Tolerances for 2.2 GeV TBA lattice

For the spreader design described here, the first and the third dipole in arc2 can be connected in series, as can the quadrupoles symmetrically placed in the arcs. Both these cases are included in addition to all magnets being powered independently (no correlations in the errors). The results of these errors on beam parameters: normalised horizontal and vertical projected emittances, energy spread, bunch length and beam centroids in the horizontal and vertical planes are compared. The values of these parame- ters without any errors in presence of CSR and ISR are mentioned at the top of Table 5.6 with “No Error". The effect of errors have been simulated for 100 machines with different sets of random errors in position and field strengths. The 90^{th} percentile of the results from these 100 simulations are listed in Table 5.6.

5.6.2 Tolerances for 2.2 GeV DBA Lattice

To understand the effect of misalignments and field errors in DBA lattices, two FODO based DBA lattices as shown in Fig. 5.57 are used: one with 6° dipoles giving ∼6 m transverse offset in ∼40 m distance and another using two 3° dipoles. The lattice with 3° dipoles uses four pairs of dipoles, with the dipoles within each pair separated by a phase advance of π. The total bending angle in both the 6° and the 3° dipole lattices is 24°. The optics and projected emittances (from tracking) are shown in Fig. 5.58. The CSR compensation is similar in both cases, but lattice with 3° dipoles gives a transverse offset

Table 5.6: Effect of errors on 2.2 GeV beam spreader based on TBA lattice. The values given are the 90th percentile of the distribution from 100 sets of different random errors.

	$\epsilon_x \times 10^{-6}$ [m.rad]	$\epsilon_y \times 10^{-6}$ [m.rad]	$\frac{\sigma_p}{p} \times 10^{-4}$	$\sigma_l \times 10^{-6}$ [m]	Horz Centroid [mm]	Vert. Centroid [mm]
No Error	0.3275	0.3000	1.9938	25.02	8.5×10^{-3}	2.2×10^{-8}
Dipole FSE=1×10^{-3} Uncorrelated errors	0.3541	0.3000	2.0429	25.07	0.3197	5.9×10^{-8}
Quad FSE=1×10^{-3} Uncorrelated errors	0.3322	0.3000	2.0452	25.02	-1.8×10^{-5}	6.2×10^{-8}
Dipole TILT=1×10^{-3}	0.3277	0.3000	2.0443	25.03	-9.6×10^{-5}	2.3×10^{-6}
Quad DX=1×10^{-4}	0.4229	0.3000	2.040	25.11	2.842	5.8×10^{-8}
Quad DY=1×10^{-4}	0.3277	0.3268	2.040	25.03	-1.0×10^{-5}	1.09
Quad TILT=1×10^{-4}	0.3336	0.3071	2.040	25.03	-9.7×10^{-5}	8.2×10^{-5}
All above errors	0.4769	0.3292	2.0433	25.14	2.556	1.156
Dipole FSE=1×10^{-3} Correlated errors	0.3546	0.3000	2.0432	25.07	0.3197	5.7×10^{-8}
Quad FSE=1×10^{-3} Correlated errors	0.3312	0.3000	2.0437	25.07	-5.1×10^{-5}	5.2×10^{-8}

of ∼9 m in ∼66 m, which is comparable to the transverse offset achieved in the TBA lattice for 2.2 GeV described in Section 5.4.1. In both these lattices, the bending angle gives enough transverse separation at the start to avoid clash of magnets with the straight on beam line and the projected as well as slice horizontal emittance are maintained close to the design value.

5.6.3 Comparison of Tolerances

The values of beam parameters for the DBA lattices without any errors in the presence of CSR and ISR are given with “No Error" in Tables 5.7 and 5.8. The effects of errors have been simulated for 100 machines with different random errors in position and field strengths. The 90th percentile of the results from these 100 simulations for the 6° dipole

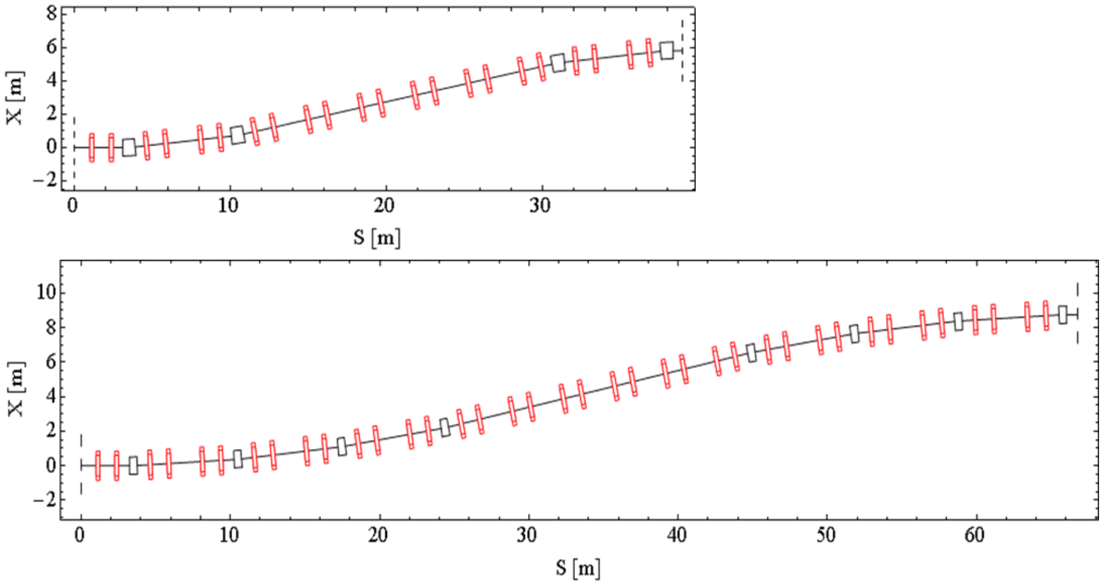

Figure 5.57: DBA lattices used for comparison of tolerances. The one on the top uses 6° dipoles, two bending in one direction and other bending in opposite direction, the total bending experienced by the beam is 24°. The one on the bottom uses four 3° dipoles bending the beam one way separated by number of FODO cells and then bending the beam back by four 3° dipoles. The total bending is by 24°.

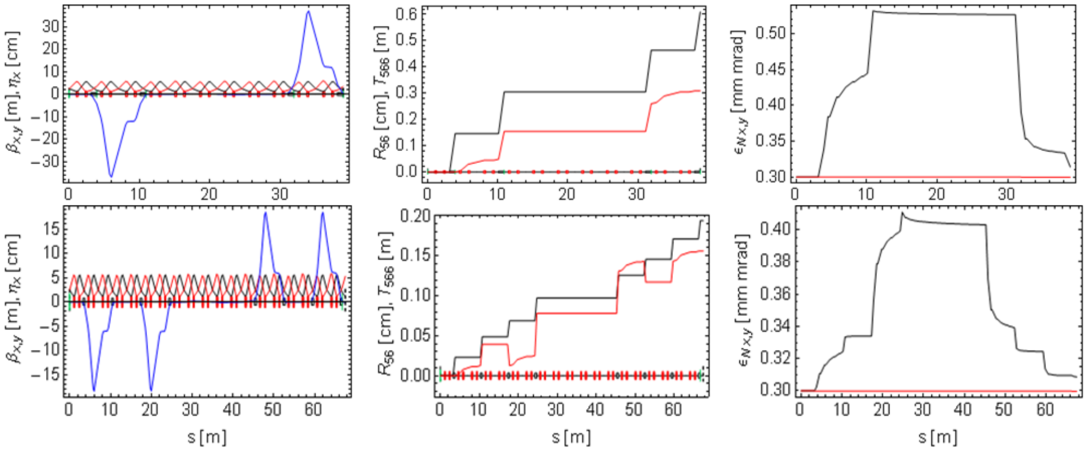

Figure 5.58: Left to right: Optics, R_{56} (black) and T_{566} (red) and normalised projected emittances for the lattices in Fig. 5.57.

Table 5.7: Effect of errors on 2.2 GeV beam spreader based on 6° DBA (based on FODO) lattice. The values given are the 90^{th} percentile of the distribution from 100 sets of different random errors.

	$\epsilon_x \times 10^{-6}$ [m.rad]	$\epsilon_y \times 10^{-6}$ [m.rad]	$\frac{\sigma_p}{p} \times 10^{-4}$	$\sigma_l \times 10^{-6}$ [m]	Horz Centroid [mm]	Vert. Centroid [mm]
No Error	0.3140	0.3000	2.76	26.14	6.36×10^{-3}	4.30×10^{-4}
Dipole FSE=1×10^{-3} Uncorrelated errors	0.3146	0.2998	2.764	26.204	9.44×10^{-5}	5.06×10^{-7}
Quad FSE=1×10^{-3} Uncorrelated errors	0.3136	0.29986	2.764	26.184	3.46×10^{-5}	5.07×10^{-7}
Dipole TILT=1×10^{-3}	0.3135	0.2998	2.764	26.14	6.3×10^{-6}	1.26×10^{-6}
Quad DX=1×10^{-4}	0.3164	0.2998	2.767	26.252	0.871	5.0×10^{-7}
Quad DY=1×10^{-4}	0.3135	0.3040	2.764	26.14	9.2×10^{-6}	6.37×10^{-5}
Quad TILT=1×10^{-4}	0.3136	0.3003	2.764	26.140	6.43×10^{-6}	1.144
All above errors	0.3172	0.3043	2.761	26.20	0.937	1.44
Dipole FSE=1×10^{-3} Correlated errors	0.3146	0.2986	2.764	26.20	0.943	5.06×10^{-7}
Quad FSE=1×10^{-3} Correlated errors	0.3137	0.2994	2.765	26.02	8.95×10^{-6}	2.68×10^{-7}

lattice are listed in Table 5.7 and that of the lattice with 3° dipoles are listed in Table 5.8. Comparison of these two tables show that the effect of all errors are slightly worse in the lattice with 3° dipoles. Therefore, the tolerances of TBA lattice are compared with this double DBA lattice.

Before comparing the tolerances of TBA and DBA (based on FODO) lattices, it is important to point out that for the identical starting beam parameters, the beam parameters at the exit of the beam spreader without any errors are significantly different; particularly, the horizontal emittance (0.3275/0.3089 mm.mrad), momentum spread (1.99 /3.59×10^{-4} and bunch length (25.02/25.72 μm) for TBA/DBA FODO, respectively. The different values in the error-free cases need to be taken into account when comparing

Table 5.8: Effect of errors on 2.2 GeV beam spreader based on 3° double DBA (based on FODO) lattice. The values given are the 90^{th} percentile of the distribution from 100 sets of different random errors.

	$\epsilon_x \times 10^{-6}$ [m.rad]	$\epsilon_y \times 10^{-6}$ [m.rad]	$\frac{\sigma_p}{p} \times 10^{-4}$	$\sigma_l \times 10^{-6} [m]$	Horz Centroid [mm]	Vert. Centroid [mm]
No Error	0.3089	0.29979	3.59	25.72	6.59×10^{-2}	5.94×10^{-4}
Dipole FSE=1×10^{-3} Uncorrelated errors	0.3127	0.2998	3.591	25.49	0.0424	7.08×10^{-7}
Quad FSE=1×10^{-3} Uncorrelated errors	0.3090	0.2997	3.589	25.48	6.91×10^{-5}	7.10×10^{-7}
Dipole TILT=1×10^{-3}	0.3084	0.2998	3.59	25.42	6.51×10^{-5}	8.95×10^{-7}
Quad DX=1×10^{-4}	0.3320	0.2998	3.588	25.55	1.218	7.1×10^{-7}
Quad DY=1×10^{-4}	0.3084	0.3201	3.590	25.48	6.49×10^{-5}	2.12
Quad TILT=1×10^{-4}	0.3085	0.3001	3.590	25.42	6.51×10^{-5}	9.75×10^{-6}
All above errors	0.3321	0.3204	3.594	25.54	1.374	1.321
Dipole FSE=1×10^{-3} Correlated errors	0.3087	0.2997	3.590	25.49	9.27×10^{-3}	7.09×10^{-7}
Quad FSE=1×10^{-3} Correlated errors	0.3106	0.2997	3.358	25.05	6.53×10^{-5}	7.05×10^{-7}

the effects of errors. Comparing the effect of errors in the 3° double bend lattice, it can be observed that the quadrupole displacement in the horizontal plane increases the horizontal emittance and beam offset more in the TBA, whereas the DBA lattice is more sensitive to displacement in the vertical plane. Dipole field errors have a larger impact on the horizontal emittance and beam centroid in the TBA lattice than in the DBA lattice. The errors in the TBA lattice have very little effect on bunch length as the lattice is isochronous, whereas the DBA lattice can change the bunch length (and thus the bunch peak current) due to finite R_{56} if there is residual chirp at the entrance of beam spreader. Even though the bunch centroid can be corrected for systematic errors using corrector magnets, the increase in emittance is difficult to compensate.

5.7 Requirements and Importance of Diagnostics and Instrumentation in Beam Spreader

In order to ensure that the required high quality bunches are delivered to FELs, it is important to characterise the bunches in 6D phase space. Ideally, this should be done before the beam enters the FEL. If a beam spreader is included in the design of the facility, it would be ideal to measure the bunch phase space and slice parameters before and after the beam spreader. However, due to implications for the cost of the facility, an optimum solution of having a dedicated section for full characterisation may be included before the spreader, and some additional diagnostics should be included within and after the spreader to ensure that the bunch properties do not deteriorate too far. If the beam spreader design provides identical beam parameters to a number of FEL lines, it should be sufficient to carry out detailed characterisation only in one beam line, for example, as proposed in the case of NLS [37], where a dedicated beam line parallel to other FEL lines was included for full characterisation. The layout and requirements of different FEL beam lines can however vary significantly (for example, the SwissFEL beam line to Athos is at lower energy than the Aramis beam line) and the unique aspect of each facility needs careful consideration at the design stage. Another important factor is the time structure (bunch repetition rate and separation between bunches) and how bunches are distributed to the FEL beam lines.

The bunch properties that need to be characterised at various bunch charges are: energy, projected and slice transverse emittances, bunch length and projected and slice energy spread. Measurement of energy and energy spread need a spectrometer line, consisting of a dipole with a precisely known magnetic field. It is also useful to have quadrupole magnets in the spectrometer line to control the dispersion and beam size on the downstream optical screen where beam position and beam size are measured as a function of spectrometer dipole field to obtain energy and energy spread values. If the beam power is high (from 100s of watt to 100s of kW depending upon the bunch structure and bunch repetition rate), it is important to decide on the strategy (for example sending only a few bunches) of how beam energy and energy spread could be measured as it will lead to a need for multiple high power beam dumps raising issues of more demanding and expensive radiation shielding.

The projected emittances can be measured using a number of methods; for example by scanning a quadrupole magnet strength and measuring the beam size on a downstream optical screen, or by measuring beam sizes on number of screens located at correct phase advances [119, 154]. In the first method, it is possible to record a number of shots at one setting of the quadrupole to take into consideration the jitter (fluctuations or small variations caused due to limitations on the technical systems) as the same screen remains inserted. When using multiple screens, it is necessary to extract each screen before recording the beam size on the next screen. The DBA spreader lattice based on FODO would readily allow incorporating screens at appropriate phase advances whereas the spreader lattice based on TBA would need a separate section with FODO to incorporate the multiple screens. For measuring bunch slice properties, a combination of a transverse deflecting cavity (TDC) and a screen located with an appropriate phase advance from the TDC can be used.

The TDC also provides high resolution and accurate measurement of bunch length but it is invasive to beam operation and therefore other non-invasive bunch length monitors need to be incorporated (for example, for the purpose of providing a feedback to small changes in RF phases). The likely place for these monitors is just after the bunch compressors but having a non-invasive bunch length monitor at the exit of spreader before entering the FEL is beneficial for tuning the beam line close to the design parameters.

The beam lines incorporating the FELs are long (10-100s of meters) and typically have small undulator gaps (6-8 mm to reach shorter photon wavelength at beam energy of a few GeV). The straightness of the trajectory through these long FEL sections relies on high resolution beam position monitors and beam based alignment. For the FEL to work properly, the beam orbit (offset and angle) entering the FEL section through the beam spreader has to be corrected and maintained to high accuracy. Thus the beam orbit through the beam spreader has to be measured accurately and corrected before entering the FEL. Thus, there is a need to incorporate a combination of steering (small dipole) magnets in the horizontal and vertical planes and BPMs located at correct phase advances throughout the spreader as in the upstream accelerator part.

Another important beam parameter is the time of flight in the beam spreader. The correct setting of R_{56} is necessary to ensure the isochronicity of the spreader design in the case of a spreader design based on TBA. A non-zero value of R_{56} (as in the case of a spreader based on a DBA lattice) combined with a finite beam chirp from the upstream accelerator can lead to a change the bunch length. Equally, a non-zero R_{56} combined with energy jitter on the beam can lead to a change in the time of flight. Hence, it is important to measure the time of flight through the beam spreader accurately. As shown in Chapter 6, experiments on the ALICE TBA arc confirm that the measurement of time of flight can help to set up the beam optics correctly to achieve close to the design performance. This is even more important if the spreader design includes sextupoles, as changes in the alignment of these can lead to changes in R_{56} affecting the beam transport. The isochronicity and the achromaticity of the beam spreader needs to be guaranteed to make the beam spreader as transparent to the beam as possible, and thus a suitable diagnostics system providing the information on time of flight and spurious dispersion (arising due to magnet misalignments) is required.

With non-zero dispersion in part of the beam spreader lattice, there is a possibility to include energy collimation. The FODO based DBA lattice may also provide the required phase advance to collimate the beam halo covering all the transverse phase space. However, the collimator apertures are decided by the undulator gap and the betatron functions in the undulator and at the collimator location. Larger betatron functions in the spreader section helps to open up the collimator gaps (in order to reduce the wake fields). But, in principle, a suitably optimised FODO based DBA lattice may be able to incorporate some collimation (for example, the beam switchyard to the Athos beam line in SwissFEL). Table 5.9 summarises the diagnostics needed to measure various beam properties in a beam spreader, highlighting differences in the beam spreader designs based on TBA and FODO based DBA lattices.

Table 5.9: Possible diagnostics and instrumentation and their locations in TBA and DBA (based on FODO) beam spreaders.

Property	TBA	DBA(based on FODO)	Comments
Projected emittance	Quadrupole scan in matching section between two arcs and optical screen located downstream the quadrupole	Multiple screen measurements may be better suited if FODO quadrupoles connected in series - optical screens (atleast 3) located symmetrically at correct phase advances	Other possibilities such as wire scanners or synchrotron radiation monitor from the spreader dipole are possible in both cases.
Courant-Snyder Parameters	Quadrupole scan in matching section between two arcs - optical screen located downstream the quadrupole	Multiple screen measurements may be better suited if FODO quadrupoles connected in series-optical screens (atleast 3) located symmetrically at correct phase advances	Other possibilities such as wire scanners are possible in both cases.
Achromaticity	Dispersion measurement at exit of each arc	Dispersion measurement after pair of dipoles	Necessary to change beam energy upstream of beam spreader.
Isochronicity	Time of arrival measurements at the exit of each arc	NA - but Time of arrival information will guarantee that the optics is set up properly	If sextupoles are included, need to consider the recommendations from Chapter 6.
Bunch length	Electro-optical sampling before entry to FEL	Electro-optical sampling before entry to FEL	Additional indirect information from Coherent Transition Radiation from final spreader dipole may be useful.
Bunch charge and transport efficiency	ICT at the exit of spreader and calibrated sum signal from BPMs	ICT at the exit of spreader and calibrated sum signal from BPMs	Increase in readings of the radiation monitors and/or the beam loss monitors located along the line can provide indirect evidence of beam loss.
Beam position	BPMs located throughout beam spreader at correct phase advances	BPMs located throughout beam spreader at correct phase advances	
Collimation of beam halo	Suitable high dispersion locations	Suitable high dispersion and other locations for transverse collimation	

5.8 Summary

In order to utilise fully the potential of an X-FEL, it is desirable to incorporate a number of beam lines in the FEL facility. The scheme to switch or spread electron bunches to different beam lines is based on the time structure of the electron beam and the need to choose the rate of bunches feeding in to a particular beam line. The choice of the take-off region of the beam spreader depends on these requirements as well as on the choice of lattice design for the upstream region.

The design of the beam spreader needs to maintain the beam parameters achieved through longitudinal manipulation of bunches whilst preserving the transverse emittance in the plane of bending. With a careful design of beam spreader it is possible to minimise the detrimental effects of CSR. In addition to CSR, the incoherent synchrotron radiation increases the transverse beam emittance at higher energies. The spreader design choices based on double bend achromat and triple bend achromat presented in this chapter can preserve the transverse projected emittance for the range of electron beam parameters described here.

As demonstrated in the simulations presented in this chapter, in addition to suitable lattice design choices, a gradual bending with smaller bending angles in the dipoles is desirable to minimise the CSR effects. This however requires longer lengths of beam line to achieve the required separation for different beam lines and can increase the cost of the facility significantly. The schemes presented in this chapter can be applied at lower and higher energies than covered here. The preservation of the bunch properties will depend on the starting bunch parameters such as bunch charge, bunch length, energy chirp and transverse emittances. For the TBA and DBA (based on FODO) lattices and identical starting beam parameters, the beam parameters at the exit of the beam spreader without any errors are significantly different. The TBA lattice is found to be more sensitive to the quadrupole displacement in the horizontal plane whereas the DBA lattice is more sensitive to the quadrupole displacement in the vertical plane. Dipole field errors have a larger impact on the horizontal emittance and the beam centroid in the TBA.

To ensure that the required high quality bunches are delivered to FELs, the requirements and importance of beam diagnostics and instrumentation in the spreader design are discussed. The differences and possible options of locations of diagnostics devices and instrumentation are highlighted for the TBA and the FODO based DBA lattices.

Chapter 6

Beam Dynamics Studies of ALICE

6.1 Background and Context

The ALICE (Accelerators and Lasers In Combined Experiments) accelerator at Daresbury Laboratory was originally built as an Energy Recovery Linac Prototype (ERLP) to develop the technology and skill base for the then planned 4GLS facility [118, 155]. Even though the 4GLS did not materialise, ALICE demonstrated energy recovery and operation of the first oscillator Infra-Red Free Electron Laser on an energy recovery machine in Europe. In addition, ALICE has evolved as a test bed for various novel concepts and as a technology development facility over nearly a decade [156]. In the last few years the ALICE IR FEL has been used for cancer research [157]. The specific design choice made for ALICE of isochronous “Triple Bend Achromat (TBA)" arcs is one of the most suitable for beam spreaders as described in Chapter 5. Thus the experimental studies on longitudinal beam dynamics carried out on ALICE [158, 159, 160, 161] provide important information for spreader designs. The practical experience gained from these studies also helps to identify the requirements and suitable locations for diagnostics and suggests procedures and methods to be followed to tune the longitudinal beam transport to match closely to the design.

6.2 Overview of ALICE

The ALICE accelerator consists of a DC gun, a superconducting booster, and a main energy-recovery loop incorporating a superconducting linac, a bunch compressor chicane and an undulator as shown in Fig. 6.1. The DC gun is operated with a negative electron affinity GaAs photocathode, illuminated by frequency-doubled light (532 nm) from a mode-locked Nd:YVO4 laser with an oscillator frequency of 81.25 MHz. Two laser pulse lengths (7 psec and 28 psec) were studied in detail to measure their effect on transverse and longitudinal electron bunch properties [162, 163]. The value of 28 psec was later used in regular operation. The emitted electrons are accelerated to a kinetic energy of 325 keV. A solenoid placed at the exit of the gun is used for emittance compensation.

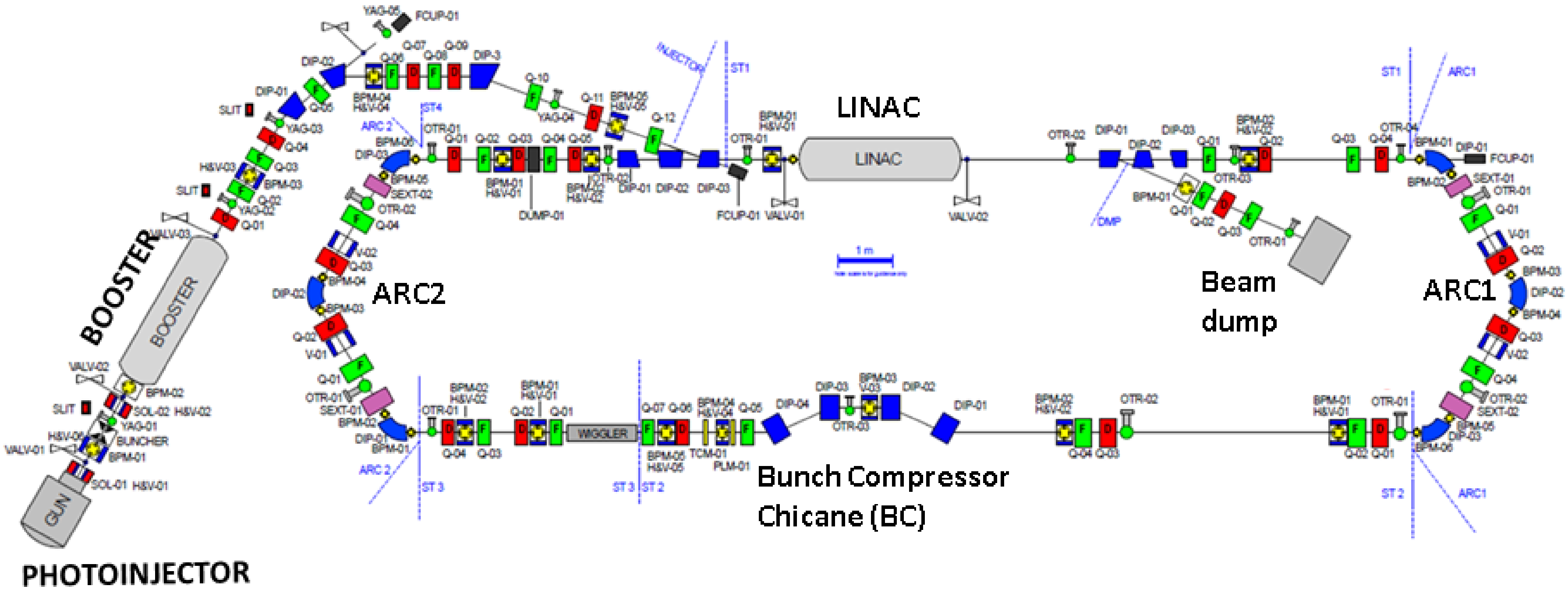

Figure 6.1: Layout of ALICE showing the DC gun driven by a photoinjector laser (PHOTOINJECTOR), buncher cavity, superconducting booster linac (BOOSTER), injection line, superconducting linac (LINAC), ARC1 (bending the electron beam by 180°), bunch compressor chicane (BC), FEL, second arc ARC2 bringing the beam for energy recovery through the linac, and a chicane to divert the low energy beam to the beam dump.

A single-cell, normal conducting cavity (buncher) operating at 1.3 GHz is used for velocity bunching of the bunch before the bunch enters the booster. The booster consists of two superconducting 9-cell TESLA-type cavities operating at 1.3 GHz which accelerate electrons to beam energy of $\sim$6.5 MeV. The injection line after the booster consists of number of quadrupoles, a double bend achromat, a dogleg formed by a dipole in the injection line and the last dipole of the merger chicane to merge the beam with re-circulation loop. The injection line is equipped with several optical screens, a charge monitor and steering magnets to correct the beam path. The dogleg is achromatic but not isochronous and has a small R_{56} (by design). The layout of the facility was constrained by the existing well shielded enclosures from previous facility in this area as well as some existing dipole magnets from other facility, resulting in a relatively long injection line ($\sim$10 m between booster exit and entry to linac). The injection line layout allows to direct the beam straight on to an optical screen, which is used for cresting the booster cavities as well as for characterisation of energy and energy spread.

The injection line merges with the last dipole of the chicane located at the entry of the linac in the main loop. The electrons get accelerated in the linac up to $\sim$28 MeV. The beam transport downstream of the linac consists of a TBA arc (ARC1), a bunch compression chicane (BC), an adjustable gap undulator forming part of a low gain oscillator FEL, a second TBA arc (ARC2) and a high energy chicane to return the beam to the linac for energy recovery. On the return path, the electrons enter the linac at 180° phase difference from the accelerating phase, so that electrons give energy back to the cavities (deceleration). To optimise energy recovery, the path length can be adjusted by mechanical movement of ARC1. The low energy electrons after energy recovery get deflected in to the beam dump line through the magnetic chicane located after the linac.

The first dipole in ARC1 and an optical screen located downstream are used for cresting the linac cavities and setting them with required off-crest phases for bunch compression. The quadrupoles outside the arcs ensure matching of the optics into/out of the arcs. The quadrupoles in the straight section ST2 (exit of ARC1 to entry of FEL) match the optics to the bunch compression chicane and the adjustable gap undulator. The quadrupoles in straight ST4 (exit of ARC2 to exit of injector merger chicane) match to the injection merger chicane and entry to linac and through the extraction chicane to the beam dump. The facility includes a number of small dipole magnets to steer the beam correctly on the design trajectory. Various diagnostic devices such as optical screens, Faraday cups and beam position monitors provide the tools to characterise the beam and its transport through the machine.

The main demands on beam quality come from the IR-FEL requirements [164]. The bunches must be compressed to $\sim$1 psec to provide a high bunch peak current, while the single bunch energy spread should be less than 200 keV (0.7%). Transverse emittance requirements are less stringent, with <10 mm.mrad (normalised) being acceptable.The

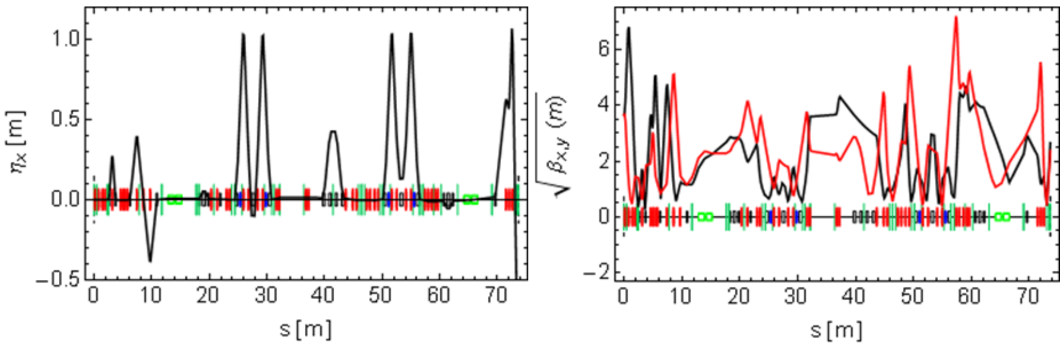

Figure 6.2: The dispersion function and $\sqrt{\beta}$ functions (horizontal in black and vertical in red) for the ALICE design lattice from booster exit to beam dump.

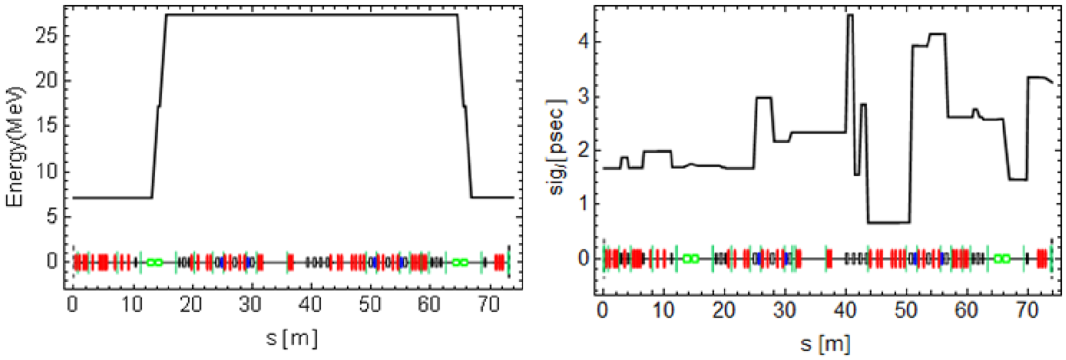

Figure 6.3: Beam energy and bunch length in ALICE starting from booster exit to beam dump.

main machine and beam parameters of ALICE are given in Table 6.1. The design dispersion function and square root of the betatron function along the lattice are shown in Fig. 6.2. Figure 6.3 shows the rms bunch length and the beam energy along the machine.

Table 6.1: Main ALICE machine and beam parameters

DC Gun Voltage	325 kV
Photocathode	GaAs
Photoinjector drive laser	Nd:YVO4
RF Frequency	1.3 GHz
RF gradients	10 MV/m
Injector energy	6.5 MeV
Bunch repetition frequency	up to 81.25 MHz (variable)
Train repetition frequency	1 - 10 Hz
Train length	up to 100μs
Beam energy	28 MeV (Max)
Bunch charge	80 pC (Max)
Normalised transverse emittance	<10 mm.mrad
Bunch length after compression	< 1psec rms

Coherent synchrotron radiation (CSR) is not an issue for the beam parameter regime

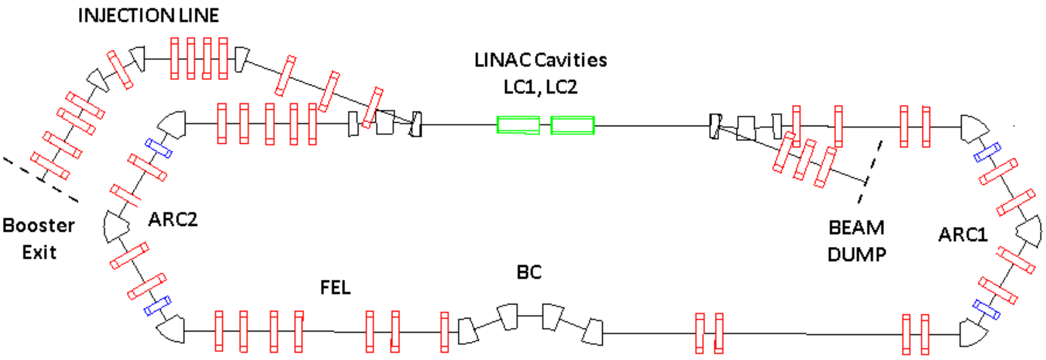

Figure 6.4: ALICE lattice used for beam tracking from exit of the booster. Red rectangles show quadrupole magnets, black shapes show dipole magnets.

chosen for ALICE, e.g. the bunch length is several psec long while passing through the arc and bunch charge up to 80 pC. Initial studies at the time of design show that the emittance blowup up to 50% may take place due to CSR if transverse emittance of ∼5 mm.mrad and a bunch length of 0.5 psec in arcs is assumed [165]. ALICE does not operate in this parameter range and so issues related to CSR cannot be tested on ALICE experimentally.

An IR-FEL has been operated on ALICE since 2010, and the facility has also been used as a THz source. Both these applications rely on short compressed bunches (bunch length of ∼1 psec) and an important aspect of the machine to deliver this is the longitudinal transport, as detailed in next section.

6.3 Longitudinal Beam Transport

The longitudinal beam transport properties in ALICE can be illustrated by tracking the beam. Simulations from the gun to the exit of the booster are performed using space charge codes. For the purpose of the studies described here, the starting point is from the exit of the booster, where the operational energy is ∼6.5 MeV. The machine layout used for simulations is shown in Fig. 6.4.

Features of the main loop relevant for longitudinal transport consist of a TBA arc, a compression chicane and a second TBA arc to de-compress the bunches on their return to the linac for energy recovery. Fig. 6.5 shows details of the layout of ARC1 namely: two quadrupoles to match the lattice functions entering the arc, three 60° dipoles (DIP-01, 02, 03), four quadrupoles (QUAD-01, 02, 03, 04), two sextupoles (SEXT-01, 02), two vertical steering magnets (VSC-01,02), and two quadrupoles at the exit of the arc to match the lattice functions to the matching section to the straight containing the bunch compression chicane and FEL. There are six beam position monitors in the arc (BPM-01, 02, 03, 04, 05, 06), one at the entry and one at the exit of each dipole magnet. Two optical screens are located symmetrically adjacent to the sextupoles.

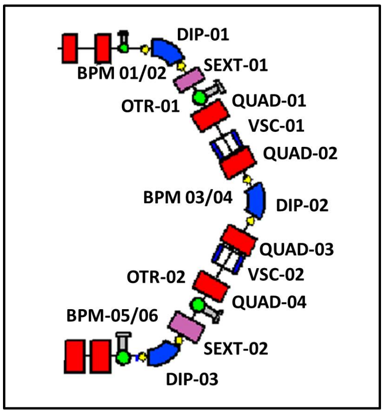

Figure 6.5: Details of ALICE ARC1 showing the locations and nomenclature of the magnets and diagnostics. The quadrupole doublets located at the entry and the exit of the arc are used to match the lattice functions to/from the arc.

All dipoles, quadrupoles and sextupoles are independently powered. The beam position monitors were not used during routine operation due to technical issues but were used with special electronics [166, 167] attached to a few BPMs at a time for some of the dedicated beam dynamics studies reported here.

In principle, the arc design is capable of generating sufficient R_{56} for bunch compression for FEL operation. However, a four dipole compression chicane is instead included for this purpose for better control over compression and linearisation. The notation used here is that of *elegant*, which assumes $z < 0$ for bunch head, and thus the R_{56} of the chicane is negative (-0.28 m). The design assumes that the bunch compression for FEL operation is achieved using the bunch compression chicane, and thus requires that ARC1 be isochronous. A combination of setting ARC2 to provide $R_{56} = +0.28$ m and off-crest operation of Linac (with respect to decelerating phase) de-compresses the bunch on second pass through Linac. This reduces the energy spread bringing it close to the initial value from the injector before the beam enters the dump line. The reduced energy spread imply reduction in beam apertures in the dump line. Thus, the arcs need only supply zero or positive R_{56} to give a full range of longitudinal manipulation. A triple-bend achromat design for the arc satisfies all this requirement to be met. TBA arc design contains the minimum number of dipoles necessary for isochronous transport [168, 169]. Given a limit on the quadrupole strength, there are constraints on the drift lengths possible in the TBA cell to provide isochronous transport. A single TBA cell for each arc was chosen [170] in order to achieve a compact design. Each dipole is ∼0.5 m long and has a magnetic dipole field of ∼0.19 T at an operating energy of ∼28 MeV. The arc has a symmetry about the centre of the middle dipole DIP-02. The contributions of the arc dipoles to R_{56} are determined by the dispersion and the bending radius of the dipole as described in Chapter 2. The requirement for an achromatic arc imposes constraints on the dispersion function and its derivative at the entrance of the central dipole. At the design stage, the

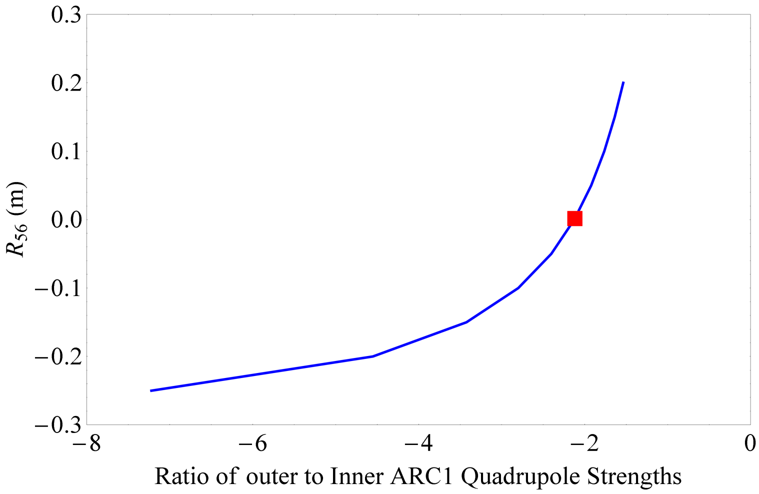

Figure 6.6: Variation of R_{56} while maintaining the achromatic condition in the arcs as the outer quadrupole strengths are varied. The red marker shows the (nominal) isochronous operating point for ARC1.

drift lengths in the arc and quadrupole strengths were chosen to give an isochronous arc with zero dispersion at the entrance and exit of the arc. The optimum solution takes into account the footprint of the arcs along with the apertures and maximum operating fields in the magnets.

For the optimised arc design in ALICE, it is possible to tune the arc quadrupoles to give small positive or negative values of R_{56} while maintaining the achromatic condition. Fig. 6.6 shows the variation of R_{56} when ARC1 outer quadrupoles QUAD-01/04 and inner quadrupoles QUAD-02/03 are varied independently to keep the achromatic conditions. The value of R_{56} has a stronger dependence on the outer quadrupoles QUAD-01/04 than on the inner quadrupoles QUAD-02/03. Fig. 6.7 shows the dispersion function from the entry of ARC1 to the exit of ARC2 for three values of $R_{56} = 0, -0.28\,\text{m}, +0.28\,\text{m}$ in ARC1, and the T_{566} values for the corresponding settings. The chicane and ARC2 are set to give $R_{56} = -0.28\,\text{m}$ and $+0.28\,\text{m}$, respectively. The adjustability of this design makes it possible to obtain R_{56}=+0.28 m in ARC2 and when combined with off-crest deceleration through Linac, results in obtaining smaller energy spread required for the energy recovery. This is achieved by driving the dispersion to a negative value in the central dipole using quadrupoles; tuning of R_{56} and T_{566} is possible by adjusting quadrupoles and sextupoles, respectively in the arcs. Sextupoles are required in the first arc to linearise the longitudinal phase space at the FEL as mentioned in Chapter 3, whilst those in the second arc minimise the energy spread after deceleration so that the disrupted electron bunches may be cleanly extracted to the beam dump [165]. As mentioned in Chapter 3, the chicane provides a non-linear compression T_{566} which scales with R_{56} of the chicane as T_{566}/R_{56}=−3/2. Thus it is not possible to have independent control over T_{566} for a chosen R_{56} in the

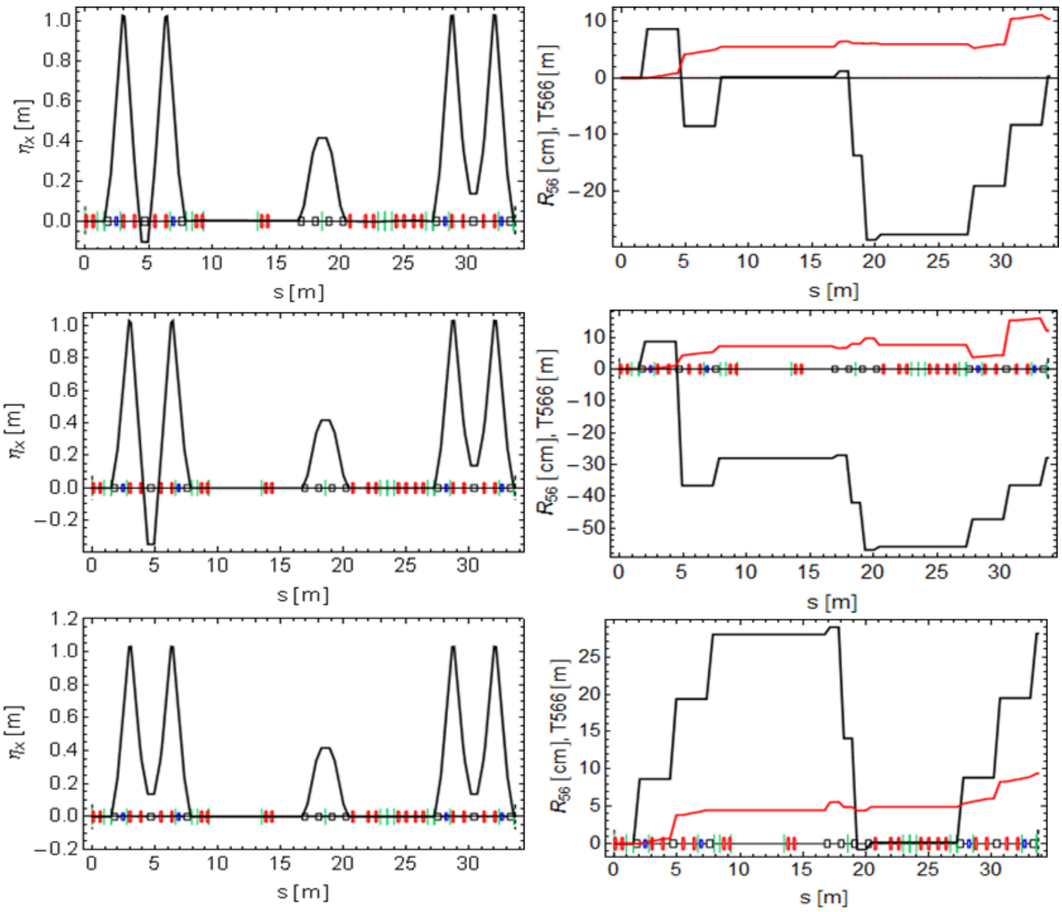

Figure 6.7: Dispersion functions (left) and R_{56} (black) and T_{566}(red) (right) from entry of ARC1 to exit ARC2 for 3 different quadrupole settings while retaining the achromatic condition. R_{56} (ARC1)=0 (top), -0.28 m (middle), $+0.28$ m (bottom). The chicane gives R_{56}=-0.28 m and ARC2 is set to give R_{56}=+0.28 m in all three cases.

chicane. It is however possible to manipulate T_{566} using sextupoles in the arcs, without affecting the R_{56} provided by the chicane.

The chicane is composed of rectangular dipoles which are tilted (in the horizontal plane) at half the bend angle. This minimises the deviation of beam trajectory from the centre of the poles which relaxes demands on the magnetic field quality. The R_{56} at the chicane is given by summation of the R_{56} from ARC1 and the chicane. Thus a non-isochronous arc has important consequences for achieving bunch compression required for the FEL operation.

As mentioned in Chapter 3, linearisation of the longitudinal phase space is required to achieve the required bunch peak current. This is achieved in ALICE by incorporating two sextupoles in each arc at locations with non-zero dispersion. In an ideal machine, the centres of the sextupoles are aligned with the reference (or design) trajectory and the beam entering the arc is assumed to follow this reference trajectory. However, in ALICE, these conditions were not strictly enforced for the studies reported here, because

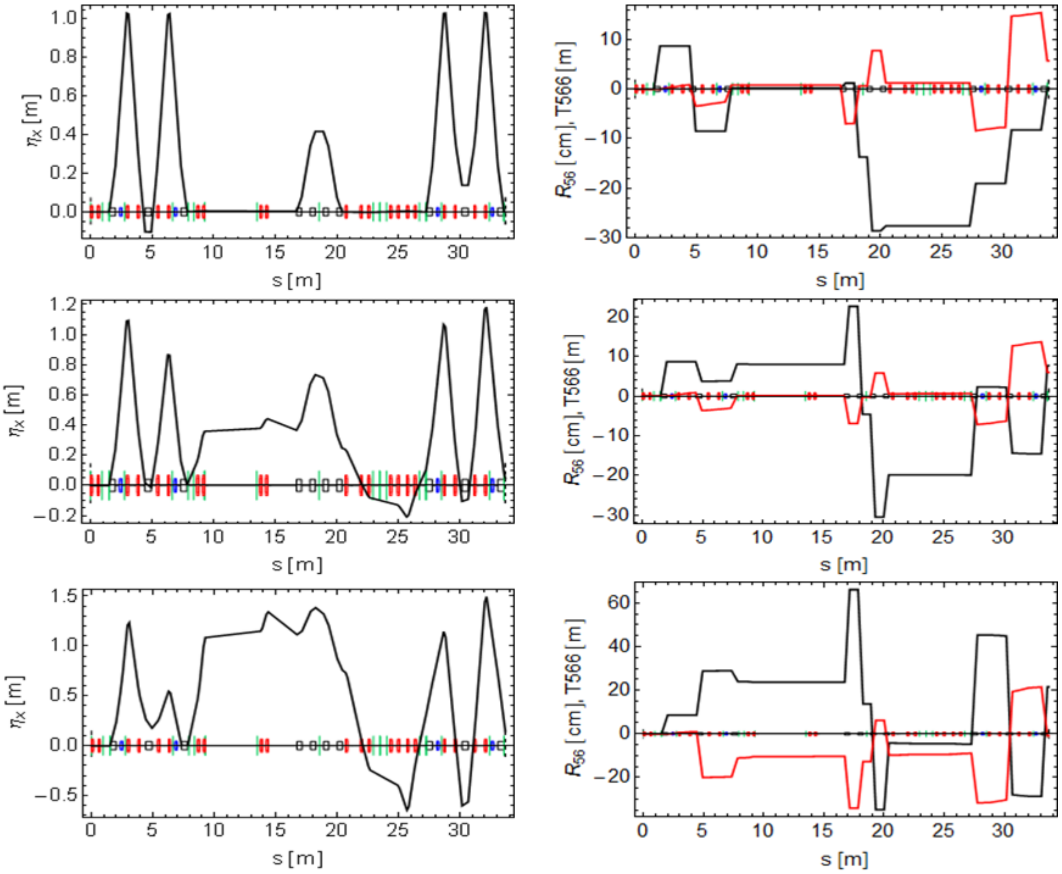

Figure 6.8: Changes to dispersion (left) and R_{56} (black) and T_{566} (red) (right) from entry of ARC1 to exit of ARC2. Top to bottom: with no beam off-set through first sextupole operating at K_2=219 m^{-3}, +5 mm beam offset in SEXT-01 set at K_2=219 m^{-3}, beam offset +5 mm through SEXT-01 set at K_2=657 m^{-3}.

of limitations on the ability to measure and correct the trajectory. The lack of capability to de-gauss the arc magnets (in order to set them correctly corresponding to the beam energy) adds further to the deviation from an ideal trajectory from day to day. As a result of this, the beam passing off-axis in powered sextupoles experiences a quadrupole field. This quadrupole field not only modifies the dispersion function (affecting the R_{56} and T_{566} at the exit of the ARC1) but also changes the transverse optics. Fig. 6.8 shows how the dispersion and R_{56} as well as T_{566} change for a beam offset of +5 mm through the centre of first sextupole powered at two different operational settings of sextupoles. Thus, a combination of beam offset and powered sextupoles can adversely affect the intended longitudinal beam transport.

For tracking the beam through ALICE, the starting point is from the exit of the booster, where the operational energy is ∼7 MeV. Two different initial beam distributions are considered: first with a Gaussian distribution in transverse and longitudinal planes and the second based on tracking a bunch with the space charge code ASTRA [171]. For tracking using a Gaussian bunch, an electron bunch is tracked through the lattice starting

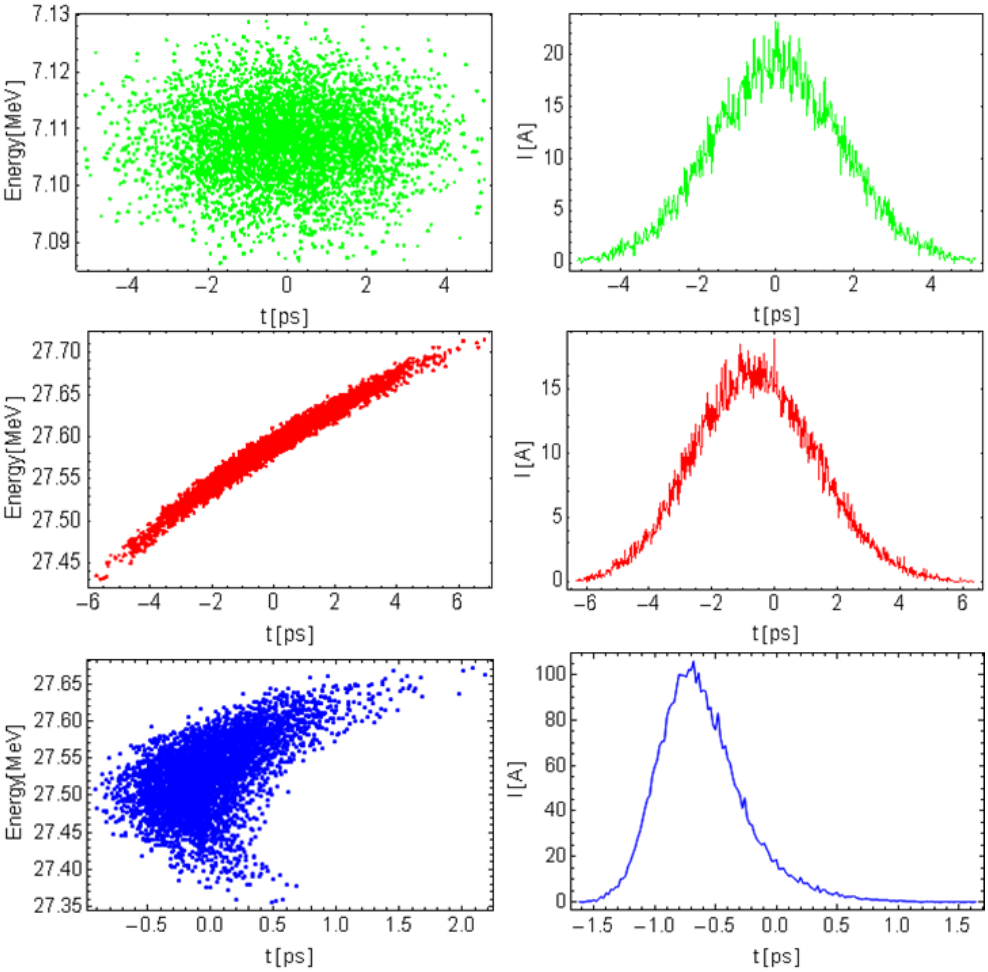

Figure 6.9: Longitudinal phase space (left) and slice current (right) starting with an ideal Gaussian bunch at the exit of booster. Booster exit (green), ARC1 exit (red) and chicane exit (blue). Sextupoles in ARC1 are not powered.

from booster exit. The transverse distribution is calculated using the Courant–Snyder parameters and normalised beam emittances of 5 mm.mrad. An uncorrelated fractional energy spread of 0.001 and rms bunch length of 500 μm are used. In order to achieve optimum bunch compression, ARC1 is operated as isochronous and bunch compression is done using the chicane. The linac cavities need to be operated at 10° off-crest to compress the bunch. The longitudinal phase space and the slice current at the exit of the booster, exit of the linac and the exit of the chicane are shown in Fig. 6.9. The longitudinal curvature is corrected using sextupoles located in the arc as shown in Fig. 6.10. The sextupole strengths are required to be set at 300 m^{-3}.

The bunch tracking simulations of the injector (cathode to exit of the booster) for the operating experimental settings give a bunch distribution with positive chirp. In order to cancel this chirp, the linacs need to operate at 13° off-crest. The longitudinal phase space and the slice current at the exit of the booster, exit of the linac and the exit of the chicane in this configuration are shown in Fig. 6.11. The longitudinal curvature is

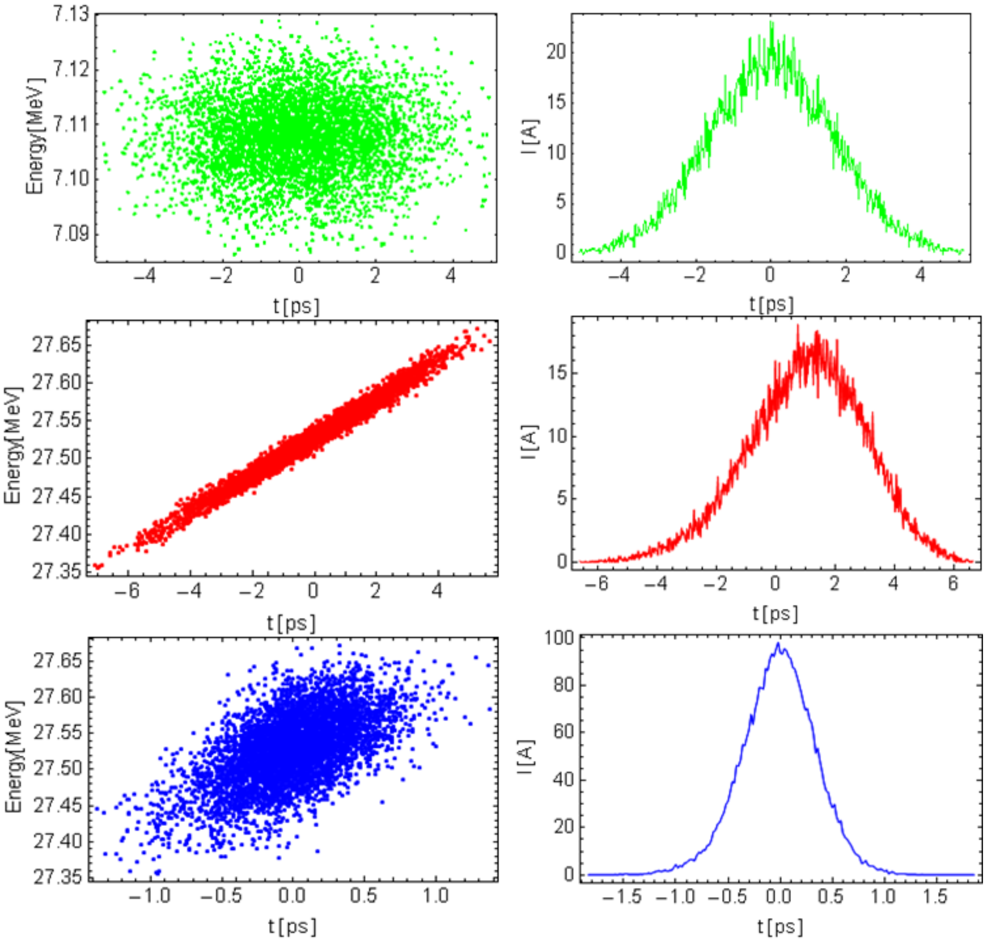

Figure 6.10: Longitudinal phase space (left) and slice current (right) starting with an ideal Gaussian bunch at the exit of booster with both sextupoles in ARC1 powered at 300 m^{-3}. Booster exit (green), ARC1 exit (red) and BC exit (blue).

corrected using sextupoles located in the arc resulting in higher slice current as shown in Fig. 6.12. The sextupole strengths are required to be set at 500 m^{-3} to recover a similar slice current as before.

6.4 Experimental Studies

The off-axis sextupoles also affect the transverse beam shape because of both the linear focusing from the quadrupole component and also because of second-order effect. The simulated transverse beam shapes with on-axis and off-axis sextupoles are compared in Fig. 6.13. The experimentally recorded beam shape on the optical screen downstream of the arc qualitatively shows the effect of a perturbation in the linear optics as well as non-linear distortion from the sextupoles (Fig. 6.14). Due to screen saturation it is not possible to quantitatively compare the beam image in this case with simulations.

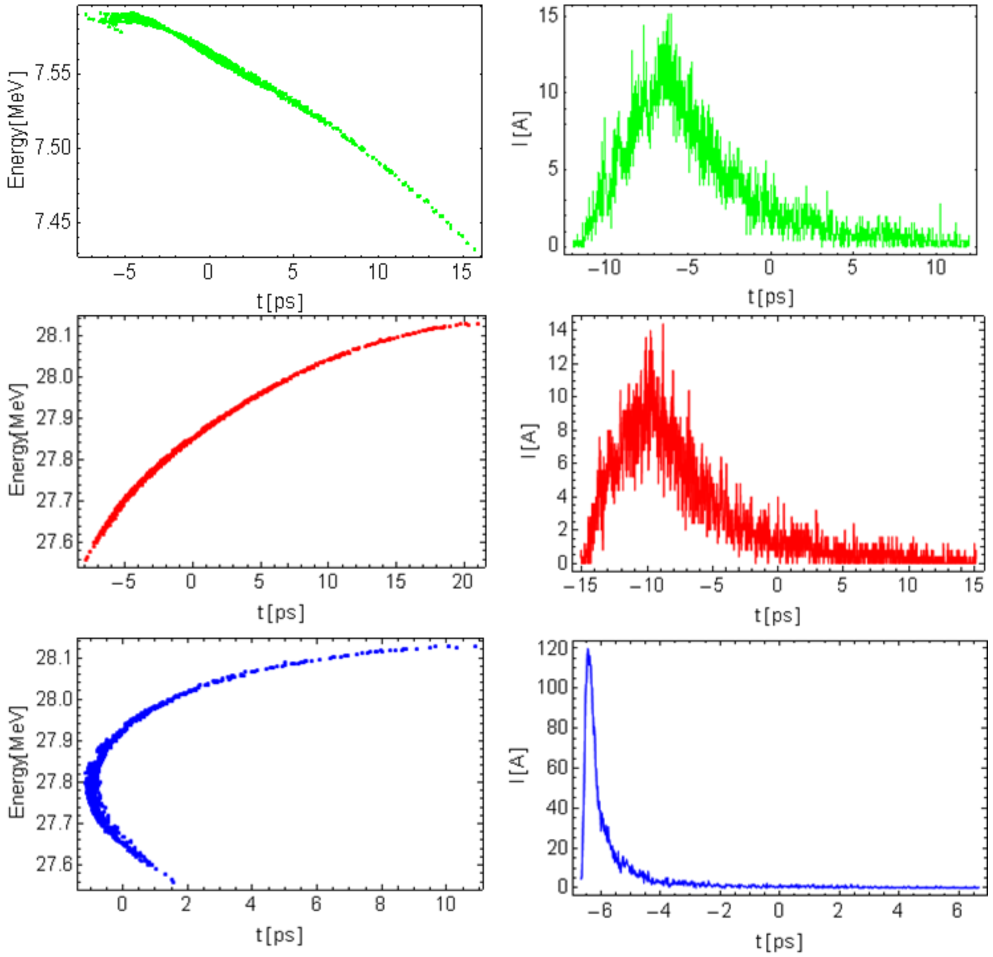

Figure 6.11: Longitudinal phase space (left) and slice current (right) starting with tracked bunch for experimental settings at the exit of booster. Booster exit (green), ARC1 exit (red) and BC exit (blue). ARC1 sextupoles are not powered.

6.4.1 Time of Arrival Measurements

Time of Arrival (TOA) measurements converted to relative path length can be used to extract the lattice quantities R_{56} and T_{566} if the path length is measured whilst varying the beam energy. For the measurement reported here, the voltage impulse of the passing electron bunch on a BPM was observed on a high resolution oscilloscope. The button BPMs used for these measurements give a clear zero cross in the voltage impulse (shown in Fig. 6.15) when the bunch arrives. The shape of the voltage impulse does not depend on the size of the signal due to beam position or bunch charge. For measurements of R_{56} in ARC1 a button BPM (BPM-06) located at the exit of the final dipole DIP-03 was used.

The TOA of the bunch is measured relative to the nearest zero-crossing of the Master Oscillator signal. The Master Oscillator drives the timing and synchronisation of the RF and laser as well as the timing signals to other devices. The TOA for a given beam energy and lattice setting is measured as the average TOA of the first bunch in each bunch train,

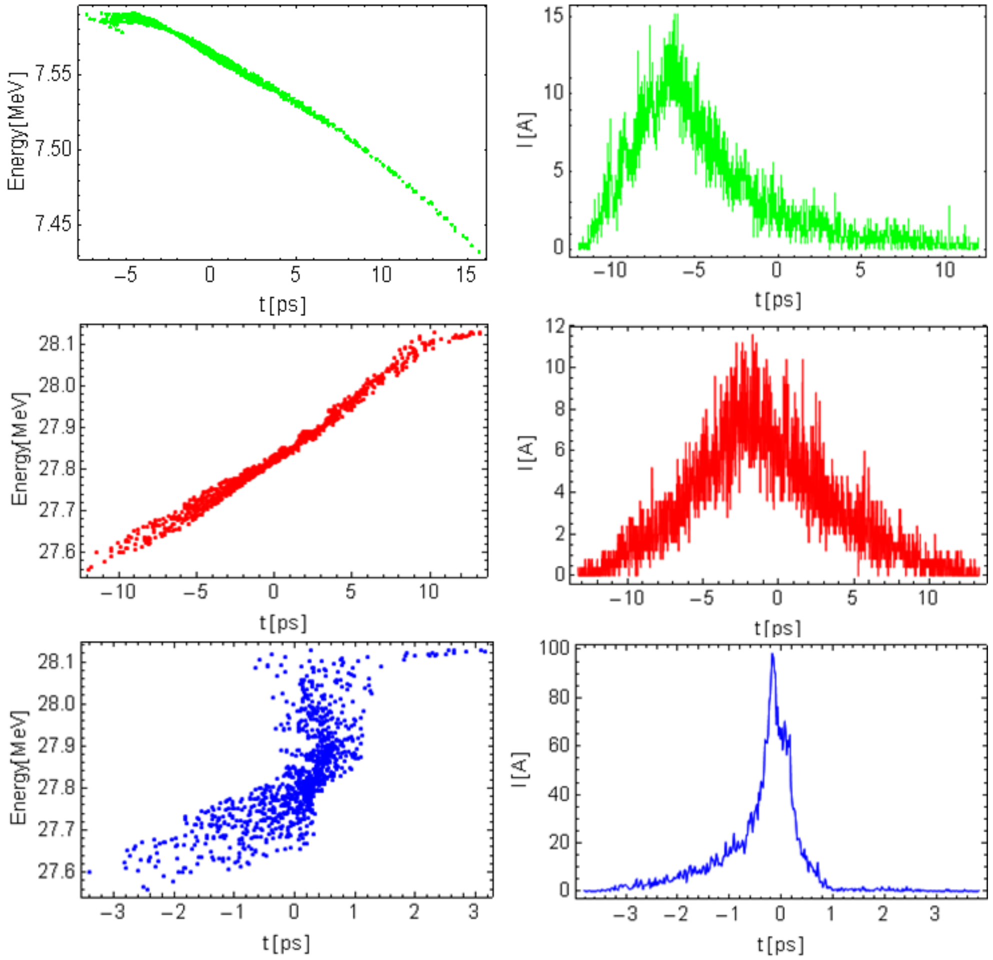

Figure 6.12: Longitudinal phase space (left) and slice current (right) starting with tracked bunch for experimental settings at the exit of booster. Booster exit (green), ARC1 exit (red) and BC exit (blue). ARC1 sextupoles are set at K_2=500 m^{-3}.

over many trains. The TOA distribution was measured over 100 trains, which gives an accuracy of around 0.5 psec (0.15 mm) in the TOA (path length) measurement. The TOA was measured at different beam energies (a few percentage around the nominal energy). The curve of path length vs energy deviation was fitted with a polynomial, the coefficients giving the matrix elements R_{56}, T_{566} directly.

The measured and simulated path length without powering the sextupoles in ARC1 are shown in Fig. 6.16. The matrix elements R_{56} and T_{566} from fitting a polynomial are shown in Fig. 6.17 and Fig. 6.18, respectively. The measured experimental data on these figures show the discrepancy with simulations.

Fig. 6.19 shows a comparison of experimental measurements and simulated results with SEXT-01 off, set at 219 m^{-3} and set at 657 m^{-3}. For simplicity the effect of sextupoles, results with only one sextupole are included here but the second sextupole affects the beam transport in a similar way to the first. The sextupole has the expected effect on the dependence of path length on beam energy in ARC1.

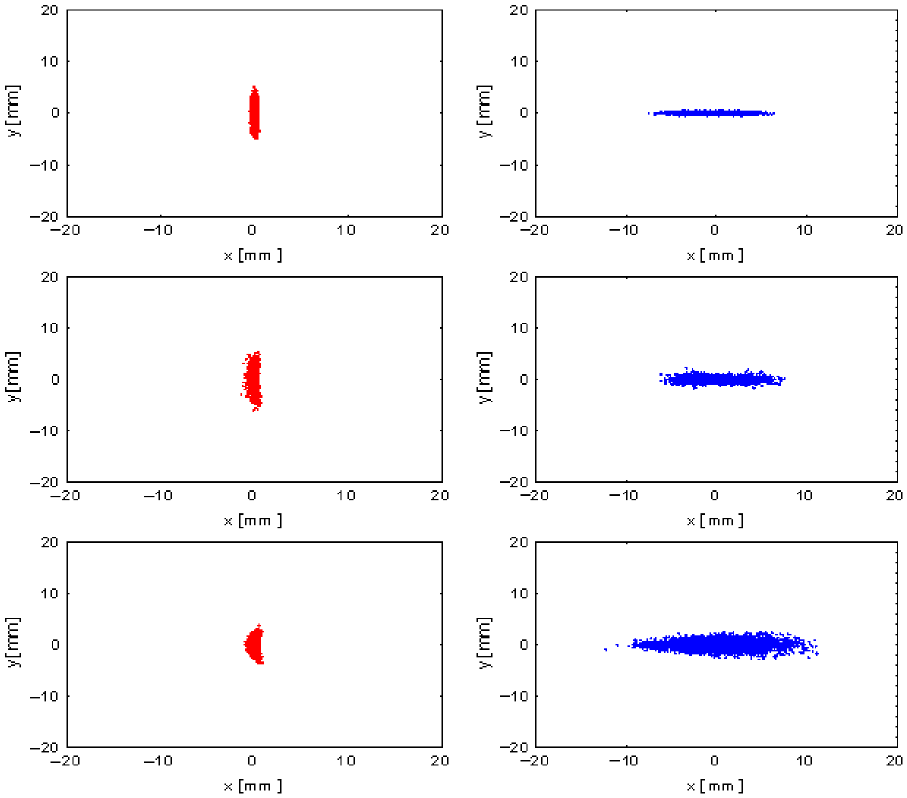

Figure 6.13: Transverse beam shape at the exit of ARC1 (left) and at the exit of the bunch compression chicane (right) without sextupoles (top), with both sextupoles operating at K_2=648 m^{-3} without transverse offset (middle) and with +5 mm transverse offset in horizontal plane (bottom).

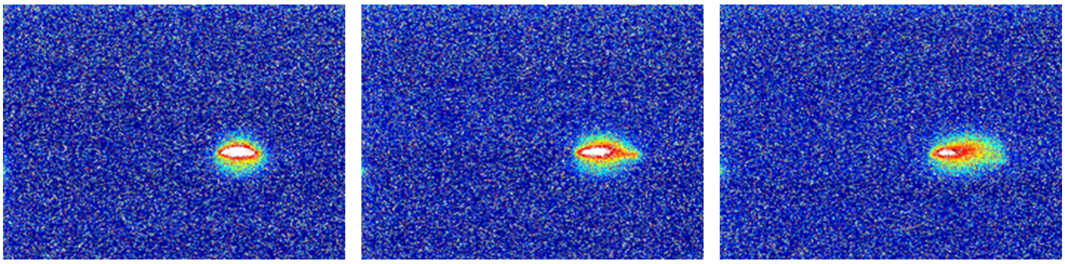

Figure 6.14: Screen images before chicane when ARC1 SEXT-01 is off (left), set at K_2= 300 m^{-3} (middle) and K_2= 750 m^{-3} (right).

In order to see how the path length changes if the beam passes off-axis through the sextupoles, *elegant* simulations are carried out by passing the beam off-axis through SEXT-01 by +5 mm and -5 mm. The path length curves are shown in Fig. 6.20 and Fig. 6.21 and the values of R_{56} and T_{566} calculated using these curves are given in Fig. 6.22 and Fig. 6.23. Since the measured path length curves are qualitatively different from the simulation results for higher values of sextupole strengths, it can be inferred that the beam offset through sextupoles is much smaller than ±5 mm. Separate studies carried out on steering the orbit through SEXT-01 by changing ARC1 dipole (DIP-01) current, gives an

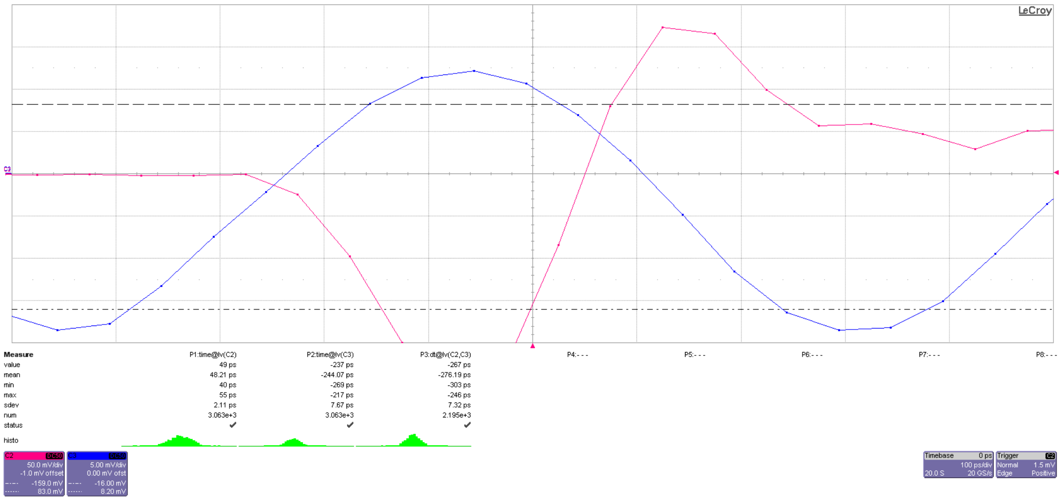

Measure	P1:time@lv(C2)	P2:time@lv(C3)	P3:dt@lv(C2,C3)	P4:- - -	P5:- - -	P6:- - -	P7:- - -	P8:- - -
value	49 ps	-237 ps	-267 ps					
mean	48.21 ps	-244.07 ps	-276.19 ps					
min	40 ps	-269 ps	-303 ps					
max	55 ps	-217 ps	-246 ps					
sdev	2.11 ps	7.67 ps	7.32 ps					
num	3.063e+3	3.063e+3	2.195e+3					
status	✓	✓	✓					
histo								

Figure 6.15: High resolution oscilloscope traces showing ARC1 BPM-06 trace (magenta) and master oscillator signals (blue). The relative time between the zero-cross in the voltage impulse from BPM-06 is measured with respect to fixed timing signal from the master oscillator to measure time of arrival of bunch at the exit of ARC1.

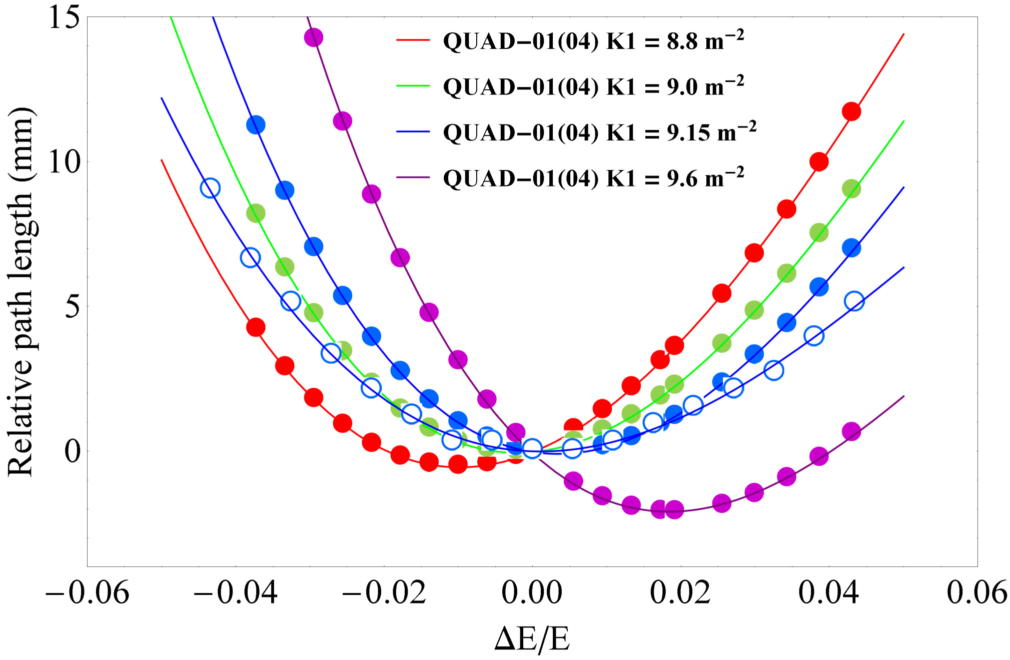

Figure 6.16: Simulated with *elegant* (filled markers) and experimentally measured (unfilled markers) path length at the exit of ARC1 without powering sextupoles by varying strengths of ARC1 outer quadrupoles.

estimated beam offset of ∼2.5 mm at the SEXT-01 location [160]. Fig. 6.24 shows the simulated path length curves for SEXT-01 horizontally offset by +2.5 mm. Figure 6.25 and Fig. 6.26 compare the measured values of R_{56} and T_{566} with simulations using SEXT-01 on axis and horizontally offset by +2.5 mm. Although there is poor agreement between the measurements and simulations for the R_{56} values, the values of T_{566} agree very well

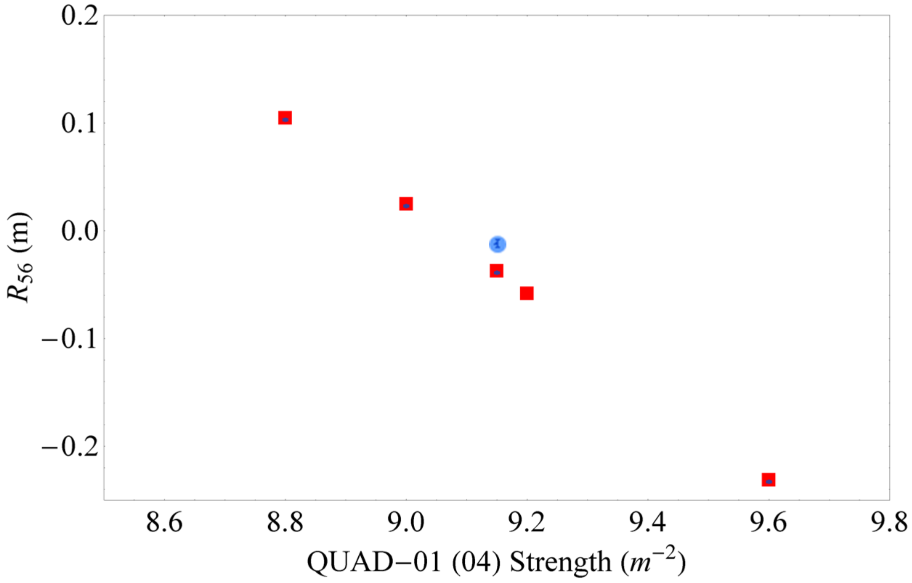

Figure 6.17: Estimated values of R_{56} from fitted polynomials in Fig.6.16. Red markers shows simulated data and blue marker show the estimated R_{56} from experimental data. Error bars from polynomial fitting are superimposed on the markers.

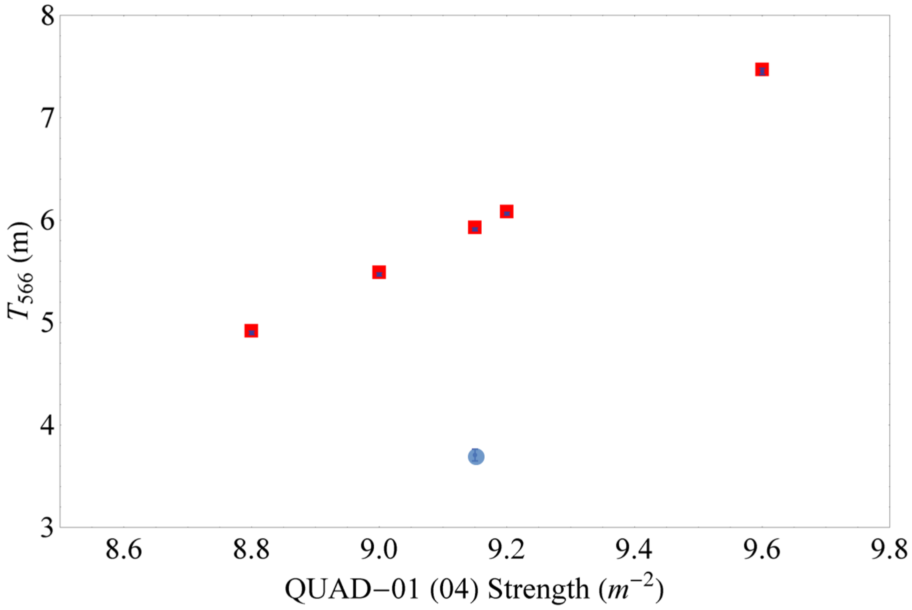

Figure 6.18: Estimated values of T_{566} from fitted polynomials in Fig.6.16. Red markers shows simulated data and blue marker show the estimated T_{566} from experimental data. Error bars from polynomial fitting are superimposed on the markers.

for moderate and higher sextupole strengths. The discrepancy between measurements and simulations in the value of R_{56} and T_{566} with sextupoles off could be attributed to several factors such as: not de-gaussing or not properly de-gaussing the magnets, effects

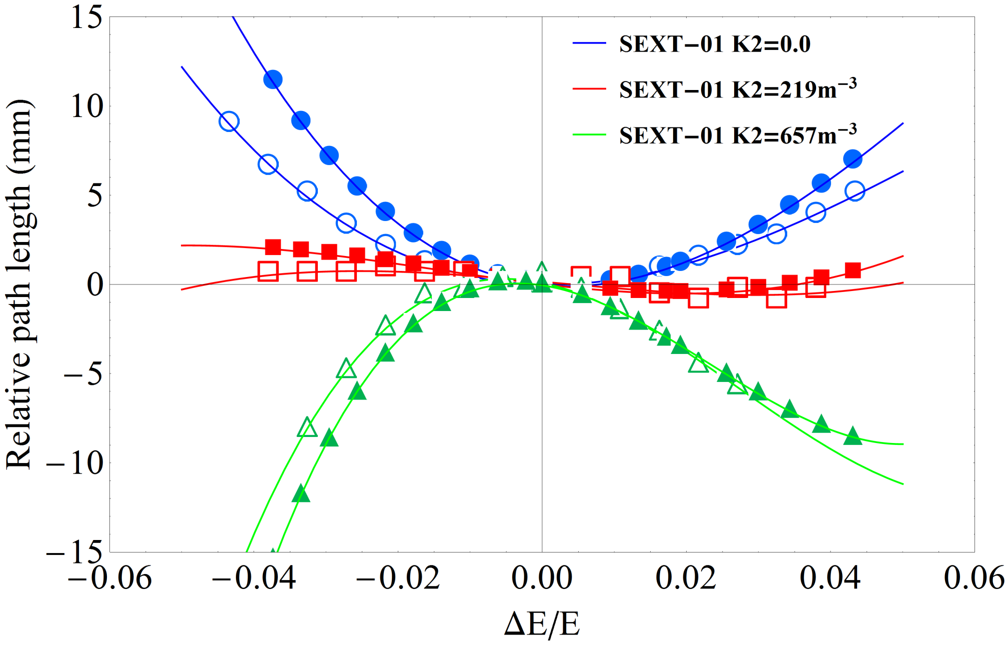

Figure 6.19: Simulated with *elegant* (filled markers) and experimentally measured (unfilled markers) path length at the exit of ARC1 for SEXT-01 off, set at K_2=219 m^{-3} and K_2=657 m^{-3}.

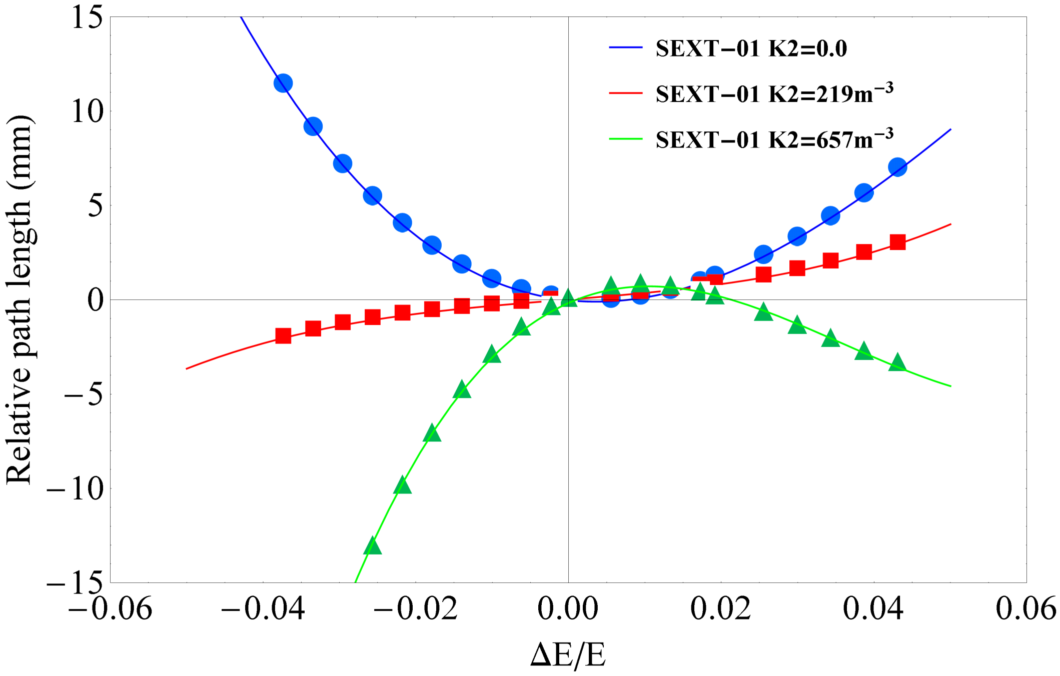

Figure 6.20: Simulated path length as a function of energy deviation for SEXT-01 on axis and horizontally offset by +5 mm.

from higher order magnetic terms, fringing field in dipoles and (as explained in the next section), differences in charge, transverse position and/or energy of the first bunch in the train compared to the rest of the long bunch train.

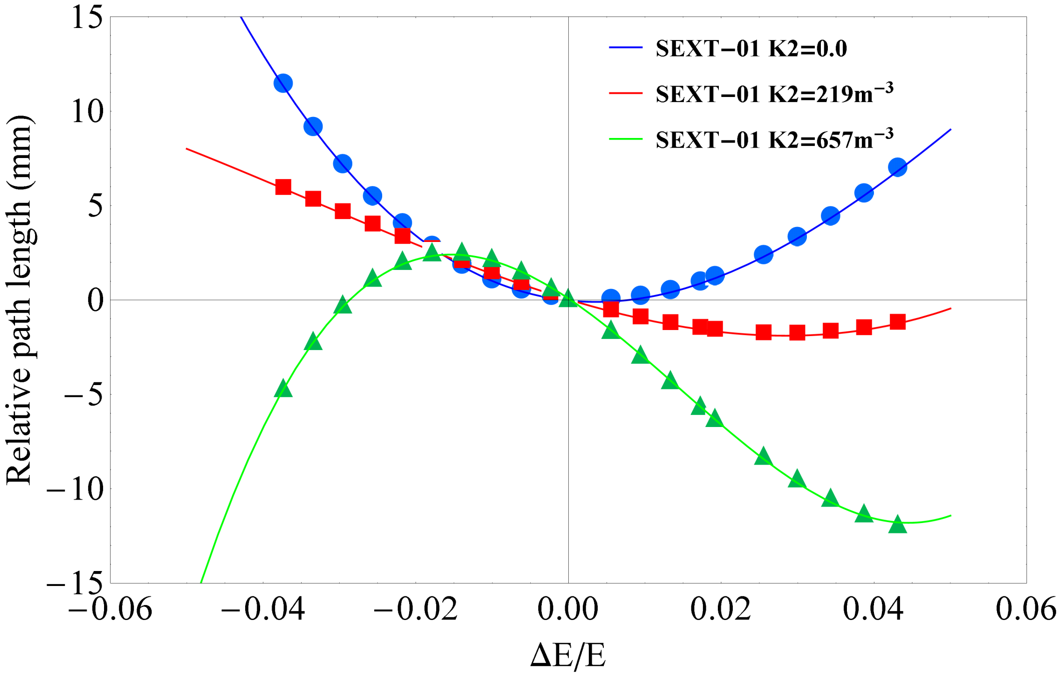

Figure 6.21: Simulated path length as a function of energy for SEXT-01 on axis and horizontally offset by -5 mm.

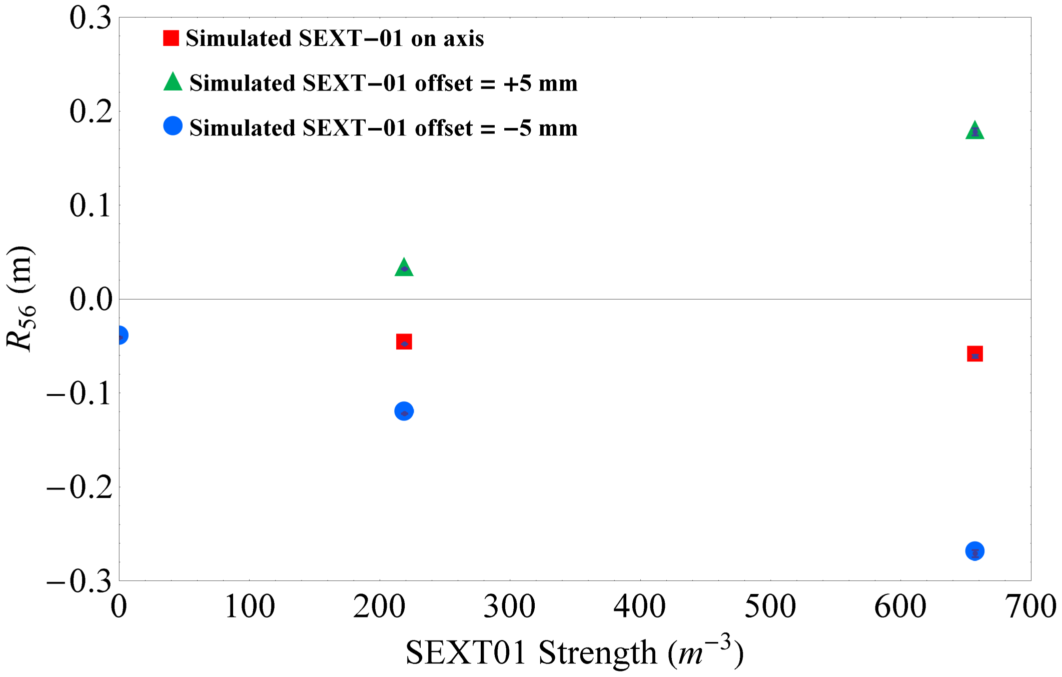

Figure 6.22: Simulated R_{56} for SEXT-01 on axis, and for SEXT-01 offset horizontally by ±5 mm.

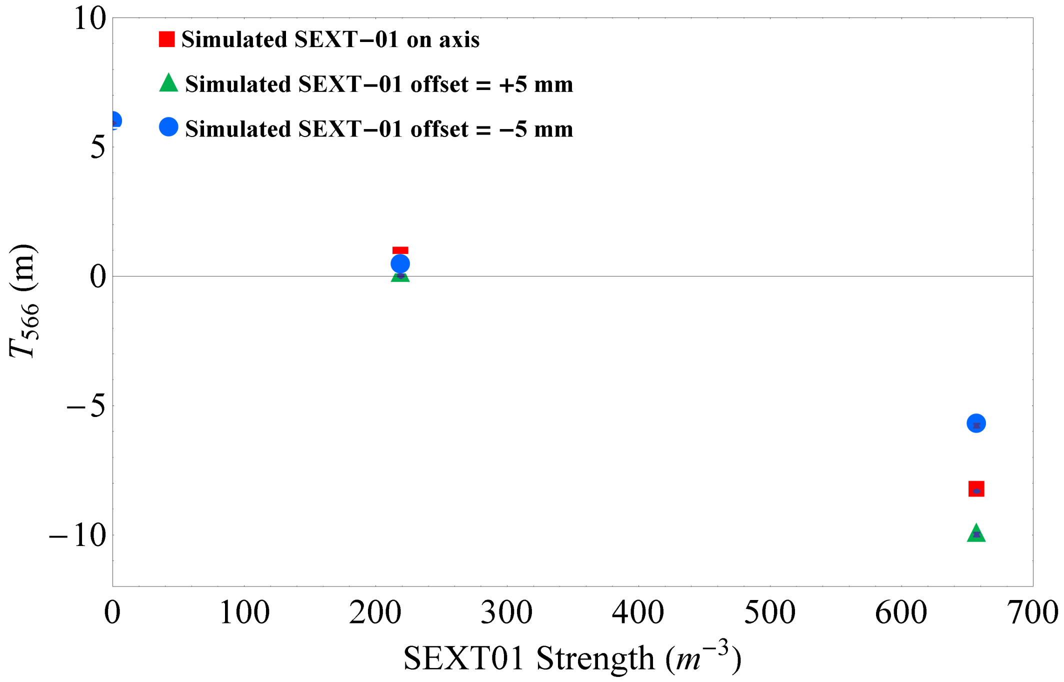

Figure 6.23: Simulated T_{566} for SEXT-01 on axis, and for SEXT-01 offset horizontally by ±5 mm.

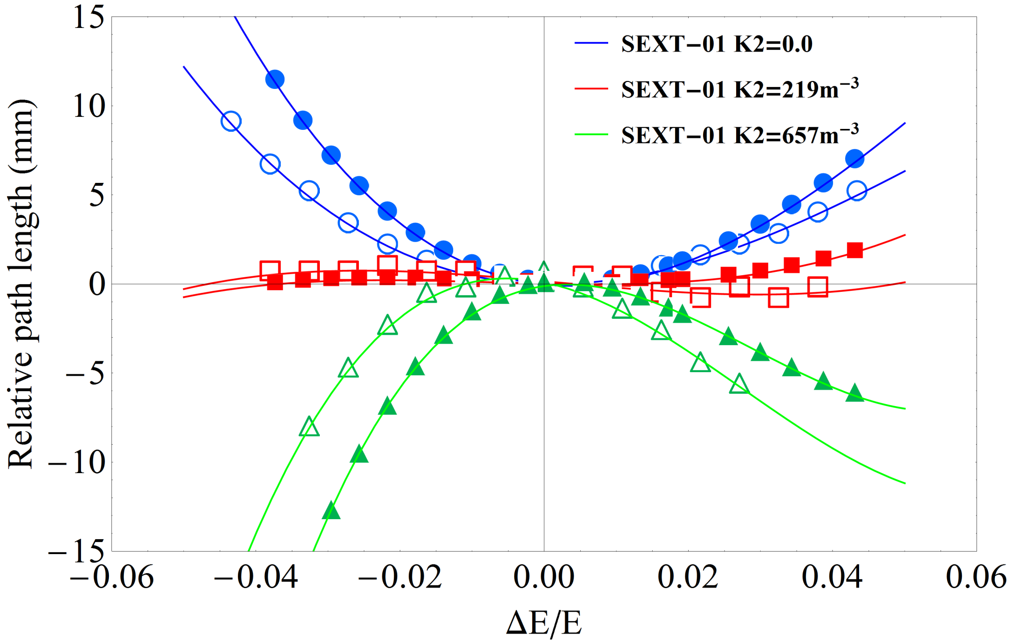

Figure 6.24: Simulated path length as a function of energy deviation for SEXT-01 horizontally offset by +2.5 mm. SEXT-01 off, set at K_2=219 m^{-3} and K_2=657 m^{-3} (filled markers) and experimentally measured (unfilled markers) path length at the exit of ARC1.

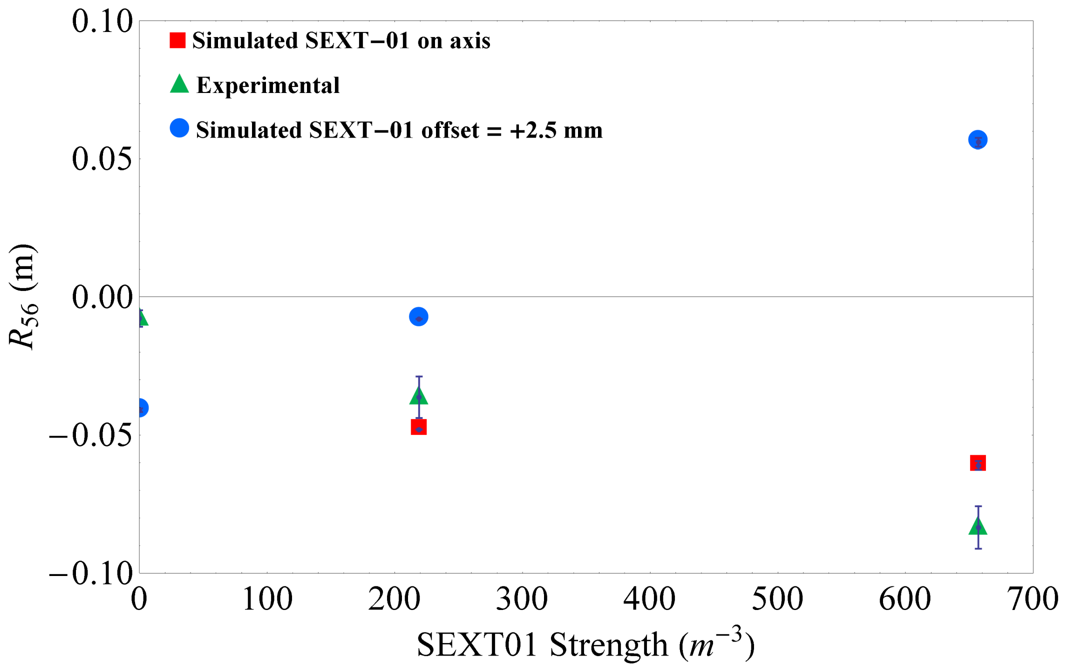

Figure 6.25: Simulated R_{56} with SEXT-01 on axis and horizontally offset by +2.5 mm compared with the measured R_{56} at the exit of ARC1.

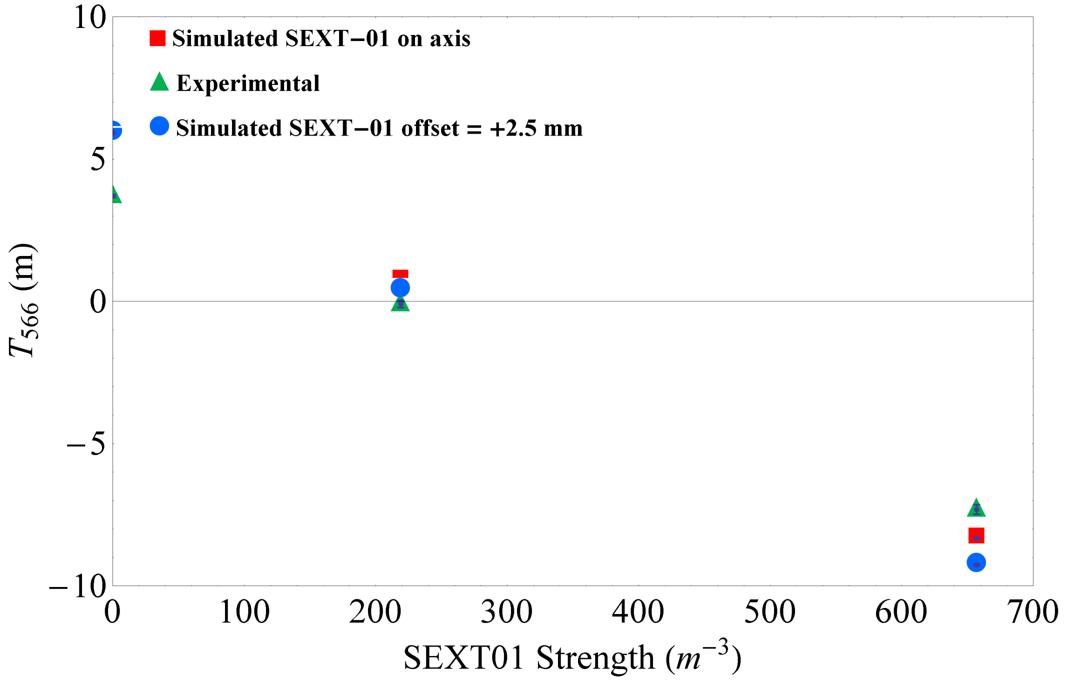

Figure 6.26: Simulated T_{566} with SEXT-01 on axis and horizontally offset by +2.5 mm compared with the measured T_{566} at the exit of ARC1.

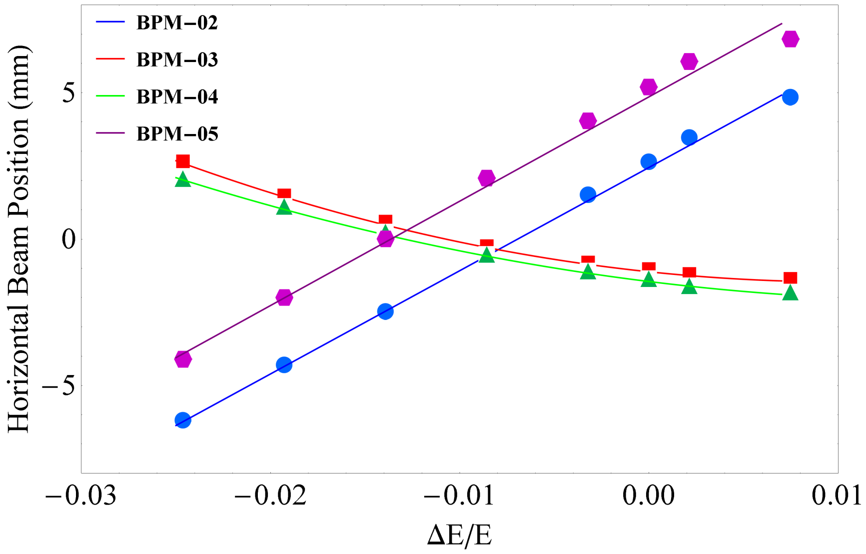

Figure 6.27: Measured horizontal beam positions at BPM-02, 03, 04, 05 in ARC1 (sextupoles off) as a function of energy.

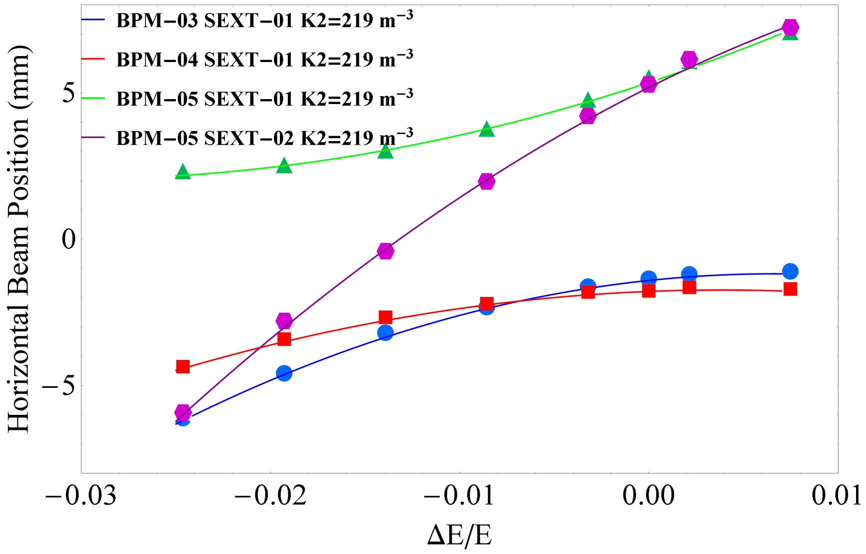

Figure 6.28: Measured horizontal beam positions at BPM-03, 04, 05 in ARC1 (sextupoles set at 219 m^{-3}) as a function of energy.

6.4.2 Dispersion Measurements

Dispersion was measured in ARC1 by changing the beam energy using the gradient of the first linac cavity (LC1) and observing the corresponding change in beam trajectory. The measured dispersion at entry to the arc (BPM-01) was found to be ∼25 mm instead of (the design value of) zero. This is likely to be due to leaking of some dispersion from the injection line and/or remanent fields from the beam dump chicane magnets, as well as the beam passing off-axis through the quadrupoles. The beam position was measured as a function of beam energy on BPMs 02-05 with and without switching on the sextupoles.

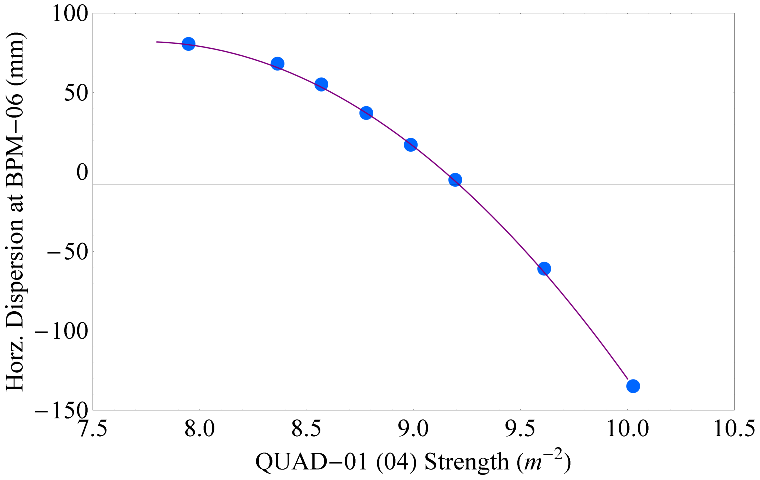

Figure 6.29: Measured dispersion at BPM-06 as QUAD-01(04) strengths are varied.

The results are shown in Fig. 6.27 and Fig. 6.28. The setting of SEXT-01 to 219 m^{-3} corresponds to an FEL setup used in regular machine operation (where linearisation and compression of the electron bunch is important). SEXT-02 does not normally show any improvement in the FEL setup and is also set at 219 m^{-3} for these measurements. By fitting either a straight line or second order polynomial to these curves, the linear term with $\Delta E/\mathrm{E}$ gives the linear dispersion. The measured linear dispersions are compared against simulations in Table 6.2. Due to low dispersion at BPM-03 and BPM-04 locations, the second order dispersion contribution shows a slight curvature on the data. Since the beam passes off-axis in the sextupoles, as alignment studies in the ARC1 confirm, switching on the sextupoles modifies the linear dispersion (because of the quadrupole kick) as well as increases the second order dispersion.

During the dispersion measurements described above, the ARC1 BPM-06 was connected to the scope for TOA measurements and was not available for the dispersion measurements. In a dedicated experiment carried out separately, the achromaticity of ARC1 was measured whilst the outer quadrupoles QUAD-01(04) were scanned. Fig. 6.29 shows the measured dispersion function at BPM-06 as a function of the outer quadrupole srtengths. For the QUAD-01(04) strengths of 9.15 m^{-2}, the dispersion is ∼25 mm at this BPM-06, which is very close to the dispersion measured on the BPM-01, demonstrating possible symmetry in the dispersion in ARC1 when the sextupoles are not powered. (However, the derivative of the dispersion function is not measured and could be different at the entrance and the exit of the arc).

It is important in machine operation to tune the arc to be achromatic, otherwise the dispersion function will be modified at the bunch compression chicane, affecting the path length with beam energy. As shown in Fig. 6.8, the dispersion in straight ST2 can be significantly higher if beam passes off-axis through powered sextupoles. Having a non-zero dispersion also makes the emittance measurements using quadrupole scans in ST2 more

Table 6.2: Simulated and measured linear dispersion in ARC1

Location	Simulated Dispersion (m)	Experimental Dispersion (m)
BPM-01	0.0	+0.025 ± 0.002
BPM-02	0.33	+0.352 ± 0.006
BPM-03	-0.0968	-0.068 ± 0.002
		+0.068 ± 0.0034 with SEXT-01=219 m^{-3}
BPM-04	-0.08521	-0.080 ± 0.002
		+0.025 ± 0.0028 with SEXT-01=219 m^{-3}
BPM-05	0.3424	+0.356 ± 0.013
		+0.214 ± 0.0061 with SEXT-01=219 m^{-3}
		+0.323 ± 0.012 with SEXT-02=219 m^{-3}
BPM-06	0.0	+0.025 ± 0.002

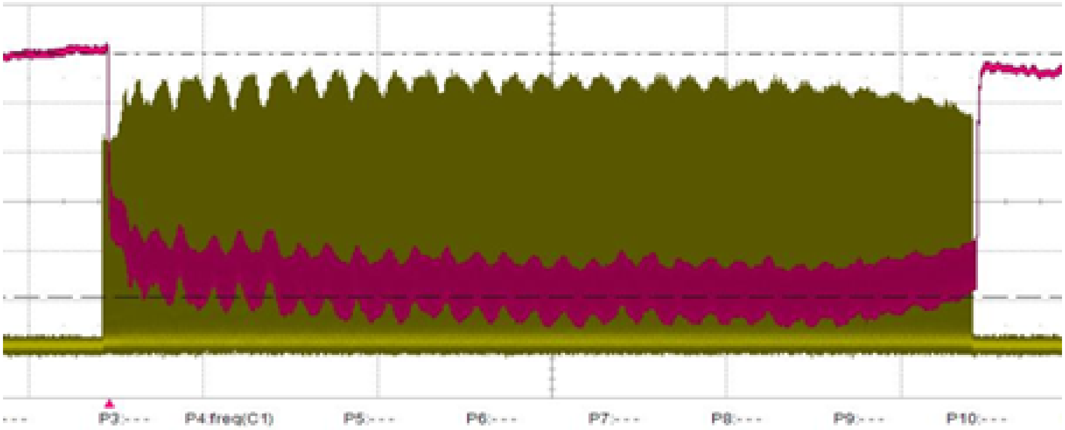

Figure 6.30: Bunch charge measured with FCUP (magenta) and PI laser power (green) measured with photodiode showing a number of characteristic features observed in the measured charge. Both devices show bunch-by-bunch charge variation of about 20% and some droop in the bunch charge.

complicated.

6.5 Performance Limitations and Diagnostics

There are a number of characteristic features observed in the measured charge and beam position as a function of position along the bunch train in ALICE [167, 172, 173, 174]. Figure 6.30 shows the bunch-by-bunch charge variation measured by a Faraday Cup (FCUP - located in the injection line) and a photodiode (PD). The PD routinely used for monitoring the PI laser pulse train power, is installed after a splitter the other output of which (through an adjustable attenuator) is directed to the gun cathode. The attenuator is used to set the bunch charge. The FCUP and PD signals were digitised using an oscilloscope and read across the ALICE computer network. The FCUP signal shows some droop in the bunch charge which is seen towards the right of the trace. Individual bunches

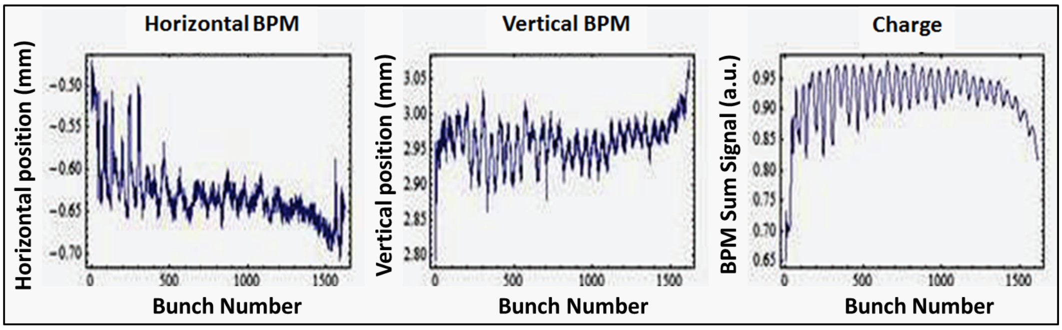

Figure 6.31: BPM signal showing horizontal position, vertical position and BPM sum signal proportional to bunch charge along the bunch train.

can be seen as a ripple about 20%.

The bunch-by-bunch BPM signal observed in ARC1 is shown in Fig. 6.31. The signals for horizontal and vertical position and bunch charge show some transient variations at the start of the bunch train, and some transients again at the end of the bunch train. Variations in bunch charge are up to 10%. The largest transverse variations are about ten times the BPM thermal noise (the BPM resolution was 20μm/10μm in horizontal/vertical plane for bunch charge 40 pC). The transverse transients and variations depend on the tuning of the machine. For dispersion measurements, the horizontal beam position obtained from the plateau was used, whereas the first bunch in the train was used for the time of arrival measurements.

The sextupoles are located close to BPM-02 and BPM-05, where the dispersion is $\sim$0.5 m. The horizontal beam positions in both these BPMs were typically 1-5 mm. With quadrupoles QUAD-01 and QUAD-02 switched off, it was possible to centre the beam (within 1 mm) on BPM-02 and BPM-03 by a slight change of ARC1 DIP-01 and horizontal steering upstream. Similarly, the beam could be centred in BPM-04 and BPM-05 by a slight change of DIP-02. However, with the quadrupoles and sextupoles on, the orbit correction was difficult to achieve whilst maintaining good lasing performance. The alignment studies indicate that the beam typically is off from the design trajectory by few millimetres (or the magnets are misaligned transversely by a few millimetres) in quadrupoles and sextupoles. These observations suggest the usefulness of having BPMs adjacent to sextupoles. The other major limitation in ALICE comes from the fact that not all magnets can be de-gaussed as unipolar power supplies are used.

6.6 Implications for Beam Spreader Designs

The experimental studies on ALICE longitudinal transport demonstrate that the effective R_{56} value across the arc is sensitive to the alignment of the sextupoles. This sensitivity can be used to provide information on the offsets of the sextupoles and can be used as an aid for their alignment. The isochronous condition of TBA lattice can be achieved by varying the beam energy as well as by variation of the quadrupole strengths. The sensitivity of the value of R_{56} to sextupole strength allows the isochronicity and orbit correction to be found by measuring the time of flight as a function of beam energy.

The results of the studies reported in this chapter emphasise the fact that if sextupoles are included in an achromatic and isochronous beam line, it is important that the beam trajectory is centred in the sextupoles. There are a number of design features that can be implemented to help ensure that this can be achieved.

- BPMs should be located at points of maximum dispersion, and where the symmetry in the dispersion can be verified.
- BPMs should be located on either side of every sextupole (or if practically possible, in the centre of the sextupoles).
- A time of arrival monitor should be located at suitable positions along the beam line to provide a quick way to set the correct longitudinal transport.

Even if the spreader design does not include sextupoles, a time of arrival monitor will still be useful for setting the correct longitudinal transport. In addition, proper de-gaussing of all the magnets needs to be ensured for repeatability of tuning the optics and achieving close to the design performance. This will be more important if beam energies are in the sub-GeV range. The proposed diagnostics should allow an accurate measurement of the dispersion function at the important locations in the spreader. These factors are considered in Chapter 5 to propose diagnostics for various spreader designs.

6.7 Summary

The Accelerators and Lasers in Combined Experiment (ALICE) at Daresbury Laboratory is an energy recovery linac test facility. The facility was originally developed as a prototype for energy recovery fourth generation light source and has until recently been used for several applications. The layout of the ALICE facility includes two 180° arcs to bring the beam back to the linac for energy recovery. The design chosen for each of these arcs is based on triple bend achromat, which uses three dipoles and two quadrupoles between a pair of dipoles. This design allows the configuration to be achromatic and isochronous as well as provides a flexibility to change the sign of the longitudinal dispersion (R_{56}). The TBA design is of particular interest in beam spreader designs presented in Chapter 5 and thus the experimental studies carried out on ALICE can provide experience on tuning of these arcs. ALICE operational regime of bunch charge and bunch length are well below coherent synchrotron radiation and studies related to CSR in TBA arcs which may be relevant to the beam spreader design cannot be tested experimentally on ALICE.

The simulations and measurements presented in this chapter highlight the issues related to alignments of sextupoles in TBA arc. When the beam passes off-axis through the powered sextupoles, the isochronicity of the arc is no longer maintained. This can cause the operational settings to vary considerably compared to the design settings. The correction of higher order dispersion which is meant to be provided by the sextupoles in the arc thus influences the isochronicity. This reduces the desired bunch compression resulting in reducing the peak bunch current which is detrimental for FEL operation.

The results of variation in path length with energy and dispersion measurements presented in this chapter confirm that the sextupoles are not aligned on the design orbit. It is possible to derive some conclusions from these studies and provide recommendations on necessary diagnostics and their locations in beam spreader designs presented in Chapter 5. However, the differences in bunch structure (macropulse with number of bunches) of ALICE, its low operating energy (and not having a possibility to degauss all magnets) should be considered when considering a high energy FEL driver for X-ray FEL.

Chapter 7

Summary, Conclusions and Future Work

7.1 Summary

A number of accelerator driven X-ray FELs have become operational in past decade and a few more will become operational in next couple of years. The three main requirements on the electron beam driving the X-ray FEL are: a high peak bunch current, very low transverse emittance and very small energy spread. These requirements are satisfied by a specially optimised accelerator design based on a photoinjector and several linear accelerator modules with suitable bunch compression and linearisation schemes. These requirements are relatively easier to meet if the accelerator layout is restricted to a linear geometry, however, in some cases (depending on the beam parameters) it may be possible to achieve them using a re-circulation or energy recovery linac. Irrespective of the choice of accelerator configuration, such a facility can cater for only few experiments at a time by splitting the radiation. Compared to third generation light sources based on storage rings, the number of experiments on FEL facilities is thus highly restricted. In order to provide suitably tailored beams for different and multiple experiments, it is desirable to include a beam spreader as part of the facility. In order to preserve the properties of electron bunches (achieved through a careful design of the upstream facility) in the beam spreader, the bending of the beam needs to done gradually as presented in Chapter 5. This implies that the length of the beam spreader to mitigate effects of incoherent and coherent synchrotron radiation (ISR and CSR) increases at higher energies. It should also be noted that there is a push to increase the gradients in the linacs to shorten the foot print of FEL driven facilities; but as presented in this thesis, the length of the beam spreader and possible future upgrade to number of beam lines may dominate the overall footprint of the facility (and thus the cost).

A review of beam spreader designs in operational and planned X-ray FEL facilities is presented in Chapter 5. The designs discussed in this thesis have a specific relevance for the studies carried out for UK's NLS design studies and for the studies planned for a future UK X-FEL facility. The two aspects of beam spreader designs, the take-off option (where beam is first diverted/switched away from the facility straight-on axis) and the lattice design including the take-off region, are described in detail. The dominating beam dynamics effects are those from CSR in bending magnets of the spreader. Depending upon the beam parameters, it is possible to mitigate/minimise the effects of CSR with a careful choice of phase advance between the dipoles, as well as appropriate tuning of the Courant–Snyder parameters. Two lattice design options, one using a Triple Bend Achromat and one with a Double Bend Achromat (obtained using a FODO lattice) are presented. The TBA design can also be optimised for a weak CSR regime using a matrix formalism. The lattice design options provide different layout configurations for the facility and have different implications for tolerances to errors as well as for the final beam parameters at the entrance of the FEL. Both these options are presented and compared.

The simulations and experimental studies carried out on ALICE emphasise the importance of a range of diagnostics to ensure setting of beam optics correctly. ALICE is operated in a bunch charge and bunch length regime where CSR is absent and in consequence the studies are focussed on errors arising from alignment of sextupoles (resulting, for example, in spurious dispersion and isochronicity of the arcs). The knowledge gained from these studies is used to suggest possible useful locations of beam diagnostic devices and instrumentation in TBA and DBA configurations for beam spreaders for a future X-ray FEL.

7.2 Conclusions

The review of beam spreader designs and the studies presented in this thesis show that the choice of beam switching is dictated by the starting bunch parameters, bunch repetition rate and number of beam lines in a FEL facility. A DC dipole magnet will be adequate for a low repetition rate facility with a few beam lines. On the other hand, for a high repetition rate facility, it would be advantageous to switch the beam using a combination of kicker and septum or a deflecting cavity. The design philosophy depends entirely on user requirements, the number of beam lines and the bunch repetition rate to every beam line.

The effect of CSR on emittance growth in the plane of bending can be mitigated and minimised by maintaining a phase advance of π between consecutive pairs of dipoles in both TBA and DBA (based on FODO lattices). This scheme works as long as the bending is gradual and bending magnets are short and the beam and lattice parameters are identical at the locations of dipoles. For the beam parameter regime chosen for the studies at 2.2 GeV, it is possible to cancel the increase in emittance due to CSR if the bending angle is kept below $\approx 6^\circ$. For higher dipole angles, not only the compensation does not work perfectly but it strongly depends on the length of the magnet, the longer the magnet, the worse is the CSR compensation. At higher beam energies, the effect of ISR becomes prominent and since this incoherent effect cannot be corrected in the same way as the effects from CSR, it is important to have a lattice design which minimises the generation of ISR. Again for the beam parameters and lattices chosen here, the emittance increase due to ISR is small if the bending angle of each dipole is kept under $\approx 6^\circ$.

The conditions of achromaticity and isochronicity are met only in the TBA lattice but non-isochronicity in the DBA lattice may be acceptable for some beam parameter regime. The two lattices based on the TBA and the DBA configurations presented in this thesis use beam energies of 2.2 GeV and 6.6 GeV, which are specifically targeted for design studies carried out for NLS and for possible application to a future UK X-FEL. This does not however rule out application of these designs in other beam parameter regimes. In fact, a DBA lattice has been suggested by the author for a Plasma Accelerator Research Station (PARS) on CLARA at 250 MeV [175].

The normalised beam emittance value of 0.3 mm.mrad used in most of the cases presented here is extremely challenging to achieve and maintain over distances of several hundred meters from the cathode. However, this value is deliberately used to ensure that the validity for CSR compensation schemes will work even in this challenging regime. The beam parameter regime used here does satisfy the Derbenev criterion for the 1-D CSR model used for the CSR simulations in *elegant* code. However, for very short bunches (e.g. single spike experiments) this criterion will not be valid and it may be necessary to use a more sophisticated CSR code such as CSRTrack to track the beam through the beam spreader.

The trade-off between number of dipoles (and power supplies powering them) to obtain a particular transverse offset in certain length has important consequences to the cost of the facility. For example, the design DBA lattice using 6° dipoles gives ≈ 6 m transverse offset in ≈ 40 m length. Total number of magnets are 4 dipoles and 22 quadrupoles. This distance can be increased if longer FODO cells are used. A TBA design with two arcs gives ≈ 6.5 m transverse offset in 75 m and includes 6 dipoles and 24 quadrupoles. Thus, in principle it is possible to achieve similar transverse offset in given length using either the DBA or the TBA. It is worth pointing out that the scaling of 2.2 GeV spreader design to 6.6 GeV does not increase the length of the spreader three times. But as the magnets get longer and the transverse offset in given length could increase, the longer magnets start deteriorating cancellation of CSR kicks. Thus a simple scaling by length of the dipoles does not work and there may be a need to use several shorter dipoles instead of one long one. This can impact directly on the cost of the facility. The tolerance studies with four 6° dipoles and eight 3° dipoles indicate that the lattice with more magnets is less tolerant to the errors. Thus there is a trade-off between number of magnets, their power supplies and the length of the beam line to achieve particular transverse offset with cost of the facility.

The designs at 6.6 GeV studied here (as well as the beam spreader designs adopted at higher energies at the European X-FEL and SwissFEL) confirm that the optimised design choice would be to first switch the beam in the vertical plane to avoid a physical clash of elements in the first few meters of the beam spreader, and then bring it back to the horizontal plane when sufficient separation is achieved. This generates dispersion in the vertical plane in addition to the horizontal plane and thus the implications for the beam parameters and tolerances to lattice errors need to be carefully considered.

Having multiple beam lines feeding different FEL beam lines also leads to the need to consider the design requirements on collimation and beam dumps. This is especially important if the beam power is in the kW to sub MW regime. The shielding requirements of high power beam dumps and the implications for the layout (and hence the cost) may rule out having a separate beam dump at the end of every beam line. In this case, the optimum solution would be to combine the electron beams from all FEL beam lines and transport to a single adequately shielded high power beam dump.

In order to make sure that the beam spreader is indeed transparent to the beam properties achieved in the upstream accelerator, it is of utmost importance to have diagnostics devices optimally distributed (BPMs and screens at correct phase advances) along the spreader. The diagnostics to measure path length and bunch slice properties are important to locate after the spreader. If sextupoles are included in the beam spreader, it is essential to ensure that they are correctly aligned to avoid introducing additional focusing, which could disturb the isochronicity of the lattice (as demonstrated by the experimental studies on ALICE).

7.3 Future Work

The work presented here can be easily applied to a future UK X-FEL beam spreader design once the scientific case is developed and the basic beam parameters and repetition rate are finalised. It will also be possible to look into design options with switching the beam vertically to optimise the footprint of the facility. Work is in progress on technology developments to allow the use of RF deflectors for fast beam switching [126, 176, 177] and it will be interesting to compare the beam dynamics requirements and cost implications of using these devices over kicker/septum. The technical parameters of possible deflecting cavities and kicker/septum systems will need to be used in the optimised beam spreader design to study their effects on stability of the beam in the context of the demands of FEL schemes. European X-FEL, SwissFEL and LCLS-II X-ray FEL facilities will be operational in next few years, and the experience from these facilities will be valuable for making optimum and timely decisions for a beam spreader design choice for a UK X-FEL.

Appendix A

Abbreviations and Acronyms

ALICE	Accelerators and Lasers In Combined Experiment
ALPHA-X	Advanced Laser-Plasma High-Energy Accelerators towards X-rays
BBU	Beam Break Up
BPM	Beam Position Monitor
CLARA	Compact Linear Accelerator for Research and Applications
CSR	Coherent Synchrotron Radiation
CW	Continuous Wave
DBA	Double Bend Achromat
DC	Direct Current
ERL	Energy Recovery Linac
FEL	Free Electron Laser
HOM	Higher Order Mode
ICT	Integrated Current Transformet
ILC	International Linear Collider
IR	Infra Red
ISR	Incoherent Synchrotron Radiation
JLC	Japan Linear Collider
LBNL	Lawrence Berkeley National Laboratory
LCLS	Linac Coherent Light Source
NLC	Next Linear Collider
NLS	New Light Source
NSLS	National Synchrotron Light Source
PAL	Pohang Accelerator Laboratory
RF	Radio-Frequency
SACLA	SPring-8 Angstrom Compact free electron Laser
SASE	Self-Amplified Spontaneous Emission
SLS	Synchrotron Light Source
SXFEL	Shanghai X-ray Free Electron Laser
TBA	Triple Bend Achromat
TDC	Transverse Deflecting Cavity
TOA	Time of Arrival
TESLA	The Superconducting Electron-Positron Linear Collider
UV	Ultra Violet
VELA	Versatile Electron Linear Accelerator

Appendix B

RF Frequencies

	L-band	S-band	C-band	X-band
Frequency (GHz)	1.3 (E)	2.998 (E)	5.996 (E)	11.99 (E)
	1.3 (A)	2.856 (A)	5.712 (A)	11.42 (A)
Wavelength (cm)	23.08 (E)	10.01 (E)	5.00 (E)	2.50 (E)
	23.08 (A)	10.50 (A)	5.25 (A)	2.63 (A)
Time (psec)	769.23 (E)	333.56 (E)	166.78 (E)	83.39 (E)
	769.23 (A)	360.14 (A)	175.07 (A)	87.54 (A)

(E): European, (A):American

Bibliography

[1] A. Liénard. Ćhamp E'Lectrique Et Magnétique. *L'Éclairage Électrique*, 16, 1898.

[2] E. Wiechert. *Archives Neerlandaises*, 5, 1900.

[3] G. A. Schott. Electromagnetic Radiation and Mechanical Reactions Arising from it. 1912.

[4] D. Iwanenko and I. Pomeranchuk. On the Maximal Energy Attainable in a Betatron. *Phys. Rev.*, 65:343, 1944.

[5] J. P. Blewett. Radiation Losses in the Induction Electron Accelerator. *Phys. Rev.*, 69:87–95, 1946.

[6] F. R. Elder, A. M. Gurewitsch, R. V. Langmuir, and H. C. Pollock. Radiation from Electrons in a Synchrotron. *Phys. Rev.*, 71:829–830, 1947.

[7] F. R. Elder, R. V. Langmuir, and H. C. Pollock. Radiation from Electrons Accelerated in a Synchrotron. *Phys. Rev.*, 74:52, 1948.

[8] J. S. Schwinger. On the classical radiation of accelerated electrons. *Phys. Rev.*, 75:1912–1926, 1949.

[9] J. P. Blewett. 50 Years of SR. Synchrotron Radiation - Early History. *J. Sync. Rad.*, 5:135–139, 1998.

[10] Z. T. Zhao. Storage Ring Light Sources. *Rev. Accl. Sci. Tech.*, 3:57–76, 2010.

[11] A. W. Merrison. NINA - the 4 GeV electron synchrotron of the science research council. *Contemporary Physics*, 8:373–384, 1967.

[12] D. Lemke and D. Labs. The Synchrotron Radiation of the 6-GeV DESY Machine as a Fundamental Radiometric Standard. *Applied Optics*, 6:1043–1048, 1967.

[13] N. Dikansky. Electron-Positron Colliders at Novosibirsk. In *Proc. of PAC95*, pages 500–505, 1995.

[14] M. Tigner. An Electron Positron Colliding Beam Facility at Cornell. *IEEE Trans. Nucl. Sci.*, 24:1849, 1977.

[15] D. W. Lynch. Tantalus, a 240 MeV Dedicated Source of Synchrotron Radiation, 1968-1986. *J. Synchrotron Rad.*, 4:334–343, 1997.

[16] I. H. Munro. Synchrotron Radiation Research in the UK. *J. Synchrotron Rad.*, 4:344–358, 1997.

[17] W. Namkung. Review of Third Generation Light Sources. In *Proceedings of IPAC2010*, pages 2411–2415, 2010.

[18] UK Free Electron Laser (FEL) User Community. http://ukfel.org/wordpress/.

[19] L. B. Fletcher, H. J. Lee, et al. Ultrabright X-ray laser scattering for dynamic warm dense physics. *Nature Photonics: Articles*, 2015.

[20] Z. Huang. Brightness and Coherence of Synchrotron Radiation and FELs. Technical Report SLAC-PUB-15449, SLAC, 2013.

[21] Five Years of Scientific Discoveries with SLAC's LCLS, News article October 7, 2014. https://www6.slac.stanford.edu/news/news-feature-archive-2014.aspx.

[22] Free Electron Laser FLASH. https://flash.desy.de/accelerator/.

[23] SACLA. http://xfel.riken.jp/eng/research/indexnne.html.

[24] P. Schm*ü*ser. Free-Electron Lasers. *CERN-2006-002*, 429:477–494, 2003.

[25] D. Attwood. Synchrotron Radiation for Material Science Applications. EE290F, 2007.

[26] J. D. Jackson. *Classical Electrodynamics*. Wiley, New York, 1975.

[27] H. Wiedemann. *Particle Accelerator Physics*. Springer, 1999.

[28] E. L. Saldin, E. A. Schneidmiller, and M. V. Yurkov. *The Physics of Free Electron Lasers*. Springer, 2000.

[29] R. Bonifacio *et al*. Physics of the high-gain free electron laser and superradiance. *Riv. Nuovo Cimento*, 13:1–69, 1990.

[30] P. Schm*ü*ser, M. Dolhus, J. Rossbach, and C. Behrens. *Free-Electron Lasers in the Ultraviolet and X-ray regime, second edition*, volume 258. Springer Tracks in Modern Physics, 2014.

[31] C. Pellegrini and S. Reiche. *Lasers, Free-Electron*. Wiley-VCH Verlag GmbH & co., 2007.

[32] S. Schreiber. Soft and Hard X-ray SASE Free Electron Lasers. *Rev. of Accel. Sci. and Tech.*, 3:93–120, 2010.

[33] A. Wolski. A short Introduction to Free Electron Lasers. *CERN Accelerator School*, 2012.

[34] R. Bonifacio, C. Pellegrini, and L. Narducci. Collective Instabilities and High-gain Regime in a Free Electron Laser. *Opt. Commun.*, 50, 1984.

[35] J. Stohr, J. Galayda, et al. Linac Coherent Light Source II Concenptual Design Report. Technical Report SLAC-R-978, 2005.

[36] J. Murphy, C. Pelligrini, and R. Bonifacio. Collective instability of a free electron laser including space charge and harmonics. *Opt. Communications*, 53:197–202, 1985.

[37] *NLS Project: Conceptual Design Report, (Ed. J Marangos, R Walker and G Diakun)*. STFC, 2010.

[38] J. A. Clarke, D. Angal-Kalinin, et al. CLARA conceptual design report. *Journal of Instrumentation*, 9, 2014.

[39] A. Wolski. *Beam Dynamics in High Energy Particle Accelerators*. Imperial College Press, 2014.

[40] J. Rossbach and P. Schm*ü*ser. Basic Course on Accelerator Optics. *Proceedings of CERN Accelerator School*, 1:17–88. CERN-94-01, 1992.

[41] K. Steffen. Basic Course on Accelerator Optics. *CERN Accelerator School*, CERN 85-19:25–54, 1985.

[42] N. Marks. Accelerator Magnets. *CERN Accelerator School, Prague*, 2014.

[43] K. L. Brown. A First- and Second-Order Matrix Theory for the Design of Beam Transport Systems and Charged Particle Spectrometers. Technical Report SLAC-75, SLAC, 1982.

[44] D. E. Lobb. An analysis of the first order effects of misalignments in a beam transport system. *Nucl. Instrum. Methods*, 87:59–72, 1970.

[45] B. E. Carlsten. New Photoelectric Injector Design For The Los Alamos National Laboratory XUV FEL Accelerator. *Nucl. Instrum. Methods A*, 285:313–318, 1988.

[46] M. W. Gurtg, K. L. F. Bane, et al. Commissioning of the Radiabeam/SLAC Dechirper. In *Proc. of IPAC2016*, pages 809–812, 2016.

[47] P. Emma, M. Venturini, et al. Experimental Demonstration of Energy-Chirp Control in Relativistic Electron Bunches Using a Corrugated Pipe. *Physical Review Letters*, 112:034801, 2014.

[48] M. Cornacchia, P. Craievich, S. Di Mitri, et al. FERMI & Elettra Accelerator Technical Optimization Final Report. *SLAC-TN-07-006, LBNL-60958*, 2006.

[49] Y. M. Derbenev, J. Rossbach, E. L.Saldin, and V. D. Shiltsev. Microbunch Radiative Tail-Head Interaction. *TESLA FEL Report 95-05*, 1995.

[50] M. Sands. The Physics of Electron Storage Rings - an Introduction. Technical Report SLAC-121, UC-27 (AC), 1970.

[51] M. Sands. Emittance Growth from Radiation Fluctuations. Technical Report SLAC Report SLAC/AP-47, 1985.

[52] D. Douglas. Quantum Excitation Estimates for CEBAF Energy Upgrades. *JLAB-TN-038*, 1997.

[53] M. Tigner. A Possible Apparatus for Electron-Clashing Experiments. *Nuovo Cimento*, 37:1228–1231, 1965.

[54] T. I. Smith, H. A. Schwettman, R. Rohatgi, Y. Lapierre, and J. Edighoffer. Development of the SCA/FEL for Use in Biomedical and Materalss Science Research. *Nucl. Instr. and Methods A*, 259:1–7, 1987.

[55] J. B. Flanz and C. P. Sargent. Tests with an Isochronous Recirculation System. *IEEE Trans. on Nuclear Sceience*, NS-32 No. 5, 1985.

[56] G. R. Neil et al. Sustained Kilowatt Lasing in a Free Eletron Laser with Same-Cell Energy Recovery. *Phys. Rev. Lett.*, 84:4–24, 2000.

[57] L. Merminga, D. Douglas, and G.Krafft. High-Current Energy-Recovering Electron Linacs. *Annu. Rev. Nucl. Part. Sci.*, 2003.53:387–429, 2003.

[58] E. Pozdeyev, C. Tennat, J. J. Bisognano, M. Sawamura, R. Hajima, and T.I. Smith. Multipass beam breakup in energy recovery linacs. *Nucl. Instrum. Methods in Phys. Res. Sect. A*, 557:176–188, 2006.

[59] G. H. Hoffstaertter and I. V. Bazarov. Beam-breakup Instability theory for energy recovery linacs. *Phys. Rev. Spec. Top. Accel. Beams*, 7:054401, 2004.

[60] P. H. Williams, D. Angal-Kalinin, et al. A Recirculating Linac Free-Electron Laser Driver. *Phys. Rev. Spec. Top. Accel. Beams*, 14:050704, 2011.

[61] P. McIntosh. Private Communication.

[62] H. Tanaka et al. A compact X-ray free-electron laser emitting in the sub-angstrom region. *Nat. Photon.*, 6:540–544, 2012.

[63] J. S. Fraser, R. L. Sheffield, and E. R Gray. A New High-Brightness Electron Injector for Free Electron Lasers. *Nucl. Instr. and Methods A*, 250:71–76, 1986.

[64] C. P. Hauri, R. Ganter, F. Le Pimpec, A. Trisorio, C. Ruchert, and H. H. Braun. Intrinsic Emittance Reduction of an Electron Beam from Metal Photocathodes. *Phys. Rev. Lett.*, 104:234802, 2010.

[65] D. H. Dowell and J. Schmerge. The Quantum Efficiency and Thermal Emittance of Metal Photocathodes. Technical Report SLAC-PUB-13535, 2009.

[66] J. Arthur, P. Anfinrud, et al. Linac Coherent Light Source (LCLS) Conceptual Design Report. Technical Report SLAC-R-593, 2002.

[67] G. Penco. The FERMI@Elettra Commissioning. In *Proc. of IPAC2010*, pages 1293–1295, 2010.

[68] S. Schreiber, M. Görler, et al. Operation of the FLASH Photoinjector Laser System. In *Proc. of FEL2011*, pages 507–510, 2011.

[69] F. Brinker. Commissioning of the European XFEL Injector. In *Proc. of IPAC2016*, pages 1044–1047, 2016.

[70] B. L. Militsyn, D. Angal-Kalinin, et al. Beam Physics Commissioning of VELA at Daresbury Laboratory. In *Proc. of IPAC2014*, pages 2986–2988, 2014.

[71] J. Rodier, T. Garvey, et al. Construction of the ALPHA-X Photo-Injector Cavity. In *Proc. of EPAC2006*, pages 1277–1279, 2006.

[72] D. Angal-Kalinin, J. K. Jones, J. W. McKenzie, and B. L.Militsyn. Optics design and layout for the Electron Test Facility at Daresbury Laboratory. In *Proc. of IPAC2012*, pages 646–648, 2012.

[73] T. Rao. and D. Dowell. An engineering guide to photoinjectors. `https://arxiv.org/ftp/arxiv/papers/1403/1403.7539.pdf`, 2013.

[74] P. Emma. X-Band RF Harmonic Compensation for Linear Bunch Compression in the LCLS. Technical Report SLAC-TN-05-004, SLAC, 2001.

[75] M. Borland. elegant: A Flexible SDDS-Compliant Code for Accelerator Simulation. Advanced Photon Source LS-287, September 2000.

[76] Z. Huang and J. Wu. Microbunching instability due to bunch compression. Technical Report SLAC-PUB-11597, SLAC, 2005.

[77] Z. Huang, A. Brachmann, F.-J. Decker, et al. Measurements of the LCLS laser heater and its impact on the X-ray FEL performance. Technical Report SLAC-PUB-13854, 2010.

[78] Y. Kim, S. Saitiniyazi, et al. Performance Comparison of S-band, C-band, and X-band RF Linac based XFELs. In *ISU-JLAB-2012-039, Presented at FLS2012*, 2012.

[79] J. Pfingstner, E. Adli, et al. The X-band FEL Collaboration. In *Proc. of FEL2015*, pages 368–374, 2015.

[80] The International Linear Collider. `https://www.linearcollider.org/ILC`.

[81] SwissFEL Conceptual Design Report. Technical Report PSI Bericht Nr. 10-04, Paul Scherrer Institut, April 2012.

[82] M. Altarelli et al. The European X-Ray Free-Electron Laser. Technical Report DESY 2006-097, 2007.

[83] G. D′Auria, S. Di Mitri, et al. X-band technology for FEL sources. In *Proc. of LINAC2014*, pages 101–104, 2014.

[84] Y. Sun et al. Parameter Selection and Longitudinal Phase Space Simulation for a Single Stage X-band FEL driver at 250 MeV. Technical Report SLAC-PUB-14327, 2012.

[85] H. Schlarb. *Collimation system for the VUV Free-Electron Laser at the TESLA Test Facilitiy*. PhD thesis, University of Hamburg. DESY-THESIS-2001-055, 2001.

[86] D. Angal-Kalinin, F. Jackson, et al. Design of post linac beam transport for the UK New Light Source Project. In *Proc. of IPAC2010*, pages 1802–1804, 2010.

[87] F. Jackson, D. Angal-Kalinin, et al. Collimation system design and performance for the SwissFEL. In *Proc. of IPAC2012*, pages 1753–1755, 2012.

[88] Y. Ding, F. J. Decker, et al. Results from the LCLS X-band Transverse Deflector with Femtosecond Temporal Resolution. Technical Report SLAC-PUB-16105, SLAC, 2014.

[89] J. S. Schwinger. On radiation by electrons in a betatron: Transcription of a paper by J. Schwinger, 1945. In Milton, K.A. (ed.): A quantum legacy: Seminal papers of Julian Schwinger 307-331, 1996.

[90] M. Dohlus, T. Limberg, and P. Emma. Bunch Compression for Linac-based FELs. *ICFA Beam Dynamics Newsletter*, 38, 2005.

[91] E. L. Saldin, E. A. Schneidmiller, and M. V. Yurkov. On the coherent radiation of an electron bunch moving in an arc of a circle. *Nucl. Instrum. Methods in Phys. Res. Sect. A*, 398:373–394, 1997.

[92] M. Borland et al. Simple method for particle tracking with coherent synchrotron radiation. *Phy. Rev. Spe. Topics - Accelerators and Beams*, 070701, 2001.

[93] J. S. Nodvik and D. S. Saxon. Suppression of Coherent Radiation by Electrons in a synchrotron. *Phys. Rev.*, 96:180, 1954.

[94] S. A. Kheifets and B. Zotter. Shielding Effects on Coherent Synchrotron Radiation. Technical Report CERN SL-95-92 (AP)/F-TN-07/12, 1995.

[95] R. Li, C. L. Bohn, and J. J. Bisognano. Analysis of the steady-state coherent synchrotron radiation with strong shielding. In *Proc. of PAC1997*, pages 1644–1646, 1997.

[96] MAD - Methodical Accelerator Design. `http://mad.web.cern.ch/mad/`.

[97] D. C. Carey, K. L. Brown, and F. Rothacker. Third-order TRANSPORT with MAD input. A computer program for designing charged particle beam transport system. FERMILAB-Pub-98/310, 1998.

[98] T. Limberg, A. Kabel, and M. Dohlus. Numerical calculation of CSR effects using TraFic4. *Nucl. Instrum. Methods.*, A455:185–189, 2000.

[99] M. Dohlus and T. Limberg. CSRtrack version 1.2. `www.desy.de/xfel-beam/csrtrack`.

[100] CSR workshop 2002. http://www.desy.de/csr/.

[101] G. Bassi, T. Agoh, M. Dohlus, et al. Overview of CSR codes. *Nucl. Instrum. Methods A*, 557:189–204, 2006.

[102] P. Emma et al. First lasing and operation of an angstrom-wavelength free-electron laser. *Nat. Photon.*, 4:641 – 647, 2010.

[103] S. Di Mitri. Modelling Linacs and their components - A personal selection of challenges. Designing Future X-ray FELs workshop, 2016.

[104] M. Dohlus and T. Limberg. CSRtrack: Faster calculation of 3-D CSR effects. In *Proc. of the 2004 FEL conference*, pages 18–21, 2004.

[105] P. Emma and R. Brinkmann. Emittance dilution through coherent energy spread generation in bending systems. Technical Report SLAC-PUB-7554, 1997.

[106] D. Douglas. Suppression and enhancement of CSR-driven emittance degradation in the IR-FEL driver. Technical Report JLAB-TN-98-012, 1998.

[107] S. Di Mitri, M. Cornacchia, and S. Spampinati. Cancellation of coherent synchrotron radiation kicks with optics balance. *Phys. Rev. Lett.*, 110:014801, 2013.

[108] S. Di Mitri and M. Cornacchia. Electron beam brightness in linac-drivers for free-electron lasers. *Physics Reports*, 539:1–48, 2014.

[109] S. Di Mitri. *Machine design and electron beam control of a single-pass Linac for Free Electron laser: the FERMI@Elettra Case Study*. PhD thesis. Zarnike Institute PhD Thesis Series 2011-22, ISSN 1570-1530, 2011.

[110] R. Hajima. A first-order matrix approach to the analysis of electron beam emittance growth caused by coherent synchrotron radiation. *Jpn. J. Appl. Phy.*, 42:L974–L976, 2003.

[111] R. Hajima. Emittance compensation in a return arc of an energy-recovery linac. *Nucl. Instrum. Methods in Phys. Res. Sect. A*, 528, 2004.

[112] Y. Jiao, X. Cui, X. Huang, and G. Xu. Generic conditions for suppressing the coherent synchrotron radiation induced emittance growth in a two-dipole achromat. *Phys. Rev. Spec. Top. Accel. Beams*, 17:060701, 2014.

[113] K. Tiedtke et al. The soft X-ray free-electron laser FLASH at DESY: beamlines, diagnostics and end-stations. *New Journal of Physics*, 11:023029, 2009.

[114] Free-Electron Laser Strategic Review, 2016. `https://www.stfc.ac.uk/files/fel-report-2016/`.

[115] TESLA The Superconducting Electron-Positron Linear Collider with an Integrated X-Ray Laser Laboratory Technical Design Report. Technical report, 2001.

[116] S. Takeda. Japan Linear Collider (JLC). *Particle Accelerators*, 30, 1990.

[117] The Next Linear Collider. `http://www-project.slac.stanford.edu/lc/`.

[118] E. A. Seddon et al. 4GLS Conceptual Design Report, 2006.

[119] J. Frisch, R. Akre, F. J. Decker, et al. Beam Measurements at LCLS. Technical Report SLAC-PUB-15018, 2008.

[120] H. D. Nuhn for the LCLS Commissioning Team. LCLS Undulator commissioning, alignment and performance. In *Proc. of FEL09*, 2009.

[121] D. Ratner et al. Experimental Demonstration of a Soft X-ray Self-Seeded Free Electron Laser. Technical Report SLAC-PUB-16214, 2015.

[122] H. Loos, R. Akre, A. Branchmann, et al. Operational performance of lcls beam instrumentation. Technical Report SLAC-PUB-14121, 2010.

[123] J. N. Galayda. LCLS-II Project. In *Proc. of IPAC2014*, 2014.

[124] J. F. Schmerge, A. Brachmann, D. Dowell, et al. The LCLS-II Injector Design. In *Proc. of FEL2014*, pages 815–819, 2014.

[125] Y. Nosochkov, T. Taubenheimer P. Emma, and M. Woodley. Design of the LCLS-II Electron Optics. Technical Report SLAC-PUB-16025, 2014.

[126] J. Delayen, S. De Silva, R. Olave, T. Satogata, and G. Krafft. RF Beam Spreader Options for LCLS-II. Technical Report LCLS-II TN-13-05, 2013.

[127] T. Raubenheimer. LCLS-II Capabilities and Overview, LCLS-II Science Opportunities Workshop, 2015.

[128] A. Zholents, D. Bacescu, K. Chow, et al. Spreader Design for FERMI@Elettra Free Electron Laser. Technical Report LBNL-62345, CBP Note-370, 2007.

[129] C. J. Bocchetta et al. FERMI@Elettra Conceptual Design Report. Technical Report ST/F-TN-07/12, Sincrotrone Trieste, 2007.

[130] The European X-Ray Free-Electron Laser Technical Design Report. Technical Report DESY 2006-097, 2007.

[131] V. Balandin, W. Decking, and N. Golubeva. Optics for the Beam Switchyard at the European XFEL. In *Proc. of IPAC2011*, pages 2016–2018, 2011.

[132] W. Decking and F. Obier. Layout of the Beam Switchyard at the European XFEL. In *Proc. of EPAC2008*, pages 2163–2165, 2008.

[133] W. Decking. Fast Distribution of Pulses in Multiple Beam Line Facilities. Talk presented at FEL2010, 2010.

[134] V. Balandin, W. Decking, and N. Golubeva. Tilted Sexupoles for Correction of Chromatic Aberrations in Beam Lines with Horizontal and Vertical Dispersions. In *Proc. of IPAC2010*, pages 4656–4658, 2010.

[135] N. Golubeva, V. Balandin, and W. Decking. Layout and Optics of the Dump Line at the European XFEL. In *Proc. of IPAC2014*, pages 1138–1140, 2014.

[136] N. Milas and S. Reiche. Switchyard Design: Athos. In *Proc. of FEL2012*, pages 109–112, 2012.

[137] M. Paraliev, C. Gough, S. Dordevic, and H. Braun. High Stability Resonant Kicker Development for the SwissFEL Switchyard. In *Proc. of FEL2014*, pages 103–106, 2014.

[138] N. Milas and C. Gough. Design of the SwissFEL Switchyard. In *Proc. of FEL2010*, pages 433–436, 2010.

[139] T. Shintake and XFEL/SPring Joint Team. Status Report on Japanese XFEL Construction Project at SPring-8. In *Proc. of IPAC2010*, pages 1285–1289, 2010.

[140] T. Hara, K. Fukami, et al. Pulse-by-pulse multi-beam-line operation for X-ray free-electron lasers. *Phys. Rev. Accel. Beams*, 19, 2016.

[141] Z. T. Zhao, D. Wang, L. X. Yin, Q. Gu, G. P. Fang, and B. Liu. The Current Status of the SXFEL Project. *Feature Articles*, 20, 2016.

[142] H. S. Kang, J-H Han, et al. Start to End Simulations of Three Bunch Compressor Lattice for PAL XFEL. In *Proc. of IPAC2012*, pages 1738–1740, 2012.

[143] *NLS Project: Science Case and Outline Facility Design, (Ed. J Marangos, R Walker and G Diakun)*. STFC, 2009.

[144] A. A. Zholents, E. Kur, J. Qiang, et al. Design of the electron beam switchyard for an array of Free Electron Lasers. Technical Report CBP Tech Note 401, 2009.

[145] R. Brinkmann. Some Considerations on X-FEL Beam Distribution, DESY Internal Presentation, 2003.

[146] M. Paraliev, C. Gough, S. Dordevic, and H. Braun. High Stability resonant Kicker Development for the SwissFEL Switchyard. In *Proc. of FEL2014*, pages 103–106, 2014.

[147] G. A. Loew and Altermueller. Design and Applications of RF Separator Structures at SLAC. Technical Report SLAC-PUB-135, 1965.

[148] D. R. Douglas. Design Considerations for Implementing Alternative RF Separator Schemes. Technical Report CEBAF-TN-91-072, 1991.

[149] J. Corlett, L. Doolittle, P. Emma, J. Y. Jung, M. Placidi, A. Ratti, and C. Sun. The NGLS SPreader, Part II, The SRF Deflector Option. Technical Report NGLS Tech. Note 0036, 2013.

[150] R. Wanzenberg. A Fast Switchyard for the TESLA FEL-beam using a Superconducting Transverse Mode Cavity, 2000.

[151] A. Wolski. Damping Rings. *Second International Accelerator School for Linear Colliders*, 2007.

[152] M. J. Barnes, L. Ducimetiere, T. Fowlet, V. Senaj, and L. Sermeus. Injection and extraction magnets: kicker magnets. `https://arxiv.org/ftp/arxiv/papers/1103/1103.1583.pdf`.

[153] P. Williams. Private Communication.

[154] E. Prat and M. Aiba. Four-dimensional transverse beam matrix measurement using the multiple-quadrupole scan technique. *Phys. Rev. Spec. Top. Accel. Beams*, 17:052801, 2014.

[155] M. W. Poole and E. A. Seddon. 4GLS and the Prototype Energy Recovery Linac Project at Daresbury. In *Proc. of EPAC2004*, pages 455–457, 2004.

[156] F. Jackson, D. Angal-Kalinin, et al. The Status of the ALICE R &D Facility at STFC Daresbury Laboratory. In *Proc. of IPAC2011*, pages 934–936, 2011.

[157] R. Williams, A. Schofield, et al. *Physics in Medicine and Biology*, 58, 2013.

[158] F. Jackson, D. Angal-Kalinin, et al. Longitudinal beam dynamics at the ALICE Accelerator R &D Facility. In *Proc. of IPAC2012*, pages 610–612, 2012.

[159] F. Jackson, D. Angal-Kalinin, et al. Electron beam dynamics in the ALICE IR-FEL. In *Proc. of FEL2012*, pages 464–467, 2012.

[160] F. Jackson, D. Angal-Kalinin, et al. Longitudinal beam transport in the ALICE IR-FEL facility. In *Proc. of IPAC2013*, pages 2262–2264, 2013.

[161] F. Jackson, D. Angal-Kalinin, et al. Longitudinal transport measurements in an energy receovery accelerator with triple bend achromat arcs. *Phys. Rev. Accel. Beams*, 19, 2016.

[162] B. D. Muratori and Y. M. Saveliev. ALICE (ERLP) Injector Design. In *Proc. of EPAC08*, pages 196–198, 2008.

[163] Y. M. Saveliev, S. P. Jamison, L. B. Jones, and B. D. Muratori. Characterisation of electron bunches from ALICE (ERLP) DC Photoinjector Gun at two different Laser Pulse Lengths. In *Proc. of EPAC08*, pages 211–213, 2008.

[164] N. R. Thompson, D.J. Dunning, J.A. Clarke, M. Surman, A.D. Smith, Y. Saveliev, and S. Leonard. First lasing of the ALICE infra-red free-electron laser. *Nucl. Instrum. Methods in Phys. Res. Sect. A*, 680(0):117 – 123, 2012.

[165] M. Bowler. Sextupoles requirements in ERLP. erlp-desn-rpt-0032, 2004.

[166] A. Kalinin, R. Smith, and P. A. McIntosh. Diagnostic System Commissioning of the EMMA NS-FFAG Facility at Daresbury Laboratory. In *Proc. of IPAC10*, pages 1134–1136, August 2010.

[167] A. Kalinin, D. Angal-Kalinin, F. Jackson, J. K. Jones, and P. Williams. Application of EMMA BPMs to the ALICE Energy Recovery Linac. In *Proc. of IBIC12*, 117-121 2012.

[168] E. T. d'Amico and G. Guignard. First order design of a new type of isochronous arc. CERN-SL-95-120-AP, 1995.

[169] E. T. d'Amico and G. Guignard. Special lattice computation for the cern compact linear collider. *Phys. Rev. Spec. Top. Accel. Beams*, 4:021002, February 2001.

[170] H. L. Owen and B. Muratori. Choice of arc design for the erl prototype at daresbury laboratory. In *Proc. of EPAC04*, pages 425–454, 2004.

[171] J. W. McKenzie. Private Communication.

[172] D. Angal-Kalinin, F. Jackson, et al. ALICE ERL Intra-train variation investigation using bunch-by-bunch BPMs. In *Proc. of IPAC2013*, pages 2256–2258, 2013.

[173] F. Jackson, D. Angal-Kalinin, et al. Fast electron beam and FEL diagnostics at the ALICE IR-FEL at Daresbury Laboratory. In *Proc. of FEL2013*, pages 557–561, 2013.

[174] T. T. Thakker, F. Jackson, et al. Bunch train characterisation for an Infra-Red FEL driven by an energy recovery Linac. In *Proc. of IPAC2013*, pages 786–788, 2013.

[175] G. Xia, D. Angal-Kalinin, et al. A plasma wakefield acceleration experiment using CLARA beam. *Nucl. Instrum. Methods in Phys. Res. Sect. A*, 740:165–172, 2013.

[176] Y. Huang, H. Wang, R. A. Rimmer, S. Wang, and J. Guo. Ultrafast harmonic rf kicker design and beam dynamics analysis for an energy recovery linac based electron circulator cooler ring. *Phys. Rev. Accel. Beams*, 19:084201, August 2016.

[177] Y. Huang, H. Wang, R. A. Rimmer, S. Wang, and J. Guo. Multiple harmonic frequencies resonant cavity design and half-scale prototype measurements for a fast kicker. *Phys. Rev. Accel. Beams*, 19:122001, December 2016.